UNIVERSITÀ DEGLI STUDI DI MILANO-BICOCCA
DIPARTIMENTO DI SCIENZA DEI MATERIALI
SCUOLA DI DOTTORATO

Nanostructures in Catalysis - Support Effects on Metal Clusters and Oxide Thin Films

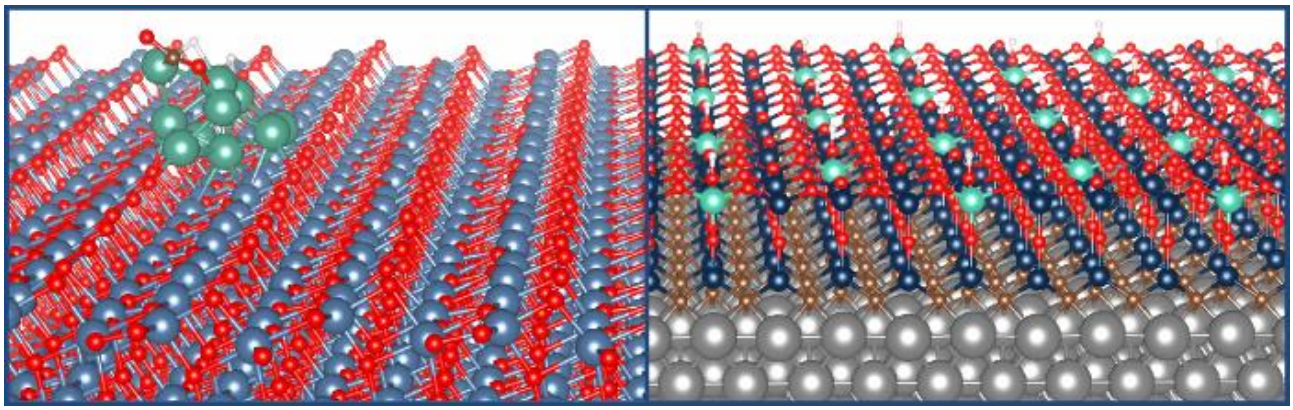

Philomena Schlexer

Registration number: 775519
Ph.D. school: Materials Science and Nanotechnology
Tutor: Prof. G. Pacchioni
Coordinator: Prof. G. P. Brivio
Academic year: 2015/16

Abstract

Catalysis has largely shaped society and will play a key part in the resolution of the energy and environment crisis we are facing in this century. The great advancements in the development of nanomaterials in the realm of nanotechnology have brought forth unforeseen possibilities also for the design of novel catalysts. The production and understanding of highly efficient catalysts based on nanostructured materials is the endeavor of the emerging field of nanocatalysis. In the last years, nanocatalysts have been studied extensively and progress in their large-scale fabrication has been demonstrated. Still, the technology is immature and further research is necessary to capitalize its full potential.

Computational approaches are well suited to investigate the functioning of nanocatalysts and provide valuable atomistic insights. An accurate and efficient method is density functional theory (DFT). In this thesis, we explored the physical and chemical characteristics of supported metal clusters and oxide thin films using mainly DFT. These materials are of special interest in catalysis and many other applications, because of their unique features emerging from the nanostructuring. In particular, we investigated the geometry, the charge state, the cluster-support interaction, and the reactivity of sub-nanometer metal clusters supported on oxides. In a case study, we also addressed size-effects on larger metal nanoparticles. Regarding the supported clusters, we find that van-der-Waals dispersion forces are important for the correct description of the cluster-support interaction. Furthermore, we establish that defects and dopants present on the supporting oxide surface have a determining influence on the clusters, inherently affecting their reactivity. Also the modification of the clusters via alloying alters the metal-support interaction which can be exploited against cluster agglomeration. Nanostructuring of the oxide support engenders new material properties and in this context we examined the features of metal-supported oxide ultrathin films. Finally, we performed mechanistic studies contributing to understand the reaction mechanism of CO oxidation on Au/TiO_2, as well as CO_2 hydrogenation on Ru/TiO_2 and Cu/TiO_2.

Keywords

Nanocatalysis, nanostructures, metal clusters, metal-support interaction, sintering, oxide ultrathin films, gold, silica, titania, density functional theory

Acknowledgements

First and foremost I would like to thank my advisor Prof. Gianfranco Pacchioni. He has been an exceptional mentor and his enthusiasm for research was contagious. I also want to thank my external revisers Prof. Beate Paulus and Prof. Jakob Schiøtz for their valuable comments and encouragements.

I thank Prof. Peter Lievens, Prof. Didier Grandjean, Dr. Salvo Cosentino, Dr. Thomas Picot and Ting-Wei Liao for the supervision and collaboration during my stay at the Katholieke Universiteit Leuven, Belgium. It was interesting and exciting to work with you at the cluster source and to explore the STM and photo-luminescence facilities. Thank you for giving me this opportunity.

Furthermore, I would like to thank Prof. Jakob Schiøtz, Prof. Thomas Willum Hansen, Bela Sebok, and Prof. Ib Chorkendorff for the supervision and collaboration during my stay at Danmarks Tekniske Universitet, Denmark. I enjoyed the time spent with you at CAMD, at the cluster source, and at the ETEM watching the Pt particles melt.

My heartfelt thanks to my colleagues in Italy for the successful collaborations, the helpful discussions and the great time spent together: Dr. Elisa Albanese, Dr. Hsin-Yi Tiffany Chen, Dr. Guido Fratesi, Dr. Sergio Tosoni, and Antonio Ruiz-Puigdollers. The financial support from the European FP7-ITN project CATSENSE (grant agreement number: 607417) is gratefully acknowledged. It was a great experience to be part of this interdisciplinary project. At last, I would like to thank very much my family and my friends for the invaluable support and motivation.

Milan, March 2017

Contents

Chapter 1 Introduction

1.1 Why we need highly efficient catalysts now and in the future

1.1.1 Importance of catalysis for society

Chemical catalysis significantly shapes our society being an integral part of the petrol industry, the production of base chemicals, and the synthesis of fine chemicals and pharmaceuticals. 85-90% of all products in chemical industry rely on catalysis at some production point, and the percentage is continuously increasing. [1] In the petrol industry, zeolites are used as catalysts for crude oil cracking. The latter is a huge global industry with roughly $4 \cdot 10^8$ "tonne of oil equivalent" (toe) of crude oil being produced in 2016 worldwide. [2] Fossil fuels account for more than 80% of global primary energy consumption and accordingly, the production and the use of fossil fuels play an essential role for society. [3,4] Also base chemicals, such as ammonia, methanol or propylene oxide, are catalytically synthesized on a large industrial scale. For instance, $1.46 \cdot 10^8$ metric tons of ammonia and ca. $1.0 \cdot 10^8$ metric tons of methanol are globally produced per year. [5,6] Ammonia is the basis for the synthesis of fertilizers which are indispensable for modern food production. [7] These are just a few examples illustrating the immense role of catalysis for society.

Catalysts lower the activation barrier of chemical reactions, making it possible to conduct the reaction at lower temperatures and/or pressures. This translates to a significant decrease of energy required for the chemical transformation. Furthermore, catalysts can enhance the selectivity of the reaction, and make the use of solvents unnecessary. Consequently, catalysis can minimize waste production. Since catalysis contributes to reduce energy consumption and pollution by by-products, it is an integral part of the "green chemistry" concept.

1.1.2 Catalysis for a sustainable future

The challenge of the 21st century is to tackle the energy and environmental crisis. The rapidly increasing global energy demand due to population growth and industrialization of developing countries results in the continuing growth in fossil fuel consumption. [8,9,10] Since fossil fuel sources are limited and unevenly distributed in the world, it is necessary to increasingly cover the energy demand by alternative energy sources. The use of fossil fuels contributes the main part of greenhouse gas (**GHG**) emissions, in particular CO_2. The CO_2 concentration in the atmosphere has increased by around 40% since the industrial revolution, reaching a value of 400 ppm in 2015. [11,12,13] Anthropogenic activities are the main

cause for this immense growth of the CO_2 level. The global pollution has severe environmental consequences, particularly the climate change. To mitigate climate change, international efforts[1] are pursued to stabilize atmospheric greenhouse gas concentrations.

Various strategies are being developed and implemented to cover the growing energy demand and to reduce GHG emissions. A first strategy is to replace more and more fossil fuels by renewable energy resources. Photo-catalysts can be used to harvest solar energy and off-peak energy of renewable sources can be used to catalytically split water ($H_2O \rightarrow H_2 + ½ O_2$). The latter can for instance be utilized in proton exchange membrane (PEM) fuel cells. The stored energy is then recovered by catalytic electrochemical combustion. Although still under development, PEM fuel cells constitute an appealing technology because of the high efficiency and zero emission. Alternatively, there are many industrial uses for H_2 in the production of base chemicals. Evidently, viable renewable energy systems will require highly efficient catalysts.

CO_2 capture and sequestration or utilization are strategies contributing to the stabilization of CO_2 atmospheric levels. In particular, the utilization of atmospheric CO_2 as a carbon source for the production of synthetic natural gas (**SNG**) and other synthetic fuels is an attractive pathway for CO_2 neutral fuel production. SNG can be distributed over existing natural gas pipelines and synthetic fuels as for instance methanol and higher alcohols constitute transportable fuels for combustion engines. Although the transformation of CO_2 into methane, methanol and higher alcohols is exothermic [1], the uncatalyzed reaction pathways are associated with large activation barriers. Thus, active catalysts are necessary to efficiently recycle atmospheric CO_2. The catalytic conversion of toxic and environmentally damaging pollutants into less harmful chemicals in exhaust catalysts is another example on where catalysis can contribute to a sustainable future. Catalysis is not only a bearing part of green chemistry, but it also plays a determining role to seize the energy and environment crisis. [14]

1.1.3 Requirements for the next generation catalysts

We have seen that catalysis shapes modern society and plays an important role in the realization of a sustainable future. The efficiency of a catalyst has thereby a great impact on the amount of energy consumed and waste produced during the chemical transformation. But what makes a catalyst efficient? There are five main aspects that influence the efficiency of a catalyst. The first aspect is the catalytic **activity**. To compare the activity of different catalysts, the turnover frequency (**TOF**) is a suitable measure. Usually, only special atomic sites are catalytically active and therefore called “active sites”. The TOF describes the number of

[1] For instance, the *Paris Agreement* of the United Nations Framework Convention on Climate Change (UNFCCC) entered into force on November 4th 2016.

revolutions of the catalytic cycle per unit time and is defined as $TOF = n/(S \cdot t)$. Here, n is the number of molecules of the desired product formed in a given time unit t. S is the number of active sites. Is the active site unknown, S can be replaced by the catalyst surface area or the mass or the volume of the catalysts used.

A second aspect defining the efficiency of a catalyst is the **selectivity**. Only in rare cases a catalytic reaction gives only one product. More often, also undesirable by-products are formed, lowering the yield of desired product. An efficient catalyst maximizes the ratio of the desired product formed. A third aspect is the **stability** of the catalyst. Many reactions occur at high temperature and/or pressures. The catalyst should remain active under reaction conditions for a long time. A fourth aspect is **recovery and recyclability**. As we will see later, some catalyst types are not easily separated from the reaction mixture which is accompanied by a considerable complication of the production routine, increasing the production cost and the amount of waste produced. It is therefore desirable that the catalyst is easily recovered from the reaction mixture. Also, the catalyst should be recyclable many times before it becomes inactive. Otherwise, the catalyst consumption produces additional costs. This brings us to another aspect which is the **cost and atom economy**. The catalyst should be made of cheap, recyclable and earth abundant materials, especially when used in a large scale.

There are three types of chemical catalysts which meet these requirements in different ways. We can distinguish between homogeneous catalysts, enzymes, and heterogeneous catalysts. Homogeneous catalysts contain catalysts particles, e.g. transition metal complexes, dissolved in a liquid solvent. Here, reactants and catalyst are in the same physical phase, usually in solution. The active centers are highly dispersed in the solvent, maximizing the accessible chemical reaction centers. Disadvantages are the necessary separation of the product and the catalyst from the reaction mixture, as well as the use of solvents. The latter have to be produced, stored and disposed, which translates into cost and pollution. Enzymes are macromolecular biological catalysts and are used similarly as homogeneous catalysts.

Heterogeneous catalysts are in a different physical phase as the reactants. Usually, heterogeneous catalysts are solid materials, i.e. bulk or powder materials, exposed to the reactants which are either in the gas-phase or in the liquid phase or in solution. In contrast to homogeneous catalysts, heterogeneous catalysts are easily separated from the products and contingent solvents. In the case of gas-phase reactions, no solvent is required. Furthermore, heterogeneous catalysts can be used over a wide range of reaction conditions, i.e. temperatures and pressures. The importance of these advantages is reflected in the fact that by far the major part (~85 %) of all catalysts used is heterogeneous. However, most solids are impenetrable by the reactant molecules and therefore the chemical reactions take place only at the sur-

face of the catalyst. So only a fraction of the material is actually active, which is a clear disadvantage regarding the cost and atom economy, since the active material is often based on late transition metals of which some are rare and costly. Zeolites constitute an exception to this. To increase the accessibility of the reactive centers and reduce the catalyst cost, transition metal nanoparticles can be dispersed on or in inert porous materials. For instance, a gold bar of 20×10×5 cm costs roughly 736 000 $ whereas a brick coated with gold nanoparticles with a coverage of one monolayer equivalent would cost roughly 21 cents. [15] Using supported nanoparticles, the merits of homogeneous (highly dispersed active material) and heterogeneous catalysts (easy catalyst separation etc.) can be combined. [16] The use of supported nanoparticles makes it in principle feasible to achieve a large part, if not all, the requirements listed above. However, unforeseen physical properties can emerge when the dimension of a material is reduced to the nanometer size regime. As we will see in the following sections, these effects can be exploited and give rise to a completely new class of catalysts: Nanocatalysts.

1.2 Nanocatalysis

1.2.1 Catalysis: A pioneer application of nanotechnology

Nanotechnology has conquered and revolutionized a multitude of fields, such as biology, biosensing, communication technology, information technology, materials science, and medicine, just to mention a few examples. Nanomaterials, especially nanoparticles, have been used long before actually being identified as nanomaterials. An example is the use of nanoparticles in medieval stained glass. [17] Nanotechnology emerged as a field in the mid 1980ies with the invention of the scanning tunneling microscope [18] and the discovery of fullerenes [19], although it was conceptualized before by Feynman [20] and Drexler [21]. Not much later in 1987, Haruta et al. discovered that Au nanoparticles below 10 nm effectively catalyze the CO oxidation reaction at surprisingly low temperatures, while bulk Au was inactive under the same conditions. [22,23] Since the emergence of nanotechnology, catalysis has been a key application and presently, nanocatalysis is a rapidly growing field. Magnetically recoverable homogeneous nanocatalysts [24], proton exchange membrane (PEM) fuel cells [25], Fischer-Tropsch nanocatalysts [26], biomass to biofuel nanocatalysts [27], and nano-photocatalysts [28] are just a few examples where nanomaterials have been successfully used as highly active catalysts.

Besides the tremendous accomplishments in the field, most commercial catalysts are still developed by "mixing, shaking and baking". Consequently, their nano-scale functionality is not well understood and therefore not well controlled. For this reason, substantial advances in nanoscience and research on nanocatalysis are still a necessity for the long-term goal of a

rational catalyst design. In fact, this goal is being pursued in academics, as well as in the industry. There are patents not only on nanocatalysts, but also on unique rational catalyst design technologies and approaches, which can be based on experimental and/or computational methods. [29,30,31] Evidently, nanocatalysis has risen to an important business. But what makes nanomaterials so successful in catalysis? In the following, we will explore size effects arising at the nano-scale and outline a few examples on how these effects can be exploited in catalytic applications.

1.2.2 Intrinsic size effects induce unforeseen properties

As the dimension of a material is reduced, new physical properties emerge that are different from the "infinite" bulk material. At which length scale such effects appear is dependent on the physical phenomenon under consideration, and on the material. We distinguish three types of nanomaterials, depending on how many of the three dimensions of the material are in the nanometer size regime: 2D nano-wells (thin films), 1D nano-wires (nanorods and nanotubes), and 0D nano-particles. The nanometer size regime spans three orders of magnitude, i.e. 1-1000 nm, and it can make a huge difference if a material is a few hundred or just a few nm thick. Nanomaterials have at least one dimension in the typical range of 1-100 nm. Is the thickness of a thin film reduced below 2 nm, we speak of ultra-thin films or two-dimensional materials. [32] Similarly, if the size of a nanoparticle is reduced in such a way that the addition or the removal of an atom significantly changes the physical properties of the particle, we speak of a "cluster". However, sometimes the term "cluster" is also used synonymously to "particle", i.e. denoting particles in general without further specification of the particles size regime.

At which size regime size effects can be expected depends on the material and on the property of interest. A property affected equally at all size regimes is the surface to volume ratio. The surface area of 2D-0D nanomaterials is largely increased with respect to the respective bulk materials with the same volume. Obviously, this has a direct influence on the catalytic activity per volume or mass. Furthermore, the abundance of facets, edges and corners is determined by the size and shape of the nanomaterial. As we will discuss later in more detail, some reactions are structure sensitive and take place preferably at special sites, such as steps. Thus, the abundance of certain geometric features can define the reactivity of nanocatalysts, in particular in the case of nanoparticles. [33,34]

Size reduction can significantly affect the electronic structure of a material. Is the extend of the wave-function of an electron larger than the material dimension, the resulting confinement effects lead to the discretization of the electronic energy levels. In this case, we speak of quantum confinement effects. A prominent example of electronic size effects is the opening of the so-called "Kubo gap" (discovered by Kubo et al.) in metal nanoparticles, which is

given by $E_g = \frac{E_F}{n}$, where E_g is the expected band gap, E_F is the Fermi-level of the bulk material and n is the number of free electrons in the nanoparticle. [35] As the size of the metal nanoparticle decreases, the continuous bands become distinct molecular-like states. Evidently, this has far-reaching consequences for the physical and chemical behavior, which in turn largely defines catalytic functionality. Also in thin films, the reduced thickness affects significantly the electronic structure, as it is for instance the case for graphene [36], molybdenum disulfide [37] and zinc oxide [38]. Nanoporous materials can also exhibit unique electronic confinement effects, or induce them on adsorbates. [39]

Also the composition and the stoichiometry of a material can be affected by a reduction of the size into the nanometer regime. The formation of new alloys and core-shell structures of bimetallic nanoparticles are two examples. [40] Similarly, the (most stable) stoichiometry of oxide nanoparticles and thin films can evolve with the size. [41,42]

We have seen that the important chemical features of materials, i.e. the chemical composition, as well as the electronic and geometric structure, can be largely affected by size effects. Novel synthesis techniques allow the control of size, shape and composition of nanomaterials which opens the possibility to design materials with tunable catalytic properties.

1.2.3 Extrinsic size effects: Interaction with the environment

As the physical and chemical properties of a given material are altered due to size effects, also its interaction with the environment is affected. In the best case, this can lead to synergetic effects so that the resulting catalyst is more active as its components. In the worst case, this can lead to a complete deactivation of the catalyst. In the following, we will go through some examples on how the interaction of a nanomaterial with its environment can change its properties.

The increase of the surface area of nanomaterials with respect to the corresponding bulk material (of the same mass) results in an increase of the surface energy. In the case of metal nanoparticles, this is the driving force for agglomeration and sintering. In other words, the inter-particle interaction can affect the size of the nanoparticles. Sintering is responsible for the deactivation of many metal nanoparticle-based catalysts, e.g. of supported Au nanoparticles, under reaction conditions. [43,44] The surface energy of thin films is a driving force to physisorb or chemisorb onto their support materials. [45,42] Some thin-films, in particular chemically unsaturated ones, probably only exist because they are stabilized by the binding to the support compensating the large surface energy.

So, size effects in nanomaterials have also consequences for their interaction with the support. In common heterogeneous catalysts, metal particles are supported on oxides like SiO_2,

Al_2O_3, MgO, TiO_2, and ZrO_2, just mention a few examples. The oxide support plays thereby a determining role for the catalytic activity. [46] A prominent phenomenon is the strong metal-support interaction (**SMSI**) which is particularly important for reducible oxides like titania or ceria. Here, the metal particles react with the support via charge transfer and/or overspill of the oxide onto the metal particles. The latter was for instance reported for Ru/TiO_2 under reaction conditions for the hydrogenation of levulinic acid to γ−valerolactone. [47] In the case of sub-nanometer clusters, the occurrence of a charge transfer between cluster and support can be sensitive to the number of atoms present in the cluster. [48]

When the clusters are deposited on 2D oxide supports, the thickness of the oxide support is as well important for the charge state of supported metal clusters. As the thickness of the oxide reaches a few atomic layers, electron tunneling through the oxide film becomes possible. Au_{20} clusters supported on ultra-thin MgO films supported on a Mo substrate become negatively charged because of a charge transfer from Mo to the Au_{20} cluster. [32] This affects the structure of the cluster which becomes planar in the charged state. The effect is attenuated as the MgO film thickness is increased. The 2D-3D geometrical transformation upon charging is typical for Au sub-nanometer clusters. This is a very nice example on how the size/thickness of the nanomaterials can be used to tune the catalyst properties. In the case of oxide thin films, the support can determine the thin films geometric and electronic structure in various ways. For instance, the growth direction of the thin film can be influenced, as well as the oxide surface termination. [49] Eventually, the presence of the metal substrate provides new binding sites, which can alter the structure and the stoichiometry of the thin films with respect to their bulk counterparts. [50,32]

The interaction of nanoparticles interact with ligands and capping agents can modify their catalytic properties. [51] The binding of ligands and capping agents with the particles, but also the ligands own steric and electronic properties can be exploited to modify the catalytic properties. For instance, chiral capping agents have been successfully used for enantioselective olefin cyclopropanation. [52] Also the reaction conditions, i.e. the gas-phase reactant mixture, the temperature and the pressure, can result in a variety of effects as morphological changes, sintering, and complete chemical modification of the catalyst. For instance, Lai et al. have observed a drastic change of the morphology of Ag nanoparticles upon exposure to 1.33 bar O_2 due to Oswald ripening. [53] Tao et al. have shown that the surface composition of Rh/Pd and Pd/Pt 50/50% bimetallic nanoparticles are different under oxidizing (NO), reducing (CO), and reaction (NO/CO) conditions. [54] Whereas the interaction with ligands and capping agents can be predicted and exploited in a controlled manner, the evolution of a nanocatalyst under reaction conditions proceeds normally without or with little control. For this reason, it is challenging to determine the working principle and the active site of a cata-

lyst under reaction conditions. This is partly due to the physical and chemical complexity of the catalyst and partly because of the limitations of experimental and computational approaches. To work towards the in situ and operando characterization of catalysts, many innovative experimental approaches have been recently developed [55], such as ambient pressure X-ray photoelectron spectroscopy [56], non-linear optical spectroscopy [57], ambient pressure scanning tunneling microscopy [58], in situ transmission electron microscopy with Cs aberration correctors [59]. Also in computational modeling, vigorous efforts are taken to develop increasingly realistic models, as we will discuss in the following chapter. [60]

We have outlined the importance of nanocatalysis as an emerging scientific field and introduced some key features of nanomaterials as catalysts. The complexity emerging from the endless variable parameters of nanocatalysts, like material composition, size and chemical environment, makes it suggestive to concentrate in more detail on the systems which are relevant for this thesis. These are oxide-supported metal clusters and nanoparticles on the one hand, and metal-supported ultra-thin films on the other hand.

1.3 Supported metal clusters and nanoparticles

1.3.1 Preparation and characterization

As defined before, we distinguish between metal clusters and nanoparticles, whereby the first denote metal particles in the non-scalable size regime, i.e. in which the addition or removal of an atom leads to substantial property changes. The nanometer size regime covers three orders of magnitude, but the interesting size regime for nanoparticles is 1-100 nm. Although gas-phase clusters are widely used for fundamental studies [61], we will concentrate on supported clusters, because an important part of this thesis deals with the cluster-support interaction.

A possibility of preparing chemically pure and highly size selected clusters is to create gas-phase clusters, perform a size selection in the gas-phase followed by soft-landing of the clusters onto the support. To prepare the gas-phase metal clusters and nanoparticles, the metal(s) of interest are evaporated. This can be done via exposure to laser pulses, electrical or magnetron discharges, or highly energetic inert gas ions. [62] The plasma or supersaturated atomic gas, respectively, is then thermalized by a buffer gas leading the mixture through a nozzle where supersonic expansion cools the gas-mixture, so that atoms and small clusters aggregate to larger clusters and nanoparticles. To study size-property relations, precise size selection is imperative. In the case of clusters, this means atomically precise selection. Dynamic field quadrupole mass selection [63] and time-of-flight mass selection [64] are two frequently used techniques for mass selection. In both cases, the clusters have to be electrically charged. Usually, neutralization occurs via charge transfer between cluster and

support. After the size selection, the particles are deposited onto the support. Especially for clusters, it is important to ensure their intact landing to maintain the exact number of atoms. For soft-landing, the clusters are deposited with less than 1 eV per atom kinetic energy. [62]

Other examples for methods which have been used to prepare nanocatalysts are thermal evaporation in vacuum [65], electron-beam lithography [66], chemical vapor deposition [67], electrochemical deposition [68], sol-gel or colloidal techniques [69], deposition-precipitation [70] and impregnation methods [71], as well as gas-phase aggregation techniques [72]. Capping agents, have been successfully used to control the shapes of Ag [73], Pt [74] and Pd [75] nanoparticles. In wet-chemistry approaches the resulting size distribution is usually much broader than in gas-phase aggregation techniques.

Relevant techniques for the characterization of supported clusters are scanning tunneling microscopy (STM), atomic force microscopy, transmission electron microscopy (TEM), as well as optical spectroscopies in the visible or infrared. On electrically conducting substrates, the geometric and electronic structure of clusters can be imaged via STM. Nilius et al. have imaged a single CO molecule adsorbed on a Au chain supported on NiAl(110). [76] They have shown how the CO molecule disrupts the delocalization of electron density waves in the chain. Another nice example is the work of Piednoir et al. who produced atomically resolved STM images of small Pd nanoparticles and clusters supported on graphite and MoS_2. [77] Impressive images during the in situ reduction of NiO nanoparticles under 1.3 mbar of H_2 gas in an environmental transmission electron microscope (ETEM) have been produced by Jeangros et al. [78] Also extended X-Ray absorption fine structure (EXAFS) and X-ray absorption near edge structure (XANES) are powerful tools to elucidate the atomic geometry [79], electronic structure modification driven by support/environment [80], and the composition of bimetallic systems [81].

1.3.2 Chemical and catalytic properties

As we have seen in the previous sections, the synthesis method [82], the cluster-support interaction [83,84], size- and shape effects [85,86,87], and the reaction conditions strongly influence the metal particles. Therefore, statements on the chemical and catalytic properties are only valid in a certain chemical environment. For instance, the catalytic activity of Au nanoparticles can be increased by several orders of magnitude in the presence of water. [88,89] Due to the great potential industrial importance of nanocatalysts, such effects have been and are currently investigated intensively. [90,56,91]

Also the support affects the particle properties. So, understanding the functionality of oxide-supported metal particles for heterogeneous catalysis applications requires characterizing the cluster-support interaction. The nature of the metal-support interaction is strongly sys-

tem dependent. The type, size and structure of the metal cluster, as well as the oxide type, surface orientation and termination, and the presence of defects can largely alter the interaction between the clusters and the support.

As the size of the systems of interest decrease and the experimental control approaches atomic resolution, the role of computational studies is growing steadily. Computational studies can contribute to understand the interaction between metal clusters and oxide supports. [92,93,94] Density functional theory (DFT) is well suited for this purpose, because structural and electronic properties of the metal-oxide interface can be predicted with acceptable accuracy while maintaining an affordable computational effort describing the large number of atoms necessary to include the oxide surface and a metal cluster. This will be discussed in more detail in the next chapter.

1.4 Supported oxide thin and ultra-thin films

1.4.1 Preparation and characterization

Thin films, and in particular oxide thin films, play an important role in heterogeneous catalysis as models of heterogeneous catalysis and, in some selected cases, as real catalysts. They can be formed in situ due to the oxidation of the metal catalyst under reaction conditions. O_2 molecules can form different super-lattices on the meal surface via on-surface chemisorption. Depending on the O_2 pressure, also stable oxide over-layers on metal particles can be formed, where also the subsurface is oxidized. [95] Furthermore, oxide thin films can also be the result of the strong metal-support interaction (SMSI), which was introduced before. [96,97] The SMSI can have promoting or deactivating effects on the catalytic activity of the catalyst. Another method to prepare thin films is atomic layer deposition (ALD), which is a key thin film deposition technique. [98] ALD can be seen as a subcategory of chemical vapor deposition, in which the surface of the support is repeatedly exposed to the separate precursor chemicals. In UHV facilities, oxide ultra-thin and thin films can be synthetized by vapor deposition of an oxide-forming material (e.g. Mg, Fe, Si) onto a transition metal support (e.g. Mo, Pt, Ru) in the presence of oxygen. [99,100] The metal support can thereby have a "directing" effect in the sense that the preferred thickness and topology of the thin film is influenced by the choice of the metal support. [49]

Oxide ultra-thin films consist of only a few atomic layers and are therewith thin enough that electrons can tunnel through them. Hence, metal supported oxide ultra-thin films can be investigated via surface science techniques which require an electrically conducting sample, such as scanning tunneling microscopy (STM). This opens up the possibility to image the atomic structure of amorphous materials in real space to gain a fundamental understanding of the topological features. [101] Other relevant characterization techniques are atomic force

microscopy, infra-red spectroscopy, low energy electron diffraction, photoemission electron microscopy, X-ray photoelectron spectroscopy, and temperature programmed desorption.

1.4.2 Chemical and catalytic properties

The chemical variety of oxide thin films is well reflected in the various different technological applications. For example, they are used as protective coating against corrosion [102], they function as insulating layers in integrated circuits [50] and can be used as oxide semiconductor thin-film transistors [103]. Due to finite size effects, but also because of the interface to the supporting material, thin and ultra-thin films constitute a unique class of materials. [104,105,106] The properties of these novel materials can be exploited in catalysis and gas-sensing, and electro-catalysis. [107,108]

Some ultra-thin films interact only weakly with the metal support, opening the possibility for small molecules to intercalate at the interface between metal support and thin film. Here, the molecules may react under the confining conditions imposed by the presence of the film. This effect was studied already extensively for carbon nanotubes and, although to a lesser extent, for graphene. [109] An examples is the work of Mu et al. who studied the CO oxidation reaction at the interface between graphene and Pt(111). [109] A weak interaction between thin-film and metal support can also be found for some metal-supported oxide films, as for instance for silica bilayers supported on Pt or Ru, and for ultra-thin ZnO films supported on Ag and Au. In these cases, it should be in principle possible to intercalate small molecules under the thin film. In fact, Emmez et al. successfully adsorbed CO and D_2 molecules at the interface between a silica bilayer and its Ru(0001) support. [110] As silica monolayers and bilayers are porous materials with pore sizes in the range of circa 0.3-0.9 nm, they may act as molecular sieves for small molecules and metal atoms. For example, Pd atoms can penetrate the hexagonal pores of a crystalline silica bilayer, while Au atoms stay on top of the silica bilayer. [111,112]

Metal-supported oxide thin films can also be used as support for metal atoms and clusters. The resulting systems are used as model catalysts, as well as constituting new catalysts. Oxide thin films can be used as templates for cluster growth. Nilius et al. have shown that ultra-thin alumina films supported on NiAl(110) have a templating effect on $Au_{3\text{-}7}$ chains due to the electronic interaction of the chains with the NiAl support. [113]

Chapter 2 Computational modeling in catalysis

2.1 Catalysis - a multiscale phenomenon

To meet the quest for highly efficient catalysts, an in-depth understanding of the catalyst working principles is required. Rational catalyst design strategies can be developed based on this knowledge. The performance of a working catalyst is ultimately limited by the molecular-level processes taking place at and in the vicinity of the active sites. However, these processes, and the active sites, are not just intrinsic properties of the catalyst, but depend notably on the reaction conditions. The gas-phase composition, the pressure and the temperature have a consequential impact on the catalyst state by defining for instance the oxidation state, and the surface composition and structure of active parts. The temperature and the gas-phase composition on and above the catalyst surface, in turn, depend on the mass transport inside the reactor. This example clearly illustrates how catalysis is a complex phenomenon being defined by physical processes which take place at different length and time scales. This multiscale character engenders challenges in understanding the working principle of a catalyst, independently on whether an experimental or a computational (or combined) investigation approach is pursued. As in many other fields, modern computational science has become a key contributor for the elucidation of catalytic phenomena. [114] How catalytic processes, taking place at different time and length scales, can be simulated is shown in **Fig. 1**. In the following, we will outline the key methods relevant for the different time and length scales, proceeding from the macro- to the microscale. Given the large importance of heterogeneous catalysis and the focus of this thesis, we will focus on heterogeneous catalysts from now on.

In terms of length, the macroscale covers reactors of a few cm, used in the laboratory, up to the 10 m industrial reactor vessels. On this length scale, simulations are used for reactor design and to describe heat and mass transport. The mass and heat transport in the reactor is influenced by the reactor design and the description of such effects is therewith equally important as the chemical properties of the active sites for the overall performance of the catalytic process. In terms of time, the macro-scale is given mainly by the residence time of the molecules in the reactor. The reactants can reside in the reactor for seconds, and can in principle remain forever on the catalyst surface, e.g. as poisons. Simulations on this length scale are based on continuum theories in which the problem-relevant differential equations are solved numerically, e.g. the Navier Stokes equations.

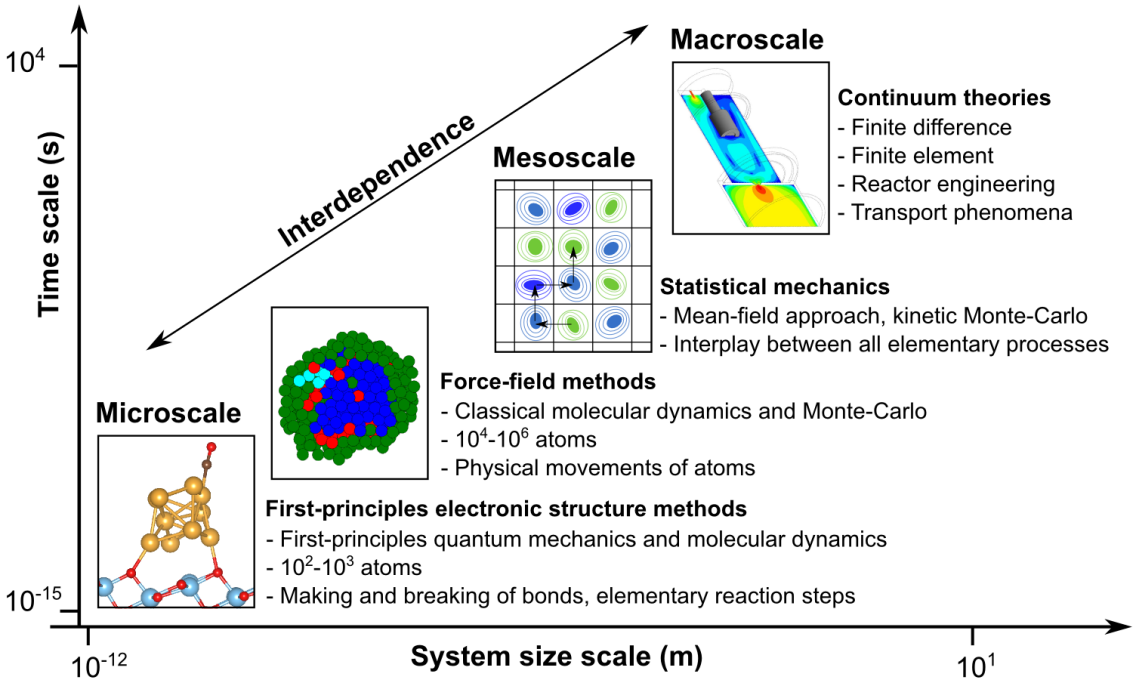

Fig. 1: Computational methods used to simulate different time and length scales of processes relevant in catalysis.

In heterogeneous catalysts, the active material is usually dispersed in/on a porous support material which is either inert or has a promoting effect on the active material. This way, the surface of the active material is maximized and the active material is stabilized under reaction conditions. Metal nanoparticles are usually used as active material, and the support particles have a size from cm to mm. The length regime between nm and mm can be seen as the mesoscale, whereby the nm length scale constitutes an intermediate between the mesoscale and the atomic scale. An interesting phenomenon taking place at the mesoscale, in terms of both length and time, are the spatiotemporal patterns observed in the Pt-catalyzed oxidation of CO. [115] In terms of time, the mesoscale is defined by the collective behavior of reaction events (ensemble average) which evolve in times from ps to ms, or even longer. [116] In particular, reactive events take place at the ps time scale, but the time between the reactive events can easily take µs. In that sense, the reactive events are "rare events". The collective evolution of these rare events can be simulated using statistical mechanics. The two main branches used are kinetic Monte-Carlo (**kMC**) simulations and the mean-field model. The mean-field model is an approximation to the kMC approach. Here, the details between the one-body adsorbate and the rest of the system are introduced as an average interaction. [4] Realistic reaction rates and the formation of long-range ordering of adsorbates due to adsorbate-adsorbate many-body interactions are simulated using statistical mechanics.

Between the mesoscale and the atomic scale, we can define an intermediate region which covers the nanometer length scale and ranges from the femtosecond to microsecond time scale. This is the regime of nanoparticles and enzymes. As we have seen in the previous chapter, the size, the shape, the atomic structure and the composition of the nanoparticles can have major impact on their reactivity. The composition of bimetallic nanoparticles, i.e. alloy vs. core-shell, can be simulated via classic molecular dynamics (**MD**) simulations. On the other hand, the nanoparticles show dynamic behavior under reaction conditions, changing their size and shape. Some of these features, such as the melting process, can be captured with MD. In contrast to the previous modeling approaches, MD applies atomistic models, i.e. the distinct atoms are resolved. In classical MD, the electronic structure is unknown and therefore the making and breaking of bonds cannot be explicitly simulated. For this, we have to explicitly consider quantum effects.

This brings us to the last and smallest time and length scale which is the length scale of individual atoms (and bonds) and the time scale of atomic vibrations. Here, quantum mechanics governs the physical phenomena und thus first-principles electronic structure methods are the methods of choice. In particular, DFT has become the working horse of molecular-level computations in catalysis, because of the good compromise between accuracy and computational efficiency. First-principles electronic structure methods allow us to investigate possible reaction mechanism on a molecular level; from the adsorption of the reactants over the activation barrier to the product desorption. The role of electronic structure methods in catalysis will be discussed in more detail in the next section.

We have seen that catalysis is a complex multiscale phenomenon. However, any computational model requires a certain simplification of the real system. The model should retain the chemically relevant features of the catalyst, however, it is not always clear which the relevant features are. For instance, the number of atoms that can be treated at the DFT level is limited to a few hundred and this ultimately limits the accuracy of the model. At the moment it is not computationally feasible to simulate a 5 nm metal particle supported on an oxide surface at the standard DFT level. So, the nanoparticles are normally either represented by periodic metal surfaces, or by supported sub-nanometer clusters. Therefore, reactions catalyzed by supported metal nanoparticles are still not well understood. [117]

While highly simplified models can indeed give valuable insights [118], some phenomena arise solely when the complexity of the system is reflected in an appropriate manner. To tackle the complexity of a realistic model, multiscale modeling is the method of choice. Here, the level of theory is adapted to the relevance of the different regions for the problem studied. [118] A nice example is the work of Maestri and Reuter, who hierarchically combined semi-empirical methods and first-principles calculations to investigate the water-gas-

shift and reverse water-gas-shift reactions on Rh. [119] Another example is the study of Liu et al. who used a quantum mechanics/molecular mechanics (QM/MM) multiscale modeling approach to study benzene hydrogenation reaction on molybdenum carbide nanoparticles in the process of in situ heavy oil upgrading. [117] The potential and the general impact of multiscale modeling are clearly reflected in the fact that the Nobel Prize in Chemistry 2013 was awarded to Karplus, Levitt, and Warshel "for the development of multiscale models for complex chemical systems". [118]

As well as for the individual approaches, the strong interdependence between the different scales give rise to chemical and technical challenges also for multiscale modeling. The strong interdependence between the scales is reflected in the collective behavior of reactive events, the dynamic character of catalysts, and many other effects. For instance, the type and the coverage of predominantly adsorbed species are largely dependent on adsorbate-adsorbate many-body interactions, as well as the gas-phase pressure, temperature and composition. These effects are difficult to account for, and are therefore often completely neglected in simplified models. In fact, this can be seen as a manifestation of the well-known pressure and materials gap which is not only a computational issue, but exists also in experimental studies since operando catalyst characterization is challenging. [55]

We have shortly outlined the relevant approaches used in computational modeling and we have seen that first-principles electronic structure methods play a crucial role for a molecular-level understanding of catalytic processes. In the following section, we will discuss in more detail how first-principles electronic structure methods, in particular DFT, can be used to study the working principle of catalysts and to develop novel catalysts.

2.2 Role of first-principles electronic structure methods in catalysis

2.2.1 DFT - an excellent tool for catalysis research

There are two branches of electronic structure calculations: Hartree-Fock (**HF**) and post-Hartree-Fock methods on the one hand, and density functional theory (**DFT**) on the other hand. As we will see in more detail in the next chapter, the HF method does not include electronic correlation which is however crucial to correctly predict the making and breaking of bonds. Electron correlation can be introduced via Møller-Plesset second-order perturbation theory. However, this is accompanied by a quite unfavorable scaling of the computational effort with the system size (formally $O(N^5)$). [120] DFT, on the other hand, accounts for electron correlation approximately and scales formally in $O(N^3)$ with the system size. Also linear-scaling DFT exists, but only for certain systems (with band gap) and with special approaches. Experimental bond lengths are typically reproduced within ± 0.02 Å, fre-

quencies are reproduced within 5-10% (less after scaling), and adsorption energies of molecules on transition metal surfaces can in some cases even be reproduced within 0.1-0.2 eV. [4] It is worth noting that the performance of DFT strongly and ultimately depends on the exchange-correlation functional applied and thus the numbers given above are intended as an orientation. This will be discussed in more detail in the next chapter. Due to the computational efficiency in combination with the good chemical accuracy, DFT is the standard first-principle method to investigate catalytic reactions on a molecular level. In the following, we will therefore concentrate on DFT and how it can be used for the design of new catalysts. Given the immense importance of heterogeneous catalysis, and the overall theme of this thesis, we will thereby focus on heterogeneous catalysis.

2.2.2 Thermochemistry and transition state theory

The properties calculated via DFT are valid only at T = 0 K and p = 0 bar, because temperature and pressure effects are completely neglected. However, reaction energies, in particular adsorption/desorption energies, depend largely on the reaction conditions. To connect the DFT-based atomistic insights to the meso- and macroscale, we consider the isothermal-isobaric (NpT) ensemble. The NpT ensemble is evaluated via the Gibbs free energy change of the process of interest, $\Delta G = \Delta H - T\Delta S$. ΔH is the change in enthalpy given by $\Delta H = \Delta U - p\Delta V$, where U is the internal energy and p and V are the pressure and the volume of the system, respectively. The internal energy is the thermally averaged energy of the occupied states. The largest contribution to U is the zero-point energy (ZPE) corrected ground-state energy, E_0. It is therefore a good approximation to ignore the other contributions to the internal energy and set $U \approx E_0$. The expansion term $p\Delta V$ is normally small and therefore often neglected. For the adsorbed species, the entropic contribution to the Gibbs free energy $T \cdot S_{ADS}$ is as well small, since most of the translational and rotational degrees of freedom of the molecules have been eliminated due to the bonding to the surface. [4] In principle, there is a configurational contribution to the entropy of adsorbed species, but this is a complex problem (not at last due to adsorbate-adsorbate interactions) and it can be ignored in a simplified treatment. [4] The Gibbs free energy for adsorption can thus be approximated as $\Delta G_{ADS} = \Delta E_{ADS} - T \cdot S_g.$, where ΔE_{ADS} is the ZPE-corrected DFT-based adsorption energy, S_g is the entropy of the gas-phase molecules which can be deduced from the partition function. Within the ideal gas approximation, the partition function can be easily calculated from our computational data.

The role of the catalyst is to decrease the activation barrier present in the uncatalyzed reaction. This can be achieved via the formation of intermediates and by stabilizing the transition states of elementary reactions. The transition state is a concept from transition state theory (**TST**), which is based on the idea that the potential energy surface (**PES**) of an ele-

mentary reaction can be divided into reactant and product region; the minimum energy points of these regions being the initial state and the final state, respectively. The border between the two regions is the transition state. [4] In other words, the transition state (**TS**) is a saddle point on the minimum energy path (**MEP**) between the reactant and product region of an elementary reaction. TST is based on four assumptions. The first is that the energy of the reactant region follows the Boltzmann distribution. The second assumption is that the Born-Oppenheimer approximation holds for the reaction. The third is that quantum tunneling through the reaction barrier is negligible. The fourth assumption is important for the computation of reaction rates and states that no recrossings from the product to the reactant state occur. The validity of these assumptions has to be verified from case to case. Furthermore, in harmonic transition state theory, the PES at the initial state and at the transition state is assumed to be smooth enough for a second-order Taylor expansion.

Two frequently used techniques to determine the transition state via DFT are the dimer method and the nudged elastic band (**NEB**) method. In the dimer method, the minimum energy structure of a basin in the potential energy surface (**PES**), i.e. the reactant/product structure, and an additional image which is supposed to become the transition state are needed as input. The two images are called "dimer". [121] In the NEB method, a number of intermediate images on the MEP between initial and final state are optimized in such a way that the energy of all images is minimized while the spacing to neighboring images is maintained. In a modification of the NEB method, the highest energy image is driven up to the saddle point by inverting the forces along the tangent going through the point of the MEP. This method is called climbing-image NEB method and has been used in this thesis. [122]

Once the energy barrier of the rate determining elementary reaction is known, it is possible to determine an upper limit for the rate constant k_{TST} based on first-principles thermodynamics and transition state theory via $k_{TST} = \frac{kT}{h}\exp\left(\frac{-\Delta G_{TS^\circ}}{kT}\right)$, where k is the Boltzmann constant, T is the temperature, h is the Planck's constant, and ΔG_{TS° is the standard Gibbs free energy difference between the initial state and the transition state. The exact reaction rate can then be estimated via micro-kinetic modeling or kinetic Monte-Carlo simulations. We refrain from an in-depth treatment of these methods as is not the scope of this thesis and the interested reader is referred to reference [4].

2.2.3 The descriptor-based search for novel heterogeneous catalysts

In heterogeneous catalysis, chemical reactions normally take place at the surface of a solid catalyst material. On the molecular level, heterogeneous catalysis is therefore a meeting point between condensed-matter physics and chemistry. [123] The involvement of a surface in a chemical reaction markedly augments its complexity and therefore a distinct set of con-

cepts has to be developed to describe surface chemistry. [123] In terms of catalyst design this means developing descriptors linked to the catalytic activity of a material in order to predict the performance of a potential catalyst without explicitly examining the complete reaction mechanism. As we have delineated in the previous sections, it is not trivial to establish the reaction mechanism a priori. Often, a reaction has many possible intermediates and reaction pathways, e.g. the hydrogenation of CO_2, which makes a fully first-principles based analysis prohibitive, especially when several possible catalyst materials should be screened. In the following, some important concepts are introduced which allow us to understand trends for a given class of reactions and a given class of catalyst materials. The latter is a necessary groundwork for rational catalyst design.

The catalytic process in heterogeneous catalysis can be divided into three steps. The adsorption of the reactants (or a part of them) on the catalyst surface, the reaction on the catalyst surface and the desorption of the products. The adsorption and desorption processes are thereby equally important as the reactive events. A too weak binding of the molecules to the surface can inhibit the necessary adsorption of the molecules on the catalyst and a too strong adsorption poisons the catalyst. The catalyst should therefore exhibit an "optimal binding strength" for the molecules involved. This is known as the Sabatier principle. [124] Is the catalytic activity (e.g. the turnover frequency) plotted against the binding strength, the resulting curve exhibits a volcano shape and is therefore called "volcano plot". The principle works best when the compared materials are of the same class, e.g. all closed-packed transition metal surfaces. The Sabatier principle is a qualitative concept, since no further specification on the binding strength of the catalyst is given. Therefore suitable descriptors for the binding strength must be found. Electronic structure methods allow the calculation of adsorption energies, which are not always easily determined experimentally. [125] The adsorption energy is a straight forward and convenient measure for the binding strength of adsorbates on the catalyst surface. [126]

This brings us to a second concept which is the correlation between different adsorption energies. For instance, the binding energies of carbon to transition metal (211) surfaces scale well with that of hydrogen to these surfaces. [127] It is therefore not necessary to account for both parameters independently to set up a valid volcano plot. For instance, for ammonia synthesis the nitrogen adsorption energy only can be used to construct a valid volcano plot [128], the hydrogen adsorption energy follows a linear correlation to that of nitrogen. For other reactions the binding energies of two or more molecules are needed. For instance, for ethanol synthesis from CO and H_2, the O binding energies and the C binding energies have to be taken into account, because they do not follow such a linear scaling relation. [127] A similar scaling relation applies for the activation barrier and the reaction energy. These are the Brønsted-Evans-Polanyi (**BEP**) relations. [129,130] A linear relation between the activa-

tion barrier and the reaction energy is observed for a given class of materials, i.e. the more exothermic the reaction, the smaller the activation barrier. The relation may be restricted to a certain class of materials, as for instance only to closed-packed surfaces. In cases where the structure of the active site has a major impact on the BEP relation, the reaction is called structure-sensitive. For example, there is a linear dependence of the dissociation barrier on the adsorption energy for the dissociative adsorption of N_2 on closed-packed transition metal surfaces. The same is true for stepped surfaces, but here, the activation barriers are always roughly half an eV lower than on closed-packed surfaces. [131] The BEP relations are universally valid, i.e. they have been found for different classes of materials (e.g. oxides, metals and carbides) and different classes of reactions. [132,133]

We have seen that in heterogeneous catalysis there can be a coherence between the adsorption energies of different molecules as well as a relation between the reaction barrier and the reaction energy. This implies a determining influence of the inherent catalyst properties on all these entities. To pursue this in more detail, we can analyze the bonding between the molecules and the catalyst. The following concept aims to simplify the description of the chemisorption of molecules on transition-metal surfaces. When a molecule is brought in contact with a transition metal surface, it interacts with the metals sp- and d-bands. The interaction between the molecule and the sp-band of a given transition metal leads to a stabilization and broadening of the molecules valence states, which become renormalized. This behavior is similar for the different metals. Chemical differences in the adsorption mode of a molecule on different transition metal surfaces are due to the interaction of the molecules with the metals d-band. According to the d-band model, coupling to the d-band splits the renormalized valence states into bonding and anti-bonding states. The bonding states are below the renormalized states, and the anti-bonding states are above the d-states. So, the position of the d-band with respect to the Fermi-level determines in how far the anti-bonding states are filled. This in turn affects the binding strength. So, as the energy of the d-band increases with respect to the Fermi-level, the stronger the adsorption energy. A linear dependence of the adsorption strength on the position of the d-band center with respect to the Fermi level has indeed been found for different adsorbates and surfaces. [134,135] The d-band center is defined as $\varepsilon_d = \frac{\int_{-\infty}^{\infty} n_d(\varepsilon)\varepsilon \, d\varepsilon}{\int_{-\infty}^{\infty} n_d(\varepsilon) \, d\varepsilon}$, where $n_d(\varepsilon)$ are the d-projected states and ε is the energy, e.g. with respect to the Fermi-level $\varepsilon = E - E_F$. So, the d-band center can be directly deduced from first-principle electronic structure calculations. The correlation between the relative position of d-band center with respect to the Fermi-level and the adsorption strength is a powerful tool to screen various metal surfaces without explicitly adsorbing the molecule of interest on all of them.

We have seen that the tremendous complexity of reactions taking place on solid surfaces can be simplified via the Sabatier principle, the scaling relations, the BEP relations and the d-band model. However, all these means are of limited help if the active site of the catalyst is unknown. For instance, it can make a determining difference if an N_2 molecule is split on a terrace site or a step. So, the model has to be designed with care reflecting all important features of the catalyst. In the next section we will see that this can be a formidable challenge.

2.2.4 The search for the active site

To understand the working principle of a heterogeneous catalyst, it is necessary to know on a molecular level, where exactly the reactants adsorb, how they (possibly) dissociate, react with other components and desorb. As we have seen before, electronic structure methods are well suited for the search of the active site. A necessary condition is, however, that the model captures the important features of the catalyst. Real catalytic systems can exhibit a degree of complexity that current computing methods simply cannot capture. Therefore, a combined experimental and computational approach is beneficial. In the following, we will explore different types of heterogeneous catalysts and discuss advances made in the search of the active site.

Many heterogeneous catalysts are impenetrable for molecules, and the reaction takes thus place at the surface. On a surface there are various chemically distinct sites where the reaction may take place. This stands in contrast to molecular homogeneous catalysts or enzymes, where the active center can be straightforwardly determined. Here, the active site is usually given by a coordinately unsaturated metal site. Can we find an analogy also on extended metal surfaces? Let us reconsider in more detail the transition metal-based catalysts. Already on a metal fcc (110) surface, we can distinguish at least three possible adsorption sites: top, bridge and hollow. The coordination number (CN) increases from top (CN=1) to bridge (CN=2) to hollow (CN=3 or 4). The different adsorption energies of molecules on the three sites can be experimentally distinguished, e.g. via temperature programmed desorption. [1] Evidently, the different adsorption strengths may result in chemically different behavior of the adsorbed molecules. So, already on a flat perfect metal terrace, there are chemically distinguishable sites. On a real surface, also steps kinks, edges and corners, as well as point and line defects exist. Things are even more complicated on oxide surfaces, due to the presence of defects, impurity atoms, hydroxyl groups, etc. [136]

We have seen before that the activation barrier and the reaction energy is universally correlated and therefore the discussion does not only apply for the adsorption energies, but also for the reaction energies in general and the activation barriers. We have seen that in some cases we can locate in a more precise manner, where the important step of a reaction occurs,

e.g. N_2 dissociation on Ru steps. [137] However, no systematic procedure to determine the active site for a given reaction on a metal surface has been developed. It may be even questionable if the term "active site" is a good descriptor for molecules on metal surfaces under real catalytic conditions. Molecules can exhibit a large surface mobility already at mild temperatures and instead of a static relation of reactant coverages, spatio-temporal concentration changes, temperature changes, and morphological changes can be encountered. [138,139] Such instabilities make it difficult to determine the active site, especially if the system evolves chaotically. It should be mentioned that the term "chaotic" is reserved for extremely sensitive situations. But even in non-chaotic systems, the kinetic development is not always easily predicted. An example is the occurrence of hysteresis in CO coverage and reaction probability in the CO oxidation reaction on Pt/Al_2O_3. [140]

Until now, we have concentrated mainly on extended metal surfaces, but of course, there are many other types of heterogeneous catalysts. Let us therefore consider also an example of the class of inorganic solids. The conventional Ziegler-Natta catalyst for alkene polymerization is made of α-$TiCl_3$ supported on $MgCl_2$. [141] The active sites for the stereo-regular polymerization of alkenes were found to be Cl-vacancies in the α-$TiCl_3$. [142] So in this case, a well-defined active center was found.

Another class of inorganic heterogeneous catalysts is that of single-site heterogeneous catalysts. As the name already indicates, the active site of these catalysts is usually known. To this class belong materials that have individual isolated ions, atoms, molecular complexes and (bimetallic) clusters anchored to a high-area support, such as amorphous porous silica or zeolites. [143] Zeolites are used as industrial catalysts for large-scale oil refinement and petro-chemistry. [144] An immense scientific effort has been made to understand the functioning of zeolites as catalysts and the treatment of this topic would largely exceed the purpose of this section. In short, the key features of zeolites are acidic sites, introduced by substituting Si atoms in the inert silica framework by Al. The Lewis acid centers can be transformed into Brønsted acid centers by adding water. [145] The nanometer sized pores of zeolites induce confinement effects resulting not only in high shape selectivity, but also affecting other chemical properties such as the adsorption energy of reactants. [146] Single iron centers dispersed in Fe-ZSM-5 zeolitic catalysts act as active centers in the selective oxidation of methane at low temperature. [147] It is also possible to introduce small metal clusters into zeolites, which constitute the active centers in a variety of reactions. An example is the methanation of CO using small Ru clusters dispersed in zeolite-Y. [148]

Another class of heterogeneous catalyst consists of metal nanometer and sub-nanometer particles dispersed on oxides surfaces. These systems have been found to catalyze a large variety of reactions, even if neither the oxide nor the corresponding bulk metal shows cata-

lytic activity for the respective reactions. [149,150] This is especially true for supported Au nanoparticles. A lot of research is dedicated to illuminate active sites and reaction mechanisms of such catalysts. [151,152] Generally, there are several possibilities on where the reaction or a part of the reaction may take place: On the particle, on the support or at the interface between particle and support. If we reconsider the intrinsic and extrinsic size effects described in the previous chapter, it becomes clear how complex the topic is which makes the search for the active site in oxide-supported metal particles is challenging.

2.3 The goals of this thesis

The major part of this thesis is related to the European FP7-ITN project CATSENSE. The goal of the projects is to design novel high performance catalysts and biosensors based on metal clusters produced in the gas-phase and deposited on a stable support. The contribution of this thesis is the simulation of the molecular and electronic structure of mono- and bimetallic clusters in the gas-phase or supported on oxides using computational methods (mostly based on DFT). As outlined in the preceding chapters, the properties and the reactivity of metal clusters largely depend on their physical and chemical environment. DFT is a suitable computational method to investigate supported clusters; however, the Hamiltonian has to be chosen with care to capture all important electronic effects. The first goal of this thesis is therefore to test the effect of van-der-Waals forces on the cluster-support interaction of small Ag and Au clusters supported on TiO_2. The results are summarized in chapter 4.

The second goal is to compare our models to experiments to verify our methods and assist the experimental characterization. This is done in two case studies. In the first, we compare simulated and experimental STM images to investigate the geometry and the charge state of supported Au clusters. The experiments reported in this study were performed by Dr. C.-M. Yim in the group of Prof. G. Thornton, University College London. In the second case, the melting of Au and Pt nanoparticles in the gas-phase is investigated via molecular dynamics and the results are compared to those obtained via transmission electron microscopy. This study was performed with our project partners at Danmarks Tekniske Universitet under supervision of Prof. Jakob Schiøtz. The experiments were performed by Prof. T. Willum Hansen, B. Sebok, and Prof. I. Chorkendorff. The results are summarized in chapter 5.

Another major goal is to contribute to determine the sites of the oxide surface where nucleation and growth of clusters occur preferentially and the role that these sites have in determining the cluster properties. This goal is addressed in chapters 6-7. Here, we will see how the support can define the chemistry of small metal clusters supported on TiO_2 and SiO_2. The effect of defects and dopants on the geometry, the charge state and the metal nucleation and anchoring is explored.

Oxide ultra-thin films play an important role in heterogeneous catalysis as model supports for clusters, but they also occur in real catalysts, e.g. via strong metal-support interaction. Furthermore they constitute a new class of materials with potential use in catalysis. In chapter 8, we will explore the chemistry of silicon-based ultra-thin films in two case studies.

A last goal of this thesis is the simulation and prediction of chemical reactions catalyzed by supported clusters. This goal is addressed in chapter 9. In a first study, we explore mechanistic aspects of the CO oxidation reaction catalyzed by Au particles supported on titania. The experiments reported in this study were performed by Dr. D. Widmann et al. in the group of Prof. J. Behm, Universität Ulm. In a second study, we compare titania-supported Cu_{10} and Ru_{10} clusters for CO_2 activation and hydrogenation. We here explore the role of the support for the reactivity of the clusters and the effect of adsorbate-adsorbate interactions on the reaction mechanism.

Chapter 3 Methodology

3.1 The electronic structure problem

The macroscopic properties of a material are ultimately determined by its atomic-scale properties, which are governed by quantum mechanics. The mathematical apparatus of quantum mechanics is the Schrödinger equation, published in 1926. [153] Our models contain typically 30-300 atoms and the investigated properties are stationary. We therefore use the time-independent, non-relativistic Schrödinger equation, eqn. (1), which is an eigenvalue equation. Here, $\hat{H}$ is the Hamilton operator, E is the total energy (eigenvalue) and ψ is the wave-function (eigenstate) of the system.

$$\hat{H}\psi = E\psi \tag{1}$$

$$\hat{H} = \hat{T}_n + \hat{T}_e + \hat{V}_{ee} + \hat{V}_{ne} + \hat{V}_{nn} \tag{2}$$

The Hamilton operator is specified in eqn. (2), consisting of kinetic $\hat{T}$ and potential $\hat{V}$ energy operators. The index n stands for the nuclei and the index e stands for the electrons. The wave function ψ depends on all electronic and nuclear coordinates, $\psi = f(\boldsymbol{r}_i, \boldsymbol{R}_I)$, and must be anti-symmetric with respect to the exchange of two fermions. In principle, all physical properties of the system can be derived from its wave function. The wave function is however generally unknown, and is not a physical observable. Exact numerical solutions are only known for the homogeneous electron gas and systems with a small number of electrons.

To make the problem tractable also for larger systems, we introduce the Born-Oppenheimer approximation. [154,155] Here, the electronic motion is decoupled from the nuclear motion. The wave function is written as a product of electronic and nuclear wave functions, $\psi = \psi_e(\boldsymbol{r_i}, \boldsymbol{R}_I)\psi_n(\boldsymbol{R}_I)$. The nuclear motion, represented by $\hat{T}_n$, can be treated quantum mechanically or classically. Then $\hat{V}_{nn}$ becomes a constant and this gives the electronic Schrödinger equation, $\hat{H}_e\psi_e(\boldsymbol{r_i}, \boldsymbol{R}_I) = E_e(\boldsymbol{R}_I)\psi_e(\boldsymbol{r_i}, \boldsymbol{R}_I)$. Here, ψ_e and E_e are only parametrically dependent on the nuclear coordinates. In the following, we will always refer to the electronic entities ($\hat{H}_e, E_e, \psi_e, \hat{T}_e$) and we therefore drop the indices "e". To calculate the ground state wave function, we use the variational principle, stating that the ground state energy (E_0) assigned to the exact wave function (ψ) is always lesser or equal the expectation value of a trial wave function (ψ_t): $E_0 = \langle\psi|\hat{H}|\psi\rangle \leq \langle\psi_t|\hat{H}|\psi_t\rangle$. The search for the best trial wave function is the subject of wave function based electronic structure methods.

A prominent wave-function based electronic structure approach is the Hartree-Fock (HF) method. Here, the wave function is approximated by a single slater determinant ψ_{SD} of one-electron functions (spin-orbitals). The exchange is accounted for exactly. However, Coulomb-correlation effects are completely neglected and therefore the Coulomb-correlation energy E_c is defined as $E_c = E_0 - E_{HF}$, where $E_{HF} = \langle \psi_{SD} | \hat{H} | \psi_{SD} \rangle$. Neglecting the Coulomb-correlation significantly affects the structure and energetics of the system. Therefore, there are several post-Hartree-Fock approaches, which reintroduce the Coulomb-correlation. This is, however, accompanied with unfavorable scaling of the computational effort with the system size. An advantageous alternative to wave function based methods is density functional theory (DFT). DFT approximately includes Coulomb- and exchange-correlation, whilst roughly maintaining the computational effort of the HF method, i.e. significantly improving the computational effort with respect to post-HF approaches.

3.2 Density functional theory

3.2.1 Hohenberg-Kohn theorems and Kohn-Sham procedure

Density functional theory is based on the two Hohenberg-Kohn theorems, published in 1964. [156] The first theorem states, that the Hamiltonian is univocally determined by the electron density. The ground-state energy can thus be written as unique functional of the ground-state density, $E[n_0]$. The total energy functional can be divided three components, eqn. (3). These are the electron-ion interaction energy $E_{Ne}[n]$ the electron-electron interaction energy $E_{ee}[n]$, and the kinetic energy of the electrons, $T[n]$.

$$\begin{aligned} E[n] &= E_{Ne}[n] + E_{ee}[n] + T[n] \\ &= E_{Ne}[n] + F_{HK}[n] \\ &= E_{Ne}[n] + \langle \psi | \hat{V}_{ee} + \hat{T} | \psi \rangle \end{aligned} \tag{3}$$

The electron-ion interaction is given by $E_{Ne}[n] = \int n(r)\, v_{Ne} dr$, where v_{Ne} is the electrostatic potential between nuclei and electrons, or more generally the external potential. This term is system-dependent via the nuclear positions. The rest of the equation is universally valid and can be summarized to the Hohenberg-Kohn functional $F_{HK}[n]$. If the electron density is inserted to $F_{HK}[n]$, it returns the expectation value $\langle \psi | \hat{V}_{ee} + \hat{T} | \psi \rangle$. $F_{HK}[n]$ is unknown and has to be treated approximately.

The second Hohenberg-Kohn theorem states that the exact ground-state density minimizes $E[n]$, thus providing a variational principle for the ground state density such that $E_0[n_0] \leq E[n_t]$, where n_t is the trial density. The equality of the energy values holds only for $n_t = n_0$. To obtain a more useful formulation for the unknown Hohenberg-Kohn functional $F_{HK}[n]$, the following steps are pursued. In the first step, the electron-electron interaction

$E_{ee}[n]$ is split into three contributions: $E_{ee}[n] = E_H[n] + E_x[n] + E_c[n]$. Here, $E_H[n]$ is the classical Coulomb (Hartree) functional, $E_x[n]$is the exchange functional, and $E_c[n]$ is the Coulomb-correlation functional. $E_H[n]$ is known and given by $E_H[n] = \int n(\boldsymbol{r})\, v_H d\boldsymbol{r}$, where $v_H = \frac{1}{2}\int \frac{n(\boldsymbol{r}')}{|\boldsymbol{r}-\boldsymbol{r}'|} d\boldsymbol{r}'$. Note that even for a system with only one electron the Hartree-energy is non-zero, because it contains the interaction of the density with itself. This is called the self-interaction error. The second term of the electron-electron interaction, the exchange functional $E_x[n]$, is known and can in principle be calculated. [157] However, it is usually approximated to reduce the computational effort. The third term, the Coulomb-correlation term $E_c[n]$, is defined as $E_c[n] = E_{ee}[n] - E_H[n] - E_x[n]$. $E_c[n]$ is unknown, but can be treated approximately. $E_c[n]$ and $E_x[n]$ (and, as we will see later, the missing term of the kinetic energy in Kohn Sham DFT) can be summarized into the exchange-correlation functional $E_{xc}[n]$. The above mentioned self-interaction error should actually be cancelled out by the exchange term. The latter is however approximately treated in the joint exchange-correlation functional $E_{xc}[n]$. Therefore, standard DFT approaches suffer from the self-interaction error.

The second step to find a better formulation for the unknown Hohenberg-Kohn functional $F_{HK}[n]$, is to obtain a suitable expression for the kinetic energy term $T[n]$. This is addressed in the Kohn-Sham approach, published in 1965. [158] The approach is based on the assumption that we can find a reference system of non-interacting electrons which exactly produces the density of the interacting system. As this system is non-interacting, its wave function is written as a Slater determinant ψ_{SD} of spin orbitals $\varphi_i(\boldsymbol{r})$. The electron density is constructed from the spin orbitals via $n(\boldsymbol{r}) = \sum_i |\varphi_i(\boldsymbol{r})|^2$. The kinetic energy of the non-interacting system is given by $T_R[n] = -\frac{\hbar^2}{2m}\sum_i \langle \varphi_i(\boldsymbol{r})|\nabla_i^2|\varphi_i(\boldsymbol{r})\rangle$. Obviously, the kinetic energy of the non-interacting system is different from that of the interacting system, $T_c[n] = T[n] - T_R[n] \neq 0$. The energy assigned to this kinetic correlation, $T_c[n]$, is added to the unknown Coulomb-correlation term $\tilde{E}_c[n] = E_c[n] + T_c[n]$, thus resulting in a modified exchange-correlation functional $\tilde{E}_{xc}[n]$. The resulting universal functional $F[n]$ is shown in eqn. (4).

$$F[n] = E_H[n] + T_R[n] + \tilde{E}_{xc}[n] \tag{4}$$

An expression of the modified exchange-correlation functional $\tilde{E}_{xc}[n]$ can be derived by introducing the concept of the adiabatic connection. Here, the Hamiltonian of the non-interacting reference system is gradually connected with that of the interacting system via a coupling-strength parameter λ. The Hamiltonian for the varying coupling-strength values is given by $\hat{H}_\lambda[n] = \hat{V}_{Ne}[n] + \lambda\hat{V}_{ee}[n] + \hat{T}[n]$, where $\lambda = 0$ corresponds to the non-interacting system and $\lambda = 1$ to the fully interacting system. The parameter λ is gradually changed in such a way that the electron density remains unchanged. The energy difference between the

two systems is given by $E_{\lambda=1} - E_{\lambda=0} = \int_0^1 E d\lambda$. Inserting the corresponding Hamiltonians into this energy expression, we can derive $\tilde{E}_{xc}[n]$. [159] The result is shown in eqn. (5). Here, $\bar{h}_{xc}(\boldsymbol{r}, \boldsymbol{r}')$ is the coupling-strength integrated exchange-correlation hole given by $\bar{h}_{xc}(\boldsymbol{r}, \boldsymbol{r}') = \int_0^1 h_{xc}^{\lambda}(\boldsymbol{r}, \boldsymbol{r}') d\lambda$, where $h_{xc}^{\lambda}(\boldsymbol{r}, \boldsymbol{r}')$ is the exchange correlation hole corresponding to the Hamiltonian for varying values of λ.

$$\tilde{E}_{xc}[n] = \frac{1}{2} \iint \frac{n(\boldsymbol{r})\left[\bar{h}_{xc}(\boldsymbol{r}, \boldsymbol{r}')\right]}{|\boldsymbol{r} - \boldsymbol{r}'|} d\boldsymbol{r} d\boldsymbol{r}' \tag{5}$$

The exchange-correlation hole can be seen as depletion in the charge density of an electron in the vicinity of another electron due to correlation effects. This depletion is completely ignored in the classical Coulomb interaction $E_H[n]$. The exchange-correlation hole is a non-local object and contains one displaced electron, i.e. $\int \left[\bar{h}_{xc}(\boldsymbol{r}, \boldsymbol{r}')\right] d\boldsymbol{r} = -1$. This and other properties can be used to find a good approximation for the exchange-correlation functional, since the exact form of $\bar{h}_{xc}(\boldsymbol{r}, \boldsymbol{r}')$ is unknown.

3.2.2 Exchange-correlation functionals

There are various approximations to the exchange-correlation functional introduced in eqn. (5). The most basic approximation is the local density approximation (**LDA**). Here, the exchange-correlation hole of the homogeneous electron gas is taken as a base. The expression for the hole must be modified to account for the fact that $n(\boldsymbol{r}) \neq n(\boldsymbol{r}')$ in the case of the inhomogeneous density. In practice, the exchange-correlation energy density is defined as $\tilde{\epsilon}_{xc}[n] = \frac{1}{2} \int \frac{[\bar{h}_{xc}^{LDA}(\boldsymbol{r}, \boldsymbol{r}')]}{|\boldsymbol{r} - \boldsymbol{r}'|} d\boldsymbol{r}' = \tilde{\epsilon}_x[n] + \tilde{\epsilon}_c[n]$, which can be inserted into eqn. (5) to give $\tilde{E}_{xc}^{LDA}[n]$. For $\tilde{\epsilon}_x[n]$, we use the exchange energy expression of the homogeneous electron gas, which is known exactly. For the $\tilde{\epsilon}_c[n]$ part of the homogeneous electron gas, highly accurate approximations are available. The LDA approximation is a quite rough approximation. The self-interaction error is not cancelled out, leading to serious errors in the description of anions and strongly correlated systems. Hydrogen bonds are described poorly and long-range dispersion forces are neglected.

To account better for the inhomogeneity, expansions of the density in terms of its derivatives can be included into the exchange-correlation functional. The latter can then be written as $E_{xc}[n] = \int n(\boldsymbol{r})\, \tilde{\epsilon}_{xc}[n] F_{xc}\, d\boldsymbol{r}$. We drop the tilde in $\tilde{E}_{xc}[n]$ for the sake of simplicity, but still refer to the coupling-strength integrated exchange-correlation hole. $F_{xc} = f[n, \nabla n, \nabla^2 n, \dots]$ is the enhancement factor modifying $\tilde{\epsilon}_{xc}[n]$. Here, the enhancement factor is semi-local and depends on the value of the density and its derivatives at the given point. This is different from fully non-local expressions, where the value of the density at

different points is evaluated. Many popular exchange-correlation functionals are based on the generalized gradient approximations (**GGA**), which apply a second order gradient expansion ($F_{xc} = f[n, \nabla n]$). The expressions for the expansion are derived by theoretical methods and the parameterization is then done under the requirement that some of the exact conditions for the exchange-correlation hole are fulfilled.

The DFT calculations performed for the present work are mainly done within the GGA. In particular, we use the formulation developed by Perdew, Burke, and Ernzerhof (**PBE**). [160,161] The PBE functional was designed to fulfill as many as possible exact properties of the exchange-correlation hole. With respect to the LDA, it provides a better description of binding energies and bond lengths. The band gap in semi-conductors and insulators is severely underestimated in the LDA and this feature, although being slightly improved, persists also for the PBE functional and in general for GGA functionals. The self-interaction error is still not cancelled out satisfactory. This results in the erroneous description of strongly correlated systems in terms of an underestimation of the band gap, exaggerated electron delocalization as well as dispersion forces.

There are also higher level density functionals available, which can produce more accurate results than LDA and GGA. The higher rungs of the Jacob's ladder following the GGA are meta-GGA functionals which are dependent also on higher derivatives of the density, hybrid functionals which include exact exchange, and functionals based on the random phase approximation. [162] Since we made use of hybrid functionals in some cases, we will outline the idea in the next section.

3.2.3 Hybrid functionals

As discussed before, Hartree-Fock (HF) theory provides an exact treatment of exchange, whereas the exchange part in LDA and GGA exchange correlation functionals is treated approximately, leading to the well-known self-interaction error. On the other hand, the correlation approximations can be evaluated easily and quickly in DFT, while correlation is completely absent in HF theory. It is therefore of major interest to combine the strengths of both methods. A suitable way of combining both theories in hybrid functionals was proposed by A. D. Becke. [163] Hybrid functionals contain a linear combination of the DFT exchange and the exact exchange deduced from HF theory (E_x^{HF}), while the DFT correlation is retained, eqn. (6). The parameter α (with $0 < \alpha < 1$) is chosen in a rather arbitrary manner or fitted to reproduce experimental trends or parameters.

$$E_{xc}^{hyb} = \alpha E_x^{HF} + (1 - \alpha) E_x^{DFT} + E_c^{DFT} \quad (6)$$

The exact exchange is treated by using the orbital-dependent functional given by the Fock expression in eqn. (7), where $\varphi_i(\boldsymbol{r})$ are the Kohn-Sham orbitals.

$$E_x^{HF} = -\frac{1}{2}\sum_{i,j=1}^{N}\iint \frac{\varphi_j^*(\boldsymbol{r})\varphi_i^*(\boldsymbol{r}')\varphi_i(\boldsymbol{r})\varphi_j(\boldsymbol{r}')}{|\boldsymbol{r}-\boldsymbol{r}'|}d\boldsymbol{r}d\boldsymbol{r}' \quad (7)$$

Due to the larger computational effort related to the non-local exact exchange integrals, especially in periodic systems with a plane wave set-up, hybrid functionals are not as extensively used as the GGA functionals. In this work, we make use of the HSE06 hybrid functional for selected cases. In the HSE06 functional, the long-range part of the Fock exchange is replaced by the PBE exchange part to reduce the computational effort. [164,165,166]

3.2.4 The DFT+U approach

As we have seen in section 3.2.2, exchange-correlation functionals are commonly expanded around the homogeneous electron gas limit and thus fail in adequately describing properties of systems with more localized (inhomogeneous) ground states. [167] The approximate treatment of the many-body terms and the incomplete cancellation of the self-interaction in the Hartree term by these exchange-correlation functionals lead to the over-delocalization of valence states and the over-stabilization of metallic ground states. These effects lead to the qualitatively wrong description of strongly correlated materials, such as Mott insulators and transition metal oxides in general. The description of such systems improves when the accuracy of the many-body terms is enhanced, as it is the case in dynamical mean field theory [168] and (reduced) density matrix functional theory. [169] These methods are, however, computationally much more demanding than DFT and are thus not suited for the scope of this work.

A computationally less expensive approach is based on the description of the strongly correlated states by a model Hamiltonian inspired by the Hubbard model. [170] The strong on-site coulomb and exchange interactions are treated with an additional Hubbard-like term. The resulting Hamiltonian is given in eqn. (8), where $E_{Hub}[n]$ is the Hubbard correction acting on the selected states and $E_{dc}[n]$ is the double counting term, which is supposed to subtract the part of $E_{DFT}[n]$ which is now substituted by the Hubbard term. $E_{dc}[n]$ is not uniquely defined and has to be treated approximately.

$$E_{DFT+U}[n] = E_{DFT}[n] + E_U[n] = E_{DFT}[n] + E_{Hub}[n] - E_{dc}[n] \quad (8)$$

In computational chemistry, there are two main branches of the DFT+U approach. The first branch is the unitary-transformation-invariant formulation of the DFT+U method developed by Liechtenstein et al. [171] Here, the strengths of the on-site Coulomb and exchange interactions are described by the parameters U and J, respectively, which enter separately in the $E_U[n]$ correction term. The Hubbard correction is explicitly applied to the site l which exhibits the strong correlation effects. The site can for instance be the d orbitals of the transition metal. The second branch is a simpler formulation developed by Dudarev. et al. [172]

Here, only the difference $U_{eff}^{l} = U - J$ is relevant. In this approach any higher multi-polar terms are neglected. The correction term is shown in eqn. (9), where $\boldsymbol{n}^{l,\sigma}$ is the atomic orbital occupation matrix of site l with spin variable σ.

$$E_U[n] = \sum_{l,\sigma} \frac{U_{eff}^{l}}{2} \mathrm{Tr}[\boldsymbol{n}^{l,\sigma}(1 - \boldsymbol{n}^{l,\sigma})] \tag{9}$$

The corrective energy term $E_U[n]$ stabilizes idempotent occupation matrices effectively reducing the occupancy of states with occupation numbers $n_m^{l,\sigma} < 0.5$ and increasing those with $n_m^{l,\sigma} > 0.5$. The values of U and J can be computed from first principles [173] or determined empirically. In most applications, DFT+U is a semi-empirical approach, mainly used to obtain semi-quantitative enhancement of the description of electron localization and the band gap of "strongly correlated materials".

3.2.5 Dispersion forces

In the literature, dispersion forces and van-der-Waals forces are often used synonymously and also in this work, both terms will be used to denote the London dispersion forces. Dispersion forces arise from instantaneous polarization multipoles in molecules or atoms, which are a consequence of non-local electron correlation effects. The role of dispersion forces increases as the electron density of the atom or molecule becomes more dispersed, because then the electron density is more polarizable. Many important material properties arise from dispersion forces, such as the fact that Bromine is liquid at room temperature. Also for the correct description of the adsorption of molecules on metal, semi-conductor, and isolator surfaces dispersion interactions are of vital importance. For example, Carrasco et al. have shown that the accurate treatment of vdW dispersion interactions is essential to properly describe the physisorption, as well as the chemisorption of benzene and water on transition metal surfaces. [174,175] The adsorption energy as well as the geometry are significantly influenced by dispersion forces. Thus, for the description of adsorbate-surface interactions, DFT with explicit inclusion of long-range dispersion interactions is the state-of-the-art methodology. [176,177]

The commonly used LDA and PBE functionals do not include any long-range correlations and therefore fail to describe the binding of noble gas like systems where dispersion is the primary binding mechanism. [178] However, as the amount and the nature of the correlation contained in such functionals are not clearly specified, there have been attempts to compute weak interactions on their basis. [179,180] Fortunately, various approaches for the explicit (approximate) inclusion of dispersion forces have been developed. An appealing method is to include the dispersion forces directly in the exchange-correlation functional, as proposed by Dion et al. [181] In this case, the van-der-Waals density functional (vdW-DF) takes the

form $E_{xc}[n] = E_x[n] + E_c[n] + E_c^{nl}[n]$, where $E_c^{nl}[n]$ is the non-local correlation functional approximately accounting for dispersion forces. There are various flavors of vdW-DF: The original version [181], the original version with an optimized exchange part [182], and a second version of the vdW-DF [183]. The use of vdW-density functionals is computationally relatively demanding and so dispersion forces are often accounted for in a methodologically less sophisticated manner. A pragmatic and computationally less demanding method is to augment the original density functional by a damped atom-pair dispersion potential (**DFT+D2**), as proposed by S. Grimme. [184] The potential is a parameterized sum over atom pair contributions, as shown in eqn. (10).

$$E_{DFT+D2} = E_{DFT} - s_6 \sum_{i \neq j} \frac{(C_{6i} \cdot C_{6j})^{1/2}}{R_{ij}^6} f(R_{ij}, R_i^0, R_j^0) \tag{10}$$

Here, the summation is done over all atom pairs ij within a given cut-off radius. The default cut-off radius in VASP is 50 Å. C_{6i} and C_{6j} are the vdW-coefficient for the atomic species i and j, respectively. R_i^0 and R_j^0 are the vdW-radii for the atomic species i and j, respectively. R_{ij} is the interatomic pair distance. $f(R_{ij}, R_i^0, R_j^0)$ is a dumping function to smoothly fade in vdW-interactions at the relevant distance $R_{ij} = R_i^0 + R_j^0$. At smaller R_{ij}, the function becomes zero and at larger R_{ij} it becomes 1. s_6 is a functional-dependent global scaling parameter, which is 0.75 for the PBE functional. [184]

The original parameterization of this method is based on properties of the neutral elements and does neither account for the oxidation state of the atom, nor for the coordination environment. Tosoni and Sauer have shown, that changing the vdW-coefficients of positively charged ions in oxides to those of the preceding noble gas (**DFT+D2'**) can improve the description of equilibrium distances and adsorption energies with respect to MP2 and CCSD(T) calculations. [185] The DFT+D3 parameterization [186] and the Tkatchenko-Scheffler method [187] represent valid alternatives to the DFT+D2 method. In this work, however, we use the DFT+D2' approach which has been shown to provide results comparable to DFT-DF for adsorption on oxides.

3.2.6 Bloch's theorem and the plane-wave basis set

To computationally represent a periodic material, i.e. a bulk crystal, a surface, or a rod, it is convenient to use periodic boundary conditions (**pbc**). This way the infinite system can be represented with a small unit cell. This introduces no approximation if the crystal is truly infinite and without defects. Bloch's theorem indicates that it is sufficient to know the electronic wave function in the unit cell to deduce the properties of the entire perfect crystal. According to Bloch's theorem [188], the one-electron wave function $\psi_{j,\boldsymbol{k}}(\boldsymbol{r})$ in a periodic

potential can be written as shown in eqn. (11). Here, $\boldsymbol{k}$ is a wave vector contained in the first Brillouin zone, and $u_j(\boldsymbol{r})$ is a function with the crystal's periodicity and band index j. $u_j(\boldsymbol{r})$ can be expanded in a plane wave basis with $c_{j,\boldsymbol{G}}$ being the expansion coefficients. $\boldsymbol{G} = \sum_{i=1}^{3} n_i \boldsymbol{b}_i$ is any reciprocal lattice vector with n_i being integers and $\boldsymbol{b}_i$ the primitive reciprocal lattice vectors.

$$\begin{aligned} \psi_{j,\boldsymbol{k}}(\boldsymbol{r}) &= e^{i\boldsymbol{k}\cdot\boldsymbol{r}} u_j(\boldsymbol{r}) \\ u_j(\boldsymbol{r}) &= \sum_{\boldsymbol{G}} c_{j,\boldsymbol{G}}\, e^{i\boldsymbol{G}\cdot\boldsymbol{r}} \\ \psi_{j,\boldsymbol{k}}(\boldsymbol{r}) &= \sum_{\boldsymbol{G}} c_{j,\boldsymbol{G}}\, e^{i(\boldsymbol{k}+\boldsymbol{G})\cdot\boldsymbol{r}} \end{aligned} \tag{11}$$

3.2.7 The projector augmented wave (PAW) method

As we have seen in the previous section, the wave functions of electrons in a crystal can be expanded in a plane wave (**PW**) basis when periodic boundaries are applied. PWs are the exact solution for free electrons, i.e. when the potential due to the atoms is neglected. [189] A smooth potential due to the atoms could be treated as a perturbation. [189] However, the potential due to the atoms is not smooth at all and thus the wave functions deviate considerably from plane waves, especially in the regions close to the atomic cores where the potential is steep. Here, the wave functions exhibit cusps and can show strong oscillatory behavior. To describe these features with a plane wave basis, a large basis set is necessary. This, in turn, translates into a large computational effort.

There are several methods to circumvent this problem. One of the popular approaches is pseudo-potential (**PP**) theory. Here, we make use of the fact that the exact description of electronic states close to the atomic core is not necessary for the description of chemical bonding. The core electrons are brought together with the bare nuclear potential, giving the pseudo-potential. [189] This is done in such a way that the eigenvalue of the resulting pseudo-Hamiltonian is the same as that of the true Hamiltonian. The eigenstate of the pseudo-Hamiltonian is a pseudo (**PS**) wave function, which takes the form of the true all-electron (**AE**) valence wave function outside a given cutoff radius r_c^a around the core of atom a. Note that relativistic corrections can be incorporated directly into the PP in such a way that the solution of the non-relativistic Schrödinger equation contains relativistic core effects.

There are two types of pseudo-potentials: Norm-conserving [190] and ultra-soft [191]. The general disadvantages of norm-conserving pseudo-potentials are that they either need a large PW basis, or they are not well transferable between different chemical systems. [192] Ultra-soft pseudo-potentials (**US-PP**) are not norm-conserving. The charge density difference between the AE and the PS wave function is added as localized atom centered augmentation

charges. [192] This way, a small cut-off radius r_c^a can be used in combination with a smaller PW basis whilst maintaining transferability. The design of ultra-soft pseudo-potentials is however rather difficult, since many parameters have to be chosen which requires extensive testing to obtain transferability. [192]

The projector augmented wave (PAW) method developed by Blöchl [193] can be seen as advancement of the PP approach. Here, the AE wave function is given by a linear transformation of the PS wave function: $|\psi_n\rangle = \mathrm{T}|\tilde{\psi}_n\rangle$. T operates only in the augmentation sphere, i.e. $\mathrm{T} = 1 + \sum_a \mathrm{T}^a$, where a denotes the atomic site. The AE and the PS wave functions are expanded in a complete basis, also called *partial waves*, $|\psi_n\rangle = \sum_i c_i|\phi_i\rangle$ and $|\tilde{\psi}_n\rangle = \sum_i \tilde{c}_i|\tilde{\phi}_i\rangle$. Here, the index i is a shortcut for the atomic site a, the angular momentum numbers l, m and an additional index k for the reference energy ϵ_{kl}. [192] Applying the linear transformation T, it can be shown that $c_i = \tilde{c}_i$. The expansion coefficients c_i are chosen to be projector functions applied to the pseudo wave function $c_i = \langle \tilde{p}_i|\tilde{\psi}_n\rangle$. The projector functions have to satisfy the orthogonality relation $\langle p_i|\tilde{\phi}_j\rangle = \delta_{ij}$ and the completeness relation $\sum_i |\tilde{\phi}_i\rangle\langle p_i| = 1$. The PS wave function can now be projected to the all AE wave function by the linear transformation shown in eqn. (12). [192]

$$|\psi_n\rangle = |\tilde{\psi}_n\rangle + \sum_i (|\phi_i\rangle - |\tilde{\phi}_i\rangle)\langle \tilde{p}_i|\tilde{\psi}_n\rangle \qquad (12)$$

It is worth noting that with respect to other frozen core methods, no additional approximations are introduced in the PAW approach for a complete set of partial waves. Kresse and Joubert have shown that also for an incomplete basis, accurate and reliable results can be obtained. [192] The US-PP approach can be seen as an approximation to the PAW method. In the limit of very accurate augmentation charges, the US-PP approach reproduces the results of the PAW method. Given the great efficiency and the reliability of the PAW method [192], we used this method for all DFT calculations reported in this thesis.

3.2.8 The Vienna Ab initio Simulation Package (VASP)

Almost all of the electronic structure calculations and quantum-mechanical molecular dynamics for the structure optimization reported in this thesis were performed with the Vienna Ab initio Simulation Package (VASP). [194,195,196,197] VASP applies periodic boundary conditions (pbc) to the unit cell in all three lattice directions. In codes which apply pbc, a surface can be represented by a slab, which is either standing in vacuum (e.g. in the Crystal code) or, the three-dimensional periodicity is kept and thus the slab is also repeated in the direction perpendicular to the surface, as it is in the VASP code. On the one hand, the three-dimensional periodicity makes it possible to expand the Kohn-Sham one-electron orbitals in a plane wave basis set, which is free of basis set superposition errors. On the other hand, we have to manually include a vacuum region between the slabs, which has to be large enough

to minimize the interactions between the slab replicas. The vacuum region is usually chosen to be in the range of 12-15 Å. The VASP code is commercially available under a license agreement.

3.3 Molecular dynamics simulations

3.3.1 Basic machinery and Langevin dynamics

To investigate the melting temperature of Pt and Au nanoparticles, molecular dynamic (**MD**) simulations based on the Langevin dynamics [198] were performed. The general molecular dynamics machinery basically consists of three steps: In the first step the forces on the systems particles are calculated, in the second step the equations of motion are solved and in the third step the system is propagated a finite time step forward. In the following we will shortly outline the three steps. The first step is the calculation of the forces on the atoms which can be calculated via DFT, or via (semi-) empirical interatomic potentials. The forces are calculated as the gradient of the potential energy with $F_i = -\frac{\partial U}{dR_i}$ being the force acting on particle i. The method applied to calculate the forces depends on the desired accuracy and ultimately on the system size. Using standard DFT, the computational effort is by far too high to simulate the melting process of 3-10 nm metal nano-particles. Therefore, we made use of two different interatomic potential types. The first type is based on the effective medium theory (EMT) [199,200,201] and the second type is the embedded atom method (EAM) [202]. Both are many-body potentials.

The second step is the solution of the equation of motion, transforming the potential-derived force into an acceleration, eqn. (13).

$$m_i\ddot{R}_i = F_i - \gamma_i\dot{R}_i + f_i(t) \tag{13}$$

Here, m_i is the mass of particle i, $\ddot{R}_i$ is the acceleration, γ_i is the friction coefficient, $\dot{R}_i$ is the velocity, and $f_i(t)$ represents the stochastic (random) force. In order to control the temperature and thus sample the canonical (NVT) ensemble, γ_i and $f(t)$ must fulfill the fluctuation-dissipation theorem [203], eqn. (14).

$$\langle f_i(t) f_i(t')\rangle = 6kT\gamma_i\partial(t - t') \tag{14}$$

For $\gamma \to 0$, the Langevin dynamics equals the classical Hamiltonian (Newtonian MD), and for $\gamma \to \infty$ it goes over to the Brownian dynamics.

In the last step, the system is propagated a discrete time-step forward to calculate the new impulse and position of the particles. For the time propagation, the time integrator and the time step have to be chosen with care. The time integrators are based on finite difference

methods where time is divided into discrete time steps Δt. This can result in errors, in particular truncation (at large Δt) and round-off errors (due to implementation). However, in modern time integration schemes these errors are well under control. The time step, on the other hand is chosen manually and hence this is a more important source of errors. Δt must be chosen small enough to be within the time regime of the physical phenomenon of interest (in our case atomic motions, i.e. fs time regime), but large enough to cover a reasonable simulation time while keeping a low computational effort.

3.3.2 The Atomic Simulation Environment (ASE) and the ASAP calculator

The CAMPOS Atomic Simulation Environment (ASE) [204] is a set of tools and Python modules freely available under the GNU Lesser General Public License. ASE can be used to set up, run, modify, analyze, and visualize atomistic simulations. ASE serves as a framework assessing one of various calculators available to run quantum-mechanical simulations, as well as molecular dynamics simulations. As Soon As Possible (ASAP) is a calculator for large-scale classical molecular dynamics in the framework of ASE. ASAP is released under the GNU Lesser General Public License. More than 150 interatomic potentials are available for ASAP, such as the Effective Medium Theory (EMT) potentials [201] and the repository provided by the OpenKIM [205,206] project.

Chapter 4 The role of dispersion forces for the cluster-support interaction

4.1 Ag and Au clusters on TiO_2 anatase (101): The role of dispersion forces[2]

4.1.1 Introduction

Silver and gold clusters supported on oxides constitute active catalysts for a large variety of reactions and there is evidence that sub-nanometer clusters contribute to the catalytic activity. In particular, Ag and Au clusters are active for several reactions, such as CO oxidation [207,208] and propylene oxidation [209,152], and the water-gas shift reaction [149]. The two oxidation reactions are of major importance. CO oxidation is a well-studied model reaction for oxidation reactions and is the state of the art solution for CO abatement in air depollution treatments. [210] The oxidation of propylene to propylenoxide is of immense industrial importance, since propylenoxide is a precursor for the production of polymers. [211]

Titania (TiO_2) as a support has shown great promoting effects on the catalytic activity of small noble metal clusters. [212,43] For gold nanoparticles and clusters, this promoting effect is quite remarkable. [213] It is therefore interesting to study the cluster-support interactions between the Ag and Au clusters and the titania support. Titania occurs in nature in three different polymorphs: rutile, anatase and brookite. The most stable polymorph is rutile, having a lower free energy than the other phases at all temperatures. [214,215,216] The anatase phase is metastable at room temperature and is commonly used in catalytic applications. [217,218,219] Many commercial titania powder catalysts consist of a mixture of anatase and rutile. For instance, the widely used Degussa P25 contains 80-90% anatase and the rest is rutile. [220] The (101) surface is the most stable surface of titania anatase. [221] In computational studies on the interaction between metal clusters and oxides, van-der-Waals dispersion forces have long been neglected. [222,48] However, in a recent study Carrasco et al. demonstrated that their inclusion can be very important to correctly describe the adsorption of molecules on oxide surfaces. [174] Therefore, we chose to investigate the role of dispersion forces for the interaction of Ag and Au clusters with the anatase (101) surface.

[2] The content of this study is published in the Journal of Physical Chemistry: A. Ruiz Puigdollers, P. Schlexer, and G. Pacchioni, "Gold and Silver Clusters on TiO_2 and ZrO_2 (101) Surfaces: Role of Dispersion Forces.", J. Phys. Chem. C, 119 (2015) 15381-15389. http://doi.org/10.1021/acs.jpcc.5b04026

4.1.2 Computational details

The Vienna Ab Initio Simulation Package (VASP 5.2) [194,195,196,197] was used to perform periodic, spin polarized density functional theory (DFT) calculations. Generalized gradient approximations (GGA) for the exchange-correlation functional were applied within the Perdew, Burke and Ernzerhof (PBE) formulation. [160,161] The projector augmented wave (PAW) method was used to describe electron-ion interactions. [193,192] O(2s, 2p), Ti(3s, 4s, 3p, 3d), Ag (4d, 5s) and Au(5d, 6s) are treated explicitly. For strongly correlated systems, such as TiO_2 and other transition metal oxides, the self-interaction error present in GGA approaches can lead to qualitatively wrong descriptions of the electronic structure and other properties. To circumvent this error, we applied the GGA+U approach as proposed by Dudarev et al. [172] With this approach the multiple occupation of selected states is penalized, so that the underestimation of the band gap and electron delocalization is attenuated. In this work, we set the U-parameter to 3 eV for the 3d levels of Ti. An U value of 2-3 eV for the Ti 3d levels has been proposed by Hu et al. to calculate reaction energies on TiO_2. [223] A value of 3 eV also provides a good qualitative description of electronic and geometric structures. [224] For electronic relaxations, we always used the blocked Davidson iteration scheme. [225] In geometric structure optimizations, all ions were allowed to relax until ionic forces are smaller than |0.01| eV/Å. To build up the model, we first calculated the titania anatase bulk structure, which was done using a kinetic energy cut-off of 900 eV. A Γ-centered K-point grid in the Monkhorst-Pack scheme [226] was used, which was set to (8×8×4). With this setup, we obtained lattice parameters of a_0 = 3.803 Å and c_0 = 9.717 Å. The corresponding experimental values are a_0 = 3.796 Å and c_0 = 9.444 Å. [227] The deviation of the unit cell volume is 3.27%. As we will see later, we also tested the effect of dispersion forces on the titania anatase lattice parameters and found it to be negligible.

To model the (101) surface, a slab of 5 layers of [TiO_2] units was created. This slab thickness is a good compromise between computational effort and accuracy. [228] The slab was optimized, whereby all ions were allowed to relax. A kinetic energy cut-off of 400 eV was used for all slab calculations. The optimized slab model for the titania anatase (101) surface is shown in **Fig. 2**. On the (101) surface, there are two-fold and three-fold coordinated oxygen atoms, denoted as 2c-O and 3c-O, respectively. Similarly, there are five- and six-fold coordinated Ti atoms. The orthorhombic surface unit cell exhibits lattice parameters of a_0 = 3.80 Å and b_0 = 10.44 Å, **Fig. 2 (a)**. For our calculations, we used a (3×1) surface super cell exhibiting lattice parameters of a_0 = 11.4 Å and b_0 = 10.4 Å. The slabs are separated by more than 12 Å of vacuum. Dipole corrections along the axis perpendicular to the slab were applied. For structure optimizations, Γ-point calculations were performed. The K-points were increased to (3×3×1) to calculate the electronic density of states (DOS). The DOS for the slab in the (3×1) surface super cell is shown in **Fig. 2 (c).** With our computational setup,

the band gap of the slab is around 2.6 eV, which is underestimated with respect to the experimental value of bulk titania anatase of 3.0 eV. [229] Nevertheless, we do not use a larger U-value, because this worsens the agreement of the computed vs. experimental lattice parameters.

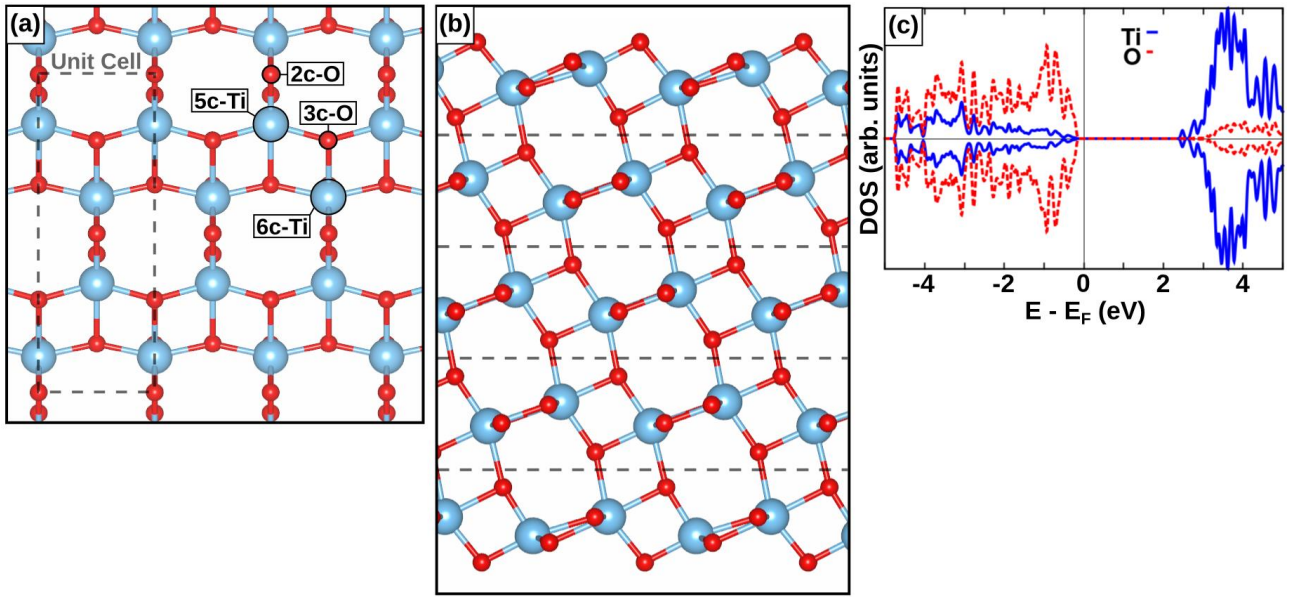

Fig. 2: Titania anatase (101) surface model. (a) Top view onto the surface. The (1×1) surface unit cell and atomic site notations (e.g. 6c-Ti for a 6-fold coordinated Ti atom) are indicated. (b) Side view of the slab consisting of 5 layers of TiO_2 units, which are indicated by the 4 dashed lines. (c) The electronic density of states (DOS) of the slab model.

To account for dispersion forces, various methods are available and in this study, three different methods have been tested, which are described in more detail in section 3.2.5. The first method is the semi-empirical pair-wise force-field developed by Grimme (**DFT-D2**). [184] The second method is a variation of the first method. Here, the vdW coefficients (R_0 and C_6) for Ti are replaced with those of the preceding noble gas in the periodic table (Ar). [185] We denote this method as **DFT-D2'**. The third method was proposed by Dion et al. [181] He developed exchange-correlation functionals accounting for the long-range correlation effects responsible for dispersion forces. Thus, this is a higher level of theory and therefore we treat the van-der-Waals density functional (**vdW-DF**) as benchmark. Note that this must in principle not necessarily mean that the vdW-DF provides a better agreement with experimental data than (semi-)empirical approaches. There are different versions of this functional and in this study we used the optB86b-vdW density functional.

The bonding between Ti and O in TiO_2 is polar covalent to ionic. Covalent and ionic bonds are quite strong, i.e. in the range of a few eV, whereas dispersion forces are roughly an order of magnitude weaker. Nevertheless, dispersion forces may affect the bulk structure. We

tested the effect of dispersion forces described at the PBE+D2 level, on the TiO_2 lattice parameters. We found that the change was less than 1 Vol-.% when going from PBE to PBE+D2. Since our aim is to test different methods to include dispersion forces, we kept the lattice parameters of the calculations without dispersion forces. We also tested the effect of dispersion forces on the Ag and Au bulk properties. Since Ag and Au have large vdW-coefficients, we considered different methods, **Table 1**.

Table 1: Experimental and computed cohesive energies per atom E_{COH} [eV] and lattice parameters a_0 [Å] of Ag and Au fcc bulk materials.

	Exp.[(a)]		PBE		PBE+D2		vdW-DF	
	E_{COH}	a_0	E_{COH}	a_0	E_{COH}	a_0	E_{COH}	a_0
Ag	2.95	4.09	2.51	4.13	3.07	4.11	2.70	4.18
Au	3.78	4.08	3.04	4.15	3.51	4.10	3.27	4.21

[(a)]Taken from reference [230].

The PBE functional underestimates the cohesive energies while slightly overestimating the lattice parameters. Both parameters (E_{COH}, a_0) are improved when dispersion forces are introduced at the PBE+D2 level. The vdW-DF functional slightly improves the cohesive energies while overestimating the lattice parameters even more than the PBE functional. The cohesive energies and the lattice parameters are always larger for gold.

In the following, we will consider the effect of dispersion forces on the cluster-support interaction of silver and gold atoms and tetramers supported on titania anatase (101). We define the adsorption energy, as shown in eqn. (15). Here, $E(M_x/TiO_2)$ is the DFT total energy of the joint system, $E(M_x)$ is the total energy of the free-standing metal cluster and $E(TiO_2)$ is the total energy of the adsorbate-free surface. All energies are associated to the structure-optimized systems.

$$E_{ADS}(M_x/TiO_2) = E(M_x/TiO_2) - E(M_x) - E(TiO_2) \quad (15)$$

4.1.3 Ag and Au atoms on titania anatase

As a first case, we tested the effect of dispersion forces on the adsorption of the Ag and Au atoms. Here, we compared only the PBE and the PBE+D2 methods. The adsorption energies of the atoms on the two most stable adsorption positions are shown in **Table 2**. Magnetic moments and Bader charges are reported for the PBE case only, because these values do not change when dispersion forces are introduced at the PBE+D2 level. We tested various adsorption positions and found the Ti-O bridge and the O-hollow position are the most stable ones, **Fig. 3**. The adsorption positions and the structural parameters are quite similar for Ag and Au, and do not change much when dispersion forces are included. Therefore, only the case of Ag/TiO_2 computed at the PBE level is shown, **Fig. 3**. We observe an enhancement

of the adsorption energies of around 0.2-0.5 eV when dispersion forces are introduced, **Table 2**. This means that the adsorption energies become more negative. The Ag atom preferably adsorbs on the O-hollow position and the Au atom prefers the Ti-O bridge site, independently of the method used.

Table 2: Ag and Au adsorption energies E_{ADS} [eV], magnetic moment μ [μ_B] on the metal atoms M and on the TiO_2 support, and Bader charges on metal atoms q(M) [|e|].

		E_{ADS}		μ		q(M)
M	Position	PBE	PBE+D2	M	TiO_2	M
Ag	Ti-O bridge	-0.24	-0.46	0.3	0.2	+0.14
	O hollow	-0.69	-1.19	0.0	0.7	+0.67
Au	Ti-O bridge	-0.43	-0.66	0.4	0.2	0.00
	O hollow	-0.16	-0.52	0.0	0.7	+0.45

To analyze in more detail the bonding characteristics, we consider the Bader charges on the atoms and the magnetic moment on the atoms, as well as on the support. On the Ti-O bridge site, the Ag atoms remains neutral, having a Bader charge close to zero and a magnetic moment of 0.3 μ_B. On the support, we detect a finite magnetic moment of 0.2 μ_B. This is due to orbital mixing between the Ag 5s state with the O 2p state of the closest O atom. When Ag is deposited on the O-hollow position, the Bader charge on Ag increases to +0.67 |e|, indicating a net charge transfer from the Ag atom to the support. The charge transfer is confirmed by the magnetic moments on Ag changing from 1 μ_B in the gas-phase to 0 μ_B on the O-hollow position. On the contrary, the magnetic moment on the Ag-free titania support is 0 μ_B and increases to 0.7 μ_B when the Ag atom is positioned at the O-hollow site. From the electronic density of states (not shown), it becomes clear that the electron is transferred to the titania conduction band minimum (CMB), having Ti 3d state character. With our computational setup, we find the electron delocalized over the Ti atoms in the slab. So, Ag adsorbs neutrally on the Ti-O bridge position, but on the O-hollow an Ag^+ ion is formed. Presumably this is due to the increased coordination by oxygen atoms.

A similar discussion can be made for the Au atom, with the difference that the Ti-O bridge position is always preferred. This is no surprise since the ionization potential of Au is much larger than that of Ag: Experimental values are 9.22 eV for Au and 7.57 eV for Ag. [231] We have seen that the adsorption energies of Ag and Au atoms are enhanced when dispersion forces are included in the calculation. The adsorption position and the charge transfer behavior are basically unaffected by dispersion forces.

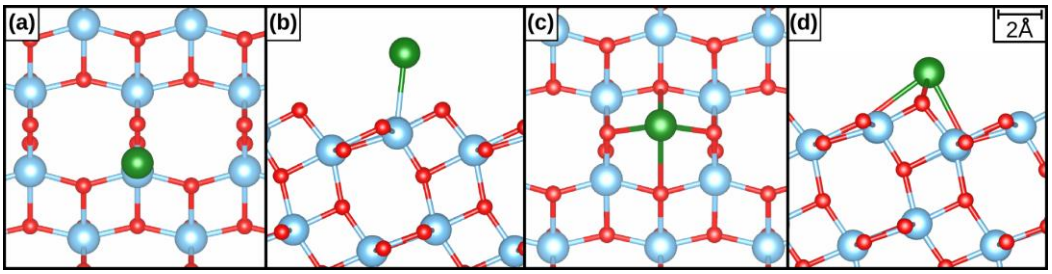

Fig. 3: Ag atom supported on titania anatase (101), geometries computed without dispersion forces. (a) Top view on Ti-O bridge position, (b) side view on Ti-O bridge position, (c) top view on the O-hollow position, and (d) side view on the O-hollow position. [232]

4.1.4 Ag and Au tetramers on titania anatase

Let us now consider the adsorption of the tetramers. The free-standing Ag and Au tetramers exhibit a closed-shell electronic structure and a rhombic geometry. [233,234] We explored many different isomers of the Ag and Au tetramers supported on titania anatase (101), including tetrahedral geometries. In the following only the two most stable isomers are discussed. Different levels of theory were applied. We used PBE, PBE+D2, PBE+D2', and the vdW-DF, **Table 3**.

Table 3: E_{ADS} [eV] of Ag and Au tetramers supported on TiO_2 computed without dispersion forces (PBE) and with different methods to account for dispersion forces.

	Isomer	E_{ADS}			
		PBE	PBE+D2	PBE+D2'	vdW-DF
Ag	A	-1.01	-2.36	-2.02	-2.06
	B	-1.05	-2.02	-1.77	-1.85
Au	A	-1.26	-2.37	-2.12	-2.43
	B	-1.55	-2.39	-2.19	-2.48

As the tetramers are deposited on the titania surface, two important isomers (A and B) are found. Isomer A is quasi the same for all different methods. The same is true for isomer B. The two isomers calculated at the PBE level are shown in **Fig. 4**. In all cases, the clusters remain neutral upon adsorption on the titania anatase surface. Only slight mixing of Ag 5s and Au 6s, respectively, with surface O 2p orbitals of the titania surface were observed in the electronic density od states (not shown). As for the atoms, the adsorption energies of the Ag and Au tetramers are significantly enhanced when dispersion forces are introduced.

For the silver tetramers the PBE+D2 method has the strongest effect on the adsorption energy. Here, the adsorption energy is roughly 1 eV larger in modulus than the corresponding PBE result. The vdW-DF gives an adsorption energy slightly smaller in modulus than that of the PBE+D2 method. The PBE+D2' method gives results similar to those of the vdW-

DF. At the PBE level, isomer B is more stable than isomer A. This order of stability is reversed when dispersion forces are introduced, independently of the method used. This is an important result, since here, the fact whether dispersion forces are included or not determines the most stable isomer. The adsorption energies of the gold tetramers are as well enhanced when dispersion forces are introduced. This time, isomer B is always more stable than isomer A. The largest enhancement of the adsorption energy is given by the vdW-DF, followed by the DFT+D2 method. This trend is different from that observed for the silver tetramers. We can conclude that dispersion forces are important for the energetics and the relative stability of isomers, whereas the individual structures of the isomers as well as their charge transfer behavior are not significantly affected by dispersion forces.

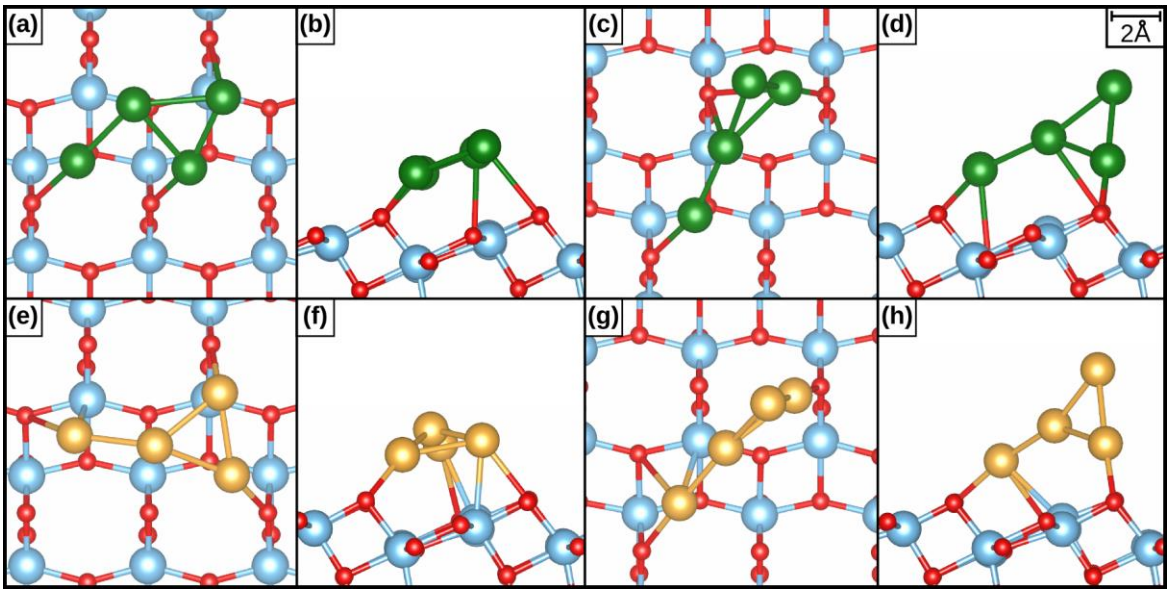

Fig. 4: Ag and Au tetramers supported on TiO_2 anatase (101). (a-b) Ag_4 isomer A, (c-d) Ag_4 isomer B, (e-f) Au_4 isomer A, (g-h) Au_4 isomer B. [232]

4.1.5 Section summary

- The effect of vdW-forces on the adsorption mode of Ag and Au atoms and tetramers was investigated. The adsorption energies of the atoms are enhanced when dispersion forces are included. The adsorption sites and the geometries of the atoms are not altered by dispersion forces. The charge state of the atoms is dependent on the adsorption site. O-hollow sites favor the formation of Ag^+ (Au^+) ions, whereas on Ti-O bridge sites, the atoms remain neutral.

- The adsorption energies of the tetramers are significantly enhanced by the inclusion of dispersion forces. Here, dispersion forces can change the order of isomer stability of the titania-supported clusters. These effects can in turn change other properties of the clusters, such as chemical reactivity and their diffusion properties.

Chapter 5 Characterization of metal clusters and nanoparticles

5.1 Structure and charge states of Au clusters on TiO_2 rutile (110)[3]

5.1.1 Introduction

Metal atoms and clusters supported on titania were subject to many surface science studies, because of their potential catalytic applications. [235,236,237,238] In ultra-high vacuum (**UHV**), scanning tunneling microscopy (**STM**) can be used to investigate the atomic structure and other properties of titania-supported clusters. Vapor deposition techniques are often available in the UHV facilities, making it possible to deposit metal atoms and investigate them via STM. [239] Perfectly stoichiometric titania anatase and rutile samples would not be suitable for this technique, since they exhibit band gaps of around 3.0-3.2 eV. [240] However the presence of intrinsic defects, like oxygen vacancies and Ti interstitials can provide occupied states at the conduction band minimum and make the titania sample conductive. [241] As described in Chapter 4, titania-supported Au atoms and clusters have potential applications in catalysis. Gong et al. investigated the interaction of Au_x (x = 1-3) clusters with the titania anatase (101) surface via STM. [235] They found that step edges and oxygen vacancies are suitable anchoring sites for the Au clusters.

In this study, a combined experimental and theoretical approach was pursued to identify structure and charge state of Au dimers and trimers supported on titania rutile (110). The (110) surface is the most stable one for titania rutile. [242] STM experiments were performed by Dr. C. M. Yim and G. Thornton at the University College London (UCL). They were able to control the adsorption position of the clusters via tip manipulation. DFT calculations were used to complement the experimental data by determining geometry, charge state and adsorption strength of the clusters.

[3] The experiments reported in this study were performed by Dr. C.-M. Yim et al. in the group of Prof. G. Thornton. We gratefully acknowledge their valuable contribution.

5.1.2 Experimental and computational details

Experimental details

The experiments reported in this study were performed by Dr. C.-M. Yim and Prof. G. Thornton, University College London. The STM measurements were performed at 78 K in a bath cryostat OmicronSTM housed in an ultrahigh vacuum chamber with a base pressure of 2×10^{-11} mbar. Samples were prepared initially by cycles of Ar^+ sputtering and annealing to 1000 K. Au atoms were deposited onto the as-prepared TiO_2 (110) sample that was held at 300 K. The Au evaporation source consisted of a Au wire wrapped with a tungsten coil which was resistively heated. Following deposition, the sample was immediately transferred to the analysis chamber for STM imaging.

Computational details

Spin polarized, periodic DFT calculations were performed with a similar setup as described in section 4.1.2. To circumvent the self-interaction error, we used the GGA+U approach as proposed by Dudarev et al. [172] We set the U-parameter to 3 eV for the Ti 3d states. To account for dispersion forces, we used the DFT-D2' method, see section 4.1.2. [184,185] All ions were allowed to relax until ionic forces were smaller than |0.01| eV/Å. Calculation of the rutile bulk structure was done using a kinetic energy cut-off of 900 eV and a Γ-centered K-point grid, which was set to (8×8×8). The obtained lattice parameters are $a_0 = b_0 = 4.64$ Å and $c_0 = 3.00$ Å give a deviation of the cell volume of 3.67 % with respect to experimental findings. [243] For the slab, Γ-point calculations were performed and wave functions were expanded in the plane wave basis up to a kinetic energy of 400 eV. To investigate the (110) surface, which is the most stable surface for rutile, we chose a (3×2) surface unit cell with lattice parameters of $a_{0,surf} = 9.02$ Å and $_{b0,surf} = 13.13$ Å. Thus, defects were separated by at least ~8-9 Å. The slab is composed of 5 TiO_2 layers and the distance between slabs was larger than 12 Å. A five-layer slab was shown to reproduce the titania rutile bulk properties comparatively well. [228] Adsorption energies are defined in eqn. (15).

To simulate the STM images, the Tersoff-Hamann (**TH**) model was used. [244] Here, the STM tip is modeled as a locally spherical potential well centered at the tip position. Consequently, the STM image only shows properties of the surface. The sum over the local density of states of the sample in the energy range between the Fermi level and the bias potential at the tip position is calculated. The tunneling current is proportional to this integrated local density of states. So, we basically create a contour plot of occupied or empty states of the sample, depending on the sample bias. The TH method is used in the constant-current mode, where topographic images are obtained.

5.1.3 Au dimers on TiO_2 rutile (110)

Various adsorption positions of the Au dimers were considered computationally. On the stoichiometric surface, the Au dimer adsorbs on a 5c-Ti site, **Fig. 5** (a-b) with a large adsorption energy of -1.91 eV. The DOS (not shown) reveal that there is no charge transfer between Au dimer and support. This adsorption mode is comparable to that found for the Au tetramers on the TiO_2 anatase (101) surface, see previous chapter. The simulated STM image, **Fig. 5** (b), shows an oval shape, which is in nice agreement with the experimental STM image shown in **Fig. 5** (c). We investigated the influence of oxygen vacancies close by the 5c-Ti adsorption position and found no significant influence on the adsorption mode.

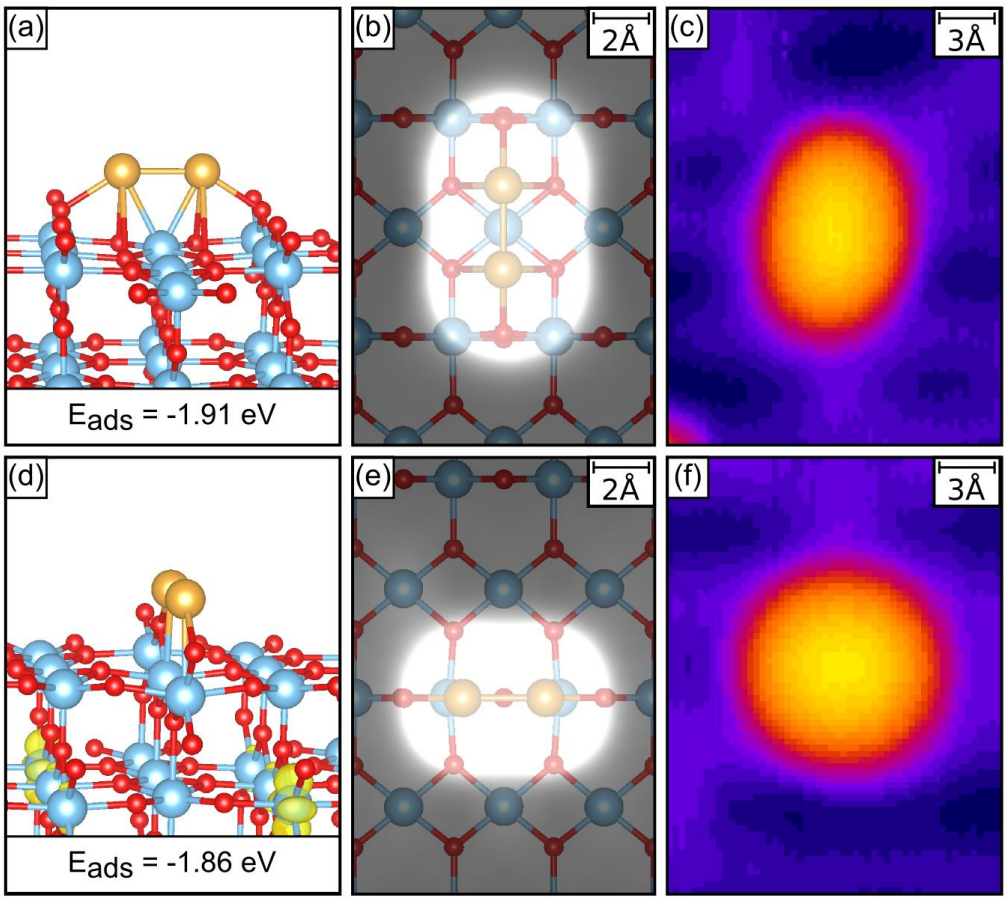

Fig. 5: Au_2 clusters supported on titania rutile (110). (a-c) Au_2/TiO_2, and (d-f) Au_2/TiO_{2-x}. (a) side view, (b) top-view overlaid with the simulated STM image (V_S = +0.8 V, d(Au-tip) = 1.00 Å, isodensity surface $5 \cdot 10^{-7}$ |e|/Å^3), (c) experimental STM image (T = 78 K, V_S = +0.8 V, I_T = 200 pA). (d) Au_2/TiO_{2-x} side view, (e) top-view overlaid with the simulated STM image (V_S = +0.8 V, d(Au-tip) = 1.00 Å, isodensity surface $5 \cdot 10^{-7}$ |e|/Å^3), (f) experimental STM image (T = 78 K, V_S = +0.8 V, I_T = 200 pA). The experimental STM images were produced by Dr. C.-M. Yim and Prof. G. Thornton, University College London.

The adsorption of the dimer in an oxygen vacancy is only slightly less favorable than the 5c-Ti site, **Fig. 5** (d). Also at this adsorption position, no charge transfer between cluster and support occurs. The 4c-Ti atoms of the vacancy transfer their excess electrons to the titania subsurface. The two electrons are shown in the spin plot in **Fig. 5** (d). Chrétien et al. found the same adsorption geometries and charge states, however they found the adsorption on the vacancy to be more stable. [48,222] The difference of the adsorption energy for the two adsorption sites (5c-Ti and V_O) is quite small in our study ($|\Delta E_{ADS}|$ = 0.07 eV) and their study ($|\Delta E_{ADS}|$ = 0.26 eV) and the different order of stability may be explained by the different methods used: We accounted for dispersion forces and used a different functional.

In the experiments, the position of the clusters can be controlled with tip pulses, which can be used to reveal oxygen vacancies located under the cluster. The experimental STM image in **Fig. 5** (f) shows a Au dimer positioned inside an oxygen vacancy. Compared to Au_2/5c-Ti, the Au_2/V_O exhibits a rounder shape. This trend is confirmed by the simulated STM images. The relative orientation of the Au-Au axis with respect to the Ti-5c rows is different for the two adsorption sites, **Fig. 5** (b, e). Whereas the Au-Au axis is oriented orthogonal to the Ti-5c rows for Au_2/5c-Ti, the Au-Au axis is oriented parallel to the Ti-5c rows for Au_2/V_O. These findings are again in good agreement with the experimental findings. Note that the Au signals in the experimental STM images appear larger than the simulated ones. This should be partially due to tip convolution effects, but also due to the choice of the electron density iso-surface, and could at last also be due to deviations of the computed electronic structure compared to the experimental one.

5.1.4 Au trimers on TiO_2 rutile (110)

Gold trimers were deposited on the stoichiometric and reduced titania rutile (110) surface. Various adsorption geometries and positions were considered. The most stable ones are reported in **Fig. 6**. We find that the Au trimer supported on the stoichiometric surface transfers one electron to the support and assumes a triangular shape. The transferred electron is shown as spin-density plot in **Fig. 6** (a). The charge transfer is also reflected in the quite large adsorption energy of -2.88 eV. The simulated STM image, **Fig. 6** (b), shows a broad round signal in good agreement with the experimental STM image shown in **Fig. 6** (c). Other less stable adsorption sites exhibit very different simulated STM images (now shown).

Is the trimer in contact with an oxygen vacancy, it assumes a chain-like shape, **Fig. 6** (d), with one Au atom located inside the vacancy. The results are in good alignment with the findings of Chrétien et al. [48,222] The trimer becomes negatively charged which is reflected by the Bader charge on Au of around -0.5 eV, and confirmed by the spin density plot showing only one electron at the lower part of the slab (not shown in **Fig. 6** (d)). The adsorption energy of the trimer on the vacancy is larger in modulus than the adsorption that of

the trimer on the stoichiometric surface. The simulated STM image is in great alignment with the experimental image. An elongated structure with a tiny constriction can be observed in both cases, **Fig. 6** (e-f). The constriction is at the opposite site of the vacancy.

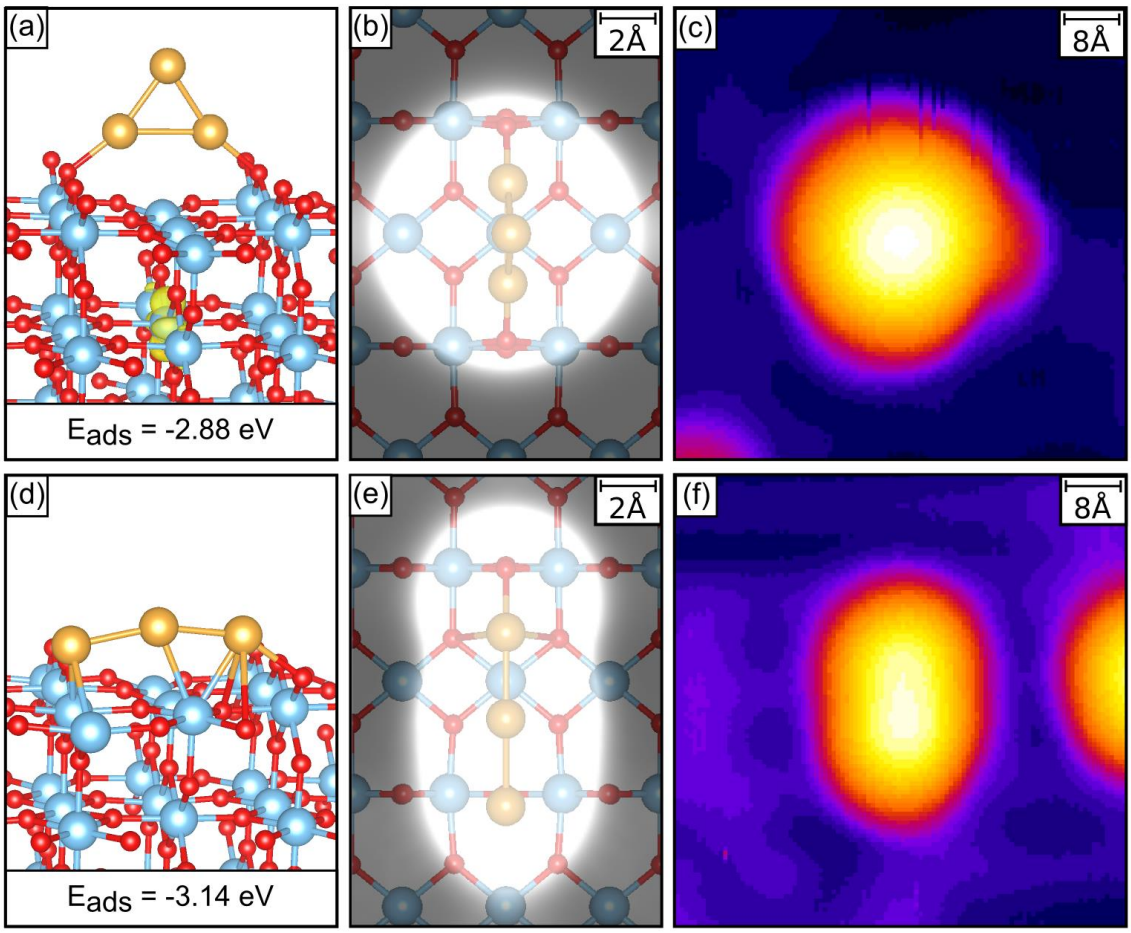

Fig. 6: Au_3 clusters supported on titania rutile (101). (a-c) Au_3/TiO_2, and (d-f) Au_3/TiO_{2-x}. (a) side view, (b) top-view overlaid with the simulated STM image (V_S = +0.8 V, d(Au-tip) = 1.00 Å, isodensity surface $5 \cdot 10^{-6}$ |e|/Å^3), (c) experimental STM image (T = 78 K, V_S = +0.8 V, I_T = 200 pA). (d) Au_3/TiO_{2-x} side-view, (e) top-view overlaid with the simulated STM image (V_S = +0.8 V, d(Au-tip) = 1.00 Å, isodensity surface $5 \cdot 10^{-7}$ |e|/Å^3), (f) experimental STM image (T = 78 K, V_S = +0.8 V, I_T = 20 pA). The experimental STM images were produced by Dr. C.-M. Yim and Prof. G. Thornton, University College London.

5.1.5 Section summary

- The adsorption modes of Au dimers and trimers supported on TiO_2 rutile (110) were investigated in a combined computational and experimental approach. A great alignment of the computed and experimental STM images is found for the different adsorption modes, verifying the computational methods applied.

- The dimers prefer to adsorb neutrally on vacancy-free parts of the substrate with adsorption energies around 2 eV.
- The adsorption mode of the trimers, on the other hand, depends strongly on the adsorption position. On vacancy-free surface parts, the trimer forms a triangle and transfers one electron to the support. When in contact to a surface vacancy, the trimer assumes a chain-like geometry with one Au atom being located inside the vacancy. In this latter case, one electron associated with the vacancy is transferred to the trimer, which becomes negatively charged.

5.2 Size-dependence of the melting temperature of Pt and Au nanoparticles[4]

5.2.1 Introduction

Common industrial catalysts consist of metal nanoparticles supported on/in oxide materials. The number of atoms in the larger nanoparticles is too large to be treated accurately with standard DFT in a reasonable amount of time. For example, a Pt particle with 10 nm diameter consists of roughly 35700 atoms. However, some of the properties of the metal particles arise solely at the nanometer size regime. Particles in this size regime can be modeled using molecular dynamics (**MD**) simulations in combination with semi-empirical potentials. This classical MD approach is computationally much less expensive than the methods based on DFT. An interesting property which can change with the particle size in the nanometer size regime is the melting temperature of the particle. [245] Metal nanoparticles usually exhibit a melting temperature depression compared to their bulk counterparts. [245] Experimental and theoretical studies indicate a linear dependence of the melting temperature T_m on the inverse particle diameter ($T_m \sim d^{-1}$). [245] In the past, different models have been proposed to describe the melting process, but so far no consensus on a model has been reached. The dependence of the melting temperature on the particle size is therefore interesting to study. The simulations and experiments reported in the literature are often limited to larger nanoparticles with diameters > 5 nm, and in the experiments usually averaging methods are applied to determine the melting point. [246]

A common experimental characterization technique for supported nanoparticles is transition electron microscopy (**TEM**). Here, a high energy electron beam (typically 100-300 keV) is transmitted through the sample. The latter must be thin enough for the electrons to travel

[4] The calculations reported in this study were performed at Danmarks Tekniske Universitet (Denmark) under supervision of Prof. Jakob Schiøtz. The experiments were performed by Prof. T. Willum Hansen, B. Sebok, and Prof. I. Chorkendorff.

through it. The electron beam interacts with the sample whereby some of the electrons are scattered and do not appear in the transmitted beam. Note that the electron beam interacts also with the electrons of the sample and therefore the imaged structure does not necessarily correspond to the atomic structure but may reflect features of the electronic structure of the sample. The transmitted electron beam is magnified and imaged on a fluorescent screen. Modern aberration-corrected TEM setups are capable of atomic resolution, especially when the atomic number of the imaged atoms is large (i.e. the nucleus is heavy) and the atomic columns of the crystalline particle are well aligned with the direction of the incoming beam.

In this study, we investigated the size dependence of the melting temperature of Pt and Au particles using a combined MD and high-resolution TEM (**HRTEM**) approach.[4] We tracked the melting of an individual Pt nanoparticle supported on a heatable SiN substrate via HRTEM. Further experiments are progressing. The melting temperature is compared to MD simulations, which provide insight to the atomic structure changes during the melting process. We chose Pt and Au particles because they are interesting for many catalytic applications and the nanoparticles do not become oxidized under ambient conditions. This makes it easy to study them with TEM. In this section, we will focus mainly on the computational part, because the experiments are still ongoing.

5.2.2 Experimental and computational details

Experimental details

The experiments were performed by Prof. T. Willum Hansen, B. Sebok, and Prof. I. Chorkendorff at Danmarks Tekniske Universitet. Mass-selected Pt and Au nanoparticles were deposited using a gas aggregation, magnetron sputtering cluster source equipped with a lateral time of flight mass filter (Nano-Beam 2011, Birmingham Instruments Ltd., United Kingdom [247,248,249]) having a base pressure in the low 10^{-10} mbar range and a mass resolution ($m/\Delta m \geq 20$). It is connected to an OMICRON Multiscan Lab XP system with a base pressure in the low 10^{-11} mbar range. During deposition, a metallic target is sputtered by argon plasma. The sputtered species aggregate into clusters and nanoparticles with different sizes in a liquid nitrogen cooled aggregation zone. [247] Helium gas is supplied to facilitate heat transfer between the chamber walls and the metal particles. The particles undergo a supersonic expansion and are focused into the mass filter, which separates the particles based on their mass to charge ration on the basis of the difference in their lateral speed after an electrical pulse [248]. The particles were deposited on Wildfire Nano-Chip XT MEMS SiNx TEM windows (DENSSolution, Netherlands [250]), which provide fast and accurate temperature control between room temperature and around 1500 K. The deposited TEM window was investigated in a FEI Titan E-Cell 80-300 ST TEM equipped with a post objective lens spherical aberration corrector. The size distribution of the SiN-supported par-

ticles of 3.4 ± 0.2 nm was determined using ImageJ. [251] The mass was chosen to fit a Wulff-constructed Pt particle, as simulated by molecular dynamics.

Computational details

Molecular dynamics (MD) simulations of Pt and Au nanoparticles have been performed using the Atomic Simulation Environment (ASE) in combination with the ASAP package. [204] Two nanoparticle shapes were considered: Wulff-constructions and round nanoparticles. The round particles were created by cutting a sphere out of the bulk fcc structure. To build up the Wulff-constructions, surface energies of the fcc metals were taken from a DFT study reported in the literature. [252] The nanoparticles were created, structure-optimized at 0 K and subsequently heated to the desired temperature using Langevin dynamics. [253] For our MD calculations, a friction constant of $\gamma_i = 8 \cdot 10^{-6}$ ps^{-1} was used. Time steps to integrate the equations of motion were set to 5 fs and the dynamics were run for roughly 10 ns. The optimizing and melting procedures were performed with EMT [254] and EAM [255,256] interatomic potentials, respectively. Polyhedral template matching (PTM) was used to analyze the atomic arrangement of the particles. [257] Here, the cut-off for the scale-invariant root-mean-square deviation was set to $\mathrm{RMSD_{max}} = 0.2$. For the data-fitting, least square regression has been used. In the temperature-energy curves, the melting region has been fitted with a second order fit function ($f(x) = ax^2 + bx + c$). A linear fit ($f(x) = ax + b$) was applied to determine the temperature-size relations.

The cohesive energies of the nanoparticles are calculated as defined in eqn. (16), where $\mathrm{E_{COH}(NP)}$ is the cohesive energy of the nanoparticle, $\mathrm{E(NP)}$ is the total energy of the nanoparticle, N is the number of atoms in the nanoparticle and $\mathrm{E(Atom)}$ is the total energy of the respective metal atom in vacuum. The surface energy of the nanoparticles is defined in eqn. (17), where $\mathrm{E_{COH}(Bulk)}$ is the cohesive energy per atom of the bulk fcc metal.

$$\mathrm{E_{COH}(NP)} = \mathrm{E(NP)/N} - \mathrm{E(Atom)} \tag{16}$$

$$\mathrm{E_{SURF}(NP)} = \mathrm{E_{COH}(NP)} - \mathrm{E_{COH}(Bulk)} \tag{17}$$

5.2.3 HRTEM imaging

The Pt nanoparticles were size selected and soft-landed on a heatable SiN window. The temperature was increased in steps of 50 K. **Fig. 7** shows HRTEM images of Pt particles at different temperatures. At room temperature and up to 1173 K, a crystalline structure of the particles can be observed. In **Fig. 7** (a), a 3.4 nm Pt particle with atomic resolution is shown. The protrusions show a crystalline hexagonal arrangement of the atoms. During the heating process and up to a temperature of 1173 K, **Fig. 7** (b), crystalline features such as lattice fringes were observed. After the temperature ramp from 1173 K to 1223 K, no particles

with crystalline features were found, even after extended search over many particles and regions on the substrate. The loss of crystallinity indicates that the melting process happens in this temperature region. Obviously, the effect of the electron beam on the melting temperature is ignored by using this approach.

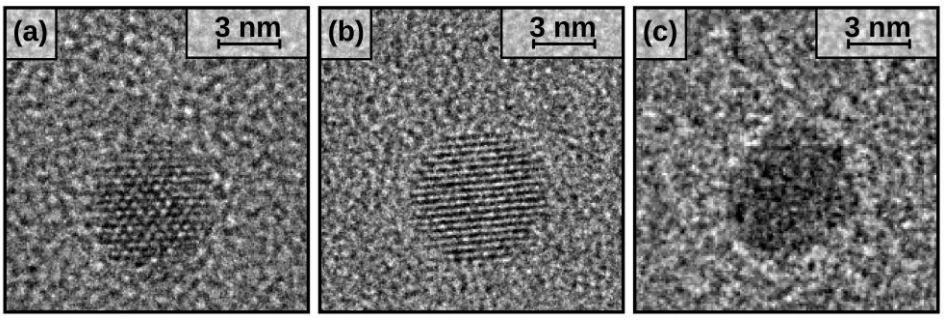

Fig. 7: HRTEM images of 3.4 nm Pt particles supported on a heatable SiN substrate at different temperatures: (a) T = 1023 K, (b) 1173 K, and (c) 1223 K. The experiments were performed by Prof. T. Willum Hansen, B. Sebok, and Prof. I. Chorkendorff, Danmarks Tekniske Universitet.

5.2.4 Molecular dynamics simulation of the melting region

The melting of platinum nanoparticles of different sizes and shapes were investigated using molecular dynamics simulations with interatomic potentials, as described in the computational details. Wulff-constructions (**WC**) and round nanoparticles were (R) considered. The particles were structure optimized at 0 K and then heated gradually to the desired temperature. The total energy, and thus the cohesive energy, of the particles thereby increased continuously. **Fig. 8** shows the cohesive energy of WC Pt particles with different diameters plotted against the temperature. We define the effective particle diameter as $D' = (2 \cdot r_{WS} \cdot N)^{1/3}$, where r_{WS} is the Wigner-Seitz radius of the element and N is the number of atoms in the particle. This way, particles of different shapes can be easily compared.

Let us firstly consider in more detail the results for simulations of the Pt particles with the EMT potential, shown in **Fig. 8** (a). The particles all melt in the temperature range between 1000 and 1400 K. Three different stages for the melting can be identified: In the first stage, the nanoparticle is heated up without melting. In this temperature regime, the energy increases with a linear slope corresponding to the inverse heat capacity. We investigated the heat capacity for Pt and Au WC particles with a first order fit in the temperature range from 0 to 500 K. We find independently from the element and the interatomic potential a value of around $C_p = 2.72 \cdot 10^{-4} \frac{eV}{K}$ which is roughly $3k = 2.59 \cdot 10^{-4} \frac{eV}{K}$ with k being the Boltzmann constant. In the second stage of the melting process, the heat capacity decreases and finally becomes negative, so that the temperature drops while the energy still increases. For

instance, for the 2.36 nm particle (blue line) this stage is observed in a temperature range of 900-1100 K. As we will see later in more detail, the particle melts completely until the end of this stage. In the last stage, the energy increases again linearly with the temperature. The temperature of the melting region increases with increasing nanoparticle diameter.

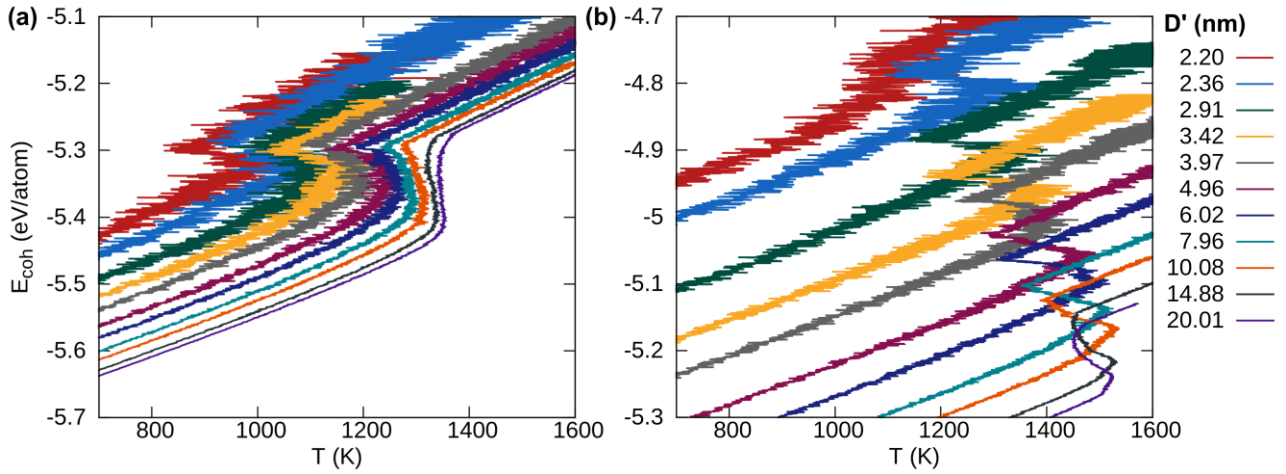

Fig. 8: Temperature dependence of cohesive energies (E_{COH}) of Wulff-constructed Pt nanoparticles. $D' = 2 \cdot r_{WS} \cdot N^{1/3}$, r_{WS} is the Wigner-Seitz radius of the respective bulk element. Particles were optimized and melted using (a) the EMT potential and (b) the EAM potential. The calculations reported in this study were performed at Danmarks Tekniske Universitet under supervision of Prof. Jakob Schiøtz.

Similar observations can be made for the EAM potential. However, comparing the two potentials we can identify three important differences. The first difference is that the cohesive energies of the particles are shifted towards more positive values when going from the EMT to the EAM potential. This is due to the fact that the potentials predict different surface energies for the nanoparticles, whereby the EMT potential underestimates the surface energies with respect to the EAM potential. The second difference is the behavior of the curve in the melting region. For the EMT potential, the melting region spreads over a larger energy range and a smaller temperature range than for the EAM potential. The third difference is the temperatures of the melting regions, which are higher for the EAM potential as for the EMT potential. The melting region of the largest two particles exceeds a temperature of 1500 K for the EAM potential, whereas it stays well below 1400 K for the EMT potential. This difference applies roughly also for the smaller particles.

We have seen in the HRTEM images in **Fig. 7** that the particles are crystalline at room temperature. However, in the experiments, the particles can deviate from a Wulff-construction (**WC**) shape, for instance due to the excess or the lack of atoms. Deviations in shape should affect the melting temperature due to the increased surface energy with respect to the perfect Wulff-construction. To investigate this effect, we considered round (**R**) nanoparticles which

have non-optimal structures, i.e. constitute local minima. The structure optimizations did not affect the shape of the round particles. We observe a similar qualitative behavior of the melting curves for the round particles as for the WC particles. The curves of the round particles (not shown) are shifted towards more positive cohesive energy values and lower temperatures. This is no surprise, since the surface energy of these particles is higher as for the WC particles and this lowers the melting temperature. As we will see later, the magnitude of these differences depends on the element and on the potential. The trends observed for the Pt particles qualitatively also apply to the Au particles.

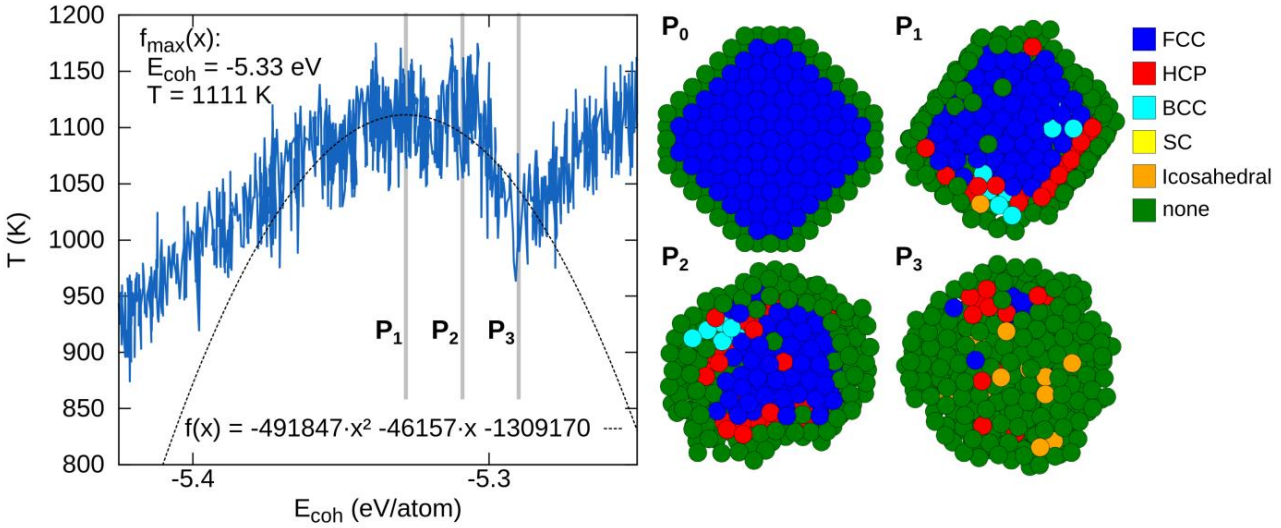

Fig. 9: Detailed analysis of the melting behavior of a Wulff-constructed Pt nanoparticle (D' = 2.9 nm), simulated with the EMT potential. T is plotted vs. E_{COH} in the melting region and the curve is fitted with a second order fit function f(x). PTM was used to determine the atomic coordination at T = 0 K (P_0) and at three different points in the melting region (P_1 to P_3). The images P_0-P_3 show cross-sections of the nanoparticle. The calculations reported in this study were performed at Danmarks Tekniske Universitet under supervision of Prof. Jakob Schiøtz.

To characterize in more detail the melting process, the change of the atomic structure has been investigated. The liquid phase of a material exhibits a complete lack of long-range order and crystallinity. The atomic coordination environment is therefore a useful parameter to determine and characterize the melting process of crystalline materials. We have investigated the atomic coordination environment of the nanoparticles using polyhedral template matching (**PTM**), as further described in the computational details. Different melting stages of a Pt particle (WC, D' = 2.9 nm) are shown in **Fig. 9**. Here, the blue curve shows the temperature plotted against the cohesive energy of the Pt particle. At the beginning, the temperature increases linearly with the cohesive energy. Around the maximum of the curve (f_{max}), we detect some structural changes at the surfaces of the nanoparticle (P_1). Here, a significant

amount of atoms at the subsurface has lost the fcc crystal structure. At P_2, the amount of atoms without identified crystal structure at the subsurface is increased with respect to P_1. The core remains thereby mainly in the fcc structure. This clearly indicates that the particle is melting from the surface to the core, forming a liquid shell during the melting process. At P_3, the particle is completely molten and the local minimum of the blue curve is reached. Further increase of the energy results in a linear temperature increase, just as before the melting process. This analysis was done also for other nanoparticles (different sizes, shapes, elements and potentials). The melting process was always similar.

The observed melting behavior agrees well with MD simulations of Cu and Ag nanoparticles reported in the literature. [258,259] We have seen that the melting proceeds almost entirely in the region with negative heat capacity, i.e. between points P_1 and P_3. Given the simplicity to determine the maximum of the fit function (f_{max}), we define the temperature at P_1 as the melting temperature. This way it is possible to investigate trends in the melting region between different particles.

5.2.5 Trends in melting temperatures of Pt and Au particles

The melting temperatures of Pt and Au particles of different shapes and sizes have been investigated as described in the previous section. Wulff-constructed (WC) and round (R) particles with diameters of 2-20 nm have been considered for Pt and Au, respectively. The melting temperatures of the different particles are plotted against 1/D' (with $D' = 2 \cdot r_{WS} \cdot N^{1/3}$) in **Fig. 10**. A linear behavior ($T_m \sim 1/D'$) is found for the Pt particles (**Fig. 10** (a)) as well as for the Au particles (**Fig. 10** (b)). Therefore, linear fit functions of the form f(x) = ax + b were used. The bulk melting temperatures of the potentials are also indicated in **Fig. 10** at $\frac{1}{D'} \rightarrow 0$, but these values are not included in the fit. In principle, the parameter b should reproduce the bulk melting temperature of the respective potential. The bulk melting temperatures predicted by the EAM potential are $T_{m,bulk}(Pt) = 1890$ K [260] and $T_{m,bulk}(Au) = 1281$ K [261]. The bulk melting temperature for Pt predicted by the EMT potential is $T_{m,bulk}(Pt) = 1357$ K[5]. Both potentials underestimate the experimental bulk melting temperatures of Pt (2042 K) and Au (1338 K). [231] Interestingly, the extrapolations $\frac{1}{D'} \rightarrow 0$ for the EAM Pt fit functions do not reproduce the literature bulk melting temperature simulated with the same potential [260]. Instead, a deviation of the extrapolated Pt bulk temperatures of 1538 and 1617 K, **Fig. 10** (a), and the bulk melting temperature of 1890 K reported in [260] deviate by more than 270 K.

[5] This value was provided by Prof. Jakob Schiøtz.

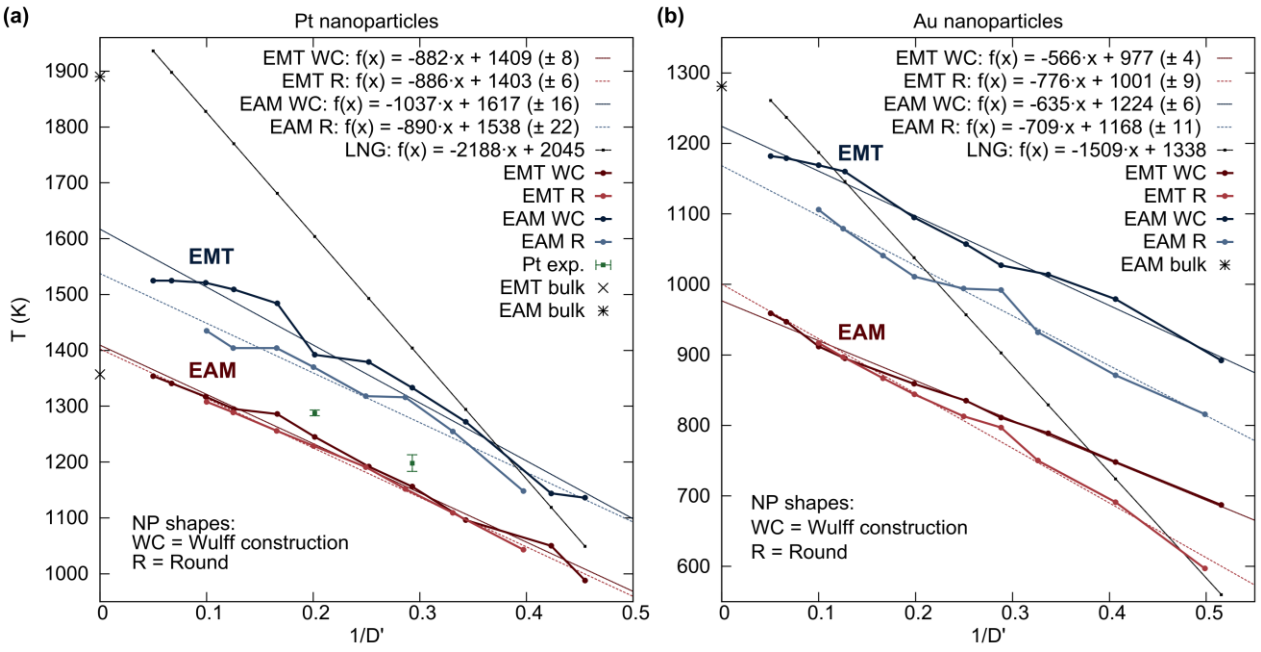

Fig. 10: Melting temperatures of (a) Pt and (b) Au nanoparticles in dependence of the inverse particle diameter, $D' = (2 \cdot r_{WS} \cdot N)^{1/3}$. The green squares in (a) are experimentally determined melting temperatures. The thin black line represents liquid nucleation and growth (LNG) model with parameters taken from ref. [245].

Let us now examine in more detail the trends in the simulated melting temperatures for the different cases. A first observation is that the EAM potentials give melting temperatures roughly 200 K higher than the EMT potentials. This is true for both elements. A second observation is that the WC particles exhibit larger melting temperatures as the round particles. This is expected given the lower surface energies of WC particles with respect to round particles. The only exception is observed for larger Au particles simulated with the EMT potential. Here, the WC and R particles melt approximately at the same temperature. The difference in the melting temperatures between WC and R particles is larger for the EAM potential than for the EMT potential. This means that the difference in surface energy between WC and R particles is more pronounced for the EAM potential than for the EMT potential. Empirically, it has been found that the melting temperature of bulk materials depends on the cohesive energy as $T_m = (0.032/k_B) \cdot E_{COH}$. [262] So, the decreased cohesive energy (larger surface energy) of a nanoparticle with respect to the corresponding bulk material has a significant effect on the melting temperature depression. A further observation is that the curves predicted by the EMT potential are quite linear whereas larger deviations from a perfect linear behavior is observed for the EAM potential. All in all it seems that the potential choice is more important than the choice of the particle shape, although the latter has also a significant influence on the calculated melting temperature.

Different melting mechanisms have been proposed in the literature. [245] In particular, we can distinguish between the homogeneous melting (HM) hypothesis, the liquid skin melting (LSM) hypothesis, and the liquid nucleation and growth (LNG) hypothesis. According to the HM hypothesis, the particle melts homogeneously, i.e. no difference between the surface and the center of the particle is observed. In the LSM, the particle forms a liquid skin, which does not become thicker during the melting process. At a certain point, the rest of the particle melts homogeneously. The LNG hypothesis is similar as the LSM, but this time the liquid shell grows during the melting process until the particle is completely molten. With the help of the PTM analysis, we have observed the formation and the growth of a liquid skin during the melting process, **Fig. 9**. It is therefore interesting to investigate if the LNG model successfully predicts the simulated data. A quantitative representation of the LNG model is given in eqn. (18).

$$\frac{T_m(\mathrm{NP})}{T_m(\mathrm{bulk})} = 1 - \frac{6V}{\Delta H_f D'}\left[\gamma_{sv} - \gamma_{lv}\left(\frac{\rho_s}{\rho_l}\right)^{1/2}\right] = 1 - \frac{\beta_{LNG}}{D'} \qquad (18)$$

Here, V is the volume of the particle, ΔH_f is the bulk latent heat of fusion, γ_{sv} and γ_{lv} are surface energies of solid-vapor and liquid-vapor interfaces, respectively, ρ_{sv} and ρ_{lv} are the densities of solid and liquid, respectively, and D' is the particle diameter (in our case defined as $D' = 2 \cdot r_{WS} \cdot N^{1/3}$). [245] To plot the lines representing the LNG model in **Fig. 10**, we used the parameters β_{LNG} and the bulk melting temperatures $T_m(\mathrm{bulk})$ from reference [245]. For both Pt and Au, respectively, the LNG model predicts a steeper slope as the simulation fits. The experimental melting temperature range of 1173-1223 K of the 3.4 nm Pt nanoparticle lies just between the predictions of the EMT and the EAM potentials. The same is true for the 5.0 nm Pt nanoparticle with an experimental melting temperature range of 1288-1293 K. Note that the experimental data for the 5.0 nm Pt particle have to be verified. Further experimental investigations are underway.

5.2.6 Section summary

- The melting temperatures of Pt and Au nanoparticles were investigated using MD simulations and high-resolution TEM experiments. An approximately linear dependence of the melting temperature on the inverse particle diameter ($T_m \sim d^{-1}$) was found in all cases. So far, we find a good agreement of the computed and experimental data.
- The choice of the interatomic potential affects the simulated melting temperature more than the particle shape. We find that the particle melting proceeds from the surface to the core, corresponding to the liquid nucleation and growth model.
- Smaller Au particles (~1.94 nm) melt already at lower temperatures (290 °C), which implies that in certain cases the particles could be molten under reaction conditions.

Chapter 6 The support is not innocent

6.1 Tuning the chemistry of Ag and Au clusters by doping the oxide support[6]

6.1.1 Introduction

Under reaction conditions, the active metal component can undergo large morphological changes, such as sintering, which can effectively deactivate the catalyst. [213,44] A possibility to reduce the lateral mass transport is to increase the interaction between particle and substrate. Intrinsic and extrinsic defects can strongly interact with the particles and therewith serve as anchoring sites. For instance, the presence of oxygen vacancies on the titania surfaces is well known to increase the adsorption energy of Au atoms and clusters. [235]

In general, oxide doping is an important strategy to modify the properties of supported catalysts and to stimulate the occurrence of a charge transfer at the metal/oxide interface. [263] There is ample evidence that this can lead not only to changes in the electronic properties of adsorbed metal particles, but also to changes in the cluster shape. [264,265] This is for instance the case for Au nanoparticles deposited on Mo-doped CaO films. [266] The Mo dopants act as electron donors to the Au clusters. The clusters change from being neutral and three-dimensional to being negatively charged and two-dimensional. The possibility to selectively charge supported nano-clusters represents an interesting way to tune the catalytic properties. In this study, we investigated the effect of oxygen vacancies, nitrogen- and niobium dopants in the titania anatase (101) surface on the cluster-support interaction. In particular, the adsorption strength and the charge state of the clusters are of interest.

6.1.2 Computational details

Spin-polarized periodic DFT calculations have been performed as described in section 4.1.2. In short, we used the PBE exchange-correlation functional [161], and applied the GGA+U approach proposed by Dudarev et. al. [172] The effective U-parameter was set to 3 eV for the Ti 3d states and to 4 eV for the Nb 4d states. Furthermore, we accounted for van-der-

[6] The content of this study is published in the Journal "Physical Chemistry Chemical Physics": P. Schlexer, A. Ruiz Puigdollers, and G. Pacchioni, "Tuning the charge state of Ag and Au atoms and clusters deposited on oxide surfaces by doping: A DFT study of the adsorption properties of nitrogen- and niobium-doped TiO_2 and ZrO_2.", PCCP, 17 (2015) 22342-22360. http://doi.org/10.1039/c5cp03834k

Waals (vdW) forces by applying the DFT+D2' approach. [160,161] To describe electron-ion interactions, the PAW method was used. [267,193] N(2s 2p), O(2s, 2p), Ti(3s, 4s, 3p, 3d), Nb(4d, 5s), Ag(4d, 5s) and Ag(5d, 6s) were treated explicitly. Structure optimizations, DOS, adsorption energies and Bader charges were calculated as described in section 4.1.2.

The titania anatase (101) surface was represented by a (3×1) surface super cell of a slab consisting of five layers of TiO_2 units, see section 4.1.2. On the titania anatase (101) (3×1) surface super cell, there are 6 2-fold coordinated oxygen atoms (2c-O) and 12 3-fold coordinated oxygen atoms (3c-O). So, removing one 2c-O, the surface concentration of oxygen vacancies is 1/6 or 1/18 per surface super cell, depending on the definition. The same consideration applies for the nitrogen-dopant, since here one O atom is being replaced by N. There are 9 Ti atoms on the surface, of which 6 are 5-fold coordinated (5c-Ti) and 3 are 6-fold coordinated (6c-Ti). The replacement of a 5c-Ti by Nb thus leads to a surface Nb concentration of 1/6 or 1/9 per surface super cell, again depending on the definition. In the entire cell, there are 120 O and 60 Ti atoms, so that the volume-based dopant concentration is low. Dopants are separated by at least 10 Å. The oxygen vacancy formation energy E_{Vo} is given in eqn. (19). Here E denotes the total energies of the structure-optimized parts.

$$E_{V_O}(TiO_2) = E(V_O/TiO_2) - \frac{1}{2}E(O_2) - E(TiO_2) \qquad (19)$$

Changing from a (3×1) to a (2×2) surface super cell, while maintaining the five layers of TiO_2 units, introduces a change in the oxygen vacancy formation energy of -0.04 eV, see **Table 32** for more details. Since this change is small, we are confident that defect-defect interactions, as well as interactions between cluster replica, are minimized in the (3×1) surface unit cell.

6.1.3 The defective TiO_2 anatase (101) surface

To understand in more detail how the presence of oxygen vacancies, nitrogen dopants, and niobium dopants influence the interaction between the metal clusters and the support, it is useful to first analyze how these defects affect the electronic structure of the oxide support. We have considered defects at the surface and at the subsurface of the slab. The exact position of the defects is shown in **Fig. 11** (a). The electronic DOS curves of the different cases are shown in **Fig. 11** (b-g). As we have seen before, the stoichiometric surface exhibits a band gap of around 2.6 eV and no gap states can be observed, **Fig. 11** (a). The removal of a neutral surface oxygen atom leads to the formal reduction of two Ti^{4+} ions to Ti^{3+}, which results in the presence of two Ti 3d states in the band gap, **Fig. 11** (c). These states are circa 0.4 eV below the conduction band minimum (**CBM**). Obviously, the removal of an oxygen atom lowers the coordination number of the respective Ti atoms.

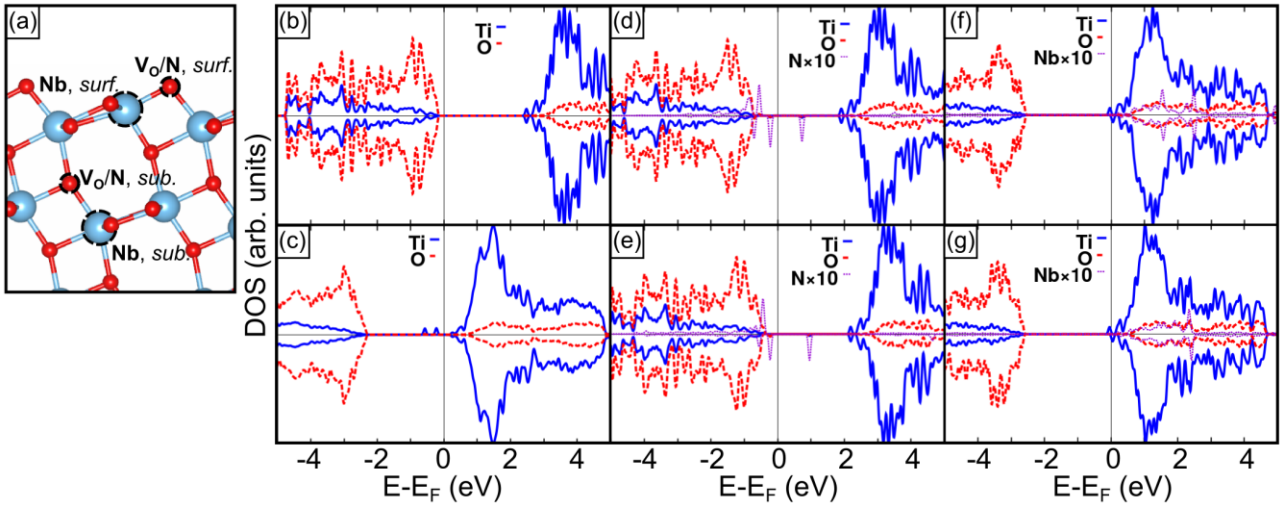

Fig. 11: Effect of oxygen vacancies, nitrogen-doping and niobium-doping on the electronic structure of the TiO_2 anatase (101) surface. (a) Positions of the defects. (b-g) DOS. (b) Stoichiometric surface. (c) Surface with an oxygen vacancy at the surface. (d) Nitrogen-dopant at the surface and (e) at the subsurface. (f) Niobium-dopant at the surface and (g) at the subsurface. [268]

Replacing an oxygen atom by nitrogen introduces electron deficiency, which is represented by the unoccupied N 2p state in the titania band gap, **Fig. 11** (d-e). The energy difference between the highest occupied and the lowest unoccupied N-projected states increases slightly when going from the surface to the subsurface dopant position. This reflects the slightly higher stability (~ 0.3 eV) of the subsurface N-dopant with respect to the surface N-dopant. A similar observation was made for the Nb-dopant. Note that a strong interaction of the dopant with the cluster at the surface may be a driving force for the dopant to migrate to the surface. Substituting a tetravalent Ti atom by a pentavalent Nb atom, an excess electron is introduced, which is transferred to the TiO_2 CBM, **Fig. 11** (f, g). The position of the Nb dopant has no influence on this behavior. The charge transfer to the CBM formally reduces the titania host and has therefore a similar effect as the oxygen vacancy. However, this time the Ti coordination numbers do not change, making the occupied Ti 3d states resulting from the Nb dopant different from those resulting from the oxygen vacancy, cf. **Fig. 11** (c, g).

6.1.4 Effect of oxygen vacancies on the cluster-support interaction

Ag and Au atoms on reduced titania

The adsorption of Ag and Au atoms on stoichiometric and reduced TiO_2 anatase (101) surfaces has been investigated. Resulting adsorption energies, magnetic moment and Bader charges are shown in **Table 4**. The best adsorption configurations are shown in **Fig. 12**. Let us consider first the adsorption of the Ag atom. On the stoichiometric surface, the best ad-

sorption position is the 2c-O hollow site. Here, the Ag atom transfers its 5s valence electron to the titania support, as discussed in detail in section 4.1. If the Ag atom is adsorbed on top of a surface oxygen vacancy (**V_O,** *surf.*), the adsorption energy is increased by 0.9 eV with respect to that on the stoichiometric surface. Now, one electron of the vacancy is transferred to the Ag 5s state. [268] The charge transfer is reflected in the negative Bader charge on Ag and the absence of a magnetic moment on Ag, **Table 4**. The influence of the oxygen vacancy is attenuated when the vacancy is positioned at the subsurface (**V_O,** *sub.*). In this case, the Ag atom behaves just as on the stoichiometric surface, **Table 4**, **Fig. 12** (c). It seems that a direct contact between vacancy and Ag atom is needed to stabilize the negative charge on Ag. Recapitulating the insights from section 4.1.3, we can definitely conclude that the adsorption position plays a determining role for the charge state of the Ag atom.

Table 4: Adsorption energies E_{ADS} [eV], magnetic moments μ [μ_B], and Bader charges q [|e|] of Ag and Au atoms deposited on stoichiometric and reduced TiO_2 (101).

X	Surface	Position (X)	E_{ADS}	|μ|(X)	|μ|(MO_2)	q(X)
Ag	TiO_2	2c-O-hollow	-1.04	0.00	0.70	+0.66
	V_O, *surf.*	On V_O, *surf*	-1.94	0.00	0.68	-0.26
	V_O, *sub.*	2c-O-hollow	-1.05	0.00	2.46	+0.66
Au	TiO_2	5c-Ti-top	-0.61	0.41	0.21	-0.01
	V_O, *surf.*	On V_O, *surf*	-3.07	0.00	0.68	-0.46
	V_O, *sub.*	5c-Ti-top	-1.61	0.00	0.79	-0.43

Let us now consider the adsorption of Au. As we know from section 4.1.3, the Au atom adsorbs neutrally on a Ti-O bridge site on the stoichiometric TiO_2 anatase (101) surface. The adsorption is mainly realized via dispersion forces and only a minor spin contamination of the support could be detected, **Table 4**. The latter is due to a slight hybridization of the Au 6s states with the O 2p states of the support. Is the Au atom adsorbed on an oxygen vacancy, the adsorption energy is enhanced by a factor of five, **Table 4**. As in the case of Ag, the Au atom becomes negatively charged. However, the adsorption energy of Au on V_O is around 1.1 eV larger in modulus than that of Ag on V_O. This is related to the different electron affinity of the two atoms, **Table 5**. [231]

Table 5: Ionization potentials IP [eV] and electron affinities EA [eV] of Ag and Au atoms, tetramers and pentamers.

	Ag	Au	Ag_4	Au_4	Ag_5	Au_5
IP	7.57[(a)]	9.22[(a)]	5.83[(b)]	7.32[(b)]	5.52[(b)]	6.84[(b)]
EA	1.30[(a)]	2.31[(a)]	1.63[(a)]	2.56[(a)]	2.12[(a)]	3.06[(a)]

[(a)]Taken from ref. [231] , [(b)]taken from ref. [269]

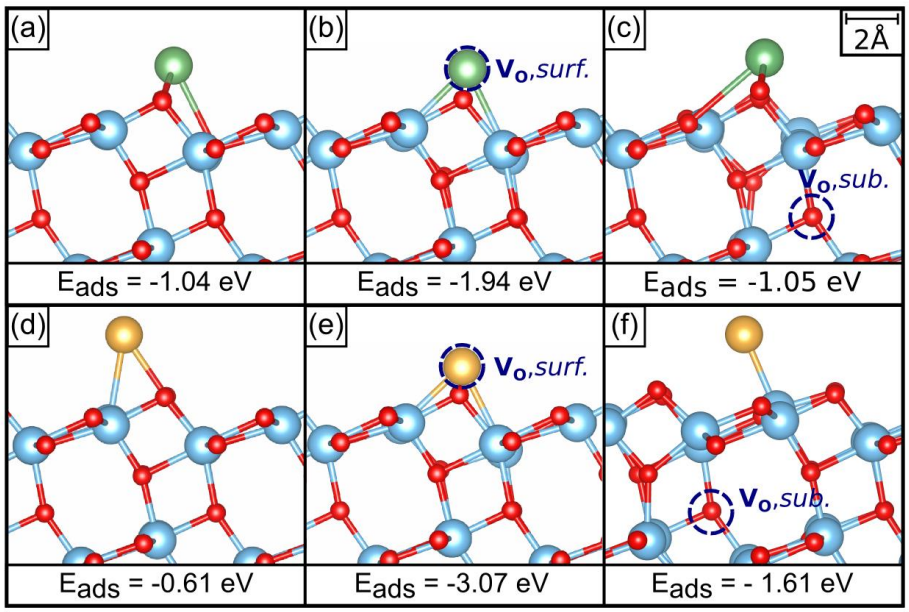

Fig. 12: Ag and Au atoms adsorbed on stoichiometric and reduced TiO_2 anatase (101). (a) Ag on the stoichiometric surface, (b) Ag on $\mathbf{V_O}$, *surf.* and (c) Ag on $\mathbf{V_O}$, *sub*. (d) Au on the stoichiometric surface, (e) Au on $\mathbf{V_O}$, *surf.*, (f) Au on $\mathbf{V_O}$, *sub*. [268]

If the Au atom is adsorbed on the TiO_2 surface with a subsurface oxygen vacancy, the same charge transfer behavior as on the surface oxygen vacancy is observed. This time, however, the adsorption energy is enhanced by only 1.0 eV (> 2 eV for the surface V_O) with respect to the stoichiometric surface. This difference can be explained by the larger separation of the transferred charge and the different interaction of the Au atom with the surface. The coordination environment on the Ti-O bridge site does not stabilize the Au^- ion as much as the under-coordinated Ti atoms in the vacancy do. We conclude that the presence of oxygen vacancies at the surface of the TiO_2 anatase (101) surface enhances the adsorption energy of the Ag and Au atoms, which become negatively charged. If the vacancy is located at the subsurface, the influence decreases.

Effect of oxygen vacancies on the adsorption of the Ag and Au tetramers

The adsorption of the Ag and Au tetramers on the stoichiometric titania anatase (101) surface was discussed in details in section 4.1.4. Here we concentrate on how the adsorption mode changes as oxygen vacancies are present on the surface. Various adsorption configurations have been investigated, but again only the most stable cases are reported. Adsorption energies, magnetic moments and Bader charges of the tetramers are summarized in **Table 6**. The adsorption energy of the Ag tetramer on the stoichiometric surface is around -2.0 eV and the tetramer exhibits a neutral charge state with a closed-shell electronic structure.

Table 6: Adsorption energies E_{ADS} [eV], magnetic moments μ [μ_B], and Bader charges q [|e|] of Ag_4 and Au_4 clusters deposited on stoichiometric and reduced TiO_2 (101).

X	Surface	E_{ADS}	$\|\mu\|(X_4)$	$\|\mu\|(MO_2)$	q(X)
Ag_4	TiO_2	-2.02	0.00	0.00	+0.36
	V_O, *surf.*	-2.91	0.00	0.00	+0.45
	V_O, *sub.*	-2.08	0.00	1.71	+0.34
Au_4	TiO_2	-2.19	0.00	0.00	+0.03
	V_O, *surf.*	-3.45	0.00	0.00	-0.82
	V_O, *sub.*	-2.41	0.00	1.61	+0.01

Is the tetramer adsorbed on a surface oxygen vacancy, the adsorption energy is enhanced by around 0.9 eV. The charge state of the tetramer remains the same as on the stoichiometric surface, which is reflected in the Bader charges and the magnetic moment on the tetramer. The magnetic moment of the support is zero, although the surface vacancy is present and no charge transfer occurs. This is due to the strong interaction of the tetramer with the vacancy, reflected in the fact that two of the Ag atoms are situated in the vacancy, **Fig. 13** (a-b).

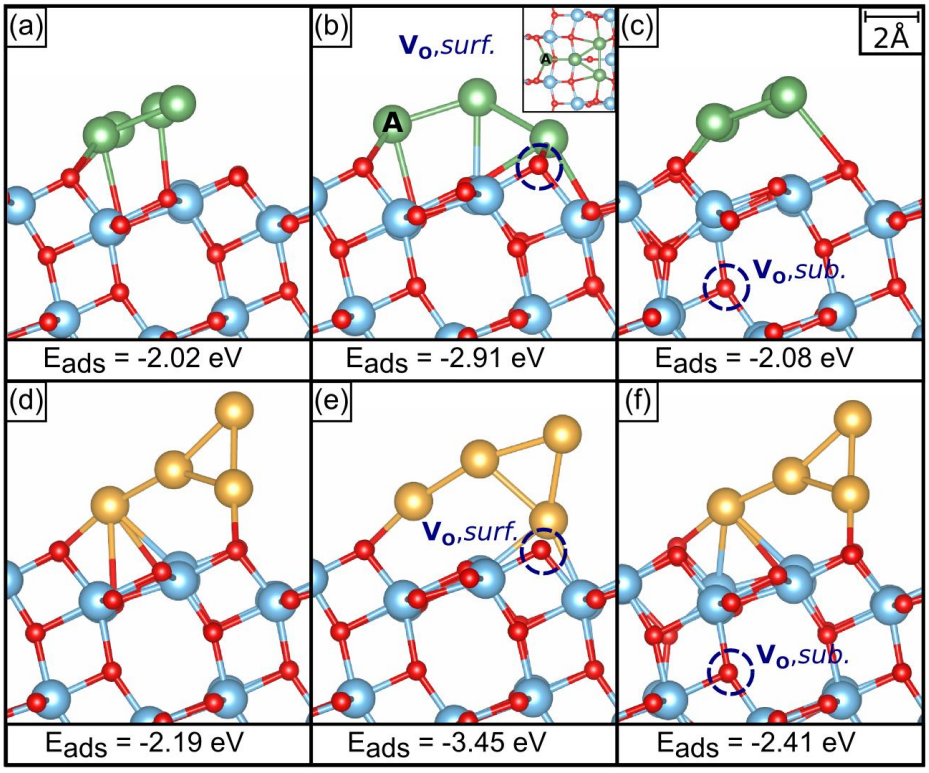

Fig. 13: Ag and Au tetramers adsorbed on stoichiometric and reduced TiO_2 anatase (101). (a) Ag_4 on the stoichiometric surface, (b) Ag_4 on **V_O,** *surf.* and (c) Ag_4 on **V_O,** *sub.* (d) Au_4 on the stoichiometric surface, (e) Au_4 on **V_O,** *surf.* and (f) Au_4 on **V_O,** *sub.* [268]

From the DOS, it can be seen, that the Ti 3d states assigned to the vacancy form a singlet state, **Fig. 14** (b). This explains the absence of the magnetic moment on the support. Is the vacancy positioned at the subsurface, the adsorption mode of the Ag tetramer is similar to that on the stoichiometric surface, just as in the case of the Ag atom.

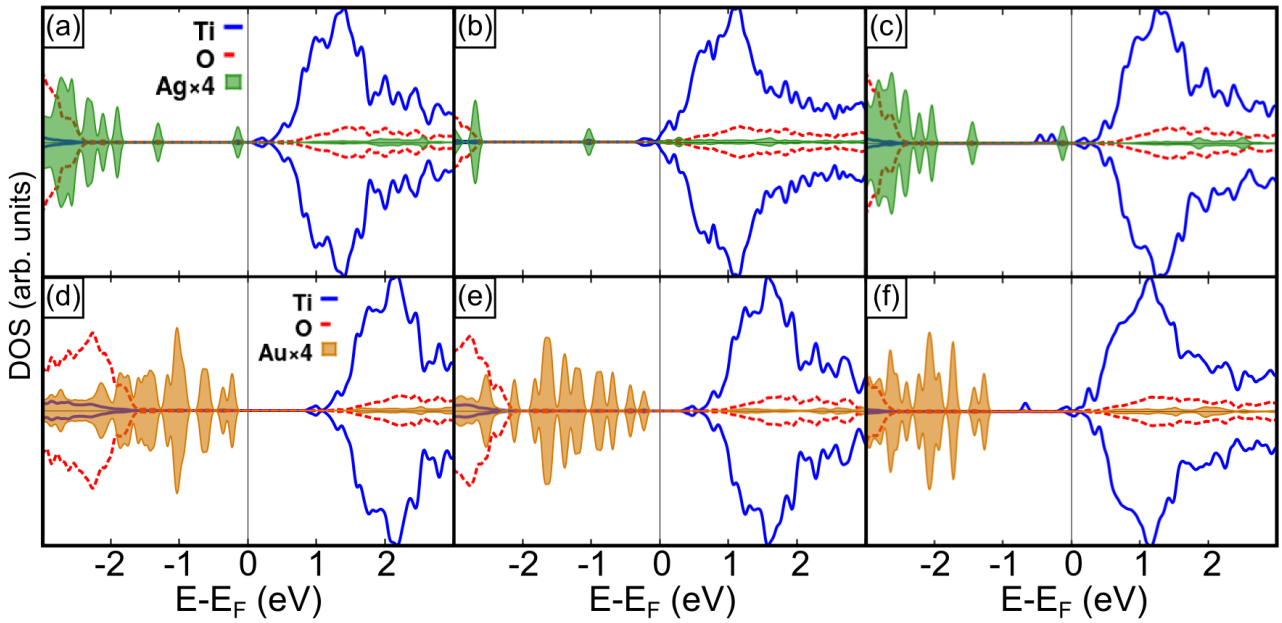

Fig. 14: DOS Ag and Au tetramers adsorbed on stoichiometric and reduced TiO_2 anatase (101) surfaces. (a) Ag_4 on the stoichiometric surface, (b) Ag_4 on TiO_2 with a surface oxygen vacancy and (c) Ag_4 on TiO_2 with a subsurface oxygen vacancy. (d) Au_4 on the stoichiometric surface, (e) Au_4 on TiO_2 with a surface oxygen vacancy and (f) Au_4 on TiO_2 with a subsurface oxygen vacancy. [268]

Let us now consider the adsorption of the Au tetramer. The most stable isomer of the Au tetramer on the stoichiometric surface is different from that of the Ag tetramer, as discussed in section 4.1.4. Is the Au tetramer adsorbed on a surface oxygen vacancy, one Au atom of the tetramer refills the vacancy, **Fig. 13** (e). This is different from the Ag tetramer, where two atoms are located in the vacancy. The presence of the vacancy enhances the adsorption energy of the Au tetramer by around 2.5 eV with respect to the stoichiometric surface. The DOS reveal the hybridization of Ti 3d states with the Au states, **Fig. 14** (e), indicating the formation of polar-covalent Au-Ti bonds. Is the oxygen vacancy positioned at the subsurface, the Au tetramer behaves similar as on the stoichiometric surface. The presence of oxygen vacancies enhance the adsorption energy of Ag and Au atoms and tetramers. In 3 of 4 cases, the surface oxygen vacancy introduces a negative charge on the adsorbate. The interaction between the adsorbates and the vacancies are reduced when the vacancy is located at the subsurface. Here, only the Au atom becomes negatively charged. Evidently, reducing the surface of TiO_2 (101) can help to anchor Ag and Au clusters consisting of a few atoms.

6.1.5 Effect of nitrogen-doping on the cluster-support interaction

Ag and Au atoms on nitrogen-doped titania

The interaction of Ag and Au atoms on the nitrogen-doped titania anatase (101) was investigated. Adsorption energies, magnetic moments and Bader charges are reported in **Table 7**. As for the oxygen vacancy, a position of the nitrogen dopant at the surface and at the subsurface was considered. As we have seen in section 6.1.3, the nitrogen dopant introduces a para-magnetic gap state in the adsorbate-free surface, which results in a magnetic moment of 1 μ_B. This magnetic moment is absent when the Ag and Au atoms are adsorbed, **Table 7**. Furthermore, the Bader charges on Ag and Au are all positive, indicating a charge transfer from the atoms to the gap state.

Table 7: Adsorption energies E_{ADS} [eV], magnetic moments μ [μ_B], and Bader charges q [|e|] of Ag and Au atoms deposited on N-doped TiO_2 (101).

X	Dopant, position	E_{ADS}	$\|\mu\|(X)$	$\|\mu\|(MO_2)$	q(X)
Ag	**N**, *surf.*	-3.35	0.00	0.00	+0.60
	N, *sub.*	-2.89	0.00	0.00	+0.67
Au	**N**, *surf.*	-3.01	0.00	0.00	+0.32
	N, *sub.*	-2.14	0.00	0.00	+0.45

The adsorption configurations are shown in **Fig. 15** (a-d). The best adsorption position is always the 2c-O-hollow site, which we already know from the adsorption of Ag on the stoichiometric surface. This position stabilizes the positive charge, because the ions are coordinated by four O atoms. Compared to the adsorption on the stoichiometric surface, the adsorption energies of the atoms on the nitrogen-doped surfaces are much larger in modulus. The atoms bind strongly, with adsorption energies between -2.14 eV for Au on the subsurface nitrogen dopant and -3.35 eV for Ag on the surface nitrogen dopant. The adsorption energy of the Ag atom is always larger in modulus than that of the corresponding Au case. This is due to the fact, that Ag exhibits a lower ionization potential than gold, **Table 5**.

The charge transfers are verified by the DOS, **Fig. 15** (e-h), where the N 2p states are all filled. The atoms exhibit a closed shell electronic structure with an empty state 1.5-2.5 eV above the Fermi level. The transfer from the 5s (6s) valence state to the gap state releases quite much energy, because the gap state is located only 1.2-1.5 eV above the valence band, **Fig. 11**. As in the case of the oxygen vacancies, the direct interaction of the atoms with the surface nitrogen dopant is associated with a larger energy gain than the interaction with the subsurface nitrogen dopant, **Table 7**. We have seen that for Ag and Au atoms, a charge transfer to the support occurs. In the following section, we will see if this applies also to the Ag and Au tetramers.

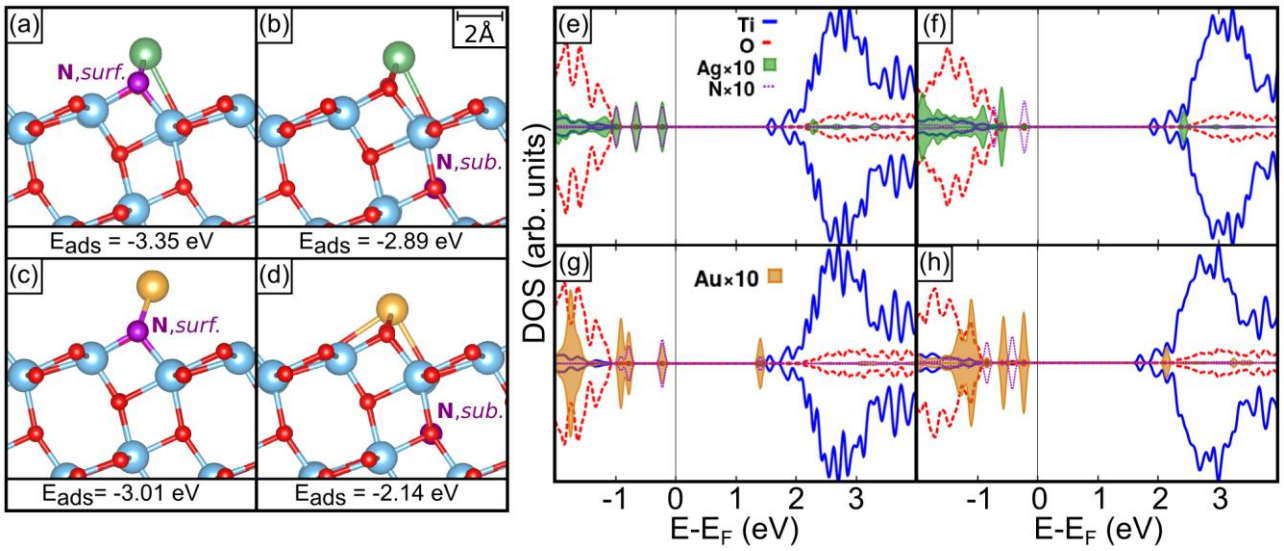

Fig. 15: Ag and Au atoms on nitrogen-doped TiO_2 (101). (a) Ag on **N**, *surf.*, (b) Ag on **N**, *sub.*, (c) Au on **N**, *surf.*, (d) Au on **N**, *sub.*, (e) DOS of Ag on **N**, *surf.*, (f) DOS of Ag on **N**, *sub.*, (g) DOS of Au on **N**, *surf.*, (h) DOS of Au on **N**, *sub.* [268]

Ag and Au tetramers on nitrogen-doped titania

The tetramers were adsorbed on nitrogen doped TiO_2, where the nitrogen dopant was either located at the surface or at the subsurface. Adsorption energies and other interesting parameters of the adsorbed tetramers are summarized in **Table 8**.

Table 8: Adsorption energies E_{ADS} [eV], magnetic moments μ [μ_B], and Bader charges q [|e|] of Ag_4 and Au_4 clusters deposited on N-doped TiO_2 (101).

X	Dopant, position	E_{ADS}	|μ|(X)	|μ|(MO_2)	q(X)
Ag_4	**N**, *surf.*	-3.82	0.33	0.16	+0.76
	N, *sub.*	-3.56	0.35	0.13	+0.78
Au_4	**N**, *surf.*	-3.54	0.52	0.25	+0.29
	N, *sub.*	-2.65	0.60	0.14	+0.49

As for the atoms, the adsorption energies of the tetramers are significantly enhanced with respect to the stoichiometric surface. The tetramers exhibit a non-zero magnetic moment on the nitrogen-doped surface, indicating that the tetramers are charged, because the tetramers exhibit a closed-shell electronic structure in the neutral charge state. The Bader charges on the tetramers are always positive, ranging from +0.29 |e| for Au_4 on the surface nitrogen dopant to +0.78 |e| for Ag_4 on the subsurface nitrogen dopant. As for the atoms, the adsorption energies of the Ag tetramers are always larger in modulus than the corresponding adsorption energies of the Au tetramers, which is due to the lower ionization potential of Au_4 with respect to Au_4, **Table 5**. Let us consider in more detail the adsorption geometries and the DOS of the tetramers adsorbed on the nitrogen-doped titania surface, **Fig. 16**. The geometries of

the isomers are similar to those supported on the stoichiometric surface, cf. **Fig. 13** and **Fig. 16**. The DOS in **Fig. 16** (e-h) reveal the absence of the gap state assigned to the nitrogen dopant on the adsorbate-free surface. Furthermore, cluster states can be seen above the Fermi level. The energy level of this empty cluster state is shifted towards the valence band when going from Ag to Au. This reflects the higher stability of the positively charged Ag tetramer with respect to the positively charged Au tetramer. Furthermore, we can see hybridization between the N 2p states and the cluster states when the nitrogen dopant is located at the surface. This explains also the slight spin contamination of the surface, see magnetic moments in **Table 8**.

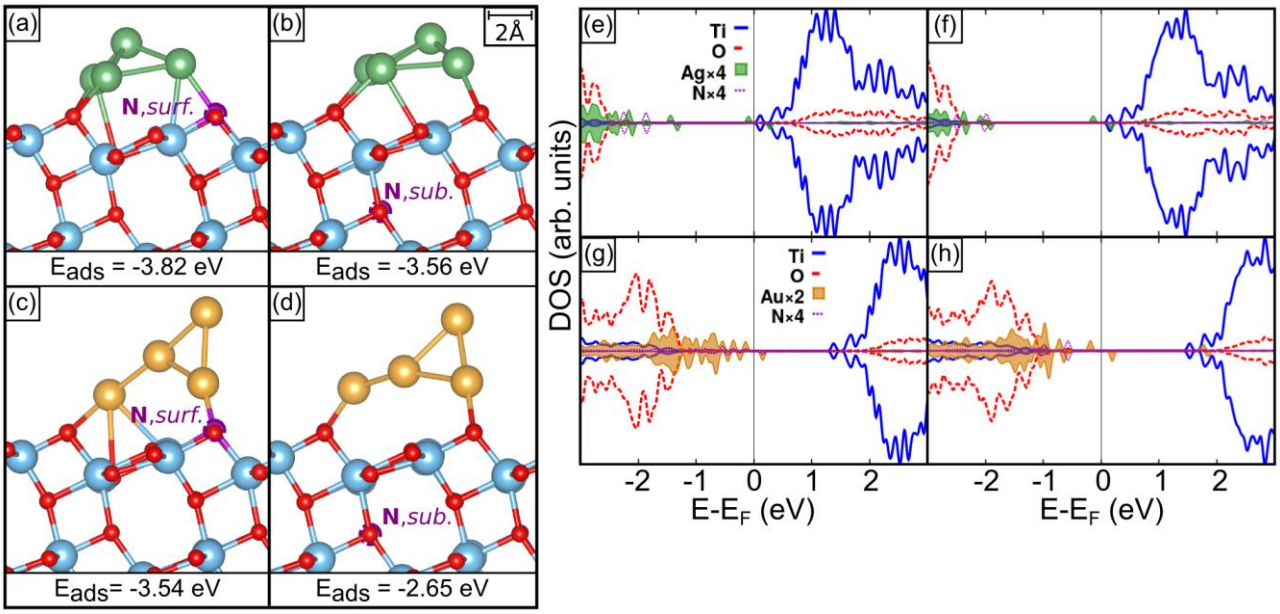

Fig. 16: Ag and Au tetramers on nitrogen-doped TiO_2 anatase (101). (a) Ag_4 on **N**, *surf.*, (b) Ag_4 on **N**, *sub.*, (c) Au_4 on **N**, *surf.*, (d) Au_4 on **N**, *sub.*, (e) DOS of Ag_4 on **N**, *surf.*, (f) DOS of Ag_4 on **N**, *sub.*, (g) DOS of Au_4 on **N**, *surf.*, (h) DOS of Au_4 on **N**, *sub.* [268]

6.1.6 Effect of niobium-doping on the cluster-support interaction

Ag and Au atoms on niobium-doped titania

The adsorption of Ag and Au atoms on the niobium-doped titania anatase (101) surface was investigated. As discussed in section 6.1.3, the niobium-dopant introduces an excess electron, which is transferred to the titania support. The adsorption energies, magnetic moments and Bader charges on the noble metal atoms are reported in **Table 9**. The adsorption of Ag on the niobium-dopant is slightly less exothermic than on the stoichiometric surface. The Ag atom adsorbs on top of the Nb-dopant, when the latter is positioned at the surface, **Fig. 17** (a). In the density of states, we see a clear hybridization between Ag and Nb states, **Fig. 17**(e). Thus, we can characterize the bonding as polar-covalent. Is the niobium-dopant posi-

tioned at the subsurface, the Ag atom behaves like on the stoichiometric surface, transferring its valence electron to the support. The charge transfer can clearly be seen in the DOS, **Fig. 17**, showing the presence of two electrons on the titania support, one from the Ag and one from the Nb atom. The Ag 5s orbital is located above the Fermi level.

Table 9: Adsorption energies E_{ADS} [eV], magnetic moments μ [μ_B], and Bader charges q [|e|] of Ag and Au atoms deposited on Nb-doped TiO_2 (101).

X	Dopant, position	E_{ADS}	|μ|(X)	|μ|(MO_2)	q(X)
Ag	**Nb**, *surf.*	-0.95	0.00	0.00	-0.25
	Nb, *sub.*	-0.95	0.00	0.00	+0.67
Au	**Nb**, *surf.*	-2.21	0.00	0.00	-0.45
	Nb, *sub.*	-1.52	0.00	0.00	-0.42

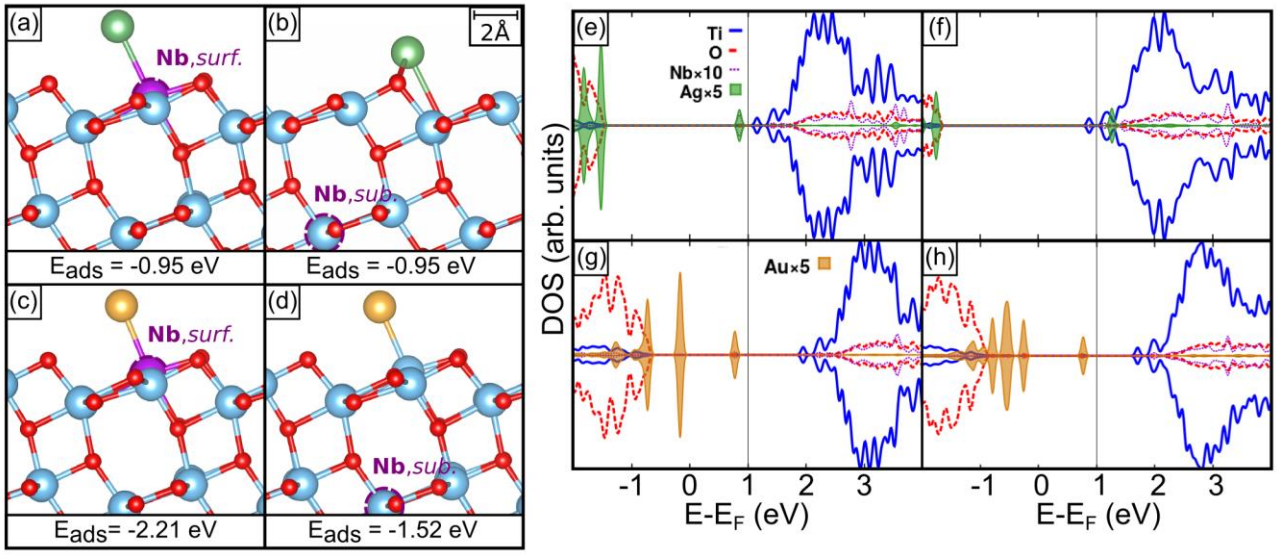

Fig. 17: Ag and Au atoms on niobium-doped TiO_2 (101). (a) Ag on **Nb**, *surf.*, (b) Ag on **Nb**, *sub.*, (c) Au on **Nb**, *surf.*, (d) Au on **Nb**, *sub.*, (e) DOS of Ag on **Nb**, *surf.*, (f) DOS of Ag on **Nb**, *sub.*, (g) DOS of Au on **Nb**, *surf.*, (h) DOS of Au on **Nb**, *sub.* [268]

Is the Au atom adsorbed on the surface niobium dopant, the adsorption energy is enhanced with respect to the stoichiometric surface. Here, only a slight hybridization of the noble metal atom with the Nb states can be observed, indicating a more ionic character of the Au-Nb bond than that of Ag-Nb, which is also reflected in the Bader charges. Interestingly, the Au atom is still negatively charged, when the niobium-dopant is at the subsurface. This stands in contrast to the behavior of Ag, but is similar to the behavior of Au on the titania surface with oxygen vacancies. The niobium-dopant has a similar effect as an oxygen vacancy, which is due to the presence of occupied Ti 3d states in both cases.

Ag and Au tetramers on niobium-doped titania

The tetramers have been adsorbed on the niobium-doped titania surface. The results are summarized in **Table 10**. The adsorption energies for the Ag tetramer on the niobium-doped titania, -2.33 and -2.01 eV for surface and subsurface dopants, respectively, are very close to that on the stoichiometric surface (-2.02 eV). The magnetic moment is always 0 μ_B on the silver cluster and ~ 0.7 μ_B on the surface. The Bader charge on the Ag clusters is always slightly positive, but formally the Ag tetramers are neutral. The adsorption configurations for the tetramers on the niobium-doped surface are similar to that on the stoichiometric surface, compare **Fig. 18** and **Fig. 13**.

Table 10: Adsorption energies E_{ADS} [eV], magnetic moments μ [μ_B], and Bader charges q [|e|] of Ag_4 and Au_4 clusters deposited on Nb-doped TiO_2 (101).

X	Dopant, position	E_{ADS}	|μ|(X)	|μ|(MO_2)	q(X)
Ag_4	**Nb**, *surf.*	-2.33	0.00	0.71	0.34
	Nb, *sub.*	-2.01	0.00	0.69	0.35
Au_4	**Nb**, *surf.*	-2.17	0.00	0.00	0.03
	Nb, *sub.*	-2.19	0.00	0.68	0.02

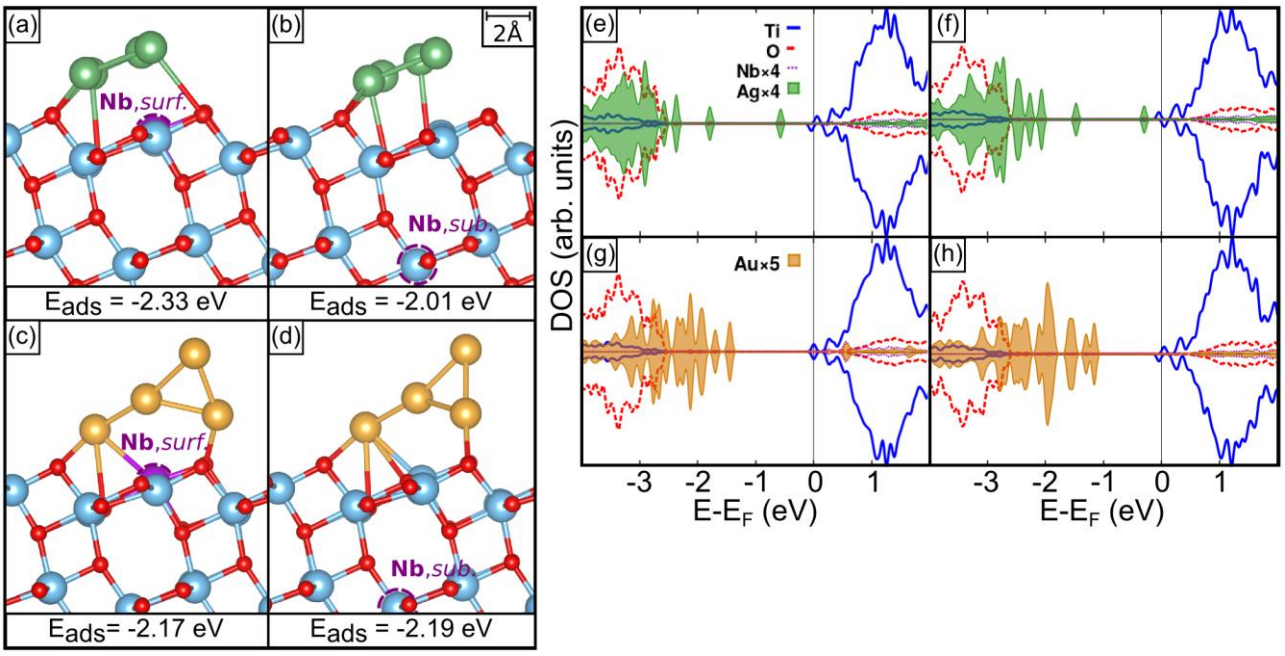

Fig. 18: Ag and Au tetramers on nitrogen-doped TiO_2 (101). (a) Ag_4 on **Nb**, *surf.*, (b) Ag_4 on **Nb**, *sub.*, (c) Au_4 on **Nb**, *surf.*, (d) Au_4 on **N**, *sub.*, (e) DOS of Ag_4 on **Nb**, *surf.*, (f) DOS of Ag_4 on **Nb**, *sub.*, (g) DOS of Au_4 on **Nb**, *surf.*, (h) DOS of Au_4 on **Nb**, *sub.* [268]

For the Au tetramers, similar observations hold true as for the Ag tetramers. No charge transfer can be observed which becomes clear in the DOS, **Fig. 18** (e-h). In the case of the surface niobium-dopant, we see a half occupied Ti 3d singlet state, although the calculation

was spin-polarized. This is an artifact due to the high delocalization of the electron in the slab resulting from the self-interaction error, which we corrected only partly with the DFT+U approach.

6.1.7 Adsorption of pentamers on the defective TiO_2 surfaces

In the sub-nanometer regime, the properties of metal clusters can change significantly when an atom is added or removed. The spin state, the ionization potential and electron affinity, as well as the geometry of the cluster can change dramatically when the number of atoms is changed. In the previous sections we have seen that the subsurface defects have a lesser influence on the adsorption modes of atoms and tetramers than the surface defects. It is therefore interesting to check if the effect of subsurface defects on the adsorption of Ag and Au pentamers is larger than for the tetramers. In the gas-phase, the Ag and Au pentamers exhibit an open shell electronic structure with one unpaired electron, giving rise to a magnetic moment of 1 μ_B. The most stable structure in the gas-phase is a trapezium with two atoms in the upper part and three in the lower part.

Table 11: Adsorption energies E_{ADS} [eV], magnetic moments μ [μ_B], and Bader charges q [|e|] of Ag and Au pentamers deposited on defective TiO_2 (101).

X	Dopant, position	E_{ADS}	$\|\mu\|(X)$	$\|\mu\|(MO_2)$	q(X)
Ag_5	Defect free	-2.71	0.00	0.84	0.82
	Vo, *sub.*	-2.59	0.00	2.90	0.81
	N, *sub.*	-4.52	0.00	0.00	0.82
	Nb, *sub.*	-2.64	0.00	0.00	0.81
Au_5	Defect free	-1.97	0.00	0.83	0.52
	Vo, *sub.*	-1.77	0.00	0.81	0.51
	N, *sub.*	-3.79	0.00	0.00	0.52
	Nb, *sub.*	-1.89	0.00	0.00	0.52

The adsorption of the pentamers supported on the stoichiometric titania anatase (101) surface, as well as on the defective surfaces have been investigated. The results are summarized in **Table 11**. Let us first consider the pentamers on the stoichiometric surface, and compare them to the tetramers. The adsorption energies of the pentamers are slightly enhanced for the Ag pentamer (-2.71 eV) with respect to the Ag tetramer (-2.02 eV). This trend is reversed for gold. Here, the adsorption energy of the tetramer (-2.19 eV) is slightly enhanced with respect to the pentamer (-1.97 eV). The adsorption configuration of the Ag tetramer is more flat than that of the Au tetramer, **Fig. 13**. This trend is retained also for the pentamers, **Fig. 19** (a-b).

Although the adsorption energies of the pentamers are quite similar to those of the tetramers, the adsorption mode is different. Whereas the tetramers adsorb neutrally on the stoichiometric surface, the pentamers transfer one electron to the support. This charge transfer is reflected in the magnetic moment, which is zero on both supported pentamers. The Bader charges on the pentamers are positive and in the DOS, **Fig. 19** (c-d), we can see the transferred electron at the CBM.

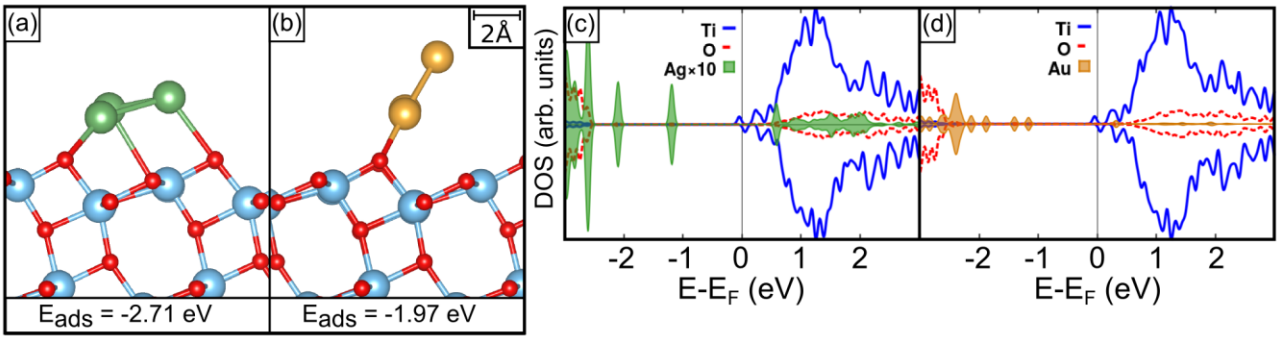

Fig. 19: Ag and Au pentamers on the stoichiometric TiO_2 anatase (101) surface. (a) Ag pentamer supported on the stoichiometric surface, (b) Au pentamer supported on the stoichiometric surface, (c) DOS of Ag_5/TiO_2 and (d) Au_5/TiO_2. [268]

Let us now proceed to the adsorption of the Ag pentamer on the defective surfaces. When the Ag pentamer is adsorbed on titania with a subsurface vacancy or a niobium-dopant, the adsorption energy is decreased in modulus with respect to the stoichiometric surface. Again, the magnetic moment is zero and the Bader charge on the pentamer is positive. Thus, these subsurface defects do not change the adsorption mode of the pentamer, apart from the slight change in adsorption energy. When the pentamer is adsorbed on titania with a nitrogen-dopant at the subsurface, the adsorption energy is increased by almost 2 eV with respect to the stoichiometric surface. Again, the pentamer transfers an electron to the support, which now fills the gap state introduced by the nitrogen-dopant. This is accompanied by a large energy gain.

For the Au pentamer, similar considerations as for the Ag pentamer can be made. The Au pentamer always transfers an electron to the support. In the case of the nitrogen dopant, the adsorption is stronger than on the stoichiometric surface; in the case of the Nb-dopant and the oxygen vacancy, it is weaker. As the Au pentamer has a larger ionization potential than the Ag pentamer, **Table 5**, the adsorption on the nitrogen-dopant releases more energy in the case of the Ag pentamer.

6.1.8 Section summary

- The effect of oxygen vacancies, Nb- and N-dopants on the titania anatase (101) surface on the adsorption mode of Ag and Au clusters was determined.
- The atoms become negatively charged upon deposition on a surface oxygen vacancy, and the adsorption energies are enhanced by 0.9 eV for Ag and by 2.5 eV for Au with respect to those on the stoichiometric surface. The adsorption energies of the tetramers are also significantly enhanced when the surface oxygen vacancy is introduced. Here, no charge transfer between the vacancy and the Ag tetramer occurs, but the Au tetramer becomes negatively charged via formation of a polar-covalent Au-Ti bond. The cluster geometry is affected by the presence of the surface vacancy, especially in the case of the Ag tetramer.
- The pentamers always transfer an electron to the support, which is associated with large adsorption energies between -1.7 and -4.5 eV. Subsurface defects and dopants do not change this behavior.
- As soon as the oxygen vacancy is in the subsurface, the effect on the adsorption mode of the atoms and clusters is largely attenuated. Here, only the Au atom becomes negatively charged.
- Nb-doping has a similar effect as oxygen vacancies. Charge transfers occur just as for the oxygen vacancies.
- N-doping induces a positive charge on all atoms and clusters. The metal atoms and clusters, respectively, transfer one electron to the N-dopant.
- The exact number of atoms in the cluster has a defining effect on the adsorption mode. This is most clearly seen when comparing the atoms and clusters on the stoichiometric surface. For instance in the case Ag clusters, the open shell cases (monomer and pentamer) exhibit charge transfer to the support, whereas the closed-shell tetramer stays neutral.

Chapter 7 Cluster nucleation and anchoring

7.1 Adsorption and dimerization of transition metal atoms on SiO_2 quartz (001)[7]

7.1.1 Introduction

Silica-supported transition metal (TM) clusters and nanoparticles constitute active catalysts for a variety of reactions and are therefore widely used in catalysis. For instance, Co clusters are active for the Fischer–Tropsch synthesis [270], Ni clusters for the dry reforming [271] of methane and CO_2 methanation [272], and various other TM clusters are active for hydrogenation reactions [273,274]. Silica is cheap, chemically inert, and mechanically stable, which makes it an attractive support for metal catalysts. [275] Under reaction conditions, the metal clusters tend to sinter, forming larger particles, which leads to a deactivation of the catalyst. [276,277] This is either due to the simple decrease of the metals surface area, or due to a sensitivity of the catalytic activity on the particle size. The sintering of the particles is promoted by a weak interaction between the metal particles and the support, and can hence be counteracted by the presence of binding sites to which the particles bind stronger. Intrinsic and extrinsic effects can serve as such anchoring sites. [278,279]

To develop sinter-resistant catalysts, it is helpful to understand on an atomistic level how metal atoms and clusters interact with the oxide surface and which are the determining aspects influencing their nucleation and aggregation behavior. In this section, we will discuss the adsorption and dimerization of late transition metal atoms supported on the fully hydroxylated quartz (001) surface.

7.1.2 Computational details

Spin polarized, periodic DFT calculations were performed using the VASP program. [194,195,196,197] A similar setup as presented in the previous Chapters was applied. In short, we used the PBE exchange-correlation functional [160,161] and the projector augmented wave (PAW) method. [193,192] O(2s, 2p), Si(3s, 3p), Co(3d, 4s), Rh(4d, 5s), Ir(5d, 6s), Ni(3d), Pd(4d), Pt(5d), Cu(3d, 4s), Ag(4d, 5s), Au(5d, 6s) states were treated explicitly.

[7] The content of this study is published in the Journal "Topics in Catalysis": P. Schlexer, and G. Pacchioni, "Adsorption and Dimerization of Late Transition Metal Atoms on the Regular and Defective Quartz (001) Surface." Top. Catal. http://doi.org/10.1007/s11244-016-0712-x

We included dispersion forces in all calculations, using the approach suggested by Tosoni and Sauer [185], which is based on the semi-empirical dispersion correction proposed by Grimme. [184] See section 4.1.2 for more details.

For the α-quartz bulk calculations, plane waves were expanded up to a kinetic energy cut-off of 900 eV. A Γ-centered K-point grid in the Monkhorst-Pack scheme was used which was set to (13×13×13). [226] The computed lattice parameters of $a_0 = b_0 = 5.036$ Å and $c_0 = 5.530$ Å are in good agreement with the experimental lattice parameters of $a_0 = b_0 = 4.916$ Å and $c_0 = 5.405$ Å. [280] To investigate the adsorption of metal atoms and dimers on the quartz (001) surface, a (2×2) surface super cell was modelled with lattice parameters of a = b = 10.07 Å and γ = 60° and with a slab thickness of 9 layers of [SiO_4] tetrahedra. To construct this model, the bulk structure was cleaved along the (001) surface, fully hydroxylated at both sides of the slab and completely structure optimized. Our model for the fully hydroxylated surface is equivalent to that of P. M. Goumans et al. [281]. They found a good convergence of surface energies and structural parameters for the hydroxylated surface and hydroxyl-free reconstructed surface without dangling bonds for 9 layers of [SiO_4] tetrahedra. Our model of the hydroxylated surface exhibits a surface concentration of hydroxyl groups of 9.10 OH/nm^2, which is in good agreement with experimental findings. [282] The concentration of hydroxyl groups on quartz is comparatively high. For instance it is almost twice as high as the average concentration on aerogel samples (~5 OH/nm^2). [283] For the slab calculations, plane waves were expanded up to a kinetic energy cut-off of 400 eV and a K-point set of (3×3×1) was used. The slabs were separated by 15 Å of vacuum. All ions were allowed to move during structure optimizations.

Adsorption energies, E_{ADS}, were calculated as defined in eqn. (20), where M_X (x = 1, 2) are the metal atoms or dimers in the gas-phase and S is the support, which can be either the defect-free (**Q**) surface or the surface with a non-bridging oxygen (**NBO**) defect. We use the notation S = Q or S = NBO to indicate the two different surfaces.

$$E_{ADS}(M_X/S) = E(M_X/S) - E(M_X) - E(S) \quad (20)$$

The contribution of dispersion interactions to the adsorption energy is defined in eqn.(21), where %DISP is the dispersion part of the adsorption energy and V_{DISP} is the dispersion potential energy added to the DFT total energy of the respective system. Note that this definition only includes geometries optimized at the DFT-D2' level.

$$\%DISP(M_X/S) = [V_{DISP}(M_X/S) - V_{DISP}(M_X) - V_{DISP}(S)]/E_{ADS}(M_X/S) \quad (21)$$

Dimerization is a possible first step for the nucleation of atoms on a surface. There are several possible scenarios for the dimerization mechanism of atoms, which are being deposited on the surface. A first option is that the dimerization occurs in the gas-phase and that the

dimer is directly adsorbed on the surface. We considered this possibility and calculated the dimer adsorption energy, eqn. (20). A second possibility, more unlikely, is the adsorption of a gas-phase atom directly on an adsorbed atom. A third possibility is the adsorption of two atoms on the surface, followed by their diffusion and dimerization on the surface. Obviously, the last two mechanisms may compete for incoming atoms, especially if the adsorbate coverage is high. Our model, including only atoms or dimers, corresponds to a situation in the low coverage regime. In that case, it can be assumed that the last mechanism is more likely and therefore we report the dimerization energy as defined in eqn. (22) and eqn. (23).

$$\mathrm{E_{DIM}(M_2/Q) = E(M_2/Q) + E(Q) - 2E(M/Q)} \tag{22}$$

$$\mathrm{E_{DIM}(M_2/NBO) = E(M_2/NBO) + E(Q) - E(M/NBO) - E(M/Q)} \tag{23}$$

To establish the extent of anchoring of atoms and dimers by defects, we calculate the trapping energy, defined in eqn. (24).

$$\mathrm{E_{TRAP}(M_X/NBO) = E_{ADS}(M_X/NBO) - E(M_X/Q)} \tag{24}$$

When the metal clusters adsorb on the fully hydroxylated quartz surface, there is the possibility that they react with surface hydroxyl groups to form molecular H_2 according to the reaction (25).

$$\mathrm{R\text{-}Si\text{-}OH\text{---}M_X \rightarrow \tfrac{1}{2}\, H_2 + R\text{-}Si\text{-}O\text{-}M_X} \tag{25}$$

Here, R-Si-OH---M_X corresponds to M_X/Q and R-Si-O-M_X corresponds to M_X/NBO. The corresponding reaction energy is given in eqn. (26) where $E(H_2)$ is the total energy of the gas-phase H_2 molecule.

$$\mathrm{E_{REA} = E(M_X/NBO) + \frac{1}{2}E(H_2) - E(M_X/Q)} \tag{26}$$

7.1.3 The SiO_2 quartz (001) surface

Silica is a commonly used support material in catalysis, because of its excellent chemical and thermal stability. There are various forms of silica available as catalyst support, whereby high-surface porous supports and sol-gel derived forms are widely used because of their structural stabilization of the supported metal nanoparticles. To represent the silica support, we use the α-quartz modification of silica, because of the possibility to represent it in a periodic super cell approach. α-quartz is the thermodynamically most stable modification of silica under standard conditions and the (001) surface is the most stable surface after surface reconstruction. [281] To capture different chemical motifs present in the commonly used silica supports, we consider the hydroxyl-free (reconstructed) α-quartz (001) surface and the fully hydroxylated α-quartz (001) surface. The two surfaces are shown in **Fig. 20**.

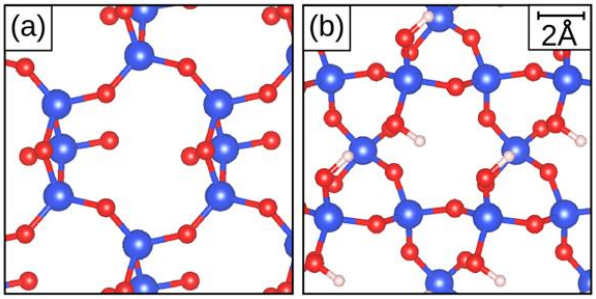

Fig. 20: Top view of the α-quartz (001) surface. The first two layers of [SiO_2] units are shown. (a) Hydroxyl-free reconstructed surface, (b) fully hydroxylated surface. [284]

7.1.4 Adsorption of the TM atoms on the quartz (001) surface

Adsorption on the defect-free surface

To characterize the interaction of the atoms with the defect-free fully hydroxylated quartz (001) surface, we determined the adsorption energy and other interesting parameters, summarized in **Table 12**. The metal atoms adsorb with small to intermediate adsorption energies between -0.25 eV for Cu to -1.53 eV for Rh. Whereas group 9 and group 10 elements exhibit intermediate adsorption energies with small contributions from dispersion forces, the group 11 elements show a weak adsorption, stemming mainly from dispersion interactions.

Table 12: Adsorption energies of atoms on the defect-free hydroxylated quartz surface E_{ADS} [eV], contribution of dispersion potential to the adsorption energy $\%_{DISP}$ [%], magnetic moments μ [μ_B], M-O distances to the two closest oxygen atoms d(M-O) [Å], Bader charges on metal atoms q(M, ads) [|e|].

	Co	Rh	Ir	Ni	Pd	Pt	Cu	Ag	Au
E_{ADS}	-0.81	-1.53	-0.97	-1.14	-1.01	-1.51	-0.25	-0.27	-0.31
$\%_{DISP}$	35	23	15	12	34	11	96	115	84
|μ|(M, gas)	3.00	3.00	3.00	2.00	0.00	2.00	1.00	1.00	1.00
|μ|(M, ads)	1.00	1.00	3.00	0.00	0.00	2.00	1.00	1.00	1.00
d_1(M-O)	1.91	2.14	2.28	1.85	2.27	1.99	3.06	3.21	3.21
d_2(M-O)	1.99	2.30	3.21	2.96	2.37	2.99	3.06	3.22	3.34
q(M, ads)	0.16	0.18	0.05	0.17	0.10	0.01	0.09	0.08	0.01

Since the adsorption modes of the elements within a group are quite similar, only the adsorption positions for the lightest homologues, i.e. Co, Ni and Cu, are shown in **Fig. 21**. The atoms are typically coordinated by oxygen atoms of surface silanol groups and the adsorption strength is reflected in the M-O bonding distances: The stronger the adsorption, the shorter the M-O bond distance.

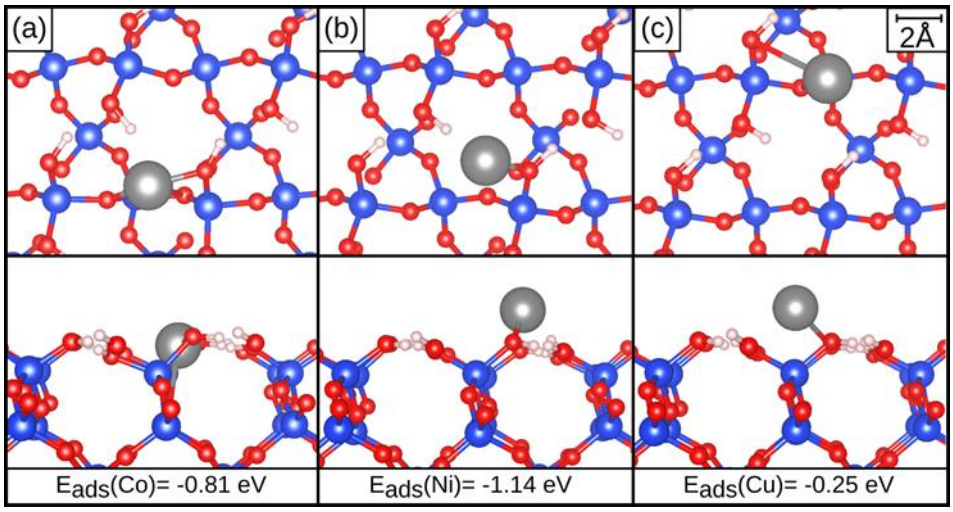

Fig. 21: Adsorption of (a) Co, (b) Ni, and (c) Cu atoms on the fully hydroxylated, defect-free quartz (001) surface. [284]

In some cases, the magnetic moment of the gas-phase atoms are different from the supported ones. However, no change of parity is observed. The change in magnetic moment is due to ligand effects. The surface silanol groups act as ligands changing the electrostatic field around the atoms, which in turn affects the electronic configuration. The Bader charges indicate no charge transfer between atoms and quartz surface occurs in any case. This is verified by the DOS, **Fig. 22** (a-c), which are shown for the lightest homologues Co, Ni and Cu.

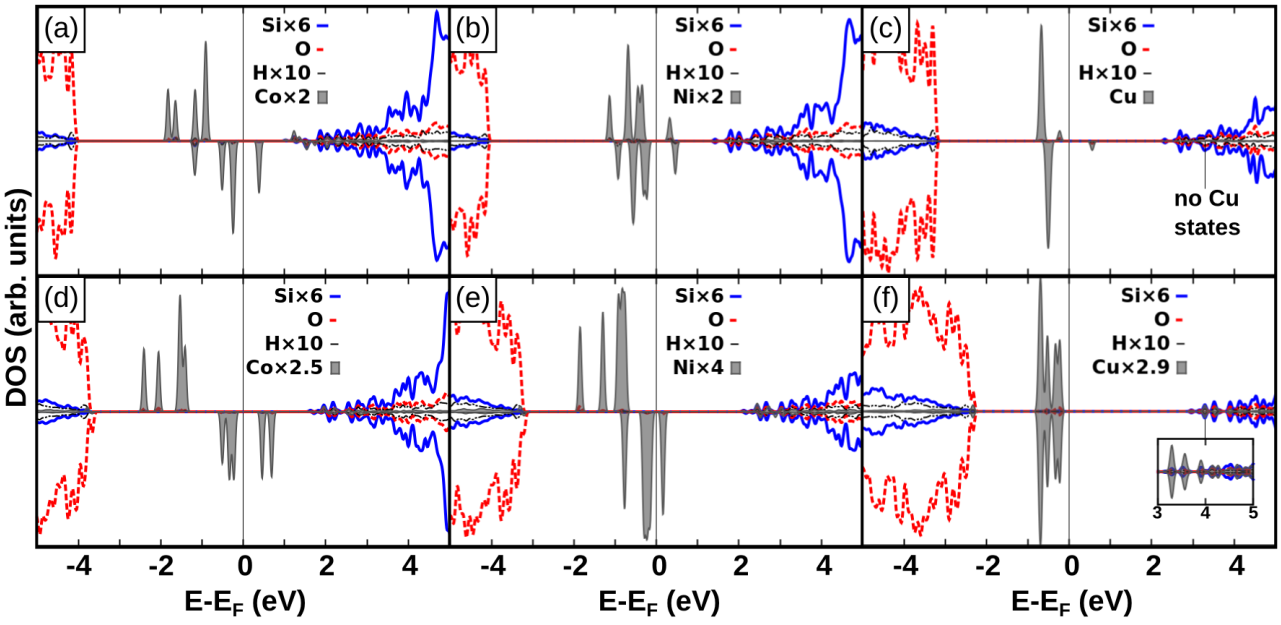

Fig. 22: Projected density of states (DOS) of atoms adsorbed on (a-c) defect-free hydroxylated quartz: (a) Co, (b) Ni and (c) Cu. (d-f) DOS of atoms adsorbed on a non-bridging oxygen defect (NBO): (d) Co, (e) Ni and (f) Cu. ***Inset in (f)***: Energy range from +3 to +5 eV with respect to the Fermi level with more enlarged Cu-projected DOS (Cu×25). [284]

Adsorption of the TM atoms on the non-bridging oxygen defect

Intrinsic and extrinsic defects can act as anchoring and nucleation points for metals supported on oxides, as we have seen in section 6.1 for Ag and Au clusters on titania. A variety of defects have been identified on the silica surface and a particularly important example in the context of cluster adsorption is the non-bridging oxygen (**NBO**) defect ≡Si-O$^{\bullet}$. [285] The defect is formally derived by the neutral dissociation of silanol groups. The NBO defect was reported to be a strong trap for electrons and Au atoms in the literature. [286,287] Electron paramagnetic resonance measurements have proven the existence of the NBO defect on the silica surface. [288] NBO defects can in principle also be formed by reaction of a surface silanol with a TM metal cluster under formation of ½ H_2. We have considered this reaction and report the reaction energy, as defined in the computational details. The interaction of the late transition metal atoms with the hydroxylated silica surface with a NBO defect are summarized in **Table 13**.

Table 13: Adsorption energies of metal atoms on a non-bridging oxygen (NBO) E_{ADS} [eV], contribution of the dispersion potential to the adsorption energy $\%_{DISP}$ [%], magnetic moments on atoms μ [μ_B], the two closest M-O distances [Å], and Bader charges on metal atoms q(M, ads) [|e|].

	Co	Rh	Ir	Ni	Pd	Pt	Cu	Ag	Au
E_{ADS}	-5.81	-5.27	-5.27	-5.78	-4.27	-5.00	-5.38	-4.28	-4.10
$\%_{DISP}$	4	6	5	4	7	5	4	7	6
E_{TRAP}	-5.00	-3.75	-4.30	-4.64	-3.25	-3.49	-5.12	-4.01	-3.79
E_{REA}	-1.79	-0.53	-1.09	-1.43	-0.04	-0.28	-1.91	-0.80	-0.57
|μ|(M, gas)	3.00	3.00	3.00	2.00	0.00	2.00	1.00	1.00	1.00
|μ|(M, ads)	2.00	2.00	2.00	1.00	1.00	1.00	0.00	0.00	0.00
d(M-O_{NBO})	1.84	2.02	1.98	1.83	2.06	1.95	1.85	2.10	2.02
d(M-O)	1.92	2.11	2.06	1.89	2.13	2.03	1.91	2.18	2.09
q(M, ads)	+0.70	+0.63	+0.55	+0.69	+0.61	+0.44	+0.69	+0.64	+0.47

Not surprisingly, compared to the non-defective surface the adsorption is much stronger, in some cases even by an order of magnitude, which is reflected in the trapping energy, **Table 13**. The relatively small adsorption energy of the atoms on the defect-free surface can result in high mobility of the atoms on the surface. At finite temperatures, the atoms may therefore diffuse on the surface until they are trapped on a defect like the NBO defect. The results are in good alignment with the findings of Lopez et al. who reported an adsorption energy of -3.79 eV for Cu and -2.85 eV for Pd using silica cluster models [35]. The deviation of the adsorption energy is due to the different computational setup used in reference 35.

The metal atoms interact with the NBO forming ≡Si-O-TM complexes. The O-TM bonding can be characterized as strongly polar covalent to ionic bond, reflected in the quite high Bader charges on the metal atoms, **Table 13**. Also in the DOS, **Fig. 22** (d-f), we observe the absence of the unoccupied O 2p state related to the adsorbate-free NBO defect. The magnetic moment on the metal atoms changes parity for all atoms, which is consistent with the picture of the charge transfer from the metal atoms to the oxygen atom. The reaction of the TM atoms with the defect-free surface to form the ≡Si-O-TM complex and of ½ H_2 is exothermic in all cases. This indicates that the TM atoms may bind strongly to the silica surface via the in-situ formation of the ≡Si-O-TM complexes. Note that we did not investigate any barriers for this reaction. As we can see in **Fig. 23**, the atoms exhibit very similar adsorption geometries, which is a manifestation of the similar bonding type present in the different ≡Si-O-TM complexes. The fact that the O-TM bonds are largest for the second heaviest homologs of the triads, **Table 13**, could be related to the increasing influence of relativistic effects for the heaviest homologs.

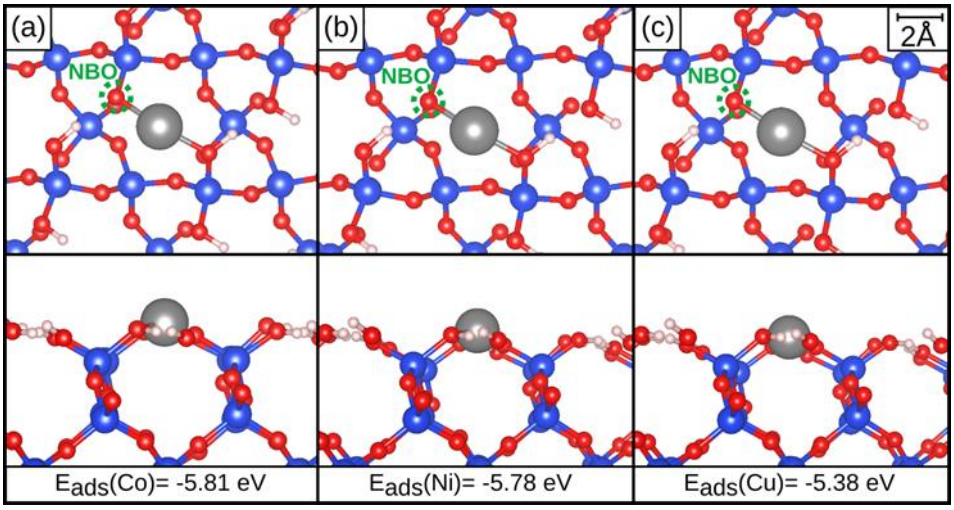

Fig. 23: Atoms adsorbed on a non-bridging oxygen (NBO) defect on hydroxylated quartz. (a) Co, (b) Ni and (c) Cu. [284]

7.1.5 Adsorption of the TM dimers on the quartz (001) surface

Adsorption on the defect-free surface

The results related to the interaction of the dimers with the defect-free fully hydroxylated silica surface are summarized in **Table 14**. In particular, the dimer adsorption energy, $E_{ADS}(M_2/S)$, is reported together with the dimerization energy (see computational details for definitions). As for the monomers, the group 9-10 dimers show a stronger adsorption with adsorption energies ranging from -0.8 eV for Co_2 to -1.42 eV for Ir_2. The group 11 dimers show slightly weaker adsorption energies in the range from -0.5 for Au_2 to -0.8 eV for Ag_2.

The weaker adsorption of the group 11 elements was also observed for the monomers. Compared to the monomers, the dimers exhibit smaller dispersion contributions, which are the result of the metal-metal interaction leading to larger effective metal-substrate distances.

The adsorption geometries of the dimers are shown in **Fig. 24**. Whereas the Co dimer lays flat on the surface, the Ni and Cu dimers are more tilted away from the surface, resulting in two chemically distinct atoms: The atom closer to the surface shows a slightly more positive Bader charge than the other one, **Table 14**. However, the Bader charges are always below +0.25 |e|, indicating the absence of a net charge transfer between adsorbates and support. The bonding, as in the case of the monomers, arises from dispersion interactions and a marginal hybridization between TM d and O 2p levels.

Table 14: Adsorption energies of TM dimers on the defect-free hydroxylated surface E_{ADS} [eV], contribution of dispersion potential to the adsorption energy $\%_{DISP}$ [%], dimerization energy E_{DIM} [eV], magnetic moments on dimers μ [μ_B], M-O distances to the two closest oxygen atoms [Å], M-M distances [Å], and Bader charges on metal atoms q(M, ads) [|e|].

	Co_2	Rh_2	Ir_2	Ni_2	Pd_2	Pt_2	Cu_2	Ag_2	Au_2
$E_{ADS}(M_2/S)$	-0.84	-1.41	-1.42	-1.33	-1.22	-1.02	-0.63	-0.78	-0.53
$\%_{DISP}$	10	18	5	7	29	5	14	11	13
E_{DIM}	-2.51	-1.53	-4.43	-2.07	-0.52	-1.76	-2.38	-2.02	-2.24
$\|\mu\|(M_2$, gas)	4.00	0.00	4.00	2.00	2.00	2.00	0.00	0.00	0.00
$\|\mu\|(M_2$, ads)	4.00	2.00	4.00	2.00	0.00	2.00	0.00	0.00	0.00
d_1(M-O)	2.12	2.07	2.17	1.96	2.14	2.18	2.10	2.28	2.38
d_2(M-O)	2.19	2.26	3.18	3.16	2.29	3.11	3.05	3.27	3.21
d(M-M)	2.05	2.40	2.24	2.11	2.62	2.32	2.22	2.57	2.49
q(M1, ads)	0.13	0.02	0.16	0.24	0.08	0.08	0.20	0.16	0.07
q(M2, ads)	0.12	0.12	-0.10	-0.11	-0.01	-0.12	-0.10	-0.09	-0.09

Depending on the preparation method, the dimers may not only form in the gas-phase, but also on the surface via combination of two already adsorbed monomers. To describe this process, we computed the dimerization energy, E_{DIM}, which provides a way to verify if the formation of a dimer is favorable with respect to two adsorbed monomers. Indeed, our data show that dimerization is an exothermic process in all cases, **Table 14**. In some cases the two TM atoms recombine releasing a large amount of energy, like in the case of Ir where this quantity is around 4 eV, **Table 14**. Interestingly, the dimerization energy is larger in modulus than the adsorption energy for all elements but Pd. The energy released upon dimerization has to be dissipated in some way, e.g. by exiting lattice vibrations. Alternatively, the dimerization of two atoms can lead to the desorption of the dimer formed.

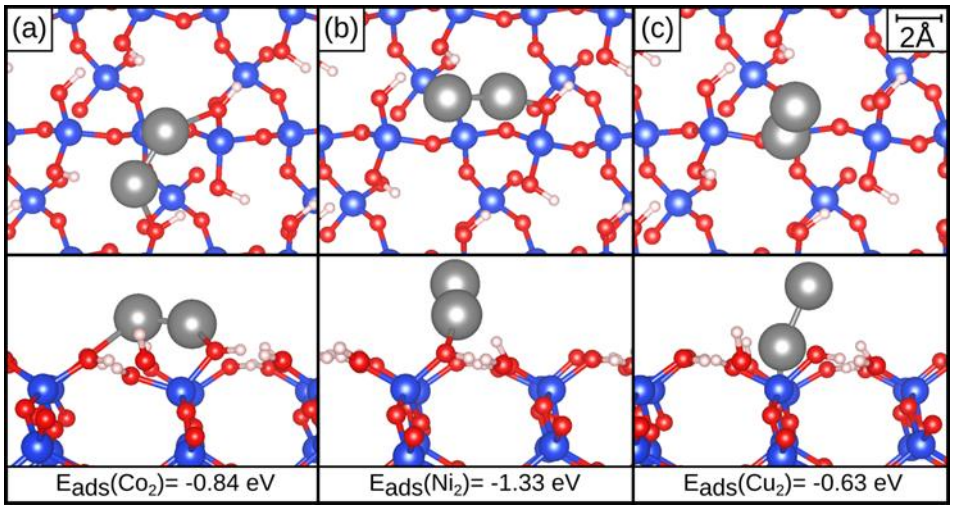

Fig. 24: Dimers adsorbed on defect-free hydroxylated quartz. (a) Co_2, (b) Ni_2 and (c) Cu_2. Adsorption energies are given with respect to the gas-phase dimer. [284]

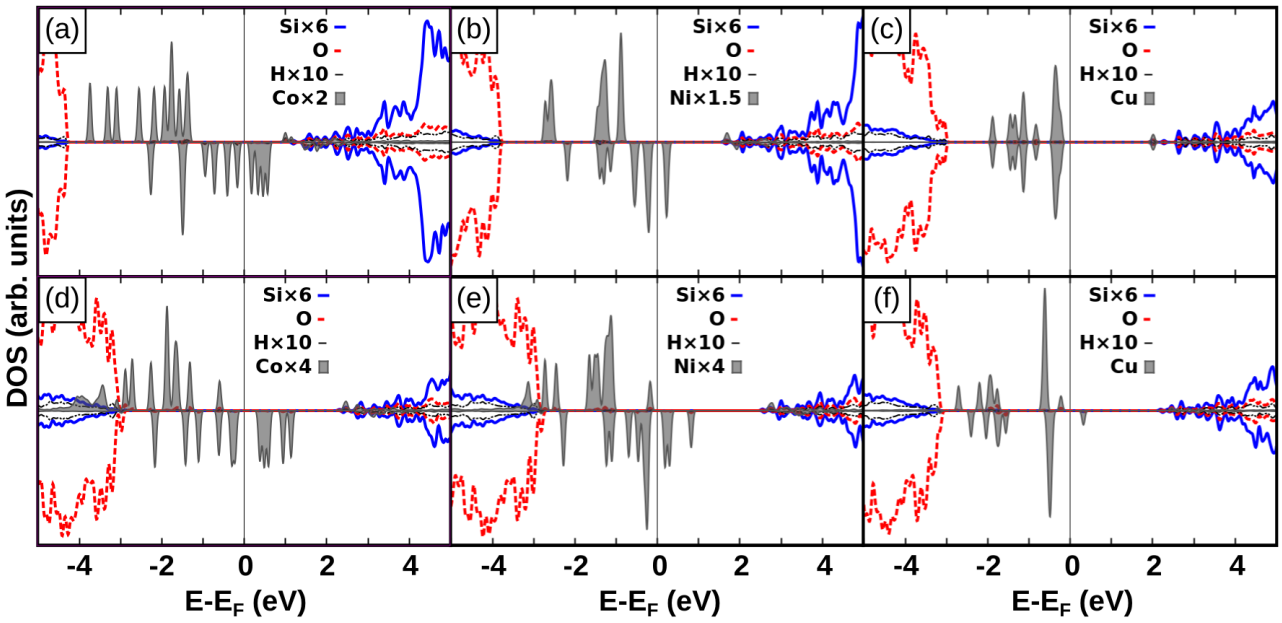

Fig. 25: DOS of dimers adsorbed on (a-c) defect-free hydroxylated quartz: (a) Co_2, (b) Ni_2 and (c) Cu_2. (d-f) DOS of dimers adsorbed on a non-bridging oxygen defect (NBO): (d) Co_2, (e) Ni_2 and (f) Cu_2. [284]

Adsorption on the non-bridging oxygen defect

As for the atoms, the adsorption of the dimers on the NBO defect was investigated. The results are summarized in **Table 15**. The adsorption of the dimers is highly exothermic with adsorption energies between -2.70 eV for Au_2 and -5.22 for Rh_2. As the atoms, the dimers form ≡Si-O-TM_2 complexes with a polar-covalent to ionic O-TM bond. One of the metal atoms is thereby directly coordinated to the oxygen atom (M1), whereas the other metal at-

om (M2) is bond to the first metal atom, **Fig. 26**. The charge transfer from the dimer to the oxygen atoms is reflected in the Bader charge on M1, which is positive on all metals. As in the case of the atoms, we observe a change of parity of the magnetic moment on the dimers with respect to the gas-phase dimers. Furthermore the paramagnetic O 2p gap state related to the TM-free NBO defect is absent in the DOS, **Fig. 25**. The strong O-TM bonding via a charge-transfer mechanism results in low contribution of dispersion forces to the total bonding strength.

Table 15: Adsorption energies of dimers on a non-bridging oxygen defect (NBO) E_{ADS} [eV], contribution of the dispersion potential to the adsorption energy $\%_{DISP}$ [%], trapping energy E_{TRAP} [eV], reaction energy E_{REA} [eV] according to eqn. (26), magnetic moments on dimers μ [μ_B], the two closest M-O distances [Å], M-M distances [Å], and Bader charges on metal atoms q(M, ads) [|e|].

	Co_2	Rh_2	Ir_2	Ni_2	Pd_2	Pt_2	Cu_2	Ag_2	Au_2
$E_{ADS}(M_2/S)$	-5.03	-5.22	-4.45	-4.58	-4.77	-4.04	-3.88	-3.19	-2.70
$\%_{DISP}$	6	8	9	7	12	11	7	16	17
E_{TRAP}	-4.19	-3.81	-3.03	-3.26	-3.55	-3.02	-3.25	-2.41	-2.18
E_{DIM}	-1.70	-1.59	-3.16	-0.69	-0.82	-1.29	-0.51	-0.41	-0.63
E_{REA}	-0.98	-0.59	0.18	-0.04	-0.34	0.19	-0.04	0.81	1.04
$\|\mu\|$(M, ads)	5.00	3.00	3.00	3.00	1.00	1.00	1.00	1.00	1.00
d(M1-O_{NBO})	1.90	2.03	2.02	1.87	2.06	2.02	1.88	2.02	2.05
d(M1-O)	2.04	2.09	2.08	1.97	2.12	2.07	1.97	2.07	2.13
d(M-M)	2.04	2.23	2.27	2.17	2.57	2.43	2.36	2.43	2.68
q(M1, ads)	0.72	0.51	0.63	0.67	0.37	0.57	0.67	0.53	0.56
q(M2, ads)	0.02	0.13	-0.09	0.04	0.23	-0.08	0.00	0.15	-0.09

Another interesting parameter is the trapping energy, which ranges from -2.18 eV for Au_2 to -4.19 eV for Rh_2 verifying the picture that atoms and dimers may be trapped at defect sites. Therefore the latter can be assumed to be effective nucleation sites during the agglomeration of atoms in a cluster growth process. For the atoms, the in-situ formation of the ≡Si-O-TM complexes under formation of ½ H_2 was exothermic for all elements, which is not the case for the dimers. Only in 5 of the 9 cases the reaction is exothermic. The dimerization energy is however exothermic in all cases, verifying that the NBO defects can act as effective nucleation sites. Especially, this time the dimerization energy is smaller in modulus than the adsorption energy in all cases. Therefore, there should be only little probability for the desorption of the dimers upon formation.

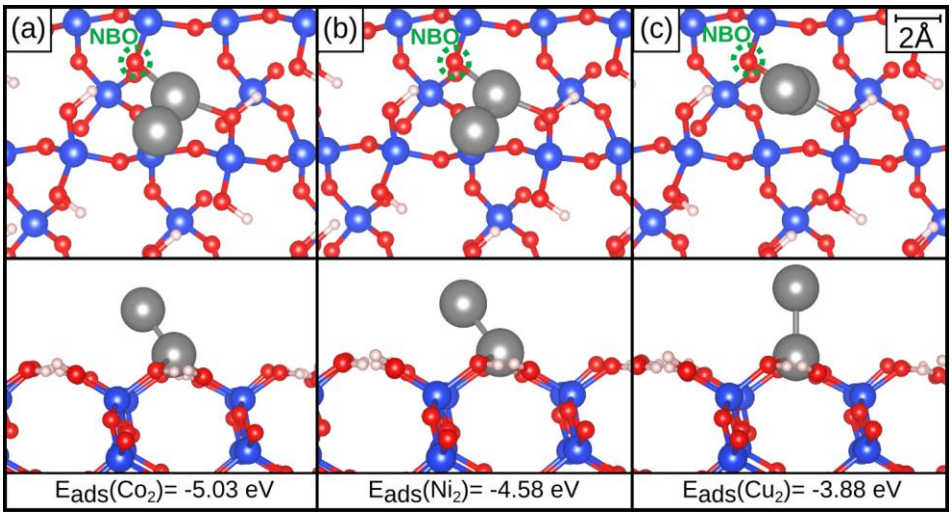

Fig. 26: Metal dimers adsorbed on a non-bridging oxygen (NBO) on hydroxylated quartz. (a) Co_2, (b) Ni_2 and (c) Cu_2. Adsorption energies are given with respect to the gas-phase dimer. The metal atoms closest to the surface are denoted as M1, the others as M2. [284]

7.1.6 Section summary

- The effect of the non-bridging oxygen defect on the hydroxylated quartz (001) surface on the dimerization and anchoring of late TM atoms supported was explored.
- Atoms and dimers may diffuse on the silica surface until they are trapped on a defect site. Or, if enough thermal energy is available to overcome a possible barrier (not investigated), the atoms (and some of the dimers) can react with the surface under the in-situ formation of the ≡Si-O-TM complexes.
- The ≡Si-O-TM complexes, as well as the pristine NBO defects, constitute effective nucleation centers and anchor the clusters against diffusion and desorption.

7.2 Anchoring of Au clusters on SiO_2 quartz via alloying with Ti

7.2.1 Introduction

Gold clusters supported on oxides, such as titania and silica, tend to sinter forming larger aggregates. Especially for gold-based catalysts this can lead to deactivation since the catalytic properties emerge with the finite size of the nanoparticles with respect to the bulk material. Several strategies to combat sintering can be pursued. For instance, micro- or mesostructuring of the oxide can provide a structural support for the nanoparticles making their migration less probable. Furthermore, defects and dopants can be introduced on the support surface, which can result in an enhanced binding of the clusters to the support, anchoring the clusters to the surface. A different approach would be to modify the clusters in order to

create an anchoring effect. In this study, we investigate how alloying gold clusters with titanium atoms affects the cluster-support interaction with silica and if that could be a reasonable way to prevent the gold clusters from sintering.

7.2.2 Computational details

The silica surfaces and the computational setup of the previous section were kept. In addition, the cohesive energies of the gas-phase clusters with respect to the atoms in the gas-phase were calculated as defined in eqn. (27) .

$$E_{COH}(Au_xTi_y) = E(Au_xTi_y) - x \cdot E(Au) - y \cdot E(Ti) \qquad (27)$$

Adsorption energies, E_{ADS}, were calculated as defined in eqn. (28), where $E(Au_xTi_y)$ are the metal atoms/dimers in the gas-phase and S is the support.

$$E_{ADS}(Au_xTi_y/S) = E(Au_xTi_y/S) - E(Au_xTi_y) - E(S) \qquad (28)$$

The support can either be the reconstructed hydroxyl-free α-quartz (001) surface (S_R), or the fully hydroxylated surface (S_H), or the fully hydroxylated surface with a non-bridging oxygen (S_{NBO}) defect center. All systems are structurally fully optimized.

When the metal clusters adsorb on the fully hydroxylated quartz surface, there is the possibility that they react with surface hydroxyl groups forming ½ H_2 according to the following reaction, eqn. (29).

$$\equiv\text{Si-OH} + Au_xTi_y \rightarrow ½\ H_2 + \equiv\text{Si-O-}Au_xTi_y \qquad (29)$$

Here, ≡Si-OH + Au_xTi_y corresponds to Au_xTi_y/S_H and ≡Si-O-Au_xTi_y corresponds to Au_xTi_y/S_{NBO}. Therefore, the corresponding reaction energy is given in eqn. (30), where $E(H_2)$ is the total energy of the gas-phase H_2 molecule.

$$E_{REA} = E(Au_xTi_y/S_{NBO}) + \frac{1}{2}E(H_2) - E(Au_xTi_y/S_H) \qquad (30)$$

7.2.3 Au_xTi_y gas-phase clusters

Before we address in more detail the adsorption of the Au-Ti bimetallic clusters on the silica support, we will shortly summarize the gas-phase properties of the clusters. Therefore, we explored many different two- and three-dimensional Au_xTi_y (x+y = 4, 5) clusters. The results are summarized in **Table 16**. To investigate the cluster-support interaction, we investigated all the tetramers (x+y = 4) and the Au_5, Au_1Ti_4 and Ti_5 clusters. The clusters of this selection are shown in **Fig. 27**. Apart from the Ti clusters, all clusters are two-dimensional.

Table 16: Cohesive energies per atom of bimetallic clusters $E_{COH}(Au_xTi_y)$ [eV], sum of Bader charges on the Au atoms Σq (Au) [|e|], and magnetic moments on the clusters μ [μ_B].

	$E_{COH}(Au_xTi_y)$	Σq(Au)	|μ|
Au_4	-1.56	0.00	0.00
Au_3Ti	-2.43	-1.46	1.00
Au_2Ti_2	-2.45	-1.30	4.00
$AuTi_3$	-2.52	-0.86	5.00
Ti_4	-2.63	---	4.00
Au_5	-1.69	0.00	1.00
Au_4Ti	-2.27	-1.41	0.00
Au_3Ti_2	-2.68	-1.86	1.00
Au_2Ti_3	-2.69	-1.48	2.00
$AuTi_4$	-2.86	-0.73	5.00
Ti_5	-2.96	---	2.00

As **Table 16** reveals, the cohesive energy increases significantly when one Au atom is replaced by Ti, and approaches more and more that of the pure Ti cluster when the content of Ti is increased. In the bimetallic gas-phase clusters, the Au atoms become negatively charged because of a charge transfer from Ti to Au, which is reflected in the Bader charges in **Table 16**. The spin density in the bimetallic clusters is mainly located on the Ti atoms.

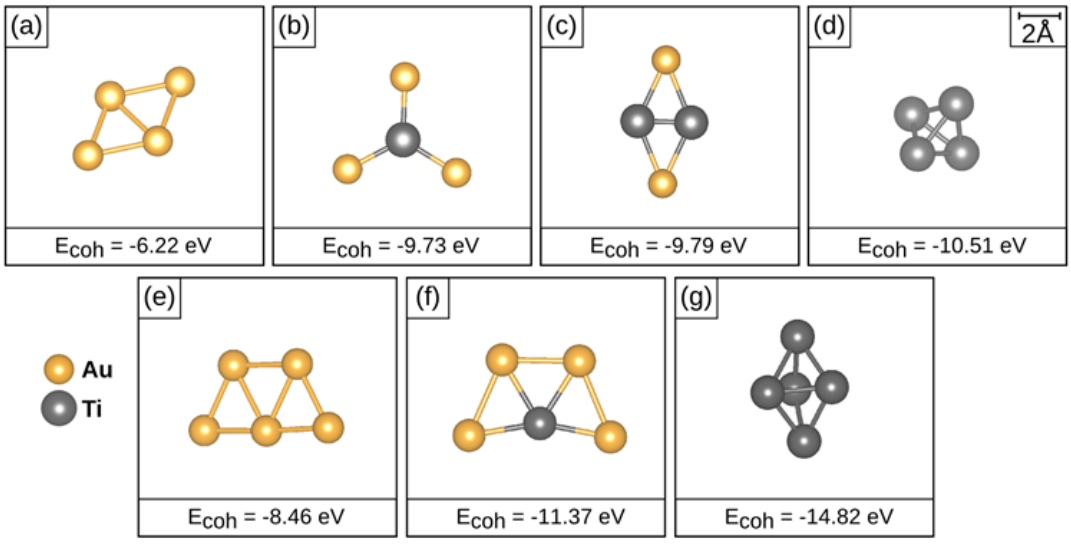

Fig. 27: Optimized structures and cohesive energies, E_{COH} (eV), of Au_xTi_y gas-phase clusters. (a) Au_4, (b) Au_3Ti_1, (c) Au_2Ti_2, (d) Ti_4, (e) Au_5, (f) Au_4Ti_1, (g) Ti_5.

7.2.4 Au_xTi_y clusters supported on the hydroxyl-free quartz (001) surface

The gas-phase clusters shown in **Fig. 27** were deposited on the hydroxyl-free α-quartz (001) surface. The most stable adsorption geometries are summarized in **Table 17** and shown in **Fig. 28**. The pure gold clusters adsorb on the hydroxyl-free silica surface only weakly via dispersion forces with adsorption energies of around -0.2 to -0.3 eV. The clusters stay neutral, which is reflected in the Bader charges close to zero, **Table 17**.

Table 17: Cluster adsorption energies $E_{ADS}(Au_xTi_y)$ [eV], on the hydroxyl-free α-quartz (001) surface, sum of Bader charges on the Au atoms Σq(Au) [|e|], sum of Bader charges on the Ti atoms Σq(Ti), sum of Bader charges on the support $\Sigma q(SiO_2)$, and total moments on the clusters μ [μ_B].

	$E_{ADS}(Au_xTi_y)$	Σq(Au)	Σq(Ti)	$\Sigma q(SiO_2)$	|μ|
Au_4	-0.21	0.01	---	-0.01	0.00
Au_3Ti	-0.40	-1.49	1.55	-0.06	1.00
Au_2Ti_2	-3.30	-1.30	1.56	-0.26	0.00
Ti_4	-4.23	---	2.92	-2.92	2.00
Au_5	-0.26	0.03	---	-0.03	1.00
Au_4Ti	-0.57	-1.16	1.63	-0.47	1.98
Ti_5	-4.61	---	3.99	-3.99	0.00

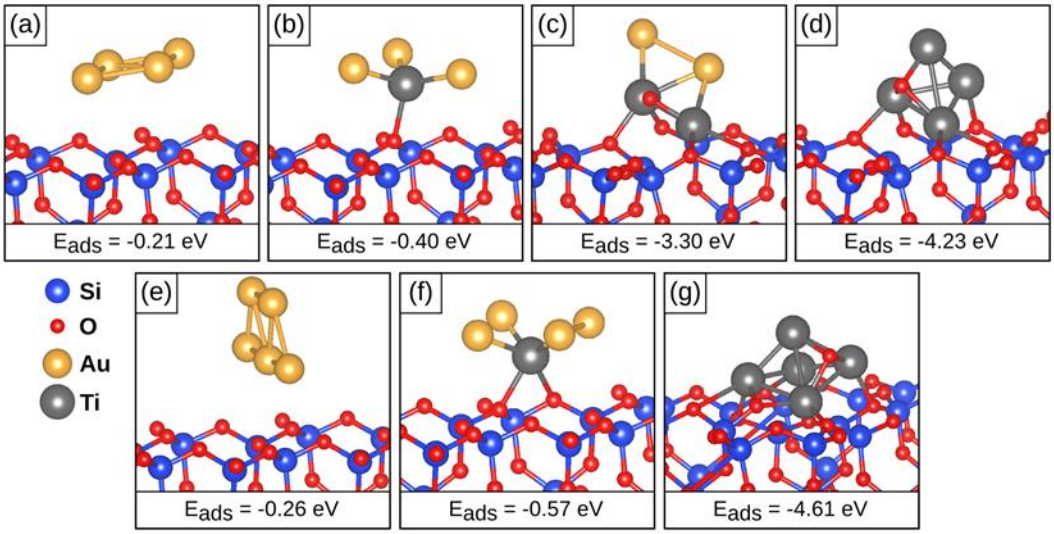

Fig. 28: Structures and adsorption energies E_{ADS} (eV) of Au_xTi_y clusters supported on the hydroxyl-free α-quartz (001) surface. (a) Au_4, (b) Au_3Ti_1, (c) Au_2Ti_2, (d) Ti_4, (e) Au_5, (f) Au_4Ti_1, (g) Ti_5.

Upon substitution of one gold atom by Ti, the adsorption energies of the tetramer and the pentamer are slightly enhanced with respect to the pure gold clusters. Au_xTi_1 clusters bind with the Ti atom to an oxygen atom of the silica surface, **Fig. 28**. When two or more Au atoms are replaced by Ti, the clusters start to react with the surface via oxygen overspill; effectively reducing the support. The reactions occurred spontaneously during structure optimizations. Here, oxygen binds exclusively to the Ti atoms. The reduction of the support be seen in $\Sigma q(SiO_2)$, which is negative, **Table 17**, and in the DOS curves, **Fig. 29** (c) and (d), where we detect occupied Si states, which are hybridized with Ti states showing the formation of Ti-Si bonds. The clusters with two or more Ti atoms show extremely large adsorption energies ranging from -3.30 eV to Au_2Ti_2 to -4.61 eV for Ti_5. The pure Ti clusters are very reactive and therefore the structures shown in **Fig. 28** (d) and (g) are probably not the global minima. However, to establish a trend in comparison to the other clusters, the geometries are sufficient.

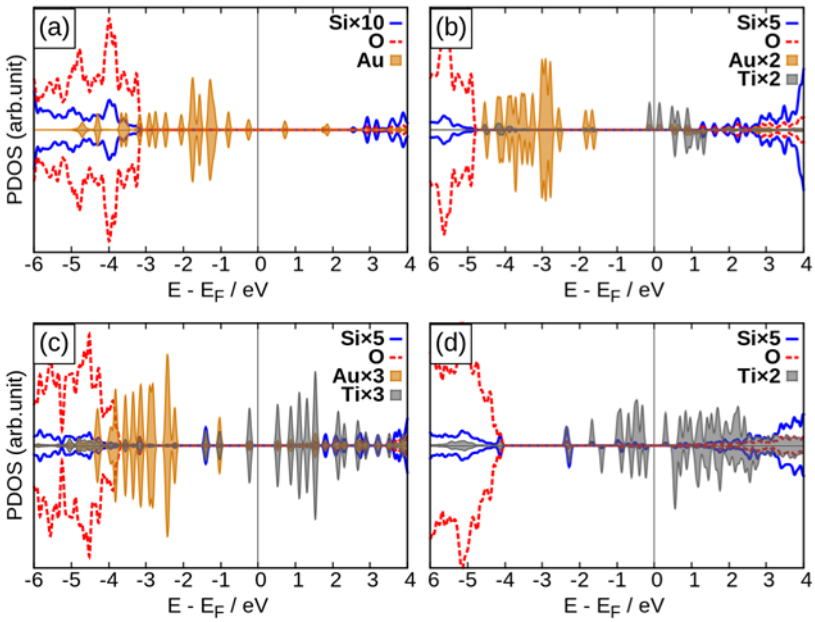

Fig. 29: DOS curves of the Au_xTi_y clusters supported on the hydroxyl-free α-quartz (001) surface. (a) Au_4, (b) Au_3Ti_1, (c) Au_2Ti_2, (d) Ti_4.

7.2.5 Au_xTi_y clusters supported on the hydroxylated quartz (001) surface

The defect-free surface

The clusters shown in **Fig. 27** were deposited on the fully hydroxylated α-quartz (001) surface. The most stable cases are reported in **Table 18** and **Fig. 30**. The adsorption energies of the clusters on the hydroxylated surface are significantly enhanced with respect to the hydroxyl-free surface. Particularly, the adsorption energies of the clusters containing one Ti atom are enhanced from roughly 0.5 eV on the hydroxyl-free surface to more than 1.5 eV on

the hydroxylated surface. This is due to ligand effects from the surface hydroxyls: The partial charges in the $Au^{\delta-}Ti^{\delta+}$ bimetallic clusters are stabilized via coordination with the surface hydroxyl groups. The Ti atoms are coordinated via oxygen atoms and the hydrogen atoms point towards the Au atoms, **Fig. 30** (b) and (f).

Table 18: Cluster adsorption energies $E_{ADS}(Au_xTi_y)$ [eV], on the fully hydroxylated α-quartz (001) surface. Sum of Bader charges on the Au atoms Σq(Au) [|e|], sum of Bader charges on the Ti atoms Σq(Ti), sum of Bader charges on the support $\Sigma q(SiO_2)$, and magnetic moments on the clusters μ [μ_B].

	$E_{ADS}(Au_xTi_y)$	Σq(Au)	Σq(Ti)	$\Sigma q(SiO_2)$	|μ|
Au_4	-0.88	-0.03	---	0.03	0.00
Au_3Ti	-1.63	-1.52	1.58	-0.06	1.00
Au_2Ti_2	-4.37	-1.30	2.58	-1.28	2.00
Ti_4	-7.25	---	2.86	-2.86	2.00
Au_5	-0.84	-0.01	---	0.01	1.00
Au_4Ti	-2.38	-1.66	1.72	-0.06	0.00
Ti_5	-6.62	---	1.97	-1.97	2.00

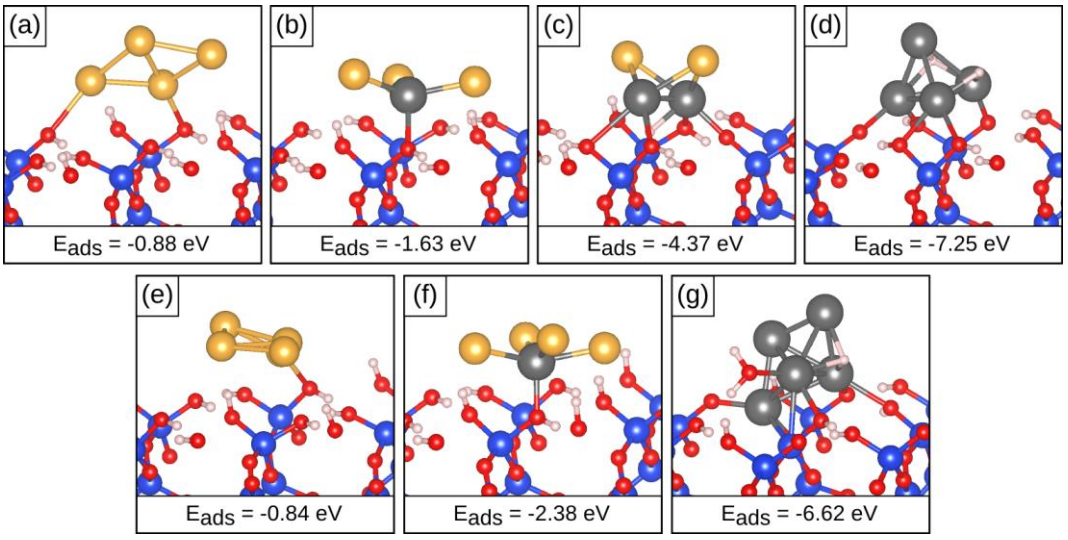

Fig. 30: Structures and adsorption energies E_{ADS} (eV) of Au_xTi_y clusters supported on the hydroxylated α-quartz (001) surface. (a) Au_4, (b) Au_3Ti_1, (c) Au_2Ti_2, (d) Ti_4, (e) Au_5, (f) Au_4Ti_1, (g) Ti_5.

For the clusters with more than one Ti atoms, we again observe a reaction of the clusters with the surface. This time the hydroxyl groups are split and the H atoms of the hydroxyl groups are adsorbed on the Ti atoms, having hydride character. [289] The hydride character of the Ti-H bond is reflected in the occupied H 1s states in the DOS (not shown). Recent studies show that this hydrogen reverse spillover is energetically favorable for late transition

metal, except for Au. [290,291] As for the clusters on the hydroxyl-free surface, the pure Ti clusters are very reactive. In the case of Ti_5, we observe the formation of water, **Fig. 30** (g).

The role of the non-bridging oxygen defect

We have seen before that the non-bridging oxygen defect (NBO, ≡Si-O$^{\bullet}$) has a substantial effect on the adsorption mode of the late transition metal atoms and dimers on silica. The unsaturated paramagnetic ≡Si-O$^{\bullet}$ binds to the clusters giving very stable ≡Si-O-M (formally ≡Si-O^{-}M^{+}) complexes, where M is the positively charged metal cluster. Since defects play an important role in the adsorption and agglomeration behavior of oxide-supported clusters, we investigated the interaction of the AuTi bimetallic clusters with the NBO defect, **Table 19** and **Fig. 31**. The adsorption of the clusters on the NBO defect is in all cases more exothermic than on the defect-free surface. For instance, the adsorption energy of the Au_4 cluster is enhanced by around 2.3 eV when going from the defect-free surface to the surface with the NBO defect. The Bader charge on Au_4 is close to 0.5 |e|, and the magnetic moment on the cluster changes the parity when going from the defect-free surface to the NBO defect. This clearly indicates the charge transfer from the metal cluster to the NBO defect. Similar observations are true for all other clusters, too, **Table 19**. The presence of the NBO defect can therefore contribute to anchor the clusters to the support.

Table 19: Cluster adsorption energies $E_{ADS}(Au_xTi_y)$ [eV], E_{REA} [eV], sum of Bader charges on the Au atoms Σq(Au) [|e|], sum of Bader charges on Ti atoms Σq(Ti), sum of Bader charges on the support $\Sigma q(SiO_2)$, and magnetic moments on the clusters μ [μ_B].

	$E_{ADS}(Au_xTi_y)$	E_{REA}	Σq(Au)	Σq(Ti)	$\Sigma q(SiO_2)$	|μ|
Au_4	-3.17	0.93	0.49	---	-0.49	1.00
Au_3Ti	-6.13	-1.29	-1.29	1.87	-0.58	0.00
Au_2Ti_2	-6.88	0.71	-1.33	2.21	-0.88	3.00
Ti_4	-9.45	1.02	---	2.25	-2.25	1.00
Au_5	-3.35	0.70	0.47	---	-0.47	0.00
Au_4Ti	-5.96	-0.36	-1.18	1.75	-0.57	1.00
Ti_5	-8.55	1.29	---	2.30	-2.30	3.00

Let us consider in more detail the Au_xTi_1 clusters. The enhancement of the adsorption energy, going from the defect-free surface to the NBO defect, is quite remarkable in these cases. For example, the Au_3Ti on the defect free surface has an adsorption energy of -1.6 eV. On the NBO defect, the adsorption energy is -6.1 eV. Here, the Ti atoms of the clusters are directly bound to the unsaturated oxygen atom. We have seen previously, that the clusters with more than one Ti atom can reduce the silica surface via oxygen and hydrogen overspill. A different way to reduce the silica surface is the formation of ≡Si-O-Au_xTi_y complexes according to the reaction ≡Si-OH + Au_xTi_y → ½ H_2 + ≡Si-O-Au_xTi_y. The reaction energies

are is reported in **Table 19**. The reaction is unfavorable for the Au clusters, which is no surprise since Au is very noble. For the Au_xTi_1 clusters, however, the reaction is exothermic. This is an interesting aspect, because hydrogen reverse overspill (we tested it also for the Au_xTi_1 clusters) is not favorable for these clusters. This ≡Si-O-Au_xTi_1 complexes are very stable, and sintering of these clusters is thus not suspected. For the clusters with more than one Ti atom, the hydrogen overspill is much more favorable than gas-phase H_2 formation.

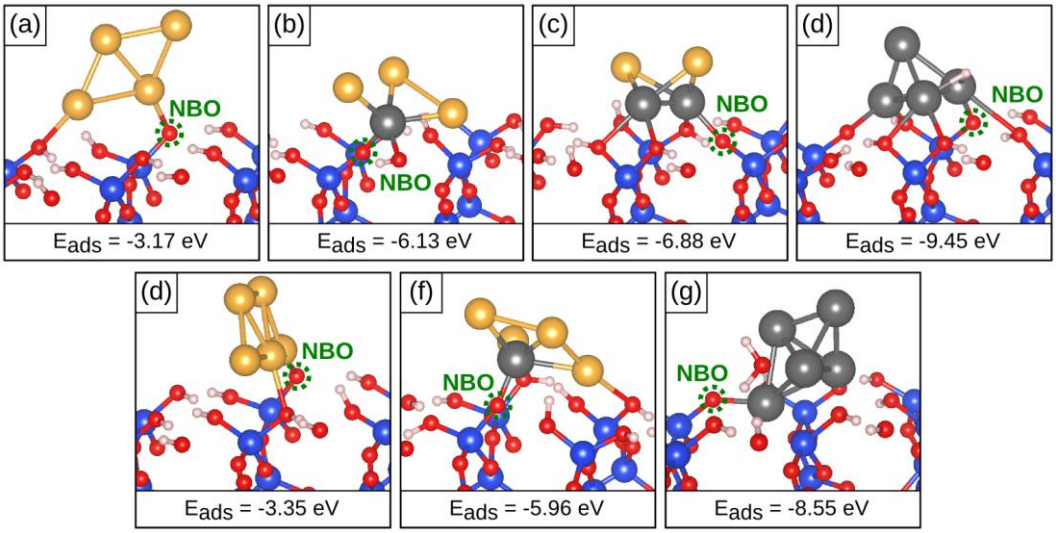

Fig. 31: Structures and adsorption energies E_{ADS} (eV) of Au_xTi_y clusters supported on the hydroxylated α-quartz (001) surface with a non-bridging oxygen (NBO) defect. (a) Au_4, (b) Au_3Ti_1, (c) Au_2Ti_2, (d) Ti_4, (e) Au_5, (f) Au_4Ti_1, (g) Ti_5.

7.2.6 Section summary

- The adsorption of Au_xTi_y (x+y = 4, 5) bimetallic clusters on the hydroxyl-free, and fully hydroxylated α-quartz (001) surface was investigated. The pure Au clusters adsorb on silica only weakly via dispersion forces. The Au clusters furthermore do not react with the surface, which makes them prone for sintering.

- Substitution of more than two Au atoms by Ti increases significantly the adsorption energy, which is due to the fact that the clusters react with the silica surface via oxygen and hydrogen reverse overspill, effectively reducing the silica.

- The substitution of only one Au atom by Ti results in an intermediate adsorption strength. The clusters with one Ti atom can react with the surface OH groups under formation of water and quite stable ≡Si-O-Au_xTi_1 complexes. This way, even a very low content of Ti can contribute to anchor the clusters to the silica support.

Chapter 8 Chemistry of supported oxide ultra-thin films

8.1 CO adsorption on a silica bilayer supported on Ru(0001)[8]

8.1.1 Introduction

In section 1.4, we have introduced the importance of oxide thin-films in technological applications and in fundamental science. In this chapter, we will concentrate on silica-based ultra-thin films, which play an important role in many applications, such as catalysis, biosensing and micro/nano-electro-mechanical systems (MEMS/NEMS). Silica ultra-thin films can be synthesized on various metals, such as Mo(112) [292], Ru(0001) [100], Ni(111) [293], Pd(100) [294], and Pt(111) [49]. Depending on the synthesis conditions and on the metal substrate, monolayers and bilayers of corner-sharing (SiO_4) tetrahedra can be synthesized. Whereas the monolayers exhibit unsaturated oxygen atoms, and chemisorb on the metal substrate, the bilayer is chemically saturated and binds to the metal support via dispersion forces. Due to the resemblance of the hexagonal porous structure of the silica monolayer to graphene, it is also called "silicatene". The bilayers ("bilayer silicatene" or "silica bilayer") are likely to be formed on the close packed surfaces of noble metals, such as Pt(111) and Ru(0001). [49] Crystalline and amorphous phases of the silica bilayer can be produced. [295] The crystalline silica bilayer exhibits pores of uniform size, which are built of six [SiO_4]-bilayer units. These hexagons are called 6 member rings and have a diameter of around 5 Å. The amorphous phase exhibits a broader ring size distribution with 4-10 member rings with pore sizes in the range of 4-10 Å. [295]

The silica bilayer, as bulk silica, is a wide gap insulator. Metal-supported silica bilayers constitute interesting hybrid materials, because an inert two-dimensional porous structure is supported on a chemically active metal. Since the pore size of the silica bilayer is in the size range of small molecules, the bilayer can be thought of as a two-dimensional molecular sieve. [110] Thus, the SiO_2/Ru hybrid system is very interesting for catalytic applications. Recently, Emmez et al. investigated the adsorption of CO on the Ru(0001)-supported silica bilayer. [110] They performed infra-red (**IR**) spectroscopy measurements and found a CO

[8] The content of this study is published in the Journal "Surface Science": P. Schlexer, G. Pacchioni, R. Włodarczyk, and J. Sauer, "CO adsorption on a silica bilayer supported on Ru(0001).", Surf. Sci., 648 (2016) 2-9. http://doi.org/10.1016/j.susc.2015.10.027

stretching frequency adsorption band at 2051 cm^{-1} at 10^{-6} bar CO at 125 K. [110] The band was red-shifted by roughly 20 cm^{-1} upon heating to 300 K. Then, the band at 2051 cm^{-1} was recovered by increasing the CO pressure to 10^{-5} bar at 300 K. [110] In the following, we address the adsorption of CO on the Ru-supported silica bilayer via DFT.

8.1.2 Computational details

In this computational section, we will include the technical details of the entire chapter. Spin-polarized periodic DFT calculations were performed with the VASP program [194,195,196,197]. The PBE exchange-correlation functional [160,161] was used in combination with the PAW method. [193,192] Structure optimizations were run until forces on ions were smaller than |0.01| eV/Å. In some of the calculations, the convergence criteria were set to F_{ion} < |0.001| eV/Å to confirm findings obtained with the less precise criteria.

We calculated the Ru hcp bulk structure using a kinetic energy cutoff of 1200 eV for the plane wave basis and a Γ-centered Monkhorst-Pack k-point mesh of (13×13×8). [226] The obtained bulk lattice parameters of $a_0 = b_0 = 2.73$ Å and $c_0 = 1.58$ Å, are in good agreement with the experimentally derived values of $a_0 = b_0 = 2.70$ Å and $c_0 = 1.58$ Å. [296] To calculate the lattice parameters of the free-standing silica bilayer, we employed a kinetic energy cutoff of 1200 K and k-point mesh of (13×13×1). The silica bilayer has approximately twice the periodicity of the Ru(0001) substrate. The resulting lattice mismatch between the (1×1) hexagonal silica bilayer surface lattice parameter and the (2×2) Ru(0001) surface lattice parameter is -2.76%, i.e. the silica bilayer has a slightly smaller surface unit cell. We kept the Ru(0001) surface lattice parameters fixed during all the following structure optimization, resulting in a strain on the silica bilayer. For many calculations, we use a (2×2) supercell of the joint SiO_2/Ru(0001) systems, i.e. a (4×4) supercell of the pristine Ru(0001). The hexagonal SiO_2/Ru(0001) (2×2) supercell exhibits lattice parameters $a_0 = b_0 = 10.92$ Å. In some cases, we used the smaller orthorhombic SiO_2/Ru(0001) supercell with lattice parameters $a_0 = 5.40$ Å and $b_0 = 9.35$ Å. In both supercells, a 5-layer Ru slab was used. The lowest two layers of Ru were held fixed during structure optimizations. The SiO_2/Ru slabs were separated by more than 12 Å of vacuum. Dipole corrections perpendicular to the surface were applied. The k-point mesh was set to (3×3×1) in the hexagonal surface unit cell and (8×4×1) in the orthogonal surface unit cell ((4×2×1) for the hybrid functional calculations).

Several methods to include dispersion forces were applied. The first method applied is the semi-empirical Grimme method, PBE+D (also called PBE+D2, but we drop the 2 for the sake of brevity) [184]. This method was used in both of the following studies. The second method used is the application of the +D only to the first layer of the Ru film, and to the silica bilayer. Here, were set to $C_6 = 0$ for the Ru atoms of the four lowest layers. We denote this as PBE+D-1L. The third method is a modified version of the Grimme method, in which

the vdW-coefficient of the Si are replaced by that of Ne to account for the fact, that in the SiO_2, we formally have Si^{4+} ions, which are less polarizable than neutral Si atoms. This approach was first suggested by Tosoni and Sauer. [185] We denote this method as PBE+D'. In the fourth approach, we make use of a vdW-DF, namely the optB88-vdW dispersion functional [182,297]. In the last approach, we combined the HSE06 hybrid functional [164,298] with 20% of HF exchange, with the normal +D correction, to have a direct comparison to the PBE+D method. In all cases, the Ru lattice parameters as calculated at the PBE level were kept. The adhesion energies of the thin films are calculated as described in eqn. (31). Here, E refers to the total energy of optimized systems with the lattice parameters of the Ru(0001) surface, and A denotes the surface unit cell area. X = 0 represents the silica bilayer and X = 3/4 represent the silicatene/silicon-carbide (see next section).

$$\mathrm{E_{ADH}(SiC_XO_{2-X}/Ru) = \{E(SiC_XO_{2-X}/Ru) - E(SiC_XO_{2-X}) - E(Ru)\}/A} \quad (31)$$

The adsorption energies are calculated as described in eqn. (32). Here, $\mathrm{TF = SiC_XO_{2-X}}$ and Y can be H or CO. The Al-OH formation energies correspond to the adsorption energy of H on the Al-doped systems.

$$\mathrm{E_{ADS}(Y/TF/Ru) = E(Y/TF/Ru) - E(Y) - E(TF/Ru)} \quad (32)$$

Interaction energies are defined in eqn. (33). Here, E is the total energy of the separate system at the structure of the joint system. For instance A//AB refers to A in the structure of the joint system AB.

$$\mathrm{E_{int}(AB//AB) = E(AB//AB) - E(A//AB) - E(B//AB)} \quad (33)$$

The silica bilayer has three oxygen layers. One at the bottom of the film (O_{low}), one in the middle of the film and one on top of the film (O_{up}). To discuss the distance between the Ru surface and the silica thin film, we define $d(Ru\text{-}O_{POS}) = z_{av}(O_{POS}) - z_{av}(Ru)$, where POS = up or low and z_{av} is the average z coordinate of the corresponding atoms. Work-functions of the systems were determined, defined as $\Phi = E_{VAC} - E_F$, where E_F is the Fermi level and E_{VAC} is the vacuum level.

To investigate CO harmonic stretching frequencies, we used the central finite difference method to calculate the force constants. 0.02 Å displacements in all Cartesian directions are applied. Only the CO and atoms directly connected to it were allowed to move. The force constants calculations were done in the hexagonal unit cell with a k-point set of (5×5×1). GGA-based functionals tendentially overestimate the bond-lengths resulting in a general underestimation of computed force constants and therewith of the stretching frequencies. [120] This bias is frequently compensated by the fact that the computed harmonic frequencies ω_e are compared to experimental fundamental frequencies ω_{01}. The latter are red-shifted with respect to the first according to $\omega_{01} = \omega_e - 2\omega_e\chi_e$. [299] For CO, the anhar-

monicity constant $\omega_e\chi_e$ is only around 13 cm^{-1}, i.e. much smaller as for instance that of OH bonds (e.g. ~76 cm^{-1} for OH in zeolites), and does not change much when the chemical environment of the molecule is changed. [300,299] Although for very large bond elongations it would be interesting to investigate the effect of anharmonicity, we retain from this endeavor because it is not the topic of this study and the anharmonicity is not trivial to determine computationally.

8.1.3 The silica bilayer supported on Ru(0001)

In this study, we analyze in more detail some bond lengths and distances and therefore we use the unit pm instead of Å. The Ru-supported crystalline silica bilayer can be synthesized with and without oxygen at the SiO_2/Ru interface. The 3O(2×2) covered Ru surface was shown to be stable under experimental conditions. [301] A lateral translation of the silica bilayer on the Ru surface gives several high-symmetry orientations of the SiO_2 with respect to the Ru(0001) surface. The center of the silica hexagons can for instance be above a Ru top, fcc or hcp position. We denote these cases as **center-top**, **center-fcc** and **center-hcp**, respectively. We computed the SiO_2/Ru(0001) system with and without oxygen at the interface. The most stable orientations are shown in **Table 20**. The supported bilayers are shown in **Fig. 32**.

Table 20: Adhesion energies E_{ADH} [kJ/mol/Å^2] of the SiO_2 bilayer adsorbed on Ru(0001) and SiO_2-Ru interfacial distance d(Ru-O_{low}) [pm].

Unit Cell	Orthorhombic		Hexagonal	
	E_{ADH}	d(Ru-O_{low})	E_{ADH}	d(Ru-O_{low})
SiO_2/3O(2×2)/Ru(0001)	-1.82	381	-1.78	377
SiO_2/Ru(0001) (center-hcp)	---	---	-2.13	307
SiO_2/Ru(0001) (center-top)	-3.06	275	-3.19	268

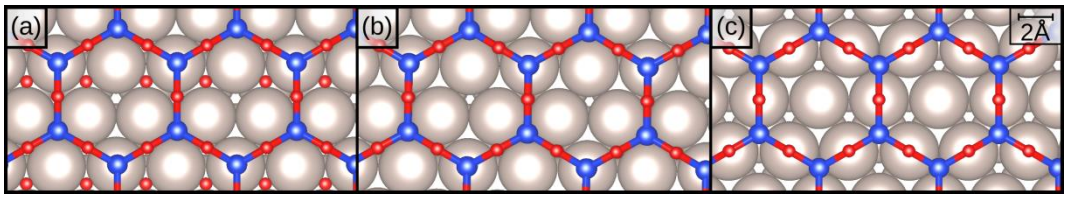

Fig. 32: Top view on supported silica bilayers. (a) SiO_2/3O(2×2)/Ru(0001), (b) SiO_2/Ru(0001) center-hcp configuration, (c) SiO_2/Ru(0001) center-top configuration. [302]

For the SiO_2/Ru(0001) system without oxygen at the interface, the center-top orientation is preferred. For the SiO_2/3O(2×2)/Ru(0001), the center-fcc orientation is the best orientation. In accordance with ref. [301], we find that the presence of interface oxygen weakens the silica-Ru interaction, reflected in the adhesion energies and film-Ru distances, **Table 20**.

8.1.4 Adsorption of CO on the pristine Ru(0001) surface

Let us first recapitulate the adsorption of CO on the pristine Ru(0001) surface in order to understand the effect of the silica bilayer. The stretching frequency of CO on Ru(0001) is known depend on the coverage of CO and/or that of other adsorbates. [303,304] The effect can be explained with the Blyholder model. The Ru back-donation into the $2\pi^*$ molecular orbital results in an elongation of the C-O distance and thus in a red-shift of the frequency with respect to the gas-phase value. The coverage effect has contributions from direct adsorbate-adsorbate interactions, e.g. dipole-dipole interactions, and substrate-mediated adsorbate-adsorbate interactions, e.g. less available electron density for back-donation with increasing coverage. Whereas CO molecules prefer a Ru top position on the pristine Ru surface, the Ru hcp site is preferred in the presence of the 3O(2×2) oxygen superstructure. A more detailed discussion can be found in the work of McEwen et al. [305] We computed the coverage dependence of the CO stretching frequency of CO on Ru(0001), **Table 21**. For the gas-phase molecule, we compute a CO wavenumber of 2125 cm^{-1} (the experimental ν is 2143 cm^{-1} [306,307]). The values are compared to those reported by McEwen et al. [305]

Table 21: PBE+D results for adsorption energies E_{ADS} [eV], vibrational wavenumbers *ν*(CO) [cm^{-1}], and bond distances *d* [pm] of CO on Ru(0001) at different coverage θ [ML]. All CO molecules are adsorbed on top of Ru atoms.

	θ	E_{ADS}	*ν*(CO)			*d*(C-O)	*d*(C-Ru)	*d*(C-C)
			PBE+D	PW91[a]	Exp.[a]			
1/16	(0.0625)	-2.26	1959	-	-	116.8	188.9	1092
1/9[a]	(0.1111)	-	-	1981	2005	-	-	-
1/3	(0.3333)	-	2005	2016	2022	116.7	189.2	472
2/3	(0.6666)	-	2063	2060	2060	116.3	190.2	273
1	(1.0)	-1.59	2104	-	-	115.8	190.0	273

[a] from ref. [305]

The possible relative distribution of the CO molecules is dependent on the surface unit cell size and shape. We used a (4×4) Ru(0001) surface super cell, **Fig. 33** (a), for coverages of 1/16 and 1, and a (3×3) Ru(0001) surface super cell, **Fig. 33** (b-c), for coverages of 1/9, 1/3, and 2/3. The experimental saturation coverage of CO/Ru(0001) is 2/3 ML. [305,110]

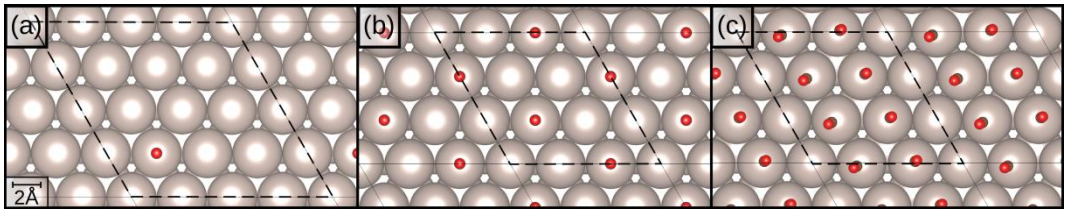

Fig. 33: Distribution of CO molecules on Ru(0001) in hexagonal unit cells at different CO coverage. (a) 1/16, (b) 1/3 and (c) 2/3 ML. [302]

On Ru(0001), the computed CO stretching frequencies are in great agreement with the experimental ones, **Table 21**. The CO stretching frequency spans values from 1959 cm^{-1} for a coverage of 1/16 ML to 2104 cm^{-1} for 1 ML. Also the adsorption energies are subject to coverage dependence, with E_{ADS} decreasing from -2.26 eV at low coverage to -1.59 eV at 1 ML coverage, **Table 21**. The relation the CO bond length and the stretching frequency can be examined using the Badger's plot [308], **Fig. 34** and eqn. (34). We determine eqn. (34) from the frequencies of CO/Ru(0001) at 1/16 ML and CO/SiO_2/Ru(0001) at 1/16 ML, both computed at the PBE+D level. Generally, the computed data at high CO intermolecular distances (low coverages) follow very nicely a linear dependence between stretching frequency and bond length in the Badger's plot. For higher coverages on the silica-free Ru(0001) surface, a slight deviation from a linear behavior is observed (see squares in **Fig. 34**.). This may be due to direct adsorbate-adsorbate interactions, e.g. dipole-dipole interactions, which affect the frequency more than the bond length. The other data points follow quite nicely the linear relation in eqn. (34), **Fig. 34**. Moreover, eqn. (34) can be used to approximately predict the stretching frequency from the bond distance.

$$\nu(\mathrm{CO})\ [\mathrm{cm^{-1}}] = -58.243 \times d(\mathrm{C\text{-}O})\ [\mathrm{pm}] + 8762.755 \qquad (34)$$

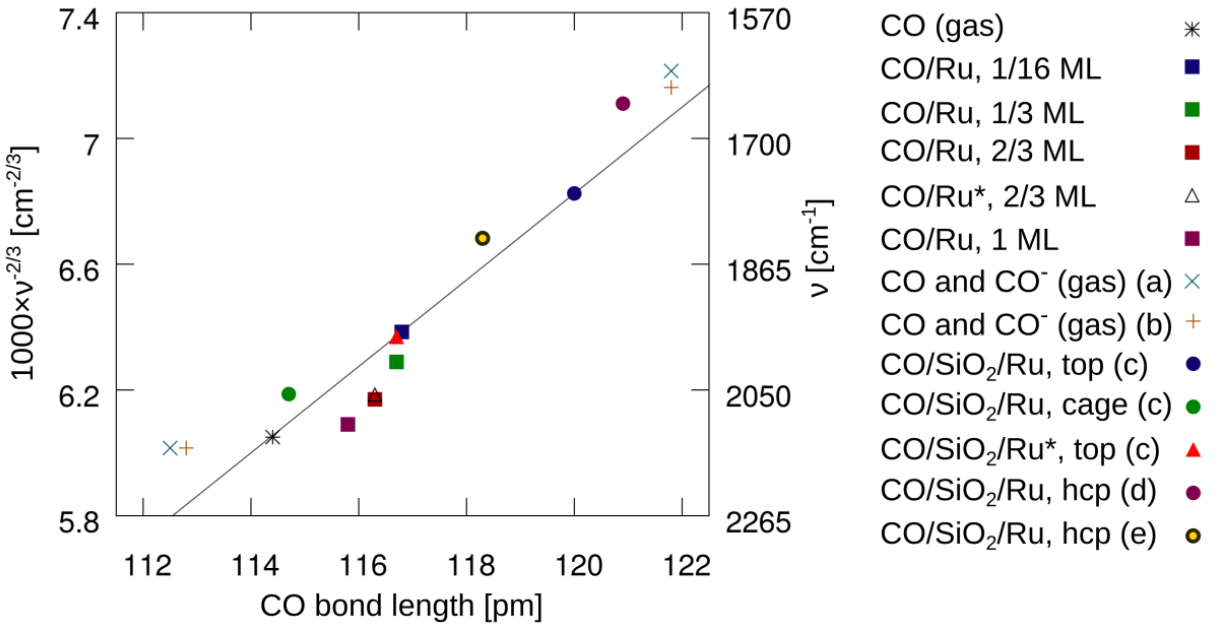

Fig. 34: The Badger's rule plot. CO stretching frequency, ν, plotted against the bond length. The data from **Table 21** (PBE+D) are shown as squares. (a) and (b) denote calculated [309] and experimental [307] CO and CO^- data. Circles denote data for CO/SiO_2/Ru (PBE+D), (c) center-top orientation, (d) center-hcp orientation and (e) CO/SiO_2/3O(2×2)/Ru in center-hcp orientation. Top, cage and hcp denote the CO positions. Triangles denote results without dispersion correction. The black line represents eqn. (34). [302]

8.1.5 Adsorption of CO on SiO_2/Ru(0001)

Exploration of different adsorption sites

The presence of an oxide ultra-thin film can change the work function of the metal support due to polarization effects. [310,311] This can in turn influence the interaction of the metal surface with adsorbates. The adsorption of CO with a coverage of 1/16 ML on the SiO_2/Ru(0001) was explored. Various positions were thereby taken into account. The results are summarized in **Table 22** and **Fig. 35** (a-c). We tried adsorbing the CO molecule also at Ru bridge sites, but these resulted unstable. The best CO adsorption position is dependent on the silica-Ru orientation. CO always takes preferably a position at the silica-Ru interface, at the center of the silica ring, **Table 22**. The most favorable configuration is with the SiO_2/Ru(0001) being in the center-top configuration, and the CO on top of the Ru atom located in the center of the silica ring, **Fig. 35** (a). The adsorption energy, -2.30 eV, is similar to that of CO on Ru(0001) at the same coverage, -2.26 eV. However, the bond length and the stretching frequency of the CO are extremely different in the two cases, cf. **Table 21** and **Table 22**. Whereas on the pristine Ru surface, the CO bond length is 117 pm and the stretching frequency is 1959 cm^{-1}, at the SiO_2/Ru(0001) interface, these values become 120 pm and 1774 cm^{-1}, respectively. This is a quite impressive bond elongation and frequency redshift, particularly with respect to the experimental band at around 2051 cm^{-1}. [110] Thus, the bonding situation requires a more detailed examination.

Table 22: Calculated adsorption energies E_{ADS} [eV], vibrational wavenumbers ν(CO) [cm^{-1}], and bond distances *d* [pm] of CO on SiO_2/Ru(0001) (see also **Fig. 35**). The CO coverage is 1/16 ML and the method applied is PBE+D.

SiO_2/Ru Orientation	CO site	E_{ADS}	ν(CO)	*d*(C-O)	*d*(C-Ru)	*d*(Ru-O_{low})
---	Gas-phase	---	2125	114.4	---	---
center-top	top	-2.30	1774	120.0	182.4	263
center-hcp	hcp	-2.05	1668	120.9	211.9	306
center-top	hcp	-1.43	1356	127.3	204.8	281
center-top	cage	-0.11	2055	114.7	437.5	268
center-top	under Si	-0.40	-	131.5	196.6	306

Inspecting **Fig. 35** (a), it becomes clear that CO is penetrating the silica ring. Electrostatic repulsion of the CO and the silica ring could be the cause for the elongation of the CO bond. As the silica bilayer is adsorbed on the Ru(0001) surface via dispersion forces, the distance of the silica bilayer and the Ru substrate may be sensitive towards the level of theory with which the dispersion forces are being described. In the following, we will examine this relation in more detail.

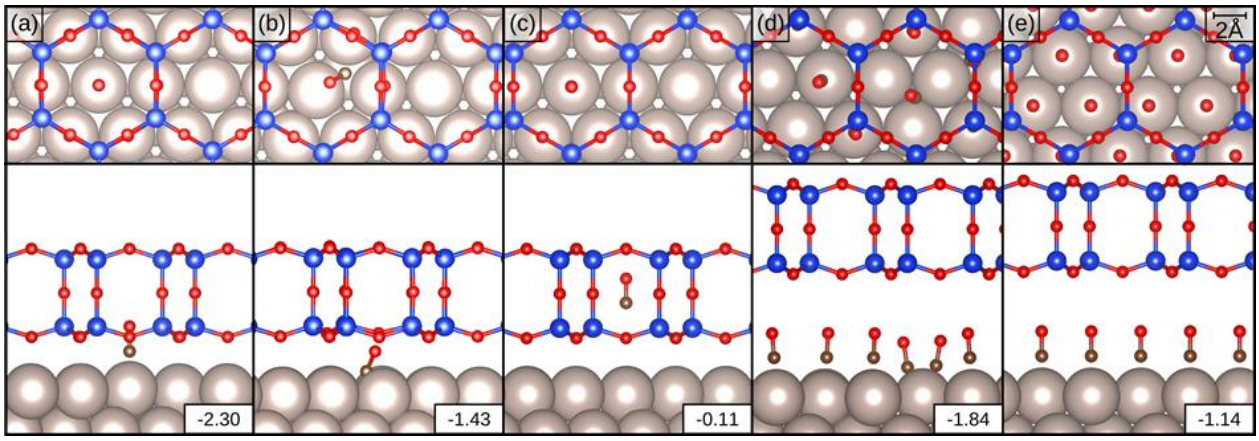

Fig. 35: CO at the interface between SiO_2/Ru(0001). (a-c) 1/16 ML CO at different positions, the silica bilayer is in the center-top orientation. (a) CO at top position, (b) CO at hcp position, (c) CO in the silica cage. (d) 5/8 ML CO under the silica film and (e) 1 ML CO under the silica film. The calculated CO adsorption energies (eV) are indicated. [302]

Role of dispersion interactions

We investigated the interaction energies between the different subsystems. The results are shown in **Table 23**. Apparently, the silica bilayer is largely attracted to the Ru surface due to the +D dispersion correction. The repulsion of the CO-SiO_2 subsystem of 0.30 eV is not enough to compensate the energy gain of -3.45 eV for the attraction of the SiO_2-Ru subsystem in the PBE+D geometry. Even if we would fill all 4 silica hexagons present in the (2×2) SiO_2/Ru(0001) surface super cell, the total CO-SiO_2 repulsion (assuming 0.30 eV × 4) may not be enough to compensate the SiO_2-Ru attraction of -3.45 eV.

Table 23: Interaction energies, E_{INT} [eV], according to eqn. (33) for different subsystems of the CO/SiO_2/Ru(0001) system.

	PBE structure			PBE+D structure		
	PBE//PBE	D//PBE	PBE+D//PBE	PBE//PBE+D	D//PBE+D	PBE+D//PBE+D
CO - Ru	-2.09	-0.36	-2.45	-2.14	-0.36	-2.50
CO - SiO_2	0.21	-0.20	0.00	0.66	-0.36	0.30
SiO_2 - Ru	-0.12	-1.42	-1.54	0.75	-4.19	-3.45

The data in **Table 23** clearly indicate the important role of dispersion forces in this context, so we checked whether we would find a similar effect also for geometries obtained at different levels of theory, i.e. with PBE+D-1L, PBE+D', PBE-vdW and HSE06+D, **Table 24**. For this test, we used the orthorhombic unit cell and all cases refer to a CO coverage of 1/8 ML. All the methods including dispersion forces give quite low SiO_2-Ru interface distances. The CO penetrates the silica hexagon resulting in CO bond lengths ranging from 118.5 pm for PBE+D' to 119.8 pm for PBE+D. The stretching frequencies range between 1797 cm^{-1} and 1861 cm^{-1} and are largely red-shifted with respect to the silica-free Ru surface of around

1960 cm^{-1}. In the dispersion-free PBE calculation, the silica bilayer detaches from the Ru surface, giving space to the CO molecule, resulting in similar values as for the silica-free Ru surface. However, all values are far below the measured wavenumber (2051 cm^{-1}) and thus are clearly incompatible with the experimental observations. [110] The comparison of the various methods shows that the structure obtained by PBE+D, **Fig. 35** (a), is not an artefact but the result of the relatively strong dispersive interaction of the silica film and the Ru(0001) surface in presence of the CO.

Table 24: CO adsorption energies E_{ADS} [eV], bond distances *d* [pm], and ν(CO) frequencies [cm^{-1}] of the CO/SiO_2/Ru system obtained using different methods, θ = 1/8 ML.

	PBE	PBE+D	PBE+D-1L	PBE+D'	PBE-vdW	HSE06+D
E_{ADS}	-1.89	-2.18	-3.07	-1.90	-1.90	-1.36
d(Ru-O_{low})	519	263	268	291	284	258
d(C-O)	116.8	119.8	119.6	118.5	118.9	118.9
ν(CO)	1960[a]	1797	1797[a]	1861[a]	1838[a]	1838[a]

[a] Value estimated according to eqn. (34).

8.1.6 Role of interfacial oxygen and Ru steps

As mentioned before, the presence of co-adsorbates, such as oxygen, can significantly change the adsorption behavior of CO on Ru(0001) [312]. We have therefore calculated one case for CO at the interface with co-adsorbed oxygen. The 3O(2×2) oxygen superstructure on Ru was considered as shown in **Fig. 32** (a). CO was adsorbed on the SiO_2/3O(2×2)/Ru(0001) system with a coverage of 1/16 ML. CO adsorbs at a Ru-hcp site with an adsorption energy of around -0.92 eV. This adsorption energy is considerably smaller than that in absence of interface oxygen (-2.30 eV). The stretching wavenumber for CO on SiO_2/3O(2×2)/Ru(0001) is 1831 cm^{-1}, which is still too small compared to the experimental finding of 2051 cm^{-1}.

The adsorption of the silica bilayer on the perfect Ru(0001) terrace results in the penetration of CO into the silica bilayer and therewith to a substantial bond elongation. On a real surface, morphological defects, such as steps may give space to the CO, resulting in shorter CO bonds and larger stretching frequencies. We considered a step in one of the surface lattice directions of the orthogonal unit cell. A CO molecule was adsorbed at the step, so that no penetration of CO molecule into the silica bilayer occurred. The resulting stretching frequency is still red-shifted with respect to the frequency CO on pristine Ru(0001) and does not reproduce the experimental findings. [110]

8.1.7 CO coverage effects in $CO/SiO_2/Ru(0001)$

Experimentally, the saturation coverage of 2/3 ML for CO on pristine Ru(0001) was reached at 100 K and 10^{-8} mbar, resulting in an IR signal at around 2060 cm^{-1} (cf. Supporting Information in [110] and [313]). The experiments on SiO_2/Ru(0001), on the other hand, were performed in 10^{-5} mbar CO. In case that the CO is able to diffuse to the SiO_2/Ru(0001) interface, this pressure should in principle be sufficient to reach the saturation coverage of CO on Ru(0001). To account for the coverage effects on the SiO_2/Ru(0001) system, we investigated different coverages, **Table 25**. Note that with our SiO_2/Ru(0001) surface unit cells, we can only compute coverages of $\theta = N/8$ and $\theta = N/16$, where N is an integer. At a coverage of 1/4 ML, all the silica hexagons are filled and subsequently added CO molecules must therefore push up the silica bilayer so that they have space to adsorb at the interface. So, for coverages above 1/4 ML, the silica bilayer is situated above the CO molecules, as shown in **Fig. 35**. For $\theta = 5/8$, two different CO adsorption modes are found: 3 of the 5 molecules adsorb on a Ru-top position (d(C-O) = 115.8-116.2 pm) and 2 molecules adsorb at a Ru 3-fold hollow position (d(C-O) = 118.8-119.7 pm), **Fig. 35** (d). For 1 ML, all CO molecules adsorb at Ru top positions, **Fig. 35** (e). At larger coverage, no penetration of the molecules into the silica bilayer occurs and we can assign experimental stretching of 2051 cm^{-1} to a coverage of around 2/3 ML, **Table 25**.

Table 25: E_{ADS} [eV], ν(CO) [cm^{-1}], and bond distances *d* [pm] for CO adsorbed on SiO_2/Ru(0001) at different CO coverages θ [ML] computed at the DFT+D level.

θ	1/16	1/8	1/4	5/8	1
E_{ADS}	-2.30	-2.18	-2.07	-1.84	-1.14
ν(CO)	1774	1797	1838	2044	2107
d(C-O)	120.0	119.8	119.3	115.8[a]	115.8
d(Ru-O_{low})	262	263	255	588	588

[a] The smallest CO distance found.

The mechanism of CO diffusing under the bilayer is certainly not trivial and therefore we desist on investigating this process in more detail. However, we estimated the barrier for diffusion through the free-standing silica bilayer. This was done performing partial structure optimization, fixing the C atom and some selected atoms from the silica film in the direction perpendicular to the film. The so estimated barrier is around 0.5 eV. Note that this is an upper limit for the barrier due to the method applied. The Ru surface is expected to lower the barrier in the lower part of the bilayer, as it was found for the diffusion of a Na atom. [314]

8.1.8 Section summary

- At low coverage, the CO prefers adsorbing on a Ru top site, penetrating the hexagon of the crystalline silica bilayer. This adsorption mode exhibits a relatively strong CO

adsorption energy of around -2.3 eV. The adsorption mode was verified using different levels of theory, and is a result of the Ru-SiO_2 dispersion interaction.

- The penetration of the CO molecule into the silica bilayer is accompanied by steric repulsion, causing an elongation of the C-O bond. The elongation of the CO bond is reflected in a large red-shift of the CO stretching frequency of the order of 200-300 cm^{-1} with respect to the gas-phase CO.
- At larger CO coverages ($\theta > 1/4$ ML), the silica bilayer detaches from the Ru surface, floating above the CO molecules. The experimental IR band at around 2051 cm^{-1} can therewith be assigned to a CO coverage of around 2/3 ML.
- For the diffusion of the CO molecules through the 6-member rings of the silica bilayer, we estimated a barrier of 0.5 eV.

8.2 A new two-dimensional material: Silicatene/Silicon-Carbide[9]

8.2.1 Introduction

In the previous section, we have already introduced the silica bilayer supported on Ru(0001). We have seen that the silica bilayer is chemically and electronically saturated and interacts with the Ru surface only weakly via dispersion forces. [315] Due to the topological resemblance of silica ultra-thin films to graphene, sometimes the mono- and bi-layers are referred to as silicatene and bilayer-silicatene, respectively. [110] The weak interaction between the Ru and the silica bilayer makes it possible for molecules like ethylene to intercalate the silica bilayer and react at the SiO_2/Ru interface. In a recent study, the formation of a new two-dimensional thin film upon such intercalation of ethylene was reported. [316] The thin-film consist of a silica monolayer on top of a [Si_2C_3] monolayer supported on the Ru(0001) surface. This new two-dimensional material is called silicatene/silicon-carbide. [316] In this study, we aim to determine the adsorption mode of the silicatene/silicon-carbide on Ru(0001) and explore its chemical properties via H adsorption and Al-doping.

8.2.2 Properties of the SiC_XO_{2-X}/Ru(0001) interface

In the following, we will compare the adsorption of silicatene/silicon-carbide (**SSC**) on Ru(0001) to that of silica bilayer. Both films exhibit a porous hexagonal structure. The center of the thin film hexagons can be oriented in various ways on the Ru(0001) surface, see

[9] The content of this study is published in the Journal of Physics: Condensed Matter: P. Schlexer, and G. Pacchioni, "Modelling of an ultra-thin silicatene/silicon-carbide hybrid film.", J. Phys. Cond. Matter., 28 (2016) 364005. http://doi.org/10.1088/0953-8984/28/36/364005

section 8.1.3. The adsorption configurations are summarized in **Table 26** and the energetically most favorable cases are shown in **Fig. 36**. For the SCC, the center-hcp is the most stable adsorption configuration with an adhesion energy of -510 meV/Å^2. For the silica bilayer, the best adsorption energy is found for the center-top configuration with an adsorption energy of around -22 meV/Å^2. The large difference in the adhesion energies of the two thin films is due to the fact that the free-standing silicatene/silicon-carbide is chemically unsaturated, since the bivalent oxygen atoms of the lowest atomic layer of the silica bilayer were replaced by carbon. It is therefore no surprise that the SCC chemisorbs on the Ru surface. As discussed before, the silica bilayer is physisorbed on the Ru surface via dispersion forces. To determine in more detail the chemical bond realized between the SCC and the Ru surface we analyze the work-function, Bader charges and bond-distances. In the following, we refer only to the most stable configurations, i.e. center-hcp for the SCC and center-top for the silica bilayer, **Fig. 36**.

Table 26: Adhesion energies E_{ADH} [meV/Å^2], of SiC_XO_{2-X} on Ru(0001), work-functions Φ [eV], and work function changes $\Delta\Phi$ [eV] with respect to Ru(0001), average Bader charges q_{AVG} [|e|], and selected distances: The thin films exhibit two layers of Si atoms, one in the top part of the film (Si, top) and one closer to the Ru support (Si, low). (Ru, top) indicates the Ru atoms at the topmost layer of the slab. Also shown are the average distance d_{AVG} [Å] and the distance in the direction perpendicular to the slab d_Z [Å] between (Ru, top) and the lowest atomic layer of SiC_XO_{2-X} (either C or O).

	silicatene/silicon-carbide			silica bilayer		
Orientation (center-x)	top	hcp	fcc	top	hcp	fcc
E_{ADH}	-420	-510	-494	-33	-22	-22
Φ	4.83	4.04	4.29	3.41	4.21	4.21
$\Phi(SiC_XO_{2-X})$-Φ(Ru)	0.03	-0.48	-0.73	-1.36	-0.56	-0.56
q_{AVG}(C)	-1.56	-1.72	-1.71	---	---	---
q_{AVG}(Si, low)	2.50	2.51	2.84	3.17	3.18	3.17
q_{AVG}(Si, top)	2.83	3.18	3.18	3.19	3.18	3.18
q_{AVG}(Ru, top)	0.17	0.27	0.26	-0.03	-0.04	-0.05
d_{AVG}(Ru-C/O)	1.92	2.11, 2.16	2.21, 2.20	2.68	3.47	3.46
d_Z(Ru-C/O) [Å]	1.92	1.39	1.43	2.68	3.10	3.07

The silica bilayer induces a reduction of the work-function by 1.32 eV when deposited on the Ru(0001) surface, which is due to polarization (compression) effects. [42,49] The deposition of the SCC results only in a small reduction of the work-function by 0.48 eV with respect to the pristine Ru surface. This is the result of two different effects. The first effect is polarization, i.e. the same effect as for silica but stronger, because the Ru-film distance is much lower for the SCC (d_Z(Ru-C) = 1.4 Å) than for the silica bilayer (d_Z(Ru-O) = 2.7 Å) and thus the pure polarization effect should be quite high. However, the second effect is

working against the first: The second effect is the formation of Ru-C bonds with bond-lengths around 2 Å. These bonds are polar covalent with electron density being transferred from the Ru atoms to the C atoms. The average Bader charge on the top-layer Ru atoms is therefore +0.27 |e|. The carbon atoms exhibit in average a negative Bader charge of -1.72 |e|, clearly showing the carbide character of the lower part of the film. The charge transfer from the Ru surface to the film creates a dipole layer, which leads to an increase of the work-function. Here, the dipole points towards the Ru surface. The overall work-function change, with respect to the pristine Ru(0001) surface, induced by the combined effect is therewith small (-0.48 eV).

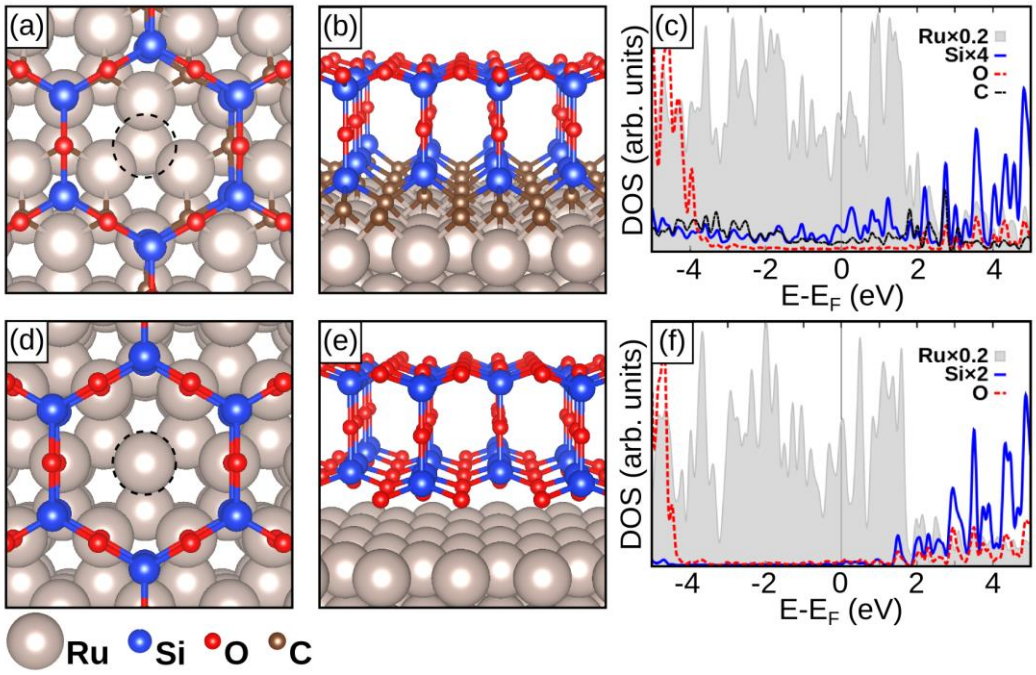

Fig. 36: Structure and DOS of SiC_XO_{2-X} on Ru(0001). (a-c) SCC (X = 3/4): (a) Top view. The center of the hexagon is above a Ru-hcp position, indicated by the dashed circle. (b) Side view. (c) DOS. (d-f) Silica bilayer (X = 0): (d) Top view. The center of the hexagon is above a Ru-top position. (e) Side view. (f) DOS. [317]

A closer inspection of **Fig. 36** and **Table 26**, reveals that the carbon atoms of the SCC film are located in Ru hcp positions and therewith coordinated by three Ru atoms. However, not all C-Ru distances are equal, **Table 26**. Two of the Ru-C distances are shorter than the third, implying that the formation of two C-Ru bonds is favored. This is no surprise, since the sp^3 hybridization imposes a tetragonal bonding symmetry and two bonds are C-Si bonds. The density of states (DOS) curves shown in **Fig. 36** (c) reveal a hybridization of C and Si states. However, a perfect tetragonal symmetry of the $[Si_2CRu_2]$ unit cannot be realized for all C atoms by rotation and/or translation of the film on the Ru(0001) surface. With the location of C atoms above the Ru hcp sites, the best agreement with a tetragonal coordination

for the C atoms can be reached. To verify the atomic structure of the SCC, we compare computed and experimental active IR modes, **Table 27**. We first reproduced computational and experimental data for the silica bilayer to verify the methods used. We find a good agreement of our active IR modes at ν_1 = 1292 and ν_2 = 624 cm^{-1} with the experimental values of ν_1 = 1300 and ν_2 = 696 cm^{-1}. [100] Computationally, we predict a slight red-shift of ν_1 and a blue-shift of ν_2 when going from the silica bilayer to the SCC. Indeed, this trend can also be found for the experimental data. [316]

Table 27: Active IR modes ν [cm^{-1}] of Silicatene/Silicon-Carbide (X=3/4) and Silica bilayer supported on Ru(0001). Computational values are scaled with a scaling factor of λ = 1.0341.

SiC_XO_{2-X}/Ru(0001)		ν_1	ν_2
Silicatene/Silicon-Carbide (X=3/4)	comp.	1289	744
	exp.[a]	1264[a]	802[a]
Silica bilayer (X=0)	comp.	1292	624
	comp.[b]	1296[b]	642[b]
	exp.[b]	1302[b]	692[b]
	exp.[a]	1300[a]	696[a]

[a]Taken from Ref. [316], [b,c]taken from Ref. [100].

8.2.3 Hydrogen adsorption

To explore the chemistry of the silicatene/silicon-carbide/Ru(0001) hybrid system, we investigated the adsorption of H atoms. Again, we compare the silicatene/silicon-carbide (**SCC**) to the silica bilayer. For the silica bilayer, we considered the center-fcc and the center-top position, which are the two most stable orientations. The H adsorption energies and other relevant parameters are summarized in **Table 28**. We adsorbed the H atoms at various positions, including oxygen atoms of the oxygen atoms in the atomic layer which is most far away from the Ru surface, **Fig. 37** (a, d), and on the Ru surface, **Fig. 37** (b, e).Let us first consider the adsorption of H on the topmost O atoms of the thin films. This adsorption position exhibits a positive adsorption energy with respect to the gas-phase H atom in the range of 0.25 eV for the SCC to 0.65 for the silica bilayer in the center-top configuration. With our approach the gas-phase dissociation energy $D_e(H_2)$ is 4.53 eV. Upon adsorption, the H atom transfers the valence electron to the Ru support, forming a surface hydroxyl group (formally $O^{2-}H^{+}$). The charge transfer which can be seen in the positive Bader charge on H, but also by the reduction of the work-function with respect to the H-free systems. For instance the work-function of the SCC is reduced by 1.73 eV with respect to the H-free system. The reduction of the work-function is proportional to d_Z(Ru– H), confirming the dependence of the work-function on the direction and modulus of the surface dipole. In this case, the dipole points away from the surface. For the adsorption of the H atoms on the Ru

surface, there are various possible adsorption sites, e.g. top, bridge, fcc, and hcp. We tested all of these possibilities, but only the most stable ones are summarized in **Table 28**. We find that the H atoms prefer three-fold hollow sites, which is in good agreement with theoretical and experimental studies for pristine Ru(0001), where H prefers the fcc site. [318,319,320] The fcc sites at the interface between the SCC and the Ru surface are not perfectly available for the adsorption of H, because of their vicinity to the C and Si atoms of the thin film.

Table 28: Hydrogen adsorption energies E_{ADS} [eV], work-functions Φ [eV], and work-function changes $\Delta\Phi$ [eV] with respect to the hydrogen-free system, average Bader charges q_{AVG} [|e|], and distance of the H atom from the Ru surface d_Z(Ru-H) [Å].

	Silicatene/Silicon-Carbide		Silica bilayer			
Center-x	hcp		fcc		top	
H position	O	Ru (hcp)	O	Ru (fcc)	O	Ru (fcc)
E_{ADS}(H)	0.24	-2.57	0.36	-2.95	0.65	-2.77
Φ	2.32	4.02	2.33	4.18	2.16	3.56
$\Delta\Phi$	-1.73	-0.02	-1.88	-0.03	-1.24	0.15
q_{AVG}(C)	-1.75	-1.70	---	---	---	---
q_{AVG}(Ru, top)	0.26	0.25	-0.06	-0.02	-0.05	-0.02
q(H)	0.68	-0.14	0.64	-0.24	0.61	-0.22
d_Z(Ru-H)	7.18	1.13	8.44	1.06	8.09	0.88

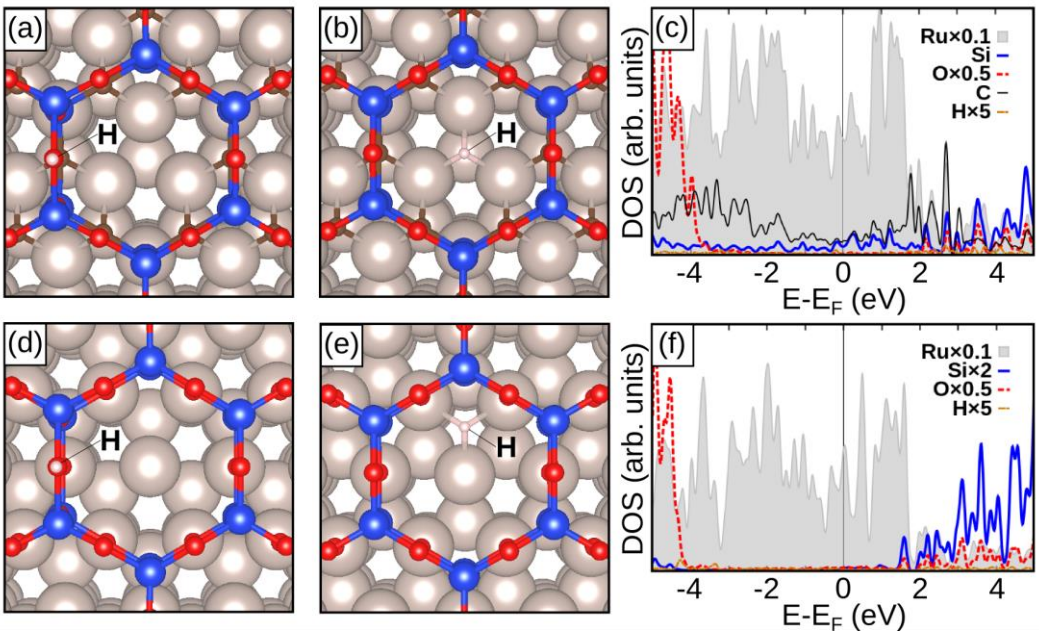

Fig. 37: H adsorption on Ru-supported (a-c) silicatene/silicon-carbide (SCC) and (d-f) silica bilayer. (a) H above the SCC film. (b) H at the interface between SCC and Ru, at a Ru-hcp position. (c) DOS of H on Ru-hcp. (d) H above the silica bilayer. (e) H at the interface between silica bilayer and Ru, at a Ru-fcc position. (f) DOS of H at the Ru-fcc position. [317]

This sterical hindrance destabilizes the adsorption position. Thus, the H atom adsorbs in the Ru hcp site with an adsorption energy of -2.57 eV. The silica bilayer in the center-top configuration is 1.29 Å more far away from the Ru surface than the SCC, leaving enough space for H to adsorb in the fcc site. Here, the adsorption energy is -2.77 eV. In **Fig. 37** (c) the DOS curves of H at the interface between SCC and Ru surface are shown. No significant changes with respect to the H-free system can be observed. The same is true for the silica bilayer. The H atoms at the Ru surface exhibit negative Bader charges of around -0.14 |e| to -0.24 |e|, **Table 28**, indicating hydride character.

8.2.4 Aluminum doping

The substitution of Si by Al is a common extrinsic defect in SiO_2. The Al-dopant introduces a paramagnetic O 2p gap state in the silica DOS (not shown). Boscoboinik et al. investigated the effect of introducing the Al dopant into the Ru-supported silica bilayer. [321] Here, the electron hole is filled via charge transfer from the Ru metal to the gap state. We investigated the substitution of a Si atom by Al in the SCC. There are four chemically distinct Si atoms in the Ru-supported SCC. The top and the bottom atomic Si layers can be distinguished on the one hand, and on the other hand, the Si atoms can be positioned above a Ru fcc or Ru top site. The Al-dopant was always preferred above the Ru fcc site. We report the results only for this possibility, **Table 29** and **Fig. 38**.

Table 29: Relative energy E_{REL} [eV], of the two different Al positions and hydroxyl formation energies E_{FORM}(Al-HO) [eV], work-function Φ [eV], work-function change ΔΦ [eV] with respect to the Al-free and H-free silicatene/silicon-carbide/Ru(0001) system, and (average) Bader charges q (q_{AVG}) [|e|].

	Silicatene/Silicon-Carbide			
	Al at bottom-layer		Al at top-layer	
	Al-O-Si	Al-H-O-Si	Al-O-Si	Al-H-O-Si
E_{REL}	0.00	---	-0.34	---
E_{FORM}(Al-OH)	---	-0.46	---	-1.52
Φ	4.24	3.36	5.63	3.47
ΔΦ	0.20	-0.69	1.59	-0.57
q_{AVG}(C)	-1.67	-1.70	-1.71	-1.71
q_{AVG}(Ru, top)	0.26	0.26	0.27	0.25
q(Al)	2.36	2.32	2.47	2.47

The substitution of Si by Al is energetically more favorable by 0.34 eV in the top layer of the SCC, whereas Boscoboinik et al. found that the substitution of Al in the Si bottom layer is preferred for the silica bilayer. [306,321] The difference is a direct consequence of the different chemical composition of the lower part of the SCC thin film with respect to the

silica bilayer. In both cases, a charge transfer from the Ru support to the Al dopant, or more precisely its atomic neighbors, occurs. The charge transfer is reflected in the work-function change and in the DOS shown in **Fig. 38** (c, f). The work-function is increased with respect to the Al-free SSC by 0.20 eV for Al in the bottom Si layer and 1.59 eV for Al in the top layer. The work-function change is proportional to the charge separation, i.e. it is larger for the more stable position of Al in the top Si layer. The magnetic moment of the doped systems is 0 μ_B, indicating the delocalization of the positive charge in the Ru slab. The DOS shown in **Fig. 38** (c) do not contain any paramagnetic O 2p gap state, confirming the charge transfer. The topmost Ru layer in the SSC is already positively charged with q_{AVG}(Ru, top) around +0.25 |e| for the Al-free system. Therefore the positive additional positive charge introduced by the Al-dopant is delocalized in the middle of the Ru slab.

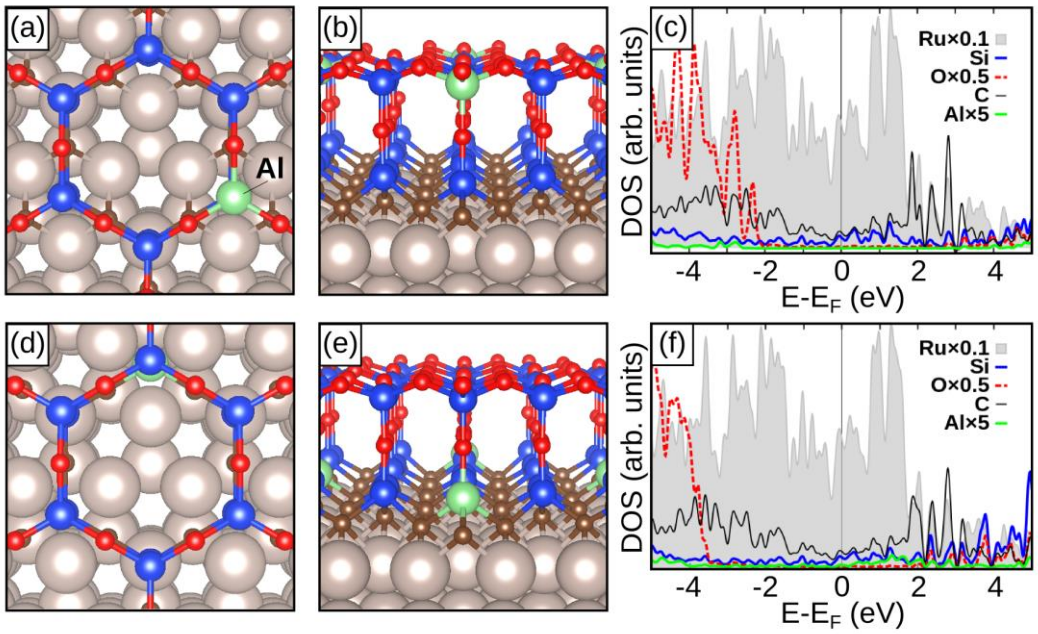

Fig. 38: Structure and DOS of (a-c) silicatene/silicon-carbide (SCC) with an Al-dopant at the top Si-layer. (a) Top view, (b) side view and (c) DOS. (d-f) SCC with an Al-dopant at the bottom Si-layer. (d) Top view, (e) side view and (f) DOS. [317]

The Al-doping in silica is often accompanied by the formation of hydroxyl groups adjacent to the Al dopant. We investigated this aspect for the Al-dopant in the top and bottom layers of the SCC, **Fig. 39**. The hydroxyl group formation energy, E_{FORM}(Al–OH) and other relevant parameters are summarized in **Table 29**. In agreement with the findings of Boscoboinik et al. [306,321], we find that the formation of hydroxyl groups is preferred in the top oxygen layer, **Fig. 39** (b). Here, the hydroxyl group formation energy is enhanced by 1.06 eV with respect to that of the Al-dopant in the bottom layer. This may result from the different geometries imposed on the oxygen atoms of the top and middle layer, cf. **Fig. 39**

(b) and (e). The steric confinement inside the thin-film, forces a Si–O–Si angle of 180°, **Fig. 39** (e), which is different from the perfect geometry for the sp^3 hybridized oxygen atoms. Since the thin film is again chemically saturated when the Al-OH group is formed, no charge transfer from the Ru to the Al-dopant is observed. The work-function is reduced with respect to the H- and Al-free SCC by 0.69 eV for Al-OH in the bottom layer and by 0.57 for Al-OH in the top layer, **Table 29**.

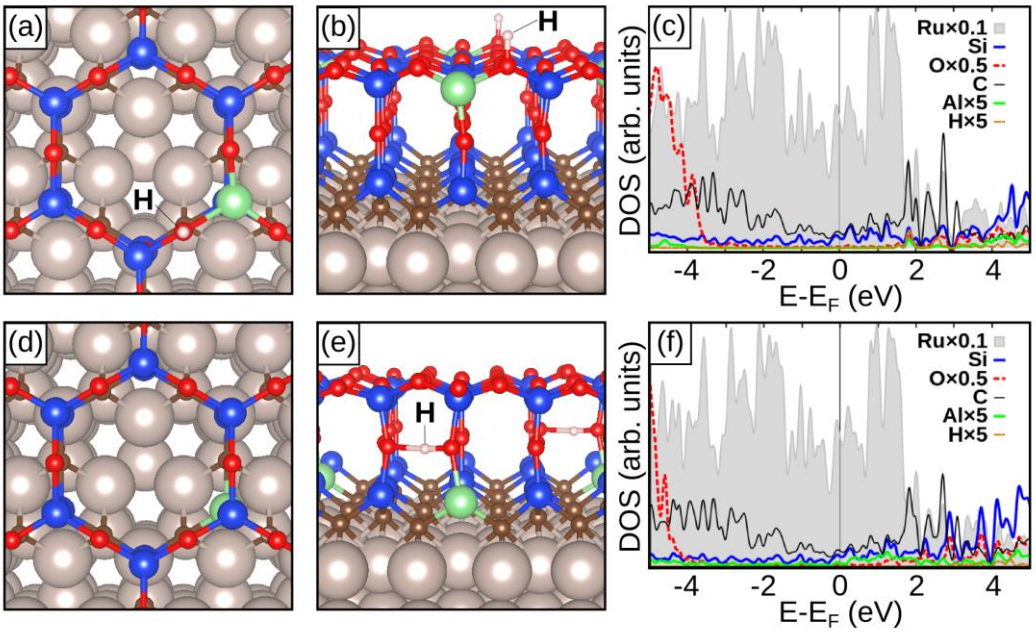

Fig. 39: Structure and DOS of (a-c) silicatene/silicon-carbide (SCC) with an [Al-OH] unit at the top Si-layer. (a) Top view, (b) side view and (c) DOS. (d-f) SCC with an Al-dopant with an [Al-OH] unit at the bottom Si-layer. (d) Top view, (e) side view and (f) DOS. [317]

8.2.5 Section summary

- The silicatene/silicon-carbide supported on Ru(0001) was compared to the Ru(0001)-supported silica bilayer. Whereas the silica bilayer is bond to the Ru surface via dispersion forces (E_{ADH} = -33 meV/Å^2), the silicatene/silicon-carbide chemisorbs on the Ru-surface with an adhesion energy of -510 meV/Å^2. The chemisorption is realized under the formation of polar covalent Ru-C bonds.

- Also the chemistry of the two supported thin-films was compared. H preferably adsorbs at the Ru(0001) surface below the films. Al-doping is more stable in the top Si layer for the silicatene/silicon-carbide, whereas a position of the Al-dopant in the bottom layer is preferred for the silica bilayer. The formation of Al-OH groups is preferred in the top Si layer in both cases, which can be explained with steric effects.

Chapter 9 Reactivity of supported metal clusters

9.1 CO oxidation on Au nanorods supported on TiO_2 anatase (101)[10]

9.1.1 Introduction

CO oxidation is a widely studied model reaction for oxidation reactions and is not least therefore well suited to investigate the working principle of oxidation catalysts. Besides being a model reaction, CO oxidation is a major solution to CO abatement in air depollution treatments. [210] Conventional catalytic converters in cars consist of monoliths covered with Pt-group metals and become active only at larger temperatures of around 300-430°C. [322] Therefore, 50-80% of the unreacted exhaust gases (hydrocarbons, CO and NO_x) are emitted during the first 2-5 minutes of operation, i.e. during the "cold start". Titania-supported gold nanoparticles of a few nanometers show great catalytic activity for CO oxidation even at room temperature and below and are thus interesting to study. [323] However, at the operating temperatures present in conventional catalytic converters, the Au particles sinter which leads to a deactivation of the catalyst. [324] So, these Au-based catalyst are far from being ready for actual applications.

An open question regarding the CO oxidation on Au/TiO_2 is the reaction mechanism. Although many studies have been dedicated to explore the mechanistic aspects, no final consensus has been established. [325,326,327] It is therefore interesting to study the behavior of Au/TiO_2 catalysts under exposure of CO and O_2. Using temporal analysis of products (**TAP**) measurements, D. Widmann and J. Behm recently reported on the capacity of Au/TiO_2 to store oxygen. [328] They found that oxygen can be abstracted from the catalyst via exposure to CO, forming CO_2. This is, however, only possible in the presence of gold, and at moderately elevated temperatures of 80°C. During the CO oxidation process, the formation of Ti^{3+} states was observed via electron spin resonance measurements. [329] The removed oxygen can be refilled by pulsing O_2. The amount of oxygen being abstracted, i.e. the oxygen storage capacity, scales with the mean particle diameter. [330] These findings clearly indicate that CO is being oxidized by the TiO_2 lattice oxygen situated at the Au/TiO_2 interface. The freshly formed CO_2 desorbs from the catalyst leaving behind an oxygen vacancies. The overall process corresponds to the Au-assisted Mars-Van-Krevelen mecha-

[10] The experiments reported in this study were performed by Dr. D. Widmann et al. in the group of Prof. J. Behm. We gratefully acknowledge their valuable contribution.

nism. [331] In this study, we investigated this mechanism in a combined computational and experimental approach. We will however mainly report on the computational part.

9.1.2 Computational details

To model the TiO_2 anatase (101) surface, we used the slab described in section 4.1.2. Depending on the case, we used (2×1), (3×1) and (2×2) surface super cells. A similar computational setup as described in section 6.1.2 was used. We included dispersion forces using the approach suggested by Tosoni and Sauer. [185] To represent the Au nanoparticles, we designed Au ***nanorods*** with periodicity along the (10) direction of the titania (2×1) and (2×2) surface super cells. The (2×1) unit cell has lattice parameters of a_0 = 7.69 Å and b_0 = 10.48 Å. This unit cell was used for a small Au rod (Au_{10}) and the larger (2×2) surface unit cell was used for a larger Au rod (Au_{24}). The lattice parameters of the titania support was kept fixed, resulting in a strain on the gold rods, which is summarized on **Table 30**.

Table 30: Strain of the nanorods consisting of N Au atoms. $a_0(TiO_2)$ [Å] is the TiO_2 lattice parameter in the direction of the rod's periodicity, $a_0(Au_N, gas)$ [Å] is the optimized lattice parameter of the free-standing rod, N is the number of Au atoms.

Surface unit cell	N	$a_0(TiO_2)$	$a_0(Au_N, gas)$	Deviation [%]
(2×1)	10	7.69	7.60	-1.2
(2×2)	24	7.69	7.79	+1.3

Adsorption energies of the Au adsorbates were calculated as defined in eqn. (35), where N = 10 or 24. All components refer to structure optimized systems. The vacancy formation energy is defined in eqn. (19) for the adsorbate-free systems and eqn. (36) for the systems including the Au rods. For the oxidation of CO with oxygen from the TiO_2 lattice, the reaction energy can be calculated as shown in eqn. (37). The adsorption energies as defined in eqn. (35) do not include any entropic terms. However for adsorption and desorption processes, the change in entropy can be important. The Gibbs free energy for the adsorption process is defined as $\Delta G_{ADS} = \Delta H_{ADS} - T(S_{ADS} - S_g)$. To get a rough estimate for the contribution of the entropy for the adsorption Gibbs free energy, we approximate $S_{ADS} \approx 0$, and $\Delta H_{ADS} \approx E_{ADS}$, cf. section 2.2.2. We calculated $T \cdot S_g$ at 298 K and 1 bar for the molecules involved in the reaction, which are 0.61 eV for CO, 0.63 eV for O_2, and 0.66 eV for CO_2.

$$E_{ADS}(Au_N/TiO_2) = E(Au_N/TiO_2) - E(Au_N) - E(TiO_2) \quad (35)$$

$$E_{V_O}(Au_N/TiO_2) = E(V_O/Au_N/TiO_2) - \frac{1}{2}E(O_2) - E(Au_N/TiO_2) \quad (36)$$

$$E_{REA} = E(CO_2) + E(V_O/Au_N/TiO_2) - E(CO) - E(Au_N/TiO_2) \quad (37)$$

CO stretching frequencies were calculated with the harmonic approximation. Harmonic force constants were calculated using the central finite difference method with 0.02 Å displacements in every Cartesian direction. The CO atoms and the Au atom directly connected to the CO molecule were allowed to move. No imaginary frequencies were obtained. The CO stretching frequencies were scaled by a scaling parameter. Scaled frequencies are calculated as shown in eqn. (5), where $\nu(CO_g) = 2126\ cm^{-1}$ and $\nu^{EXP}(CO_g) = 2143\ cm^{-1}$.

$$\nu^{SC} = \nu(CO)\nu^{EXP}(CO_g)/\nu(CO_g) \quad (38)$$

To determine the transition state for the oxygen removal we used the climbing-image nudged elastic band (CI-NEB) method. [122] In the CI-NEB calculations, the images were optimized to obtain the minimum energy path (MEP) until forces on ions were smaller than |0.05| eV/Å. We did not include any zero-point energy corrections, because they are assumed to be small with respect to the uncertainty introduced using the rod model. Atomic charges have been estimated with the Bader decomposition scheme. [332]

9.1.3 CO oxidation with TiO_2 lattice oxygen

The first step in the catalytic cycle for CO oxidation on Au/TiO_2 via the (Au-assisted) Mars-van Krevelen mechanism is the adsorption of CO. We investigated the adsorption of CO on the supported Au_{10} ***nanorod*** (Au_{10}/TiO_2 and Au_{10}/TiO_{2-X}) at different positions. We found, that CO preferably adsorbs on the gold rod on a Au-top position. The most stable adsorption positions are summarized in **Table 31** and shown in **Fig. 40**. The best adsorption positions exhibit an orientation of the CO molecule perpendicular to the surface, on top of the Au rod, **Fig. 40** (a, d). CO adsorbs on Au_{10}/TiO_2 with intermediate adsorption energies of -0.8 to -0.9 eV, **Table 31**. The interaction of the molecule with the gold rod leads to an enlargement of the C-O bond from 1.13 Å in the gas-phase to values around 1.15 Å upon adsorption. This leads to a red-shift in C-O stretching frequencies of around 60-70 cm^{-1} with respect to the gas-phase molecule. The presence of a surface oxygen vacancy in contact with the rod does not seem to have any effect on the CO adsorption properties. Note, that these systems have only one vacancy per unit cell, representing a low surface concentration of oxygen vacancies.

As we can see in **Fig. 40** (d-f), the gold rod interacts with the oxygen vacancies with one gold atom positioned inside the vacancy. The interaction is accompanied by the transfer of one electron from the vacancy to the rod. The Bader charge of the entire rod $q_{SUM}(Au_{10})$ is around -0.6 |e| in all three cases, respectively, **Table 31**. A large part of the charge is located on the Au atom which refills the vacancy, as we can see from its Bader charge $q(Au/V_O)$ of around -0.5 |e|.

Table 31: CO adsorption energies E_{ADS}(CO) [eV], CO bond distances d(CO) [Å], Au-C bond distances d(AuC), scaled computed CO stretching frequencies ν^{SC}(CO) [cm^{-1}], frequency shift with respect to the gas-phase CO molecule $\Delta\nu$, experimental frequencies ν^{EXP} (provided by Prof. J. Behm), Bader charges on the gold rod q_{SUM} [|e|], and Bader charges on the Au atom closest to the vacancy (q(Au/V_O)) [|e|].

Fig. 40	E_{ADS}(CO)	d(CO)	d(Au-C)	ν^{SC}(CO)	$\Delta\nu$(CO)	ν^{EXP}(CO)	q_{SUM}(Au)	q(Au/V_O)
(a)	-0.93	1.153	1.940	2081	-62	2110	+0.12	---
(b)	-0.86	1.153	1.957	2076	-66		+0.13	---
(c)	-0.80	1.154	1.930	2062	-80		+0.08	---
(d)	-1.09	1.153	1.925	2079	-63	2070	-0.59	-0.48
(e)	-1.02	1.153	1.951	2067	-76		-0.63	-0.48
(f)	-0.95	1.154	1.944	2080	-63		-0.60	-0.49

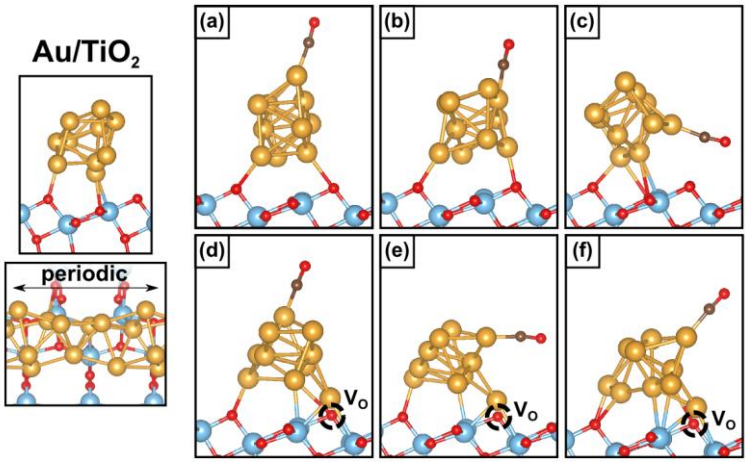

Fig. 40: CO adsorption on a gold-***nanorod*** supported on (a-c) stoichiometric and (d-f) reduced titania anatase (101). Different positions of the CO molecule were considered.

The second step is the abstraction of a titania lattice oxygen atom by the CO molecule, forming CO_2 and an oxygen vacancy. To investigate this process, we first scanned the stability of oxygen vacancies at different positions with respect to the rods, including positions at the Au/TiO_2 interface and under the gold rods. The results are summarized in **Table 32** and shown in **Fig. 41**. The adsorption energy of the gold rod is enhanced by more than 1 eV in the most cases when going from the stoichiometric surface to the reduced surface. Is the rod in close interaction with the vacancy, a charge transfer from the vacancy to the rod occurs which is reflected in the negative Bader charges on the rod. Is the rod too far away from the vacancy, the charge transfer is inhibited and the adsorption energy approaches that

of the rod on the stoichiometric surface. The interaction of the rod with an oxygen vacancy leads to a stabilization of the oxygen vacancies. This is reflected in the oxygen vacancy formation energies which, in the case of intimate Au-V_O interaction, are reduced by up to 2.2 eV with respect to the gold-free surface, **Table 32**. This effect is strongly attenuated as the rod is more far away from the vacancy. Importantly, the observed trends do not change significantly when going from the Au_{10} rod to the bigger Au_{24} rod, showing the insensitivity of the results towards the rod size in this size regime.

Table 32: Adsorption energy of Au_N rods on TiO_2 $E_{ADS}(Au_N)$ [eV], Bader charges on the gold rods $q(Au_N)$ [|e|], oxygen vacancy formation energies at the Au/TiO_2 interface $E_{Vo}(Au_N/TiO_2)$ [eV] and on the Au-free surface $E_{Vo}(TiO_2)$. The reduction of the oxygen vacancy formation energy induced by the presence of the gold rod is given by ΔE_{Vo} = $E_{Vo}(Au_N/TiO_2)$ - $E_{Vo}(TiO_2)$. E_{REA} [eV] is the reaction energy for CO oxidation with the specified lattice oxygen.

Unit cell	N	V_O	$E_{ADS}(Au_N)$	$q(Au_N)$	$E_{Vo}(Au_N/TiO_2)$	$E_{Vo}(TiO_2)$	ΔE_{Vo}	E_{REA}
(2×1)	10	---	-1.67	+0.05	---	---	---	---
		1 - a	-2.99	-0.67	3.29	4.62	-1.32	0.03
		1 - b	-2.90	-0.59	3.38	4.62	-1.23	0.12
		1 - c	-2.89	-0.75	3.40	4.62	-1.22	0.13
		2 - a	-3.89	-0.76	3.67	5.89	-2.22	0.41
		3 - a	-1.88	0.00	5.36	5.57	-0.21	2.10
		3 - b	-1.81	+0.03	5.43	5.57	-0.14	2.17
(2×2)	24	---	-0.69	+0.09	---	---	---	---
		1 - a	-2.44	-0.76	2.82	4.58	-1.75	-0.44
		1 - b	-1.59	-0.24	3.68	4.58	-0.90	0.42
		1 - c	-1.14	-0.34	4.12	4.58	-0.45	0.86
		1 - d	-0.69	-0.09	4.58	4.58	0.00	1.31

The stabilization of oxygen vacancies probably facilitates their formation, e.g. via abstraction by CO. The reaction energies for CO oxidation via abstraction of lattice oxygen (O_{latt}) are also listed in **Table 32**. The process is highly endothermic (+1.4 eV) on the gold-free surface and becomes roughly thermo-neutral when the vacancy is at the Au/TiO_2 perimeter. In the case of Au_{24}, the oxidation of CO under the formation of vacancy V_O1 – a is an exothermic process (by -0.44 eV). The formed vacancy is, however, located under the rod, i.e. not directly accessible by CO. Note that the oxygen vacancy formation energies and the CO oxidation energies reported in **Table 32** may be affected by strain release of the Au rods.

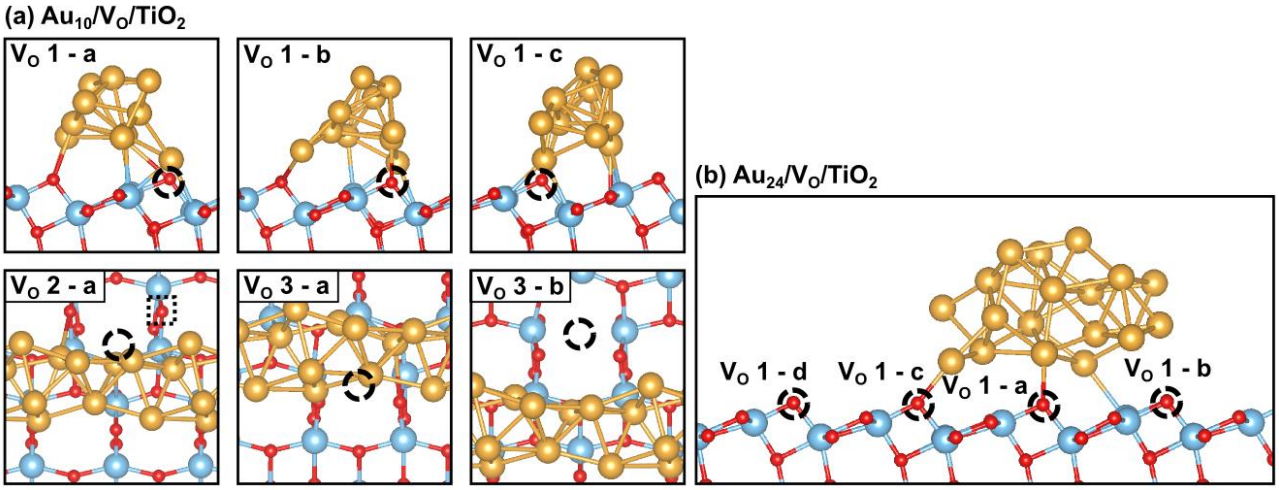

Fig. 41: Adsorption of the Au rod on titania anatase (101) with oxygen vacancies at different positions. (a) Au_{10}/TiO_{2-X}, and (b) Au_{24}/TiO_{2-X}. There are three different types of oxygen vacancies (V_O1-3) and each of them can take different positions with respect to the rod, e.g. (V_O3 a and b). For Au_{24}/TiO_{2-X}, only vacancies of type 1 were investigated. These are all shown for the rod on the stoichiometric surface in (b), but investigated separately.

We have seen that CO oxidation involving the lattice oxygen of the titania surface is roughly thermo-neutral for oxygen atoms located at the Au/TiO_2 perimeter. However, we have not yet discussed the mechanism for oxygen abstraction. To investigate the mechanism, we considered in more detail the formation of oxygen vacancy V_O1 – a at the Au_{10}/TiO_2 perimeter, **Fig. 41** (a). The mechanism is shown in **Fig. 42**.

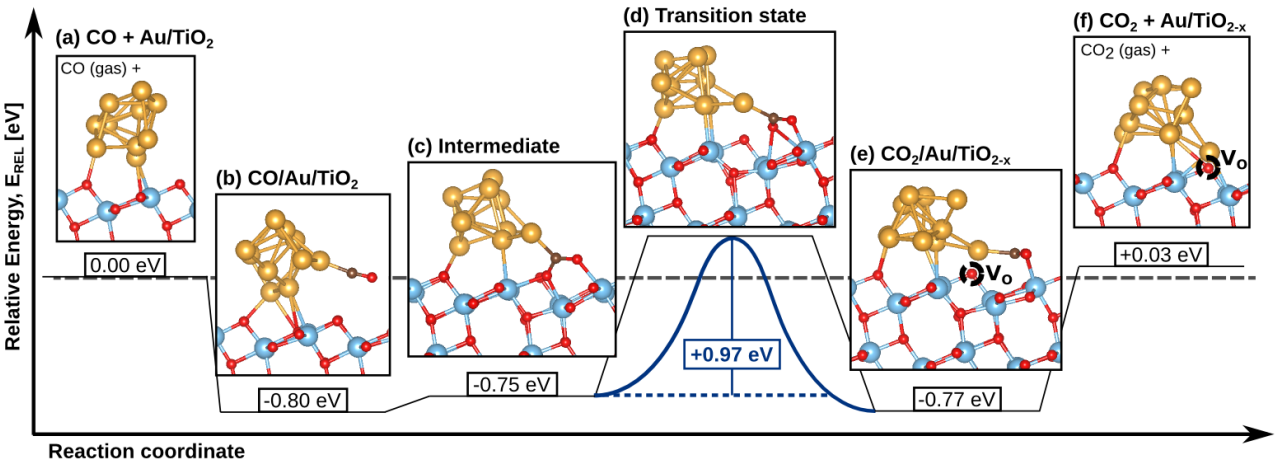

Fig. 42: CO oxidation on a gold nanorod supported on TiO_2 anatase (101). Relative energies are given with respect to the reactants shown in (a). (b-c) The CO molecule adsorbs and approaches the gold-titania interface. (c-e) CO abstracts a lattice oxygen and a gold atom refills the oxygen vacancy. This process has an activation barrier of 0.97 eV. (f) The desorption of the CO_2 molecule is endothermic by 0.8 eV.

First, the CO molecule is adsorbed on the gold rod, **Fig. 42** (a-b) and approaches the surface, **Fig. 42** (c). Then, the oxygen atom is removed while the freshly formed vacancy is refilled with an Au atom from the rod in a concerted movement, **Fig. 42** (c-e). This process shows an activation barrier of 0.97 eV. So, the CO oxidation step is an activated process, which is in good agreement with the experimental findings. Finally, the formed CO_2 desorbs.

9.1.4 Reoxidation of the catalyst

The second step in the Au-assisted Mars-van-Krevelen mechanism is the reoxidation of the catalyst. The temporal analysis of products (**TAP**) experiments performed by D. Widmann et al. show that the reoxidation of the Au/TiO_{2-x} catalyst readily precedes also at lower temperatures, indicating the absence of a barrier for the catalyst reoxidation.[11] We computationally investigated the interaction of O_2 with the reduced form of the catalyst, i.e. with oxygen vacancies present at the Au/TiO_2 perimeter. The fact that two vacancies are necessary to consume the O_2 molecule introduces an additional degree of freedom for our computations, namely the relative position of these two vacancies. Clearly, the relative position of oxygen vacancies at the Au/TiO_2 perimeter is dependent on the oxygen vacancy concentration. To tackle the complexity, we distinguish the two extreme cases of very low vacancy concentration and very high vacancy concentration. The first case can be represented by a single vacancy and the second case can be represented by two adjacent vacancies. We investigated the reoxidation of a single vacancy at different positions, employing both rod models as shown in **Fig. 43** (a.1-2) and (b.1-2). We also considered one case with two adjacent vacancies, **Fig. 43** (a.3).

Let us consider first the low vacancy concentration limit, in which we address the interaction of one oxygen vacancy with the O_2 molecule. We investigated in more detail the reoxidation of the vacancy V_O1 – a under the small rod, **Fig. 43** (a.1). This is the vacancy formed by the oxygen abstraction process discussed before, see **Fig. 42**. The detailed mechanism for the refilling process of this vacancy is shown in **Fig. 44**. The oxygen molecule adsorbs close to the vacancy with an adsorption energy of -1.90 eV. Then, the oxygen molecule dissociates with an activation barrier of only 0.16 eV. The dissociation process is exothermic by -1.53 eV. In a last step, one oxygen atom refills the vacancy, which is as well exothermic by -1.66 eV and exhibits an activation barrier of 0.94 eV. The second oxygen atom stays at the Au/TiO_2 perimeter as an oxygen adatom (O_{ad}).

[11] The experiments reported in this study were performed by Dr. D. Widmann et al. in the group of Prof. J. Behm. We gratefully acknowledge their valuable contribution.

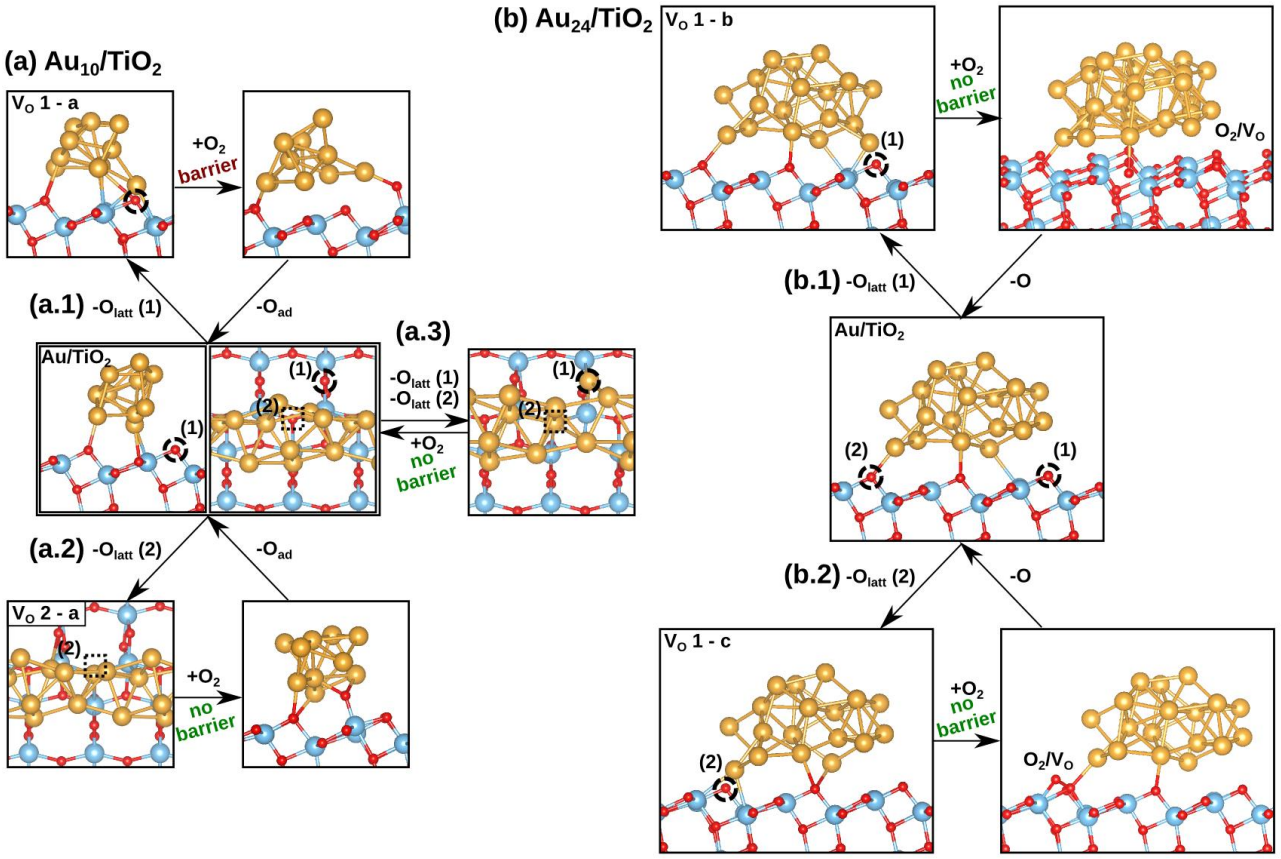

Fig. 43: Reoxidation of Au_N/TiO_{2-x} by O_2. (a) Reoxidation of Au_{10}/TiO_{2-x}. (a.1-2) Single vacancy reoxidation, (a.3) reoxidation of two adjacent vacancies. (b) Reoxidation of Au_{24}/TiO_{2-x}. (b.1-2) Single vacancy reoxidation.

We also investigated the abstraction of this oxygen adatom O_{ad} by a second CO molecule. Upon adsorption of the CO molecule on the Au atom closest to the O_{ad}, we observed the detachment of this Au atom from the rod, so that a O_{ad}-Au-CO species was formed. The latter species is shown in the overall reaction scheme for the low vacancy concentration regime in **Fig. 45** (7). The corresponding CO adsorption energy is quite large with -1.12 eV.

The abstraction of O_{ad} by the CO molecule, forming CO_2, with the Au atom moving back to the Au rod is exothermic by 0.89 eV. We tried to calculate the activation energy for this process, but the CI-NEB calculation became frozen. We calculated the CO stretching frequency of the O_{ad}-Au-CO species, whilst allowing to move the complete Ti-O_{ad}-Au-CO unit. The stretching frequency may be compared to experimental data later. The resulting scaled CO stretching frequency is $\nu^{SC}(CO) = 2120\ cm^{-1}$, being only slightly red-shifted with respect to the CO gas-phase molecule ($2143\ cm^{-1}$). The last step is the desorption of the CO_2 molecule, which is endothermic by 0.54 eV, **Fig. 45** (8).

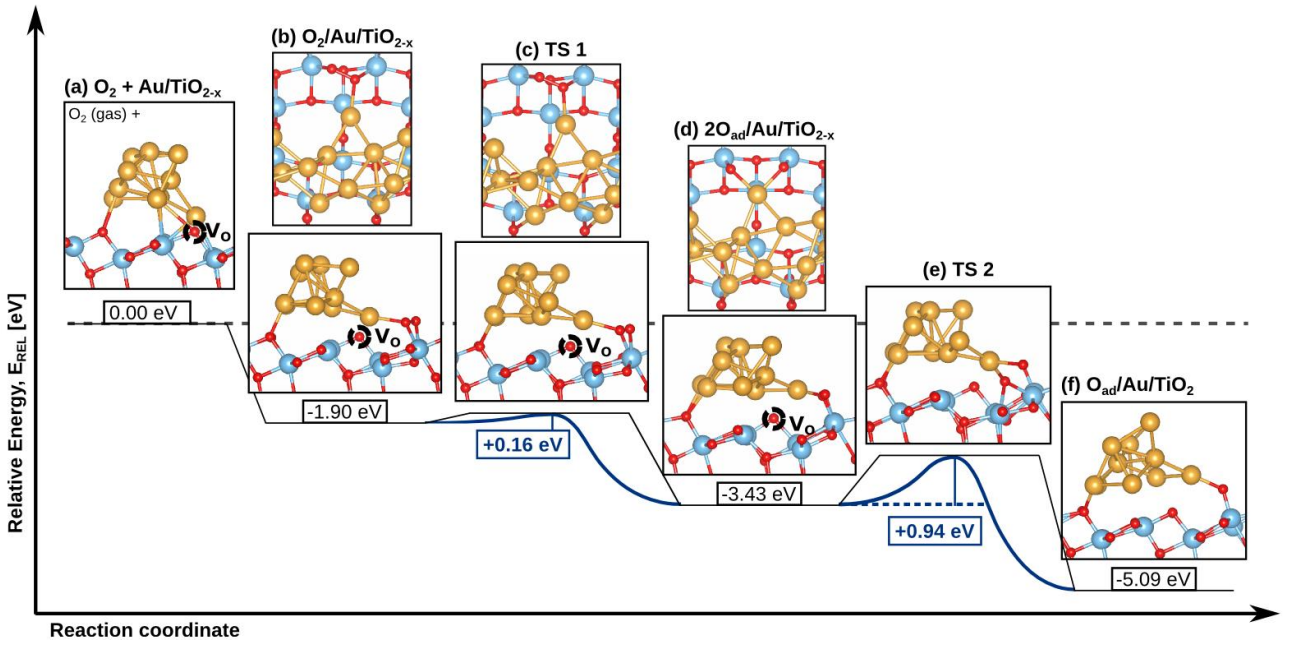

Fig. 44: Reoxidation of V_O1 – a at the Au_{10}/TiO_2 perimeter. Energies are given with respect to the reactants shown in (a). (b) O_2 adsorbs molecularly close to the vacancy. (b-d) The O_2 molecule dissociates with an activation barrier of 0.16 eV. (d-f) One of the oxygen atoms refills the vacancy. This process shows an activation barrier of 0.94 eV.

As mentioned before, the reoxidation process of V_O1 – a under the small rod exhibits an activation barrier of 0.94 eV. In other cases, where the vacancy is not in such close interaction with the gold rod, the reoxidation occurs easier. For instance, the replenishment of vacancy V_O2 – a by O_2, which is shown in **Fig. 43** (a.2). Upon positioning the O_2 molecule, with the gas-phase O-O bond length, in vicinity of the vacancy, the O_2 molecule spontaneously dissociates, leaving behind an oxygen adatom. Still at the low vacancy concentration limit, we also investigated the reoxidation of vacancies located at the perimeter between the titania surface and the big rod, **Fig. 43** (b.1-2). Here, the Au atoms interacting with the vacancy are located more distant from the vacancy. This leaves more space for the incoming O_2 molecule to access the vacancy. In fact, both of the vacancies are refilled spontaneously by the undissociated O_2 molecule, which is what also happens on the Au-free surface. [333]

As a last case, we investigated the reoxidation of two adjacent vacancies, namely V_O1 – a and V_O2 – a, at the perimeter of the small rod, **Fig. 43** (a.3). The formation energy of V_O2 – a at the Au_{10}/TiO_2 interface when vacancy V_O1 – a is already present is 4.20 eV, i.e. still 1.7 eV less than on the Au-free surface. Is the oxygen molecule brought in vicinity to the two vacancies, the oxygen molecule is spontaneously dissociated and refills both vacancies. The refilling process is exothermic by 7.4 eV. Thus, in this case, we observe the barrierless stoichiometric reoxidation of the catalyst, which is in great agreement with the experimental findings. The energy freed during the reoxidation process may contribute to activate the ox-

idation processes under reaction conditions. The resulting complete catalytic cycle for the high vacancy coverage regime is shown in **Fig. 46**. First, CO is oxidized via abstraction of titania lattice oxygen. This process exhibits a barrier of 0.8 eV. Then, a second CO abstracts another titania lattice oxygen. Note that we did not investigate this process in more detail. The reduced catalyst, **Fig. 46** point (4) now contains two adjacent vacancies. In the last phase, the vacancies are refilled by one oxygen molecule, which is a barrierless process.

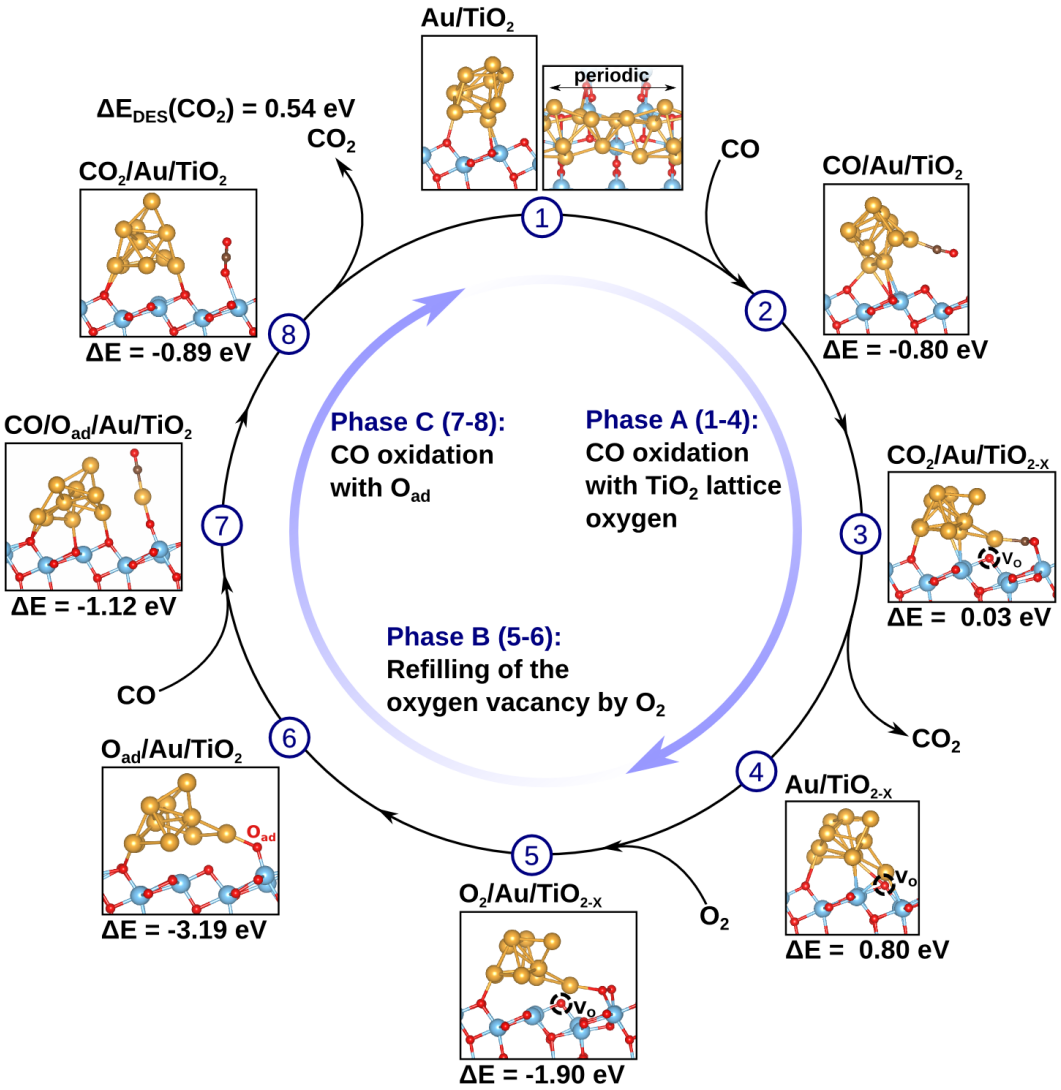

Fig. 45: Complete catalytic cycle for CO oxidation via the Mars-van Krevelen mechanism in the limit of low vacancy concentration. In the first phase **A**, titania lattice oxygen is abstracted by CO, effectively reducing the catalyst. Then in phase **B**, the oxygen vacancy is refilled by O_2 leaving an oxygen adatom. In the third phase **C**, the oxygen adatom is removed by CO.

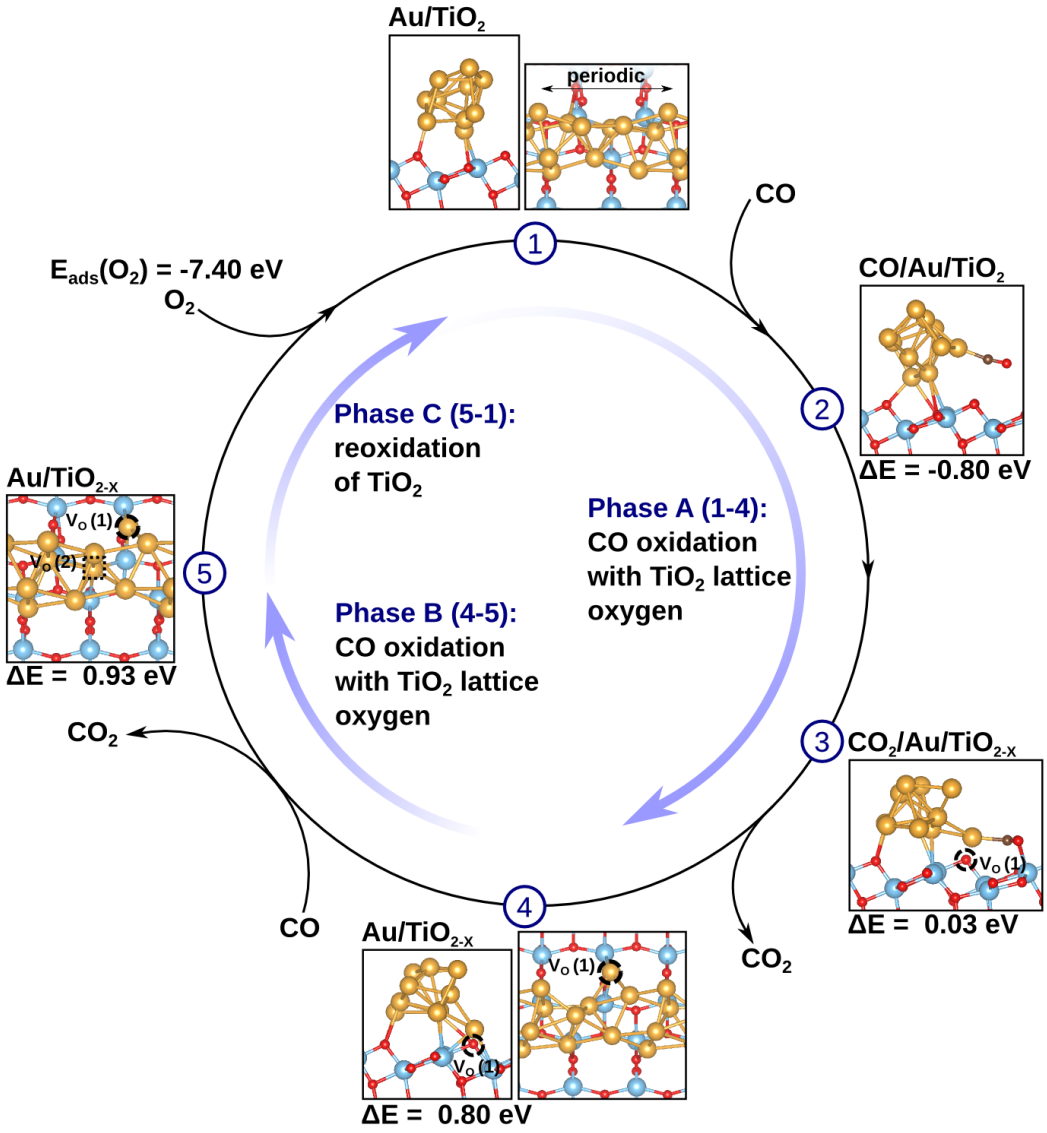

Fig. 46: Complete catalytic cycle for CO oxidation via the Mars-van Krevelen mechanism in the limit of high vacancy concentration. The first phase **A** is equal to that of the low vacancy concentration regime. Here the CO is oxidized with a titania lattice oxygen. Then, in the second phase **B**, more oxygen is abstracted from the surface. The second vacancy is formed in analogy to phase A. In the third phase **C**, the two adjacent vacancies are spontaneously refilled with an oxygen molecule from the gas-phase in a barrierless process.

9.1.5 Section summary

- Mechanistic aspects of the CO oxidation reaction on Au/TiO_2 were investigated. In particular it was determined whether the Au-assisted Mars-van Krevelen mechanism is viable at moderately elevated temperatures. The Au/TiO_2 catalyst was represented by a periodic gold rod supported on TiO_2 anatase (101).

- CO adsorbs on the Au rod and from there approaches the titania surface, where it abstracts an oxygen atom with an activation barrier of 1.0 eV. The reoxidation process may occur via various pathways, depending on the vacancy concentration. At a large vacancy surface concentration, the reoxidation of the catalyst by O_2 can occur as barrierless process.

9.2 CO_2 activation and hydrogenation on Ru_{10}/TiO_2 and Cu_{10}/TiO_2

9.2.1 Introduction

Power-to-gas processes constitute promising solutions for the storage of off-peak excess electricity arising from renewable energy sources. [334] The synthesis of methane and methanol from electrochemically generated hydrogen and CO and/or CO_2 is greatly advantageous compared to the direct storage of hydrogen. This is due to the larger volumetric energy density [335] and easier storage and transport of methane and methanol with respect to hydrogen. Methane is synthetic natural gas (SNG) and can be fed directly into the existing natural gas grid, so that the available energy transport infrastructure is utilized. [334] Methanol serves as fuel for internal combustion engines and it is an important base chemical, for instance for the production of formaldehyde. CO_2 on the other hand is a greenhouse gas and thus the possibility of capturing and recycling CO_2 from the atmosphere has strong environmental implications. The formation of methane and methanol, respectively, from CO_2 and hydrogen is exothermic. However, catalysts are necessary in both cases to overcome the large kinetic energy barriers present in the hydrogenation reactions.

Conventional catalysts for the methanation of CO_2, also denoted as Sabatier reaction, are based on Ni particles supported on non-reducible oxides, such as Al_2O_3, SiO_2, CaO and MgO. [336] Ni-based catalysts are reported to undergo large morphological changes under reaction conditions and deactivation of the catalyst normally occurs via sintering, formation of Ni sub-carbonyls, and carbon deposits. [336,337] More stable and more active catalysts are based on Ru nanoparticles supported on TiO_2. [336,338,339] For example, Garbarino et al. compared the catalytic activity for CO_2 methanation of Ru/Al_2O_3 with that of Ni/Al_2O_3 and found the Ru-based catalyst to be significantly more active. [340] Also the selectivity towards the formation of methane is high. Abe et al. reported a 100% yield of CH_4 at 160°C on 0.8 wt.% 2.5 nm Ru particles supported on TiO_2. [341] Although the methanation of CO_2 on Ru/TiO_2 has been studied extensively in past, no final consensus on the reaction mechanism has been established. [340,341,342,343] The main discrepancy lies in the question whether CO_2 is directly dissociated to CO* and O* (*= adsorbed on the catalysts), or if H* is added to the CO_2* prior to its dissociation (formate intermediate). Similar debates are carried on the methanation of CO. [343]

For the synthesis of methanol from CO_2 and H_2, $Cu/ZnO/Al_2O_3$ catalysts are most commonly used. Also here, the reaction mechanism as well as the active site(s) are subject to debate; although experiments indicate that methanol synthesis from CO_2 proceed via a formate intermediate under reaction conditions. [344,345] Bando et al. compared the catalytic activity of 5 wt.% Cu nano-particles supported on TiO_2, Al_2O_3 and SiO_2 and found the Cu/TiO_2 catalyst to perform best. [346] With in-situ FT-IR measurements, they showed that CO_2 does not bind to the Cu cluster and that formate is formed as a reaction intermediate. [346]

Given the great importance of Ru and Cu clusters in CO_2 hydrogenation reactions, we investigated the reactivity in terms of CO_2 hydrogenation of Ru_{10} and Cu_{10} clusters supported on titania anatase (101). The role of support effects, such as the support reduction, as well as CO_2 and H_2 co-adsorption effects are explored.

9.2.2 Computational details

The same computational setup as in the previous section was used. A (3×1) TiO_2 anatase (101) surface super cell was used and structure optimizations were performed at the Γ-point. Cu (3d 4s) and Ru (4d 5s) states were treated explicitly. In the CI-NEB calculations, images were optimized until forces on ions were smaller than |0.05| eV/Å.

9.2.3 Support effects on the activation of CO_2 on Ru_{10}/TiO_2

For the hydrogenation of CO_2 on Ru/TiO_2, two main mechanisms are discussed in the literature. [343] The first mechanism involves the direct dissociation of the CO_2 molecule. The second mechanism involves the addition of hydrogen to the CO_2 molecule giving a formate intermediate. In this section, we address the adsorption and the direct dissociation of CO_2 on a Ru_{10} cluster supported on the titania anatase (101) surface. We will explore how the cluster relaxation and the reduction of the titania support affect the adsorption and dissociation process. The cluster-support interaction in Ru/TiO_2 and the adsorption of H_2 on Ru/TiO_2 were investigated by Chen et al. in two extensive studies. [347,348] For our Ru_{10} cluster, we find an adsorption energy of -7.62 eV which is in good agreement with their finding of -6.94 eV, given the fact that we included vdW-forces. Also the geometry and the charge state of the cluster are well reproduced, as discussed in more detail later.

Role of the cluster relaxation on the CO_2 dissociation

In computational approaches, the catalyst must be simplified in order to make the system computationally describable. Care has to be taken in the choice of the model, because it must contain the catalyst features which define the catalyst functioning. Structural properties of the metal particle, support effects and the role of (co-)adsorbates obviously rank among those features. Another interesting parameter in this regard is the fluxionality of the

metal particle. As we have seen in the previous section, the structural relaxation of the metal particle (rod) can determine the reaction path and thus has to be considered with care. It is however common practice to fix a major part of the model to make the calculation of the minimum energy path (MEP) computationally cheaper. In order to learn about such relaxation effects on the MEP and on the activation barrier, we tested the effect of the Ru_{10} metal particle relaxation on the CO_2 dissociation.

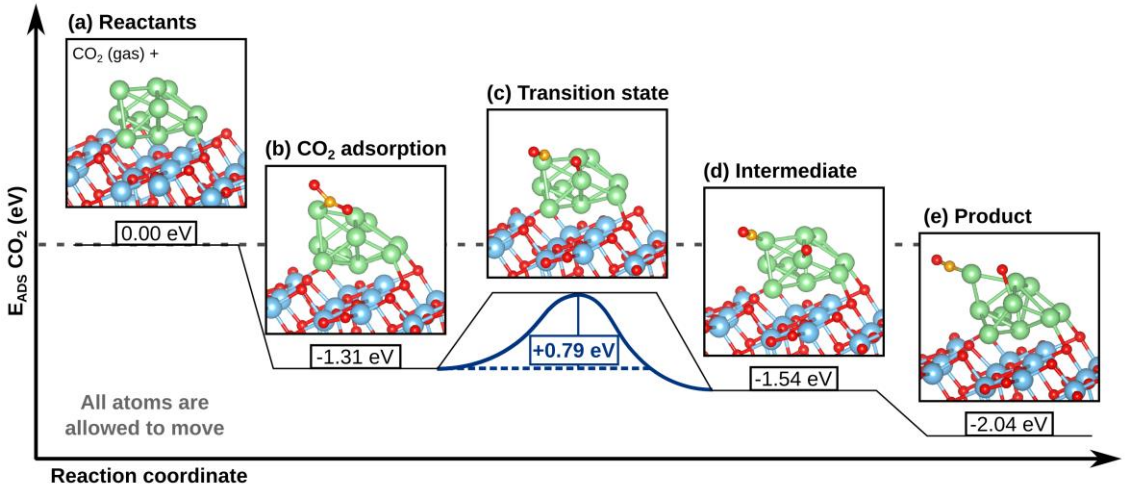

Fig. 47: Mechanism for CO_2 dissociation on Ru_{10}/TiO_2 (dissociative mechanism). All atoms are allowed to move. (a-b) CO_2 adsorbs with an adsorption energy of -1.31 eV, then (b-c) it dissociates with an activation barrier of +0.79 eV to give intermediate (d). (d-e) The CO and O components rearrange on the cluster to give the final product (e). The overall dissociation process going from (b) to (e) is exothermic by 0.73 eV.

The reaction mechanism for CO_2 adsorption and dissociation on Ru_{10}/TiO_2 is shown in **Fig. 47**. We explored various positions for CO_2 to adsorb on the Ru cluster. The best is on top of the cluster on a Ru-Ru bridge site, **Fig. 47** (b). Here the CO_2 adsorbs with an adsorption energy of -1.31 eV. The OCO angle shows very nicely the activation of the CO_2 molecule. The CO_2 molecule can now dissociate **Fig. 47** (b-d), giving an intermediate (d). The dissociation process is slightly exothermic and exhibits an activation barrier of around 0.8 eV. A rearrangement of the CO and O components gives the final product, **Fig. 47** (e). The dissociative adsorption is exothermic by -2.04 eV.

Let us now consider the reaction mechanism found when the cluster is fixed, **Fig. 48**. We start with the geometry of CO_2 already adsorbed on the cluster to concentrate on the effect of the cluster relaxation on the dissociation process. Clearly, the cluster relaxation may as well contribute to the adsorption energy of the CO_2 molecule. The adsorption position of CO_2 adsorbing on the fixed cluster was investigated by Akamaru et al. and is the same as ours. [349] Let us now consider the CO_2 dissociation on the fixed Ru cluster, **Fig. 48** (b-d).

We do not observe the formation of any intermediate stabilized by the cluster relaxation. Instead, the dissociation results directly in a product, which is similar to that of **Fig. 47** (e). However, the product in **Fig. 48** (d) is 0.43 eV higher in energy than that of **Fig. 47** (e). In summary, the reaction pathways shown in **Fig. 47** and **Fig. 48** differ by an intermediate and the stability of the product. The height of the activation barrier is, however, similar (0.79 and 0.72 eV, respectively). We conclude that in order to obtain precise insights on the reaction pathway, it is useful to relax also the cluster (and the support, if involved). To obtain a rough idea on the barrier, it may be sufficient to fix the cluster, but the validity of this approximation should be confirmed from case to case.

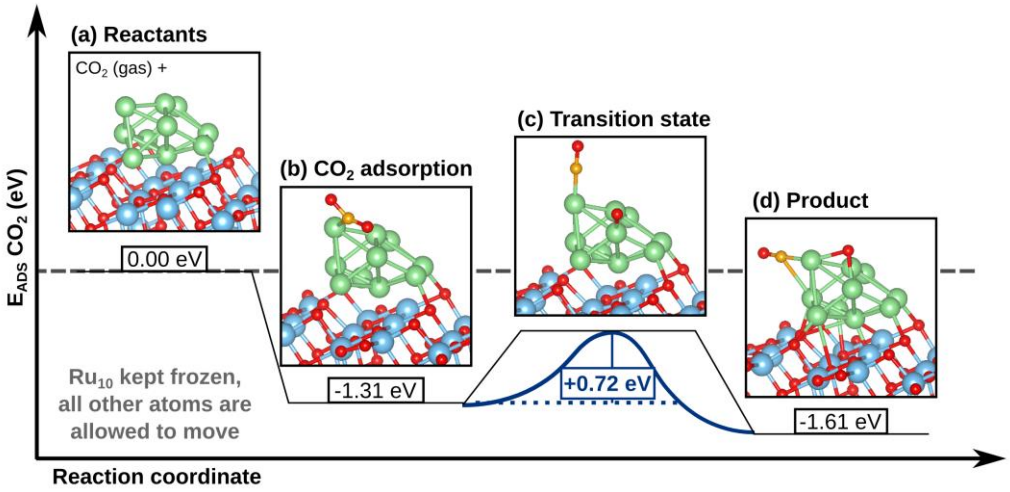

Fig. 48: Mechanism for CO_2 dissociation on Ru_{10}/TiO_2 (dissociative mechanism). The Ru cluster is kept frozen during the dissociation process. The dissociation now exhibits an activation barrier of 0.72 eV and is exothermic by 0.30 eV.

Role of support reduction

Titania is a reducible oxide and thus clusters of electropositive metals can transfer electrons to the titania support upon adsorption. Chen et al. have computationally investigated the interaction between the Ru_{10} cluster and the TiO_2 anatase (101) surface in detail. [347] They found interfacial chemical bonding between the Ru cluster and the support. In accordance with their findings, we observe a positive net Bader charge on the Ru cluster of $q(Ru_{10}) = +1.53$ |e|. A reduction of the support can attenuate the net charge transfer from the cluster to the Ru/TiO_2 interface and therewith indirectly contribute electron density available on the cluster for CO_2 activation. We investigated the effect of the oxide reduction on the CO_2 adsorption and dissociation by introducing a surface oxygen vacancy or adsorbing hydrogen atoms on the titania surface, **Fig. 49**. By introducing an oxygen vacancy, **Fig. 49** (a-c), the charge on the cluster becomes significantly reduced to $q(Ru_{10}) = +0.67$ |e|. The best adsorption position of CO_2 is now close to the vacancy, **Fig. 49** (a). Here, a dissociation of the CO_2

molecule leads to the refilling of the vacancy. However, we are interested in the dissociation of the CO_2 to give CO and O adsorbed on the cluster. Therefore, we consider the second-best adsorption position shown in **Fig. 49** (b). The adsorption energy is reduced in modulus by 0.5 eV with respect to Ru_{10} on the stoichiometric titania surface. This is due to the fact that the cluster shape is different in the two cases, affecting the Ru-Ru bridge site length, cf. **Fig. 49** (b) and **Fig. 47** (b). The structure and the adsorption energy of the final product after CO_2 dissociation, **Fig. 49** (c), are only slightly affected by the presence of the vacancy.

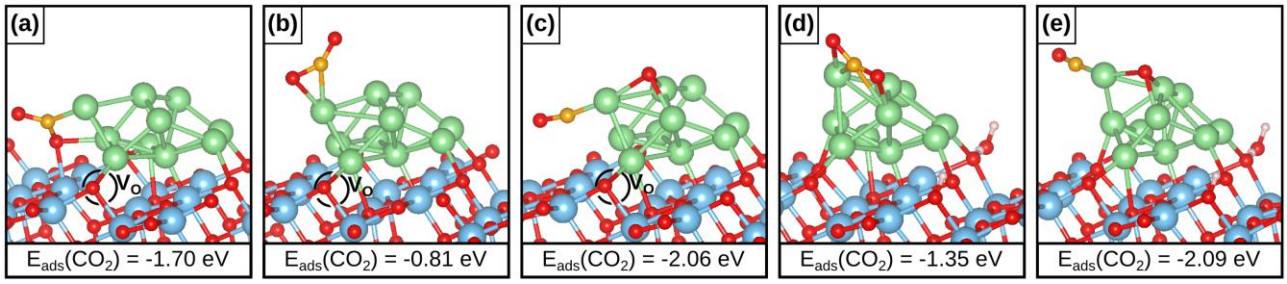

Fig. 49: CO_2 adsorption and dissociation on Ru_{10} supported on reduced TiO_2 anatase (101). (a-c) CO_2/Ru_{10} supported on TiO_2 with a surface oxygen vacancy. (d-e) CO_2/Ru_{10} supported on 2H adsorbed on TiO_2.

We have seen that the surface oxygen vacancy at the cluster/support interface constitutes a new reactive center, modifying the chemistry of the catalyst. A different way to reduce the titania support is to adsorb hydrogen atoms on the titania surface. We find that the dissociative adsorption of a H_2 molecule giving two atomic hydrogen atoms adsorbed on the titania substrate is exothermic by 0.4 eV. The value is in fair agreement with the findings of Islam et al. [350] who investigated the adsorption of hydrogen on the Ru-free titania substrate. The adsorbed hydrogen atoms transfer their valence electrons to the titania conduction band minimum, formally forming two hydroxyl groups and two Ti^{3+} centers. Although the titania substrate is now reduced, the positive net charge on the cluster is still quite large with $q(Ru_{10})$ = +1.30 |e|. The resulting adsorption and dissociation of the CO_2 molecule are therefore very similar to that of CO_2 on Ru_{10} supported on the stoichiometric titania surface, cf. **Fig. 49** (d, e) and **Fig. 47** (b, e). So, a reduction of the TiO_2 does not significantly affect the adsorption and dissociation behavior of CO_2 on the Ru cluster.

9.2.4 CO_2 and H_2 co-adsorption and reaction on Ru_{10}/TiO_2

Effect of H_2 co-adsorption on the direct CO_2 dissociation

H_2 preferably adsorbs on the Ru cluster instead of the titania substrate. [348] In the former case, the H_2 molecule spontaneously dissociates on top of the cluster with an adsorption energy of -1.32 eV, **Fig. 50** (a). This is our new reference to calculate the adsorption energy of the CO_2 molecule. We investigated various different adsorption positions also for the hy-

drogen atoms, with and without CO_2 being co-adsorbed. The best combination is shown in **Fig. 50** (b). In the presence of H atoms, the adsorption energy of CO_2 is enhanced by 0.1 eV with respect to the H-free cluster. Given the different adsorption position with respect to the H-free case, the dissociation process is significantly affected by the presence of the H atoms **Fig. 50** (b-d). The activation barrier for the dissociation process is now +1.39 eV, i.e. 0.6 eV larger than on the H-free cluster. We observe the formation of a new intermediate, **Fig. 50** (d), in which the O atom is situated on a Ru top position. A rearrangement of CO and O gives a similar structure, as the final dissociation product in the H-free case, **Fig. 50** (e). The presence of the H atoms destabilizes this configuration. Rearranging the H atoms gives the final product **Fig. 50** (f). All in all, the co-adsorption of two hydrogen atoms obstructs the adsorption and dissociation of the CO_2 molecule. The CO_2 dissociation position imposed by the presence of hydrogen results in a larger activation barrier implying that the dissociation is structure-sensitive on Ru_{10}/TiO_2. [137]

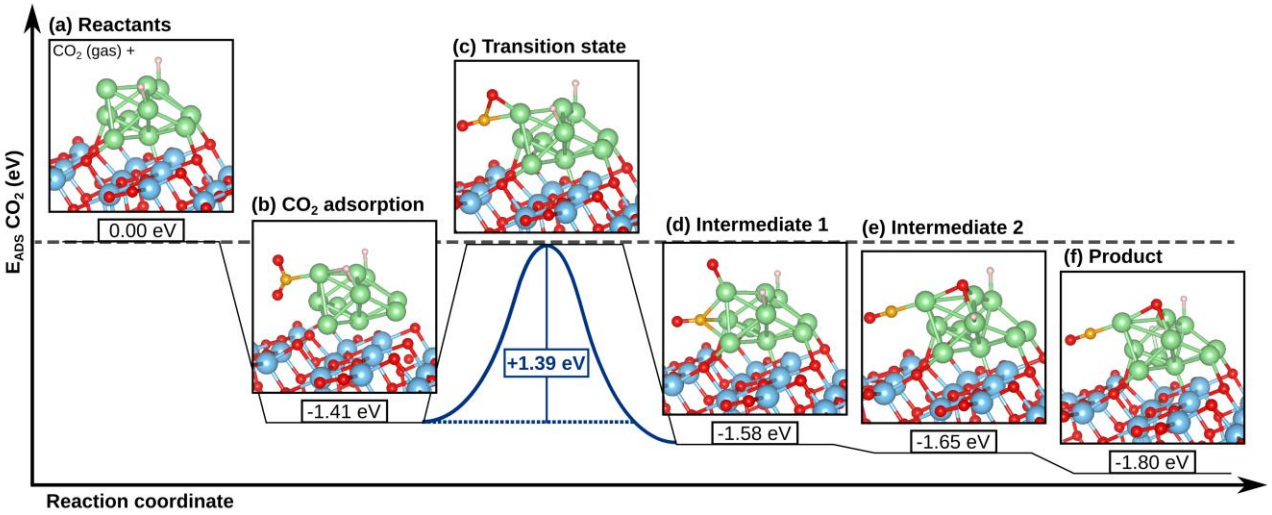

Fig. 50: Mechanism for CO_2 dissociation on $2H/Ru_{10}/TiO_2$ (dissociative mechanism). All atoms are allowed to move. (a-b) The CO_2 adsorption on $2H/Ru_{10}/TiO_2$ is exothermic by 1.41 eV. (b-d) The CO_2 dissociation process is exothermic by 0.17 eV and exhibits an activation barrier of 1.39 eV. (d-e) The CO and O components rearrange on the cluster. (f) Final product: The presence of the dissociated CO_2 molecules makes other adsorption positions of the H atoms more favorable. The addition of a H atom on the atomic oxygen in (f) results in $E_{ADS}(CO_2)$ = -2.09 eV.

We also investigated the adsorption of CO_2 on the Ru cluster covered with 30 H atoms. In fact, is has been shown that a Ru particle can adsorb up to 3 H atoms per Ru atom. In this case, there are a couple of possible positions for chemisorption available for the CO_2 molecule. In the best case, CO_2 is adsorbed and activated at the interface with an adsorption energy of around -0.9 eV which is 0.4 eV smaller in modulus than on the H-free Ru cluster. In

all other cases, the CO_2 stays linear and binds only via physisorption to the hydrogen covered cluster. We can thus conclude that the co-adsorption of hydrogen is disadvantageous for the activation and the direct dissociation of the CO_2 molecule on the Ru cluster.

H-addition to CO_2

In an alternative mechanism, the co-adsorbed molecules can interact by addition of a hydrogen atom to the CO_2 molecule. The H atom can be added either to one of the oxygen atoms (COOH) or to the carbon atom (HCOO). For the addition of the H atom, its bonding with the Ru cluster has to be broken. We assume that H transfer is facilitated when the CO_2 molecule is in close vicinity to the H atom. We therefore rearrange the best configuration of 2 H and CO_2 co-adsorbed on the cluster, **Fig. 51** (b), to give an intermediate **Fig. 51** (c).

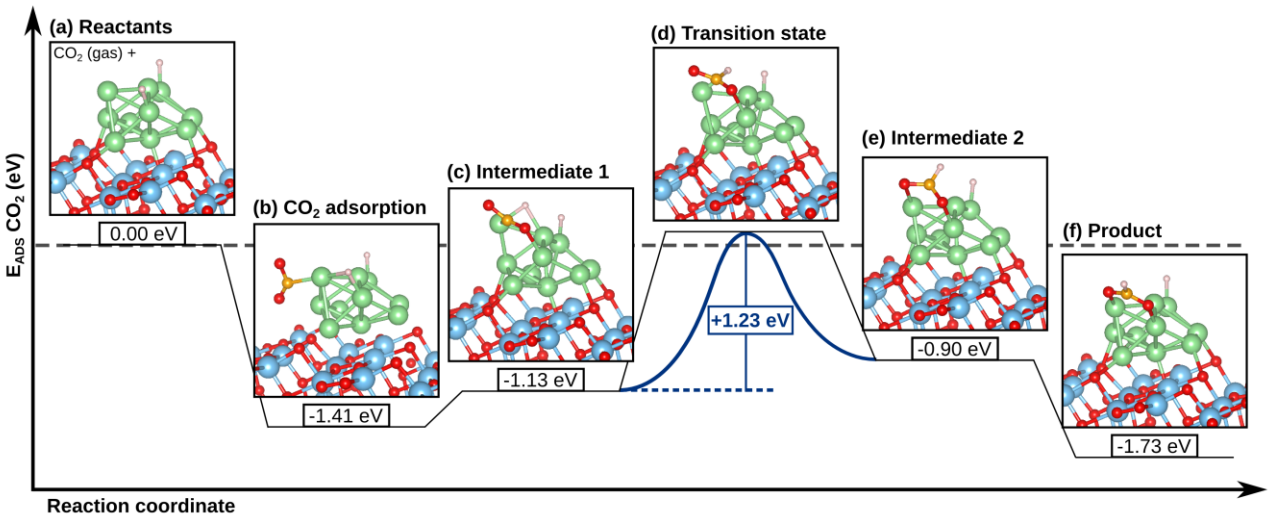

Fig. 51: Mechanism for H-addition to CO_2 (formate formation). (a-b) CO_2 adsorbs on $2H/Ru_{10}/TiO_2$ with an adsorption energy of -1.41 eV. (b-c) The CO_2 and H components rearrange to make the H-addition possible. (c-e) The H atom is added to the CO_2, which is endothermic by 0.23 eV and exhibits an activation barrier of +1.23 eV. (e-f) The formate molecule rearranges to give the final product. The addition of the second H atom on an oxygen atom of [HCOO] in (f) results in E_{ADS} (CO_2) = -0.21 eV.

We can now add the H atom to either the closest O atom (COOH), or to the C atom (HCOO). We tried both cases and found that the addition of H to O results in a less stable isomer than the addition of H to C. More precisely, the formation of COOH on Ru_{10}/TiO_2 is 0.95 eV less stable than the formation of HCOO. Thus, we investigated in more detail the second reaction pathway, **Fig. 51**. Starting from **Fig. 51** (c), the hydrogen is added to the CO_2 molecule, which undergoes a rotational movement to give a bi-dentate chelate-like coordination of the formate ion on the cluster, **Fig. 51** (c-e). The addition process exhibits an activation barrier of +1.23 eV. Further rotation gives then the final product, **Fig. 51** (f).

9.2.5 Support effects on the activation of CO_2 on Cu_{10}/TiO_2

As supported Ru particles, supported Cu particles are active for CO_2 hydrogenation. The two metals exhibit different product selectivity, the main product for Ru-based catalysts being methane, whereas Cu-based catalysts are usually designed to yield mainly methanol. Obviously, this implies a different reaction mechanism based on the different reactivity of the supported clusters. In the following, we will explore the effect of the support on the reactivity of the Cu cluster, always comparing the findings to that found for the Ru cluster.

Role of support reduction

In order to understand the interaction of the Cu_{10}/TiO_2 system with hydrogen and CO_2, we shortly investigate the cluster-support interaction. Here, all atoms were allowed to relax, because, as we have seen in the previous section, the cluster relaxation contributes to stabilize certain intermediates. The results are summarized in **Table 33** and **Fig. 52**.

Table 33: Adsorption energies E_{ADS} [eV], and Bader charges q [|e|] of Cu_{10} deposited on stoichiometric, reduced, and Nb-doped TiO_2 (101).

Surface	**Fig. 52**	$E_{ADS}(Cu_{10})$	$q(Cu_{10})$
TiO_2	(a)	-3.63	+1.60
$\mathbf{V_O}$**,** *surf.*	(b)	-4.09	+0.72
$\mathbf{V_O}$**,** *surf.*	(c)	-4.06	+1.04
4 **Nb**, *sub.*	---	-3.74	+1.60

The Cu cluster was first adsorbed on stoichiometric titania. The respective geometry is shown in **Fig. 52** (a). The adsorption energy of the Cu cluster is -3.63 eV, which is roughly half as large as that of the Ru cluster. The Cu cluster transfers two electrons to the support. This charge transfer is reflected in the Bader charge on the cluster of +1.60 |e|, and in the DOS shown in **Fig. 52** (d). In the latter, two occupied Ti 3d states are detected below the Fermi level. The valence electrons of the Cu cluster are not sufficient to form a continuous metal band, **Fig. 52** (d). This is however the case for the supported Ru cluster (compare the DOS in ref. [347]). As both, Ru and Cu clusters are positively charged the difference in adsorption energy may be due to a difference in the ionization potential.

As extensively treated in the previous chapters, the presence of defects on the oxide surface can determine the chemistry of supported clusters and we therefore explored the effect of vacancies on the adsorption mode of the Cu cluster. Two vacancy positions were considered, shown in **Fig. 52** (b) and (c). It turns out that position (b) is slightly more stable than position (c), but the energy difference is so small (0.03 eV) that both positions are of interest. In both cases, the Bader charge on the cluster is reduced significantly, and also the DOS reveal new occupied Cu states compared to the cluster supported on the stoichiometric tita-

nia surface, cf. **Fig. 52** (d) and (e). We tested various spin multiplicities, but the singlet solutions in **Fig. 52** (d) and (e) were the most stable ones. This indicates that the cluster becomes neutral when interacting directly with the vacancy.

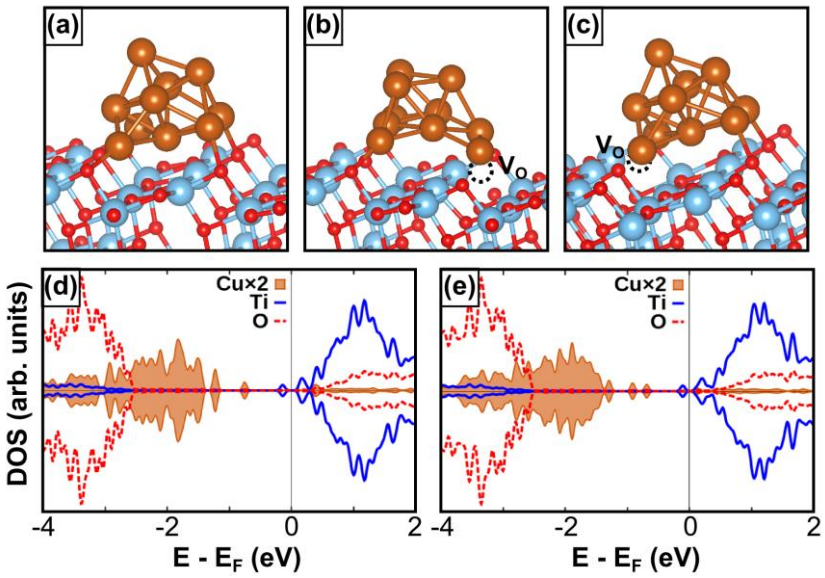

Fig. 52: Adsorption of the Cu_{10} cluster on (a) stoichiometric TiO_2 anatase (101), (b) reduced TiO_2 with an oxygen vacancy (V_O) at position 1 and, (c) at position 2. (d) DOS of Cu_{10} on stoichiometric TiO_2, (e) DOS of Cu_{10} on reduced TiO_2 with V_O at position 1.

As shown in chapter 6, Nb-dopants have a similar effect on the electronic structure of the titania support. So, we investigated the adsorption of the cluster on a titania anatase (101) surface with 4 Nb dopants present in the subsurface. Two Nb atoms were positioned in the subsurface position shown in **Fig. 11** (a), the residual two Nb atoms in the atomic Ti layer just above. Compared to the cluster on the stoichiometric surface, the Nb dopants have no effect on the adsorption mode of the Cu cluster, see **Table 33**.

9.2.6 CO_2 and H_2 co-adsorption and reaction on Cu_{10}/TiO_2

Adsorption of H_2 and CO_2 on Cu_{10}/TiO_2

In the previous section, we have seen that CO_2 is readily adsorbed and activated on Ru_{10} clusters supported on titania. On the H-free Ru cluster, the CO_2 molecule dissociates with a barrier of around 0.8 eV. This is different for the Cu_{10}/TiO_2 system, as we will see in the following. We explored the effects of the support reduction and hydrogen co-adsorption on the adsorption mode of CO_2 on Cu_{10}/TiO_2. The results are summarized in **Table 34** and **Fig. 53**. For each case, we explored many different adsorption positions and geometries. Only the most stable structures are reported. Let us consider first the adsorption of the CO_2 molecule on the Cu cluster supported on the stoichiometric titania surface. The largest adsorption

energy for the stoichiometric surface was found to be -0.66 eV, which is quite small. The molecule is bent with the C atom being coordinated to the Cu cluster and one O atom being coordinated to a 5c-Ti atom, **Fig. 53** (a).

Table 34: Adsorption energies E_{ADS} [eV], and Bader charges q [|e|] of Cu_{10} deposited on stoichiometric, reduced, and Nb-doped TiO_2 (101).

Surface	**Fig. 53**	$E_{ADS}(CO_2)$	$n(H_2)$	$E_{ADS}(nH_2/n)$	$q(Cu_{10})$ [|e|]
TiO_2	(a)	-0.66	0	---	+1.71
$\mathbf{V_O}$**,** *surf.*	(b)	-1.06	0	---	+1.43
TiO_2	(c)	---	1	-1.20	+2.27
$\mathbf{V_O}$, *surf.*	(d)	---	1	-1.32	+1.45
TiO_2	(e)	---	3	-1.12	+3.40
TiO_2	(f)	---	5	-0.40	+4.25
4 **Nb**, *sub.*	---	---	5	-0.40	+4.23
TiO_2	(g)	-0.40	1	-0.94	+2.32
TiO_2	(h)	-0.43	3	-1.04	+3.41

We investigated the adsorption of CO_2 on the systems with the vacancies at both positions reported before. The most stable case is the one shown in **Fig. 53** (b). Here, the CO_2 adsorption energy is -1.06 eV, i.e. significantly larger than at the interface between the Cu cluster and the stoichiometric titania surface, although the structures are similar. The Bader charge on the cluster is slightly reduced with respect to the stoichiometric surface. The additional electron density available on the cluster seems to have a positive effect on the CO_2 activation. The magnetic moment in this case is roughly 2 μB and so the spin-density iso-surface at 10^{-5} |e/Å^3| is shown in **Fig. 53** (b). One electron is positioned below the clusters and the other one is delocalized. We therefore assume that the enhanced adsorption energy is mainly due to more electron density available in the Cu cluster to bind to the C atom. The CO_2 can reoxidize the vacancy under CO formation, which releases 1.11 eV with respect to the structure shown in **Fig. 53** (b). Let us now explore the adsorption of hydrogen on the Cu cluster. We find that H_2 readily chemisorbs on the cluster, whereby the H atoms prefer Cu-Cu bridge adsorption sites on the cluster at low coverage, cf. **Fig. 53** (c-e). Three H_2 molecules can be adsorbed until the subsequent chemisorption of another H_2 molecule becomes endothermic. The average adsorption energy is however still negative up to larger coverages and we therefore also considered the adsorption of 5 hydrogen molecules to explore one extreme case, as it may occur at high hydrogen pressure, **Fig. 53** (f). The Bader charge on the Cu cluster increases steadily as the number of H atoms on the cluster is increased. This indicates that the Cu-H bonds have hydride character. In the DOS (not shown), we detect a hybridization of the H 1s states with the Cu valence states. In the case of 5 adsorbed H_2 molecules, the Bader charge on the cluster reaches +4.25 |e|. The Cu cluster is therewith highly

oxidized. Still, the cluster transfers two electrons to the support, as for the H-free case. We wanted to test whether this quite large charge on the Cu cluster may be enough to draw electrons from a reduced version of the support. Therefore, we tested the adsorption of $5H_2/Cu_{10}$ onto the Nb-doped support described above. The presence of excess electrons had, however, no influence on the charge state of the cluster, **Table 34**.

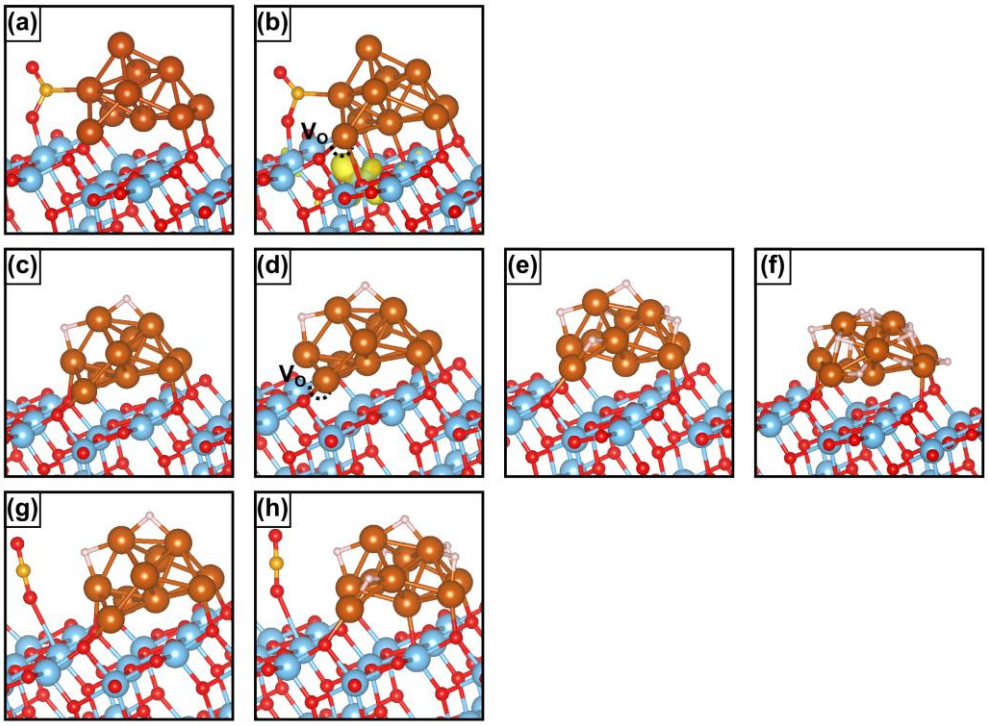

Fig. 53: Adsorption of (a-b) CO_2, (c-f) H_2, and (g-h) CO_2 and H_2 on Cu_{10}/TiO_2. (a) CO_2 on Cu_{10}/TiO_2, (b) CO_2 on $Cu_{10}/V_O/TiO_2$, (c) H_2 on Cu_{10}/TiO_2, (d) H_2 on $Cu_{10}/V_O/TiO_2$, (e) $3H_2$ on Cu_{10}/TiO_2, (f) $5H_2$ on Cu_{10}/TiO_2, (g) CO_2 and H_2 on Cu_{10}/TiO_2, and (g) CO_2 and $3H_2$ on Cu_{10}/TiO_2.

The adsorption of reactants can have a large effect on the catalyst and therefore significantly influence the adsorption of other molecules. In the case of Ru, we revealed a competing effect between H_2 and CO_2 adsorption. H_2 and CO_2 have similar adsorption energies on the Ru cluster and compete for adsorption positions. No synergy or improved CO_2 activation in the presence of H atoms on the Ru cluster was found. A similar picture is found for the Cu cluster. We tried many different adsorption positions and geometries, and we only found physisorbed CO_2 as soon as H atoms are present on the Cu cluster, **Fig. 53** (g-h). The Cu cluster seems to become inactive for the CO_2 activation. We therefore assume that the H atom is added to the CO_2 molecule coming from the gas-phase. This mechanism would be in agreement with the findings of Liu et al. [351] who investigated methanol synthesis on Cu_4/Al_2O_3, and with the findings of Studt et al. [344] who examined the synthesis on stepped Cu surfaces. Further mechanistic studies from our site are ongoing.

9.2.7 Section summary

- CO_2 activation and the first steps in hydrogenation on Cu_{10} and Ru_{10} clusters supported on TiO_2 anatase (101) were investigated.
- On the Ru cluster, CO_2 is readily adsorbed and activated. On the H-free cluster, the direct CO_2 dissociation proceeds with a barrier of 0.8 eV. At higher H-coverage, H-association is preferred because the best active sites for the CO_2 dissociation are blocked by H atoms. Instead, a H atom is added to the CO_2 under formation of a HCOO species with a barrier of 1.2 eV.
- Only weak adsorption modes of the CO_2 molecule on Cu_{10}/TiO_2 were found. Hydrogen, on the other hand readily adsorbs on the Cu cluster. Therefore, the only viable pathway for CO_2 hydrogenation on Cu_{10}/TiO_2 found in this study is an Eley-Rideal like mechanism where a hydrogen atom bound to the Cu cluster is added to the CO_2 molecule coming from the gas-phase.

Chapter 10 Conclusions

10.1 Take home messages

In this thesis, we investigated various aspects of heterogeneous catalysts based on metal clusters and oxide ultra-thin films. In a first study, we checked the quality of our computational approach by determining the role of van-der-Waals dispersion forces on the interaction between small Ag and Au clusters and the TiO_2 anatase (101) surface. We found that dispersion forces play an important role to determine the structure and the adsorption energy of the supported clusters. The DFT-D2' method was found to provide a good compromise between computational cost and accuracy. Therefore subsequent studies were based on this method.

The adsorption mode of small Au clusters supported on TiO_2 rutile (110) was investigated in a combined computational and experimental approach. The DFT results were used to assist the experimental characterization process. We found that the geometry, the charge state and the adsorption strength of the clusters depends on the specific adsorption site. Whereby Au dimers always adsorb neutrally, the charge state of the trimers depends on the adsorption site. On oxygen vacancies, the Au trimer becomes negatively charged and forms a chain isomer. On the stoichiometric surface, the trimer transfers an electron to the support and assumes a triangular shape.

In a third study, we investigated the melting temperature of free-standing Pt and Au nanoparticles using molecular dynamics. We found a linear dependence of the melting temperature on the particle diameter. The choice of the inter-atomic potential and the initial particle shape (Wulff-construction or round) affect the melting temperature of the particles in a significant way. The particles melt first at the surface forming a liquid shell which expands to the core of the particle until the particle is completely molten. The melting temperature of Pt nanoparticles supported on SiN was also investigated via transmission electron microscopy. The melting point of 3.4 nm particles was found to be in the range of the simulated values. As the smaller Au particles melt already at relatively moderate temperatures (e.g. ~290 K for 1.94 nm), it might be that for some reactions the particles are molten under reaction conditions. The melting temperatures of the nanoparticles should, however, be experimentally confirmed. The experiments are still ongoing.

In a series of DFT studies on the role of the support for the chemistry of transition metal atoms and clusters, we explored the effects of intrinsic and extrinsic defects on the adsorption mode and the nucleation behavior. It turns out that the charge state of small Ag and Au clusters can be tuned by doping the TiO_2 anatase (101) support. Nitrogen dopants introduce a positive charge on the clusters and niobium doping, as well as the presence of oxygen vacancies, can introduce a negative charge on the supported clusters. Thus, the introduction of dopants and defects can be used to anchor small Ag and Au clusters and tune their charge state. For instance, the negatively charged clusters could be used to activate electrophiles like CO_2.

On a different support, namely SiO_2 quartz (001), the adsorption and nucleation behavior of late transition metal atoms and clusters is also highly dependent on the presence of defects. The non-bridging oxygen defect can act as nucleation site, providing a strong binding site where the atoms can adsorb and dimerize. Another method to combat sintering is to modify the clusters. The adsorption of small AuTi bimetallic clusters supported on SiO_2 quartz (001) was analyzed to determine whether the presence of Ti atoms in Au clusters can help to increase the clusters binding strength to the support. Indeed, already one Ti atom can increase the adsorption energy and lead to strong metal-support interaction. Ti-containing clusters can react with the silica support via H_2 formation, H- and O-overspill, depending on the surface composition. These results imply that the sintering problem of supported Au clusters could be resolved by adding (even relatively small amounts of) Ti. However, the catalytic activity, e.g. for CO oxidation, of the bimetallic clusters may deviate from that of the pure Au clusters and further investigations in this direction should be interesting.

Not only metal clusters in the nanometer and sub-nanometer size regime are interesting catalyst, but also the nano-structuring of oxides plays an important role in heterogeneous catalysis. This aspect was addressed in two case studies in which the chemistry of silicon-based oxide ultra-thin films was explored via DFT. The adsorption of CO on the silica bilayer supported on Ru(0001) was examined. We found that CO is able to intercalate below the silica bilayer, adsorbing on the Ru metal underneath. The adsorption mode of the CO molecules thereby strongly depends on the coverage. Our results show that the diffusion of CO through the six member silica rings exhibits only a minor barrier of roughly 0.5 eV. The penetration of larger molecules through these rings should be inhibited, showing the potential functioning of the perfect crystalline Ru-supported silica bilayer as molecular sieve.

In a second study on ultra-thin films, we considered the properties of a novel two-dimensional material recently discovered by Yang et al. [316] The new ultra-thin film consist of a monolayer of corner sharing $[SiO_4]$-tetrahedra on top of a $[Si_2C_3]$ monolayer supported on Ru(0001), and is therefore called “silicatene/silicon-carbide”. Although being

structurally similar to the silica bilayer, the silicatene/silicon-carbide exhibits chemically quite different properties, ranging from the different adsorption mode on the Ru support to the preferred sites of Al dopants. This ultra-thin film may be interesting for metal/oxide/semiconductor systems.

In the last part, we explored mechanistic aspects of reactions catalyzed by supported metal clusters via DFT. We inspected the oxidation of CO on Au nanorods supported on TiO_2 anatase (101). We find that the CO can be oxidized via abstraction of TiO_2 lattice oxygen in the presence of Au, effectively reducing the catalyst. For this mechanism, we compute an activation barrier of around 1.0 eV. We furthermore establish that the reoxidation of the catalyst can occur barrierless at larger vacancy concentrations. So, the CO oxidation mechanism may be temperature dependent, as the Au-assisted Mars-van Krevelen mechanism is a viable reaction pathway at higher temperatures. This is in accordance with experimental findings. [329]

In a second study, the activation of CO_2 on Ru_{10} and Cu_{10} clusters supported on TiO_2 anatase (101) was considered. Whereas CO_2 readily adsorbs on the Ru cluster becoming activated, the CO_2 is unable to chemisorb on the Cu cluster. On the Ru cluster, direct CO_2 dissociation and H-addition to CO_2 are competing reaction pathways for the hydrogenation of CO_2. Here, the preferred reaction mechanism depends on the pressure-dependent H_2 coverage on the Ru cluster. In the case of Cu, a H atom adsorbed on the cluster is added to the physisorbed CO_2 molecule.

All in all, we can conclude that in the size regime of clusters and oxide ultra-thin films, already small changes in the system can completely change the chemical and catalytic properties. The presence of defects and dopants in the oxide support, but also alloying of small metal clusters, can result in important changes of the chemistry and the nucleation behavior of the clusters. The same is basically true also for oxide ultra-thin films. Here, the change of just one atomic layer engenders a completely new material. These features of nano-materials open up new possibilities to design heterogeneous catalysts with controlled reactivity.

10.2 Future development

With the studies presented in this thesis we contributed insights to several important aspects in heterogeneous catalysis, such as support effects, effects of nanostructuring, but also the effect of reactant co-adsorption on supported metal clusters. As all of these aspects constitute research fields by themselves, it becomes clear that it is difficult to overestimate the work still to be done in order to approach a rational catalyst design. But even considering the individual systems examined in this thesis, we find vast possibilities for further research.

In particular, regarding the characterization part, it would be interesting to extend the STM studies also to larger clusters, i.e. Au_n with n = 4, 5, 6 and one or two larger examples like Au_{10} and Au_{20}. Regarding the melting of the nanoparticles, the effect of the support has been completely ignored in the calculations. So, it is of interest to check the effect of confining effects induced by the support. Furthermore, we are still awaiting more experimental results.

The effect of defects and dopants in the oxide support on the chemistry of adsorbed clusters is a large field and in this thesis only some examples were examined. Generally it would be interesting to check also other surface features like hydroxyl groups in the case of titania and dopants in the case of silica. Also, we only investigated crystalline support structures. For titania, the effect of interfaces between anatase and rutile on the cluster adsorption should be interesting to study. For silica, cluster adsorption on amorphous surfaces may be an aspect to examine. Calculations of activation barriers for H-overspill on Au_nTi_1 (n = 4, 5) clusters could be complementing the present results. Generally, the investigation of larger clusters and bimetallic clusters is of interest, as their properties and behavior cannot necessarily be deduced from the present results.

The field of ultra-thin oxide films is broad and there are many aspects still to be explored. In particular, reactions in the confined space between the silica bilayer and the Ru support is can exiting research topic. It may be interesting to introduce heavier homologues of Si into the silica bilayer. Ge, for instance, is like Si a glass former and could induce structural changes in the silica bilayer if some Si atoms were replaced by Ge. Mechanical properties of the silica bilayer should be of interest, especially in comparison to graphene.

Regarding the mechanistic studies, more efforts have to be pursued to bridge the pressure and materials gap. Attempts in this direction could involve the investigation of CO and CO_2 coverage effects and the effect of water on the catalyst. This is true for CO oxidation and CO_2 hydrogenation. Also, it would be nice to compute the Gibbs free energy relations, as well as reaction rates and compare them to experimental data.

Generally it can be said that much of the research in this thesis actually concentrates on understanding the functionality of particular nanomaterials as catalysts. On the one hand, such fundamental studies are important since the so gained atomistic knowledge of the working principle of catalysts is a necessity for a rational catalyst design. On the other hand, more efforts have to be undertaken towards bridging the pressure and materials gap in order to rely on more and more realistic models. Of course the final more ambitious goal should be to actually design novel catalysts on the basis of computations. [352]

References

1 Chorkendorff, I. and Niemandtsverdriet, J.W. *Concepts of Modern Catalysis and Kinetics*. Wiley-VCH, Weinheim, 2007.

2 OECD (2016), Crude oil production, DOI:10.1787/4747b431-en, Accessed on 11/12/2016.

3 Mohr, S. H., Wang, J., Ellem, G., Ward, J., and Giurco, D. Projection of world fossil fuels by country. *Fuel*, 141 (2015), 120-135.

4 Nørskov, J. K., Studt, F., Abild-Pedersen, F., and Bligaard, T. *Fundamental Concepts in Heterogeneous Catalysis*. John Wiley & Sons, New Jersey, 2014.

5 U.S. Geological Survey, Mineral Commodity Summaries, January 2016, minerals.usgs.gov/minerals/pubs/commodity/nitrogen/mcs-2016-nitro.pdf, Accessed on 03/01/2017.

6 Alvarado, M. *IHS Chemical Bulletin, http://www.methanol.org/the-methanol-industry*. Accessed on 03/01/2017.

7 Schlögl, R. Catalytic synthesis of ammonia - A "never-ending story"? *Angew. Chem. Int. Ed.*, 42 (2003), 2004.

8 *World energy outlook*. IEA, 2013.

9 *BP energy outlook 2035*. BP, 2014.

10 *Climate change 2013: The physical science basis. Contribution of working group I to the fifth assessment report of the intergovernmental panel on climate change*. IPCC, Cambridge (UK), NY (USA).

11 Bauer, N., Bosetti, V., Hamdi-Cherif, M. et al. CO_2 Emission mitigation and fossil fuel markets: Dynamic and international aspects of climate policies. *Technol. Forecast. Soc.*, 90 (2015), 243-256.

12 Vlachos, D.G. and Caratzoulas, S. The roles of catalysis and reaction engineering in overcoming the energy and the environment crisis. *Chem. Eng. Sci.*, 65 (2010), 18-29.

13 Dlugokencky, E.J., Hall, B.D., Crotwell, M.J., Montzka, S.A., Dutton, G., Mühle, J., and Elkins, J.W. Long-lived greenhouse gases. In *State of the Climate in 2015*. Bull. Amer. Meteor. Soc., 2016.

14 Gray, H. B. Powering the planet with solar fuel. *Nat. Chem.*, 1 (2009), 7.

15 Liang, S., Hao, C., and Shi, Y. The power of single-atom catalysis. *ChemCatChem*, 7 (2015), 2559.

16 Raipur, T. Catalysis: A brief review on Nano-Catalyst. *J. Energy Chem. Eng.*, 2 (2014), 106-115.

17 García, M. A. Surface plasmons in metallic nanoparticles: Fundamentals and applications. *J. Phys. D: Appl. Phys.*, 44 (2011), 283001.

18 Binnig, G. and Rohrer, H. Scanning tunneling microscopy. *IBM J. Res. Dev.*, 30 (1986), 355-369.

19 Kroto, H. W., Heath, J. R., O'Brien, S. C., Curl, R. F., and Smalley, R. E. C_{60}: Buckminsterfullerene. *Nature* , 318 (1985), 162-163.

20 Feynman, R. P. There's plenty of room at the bottom. *Eng. Sci.* , 23 (1960), 22-36.

21 Drexler, K. E. and Minsky, M. *Engines of creation*. Fourth Estate, London, 1990.

22 Haruta, M., Kobayashi, T., Sano, H., and Yamada, N. Novel gold catalysts for the oxidation of carbon monoxide at a temperature far below 0°C. *Chem. Lett.*, 2 (1987), 405-408.

23 Haruta, M., Yamada, N., Kobayashi, T., and Iijima, S. Gold catalysts prepared by coprecipitation for low-temperature oxidation of hydrogen and of carbon monoxide. *J. Catal.*, 115 (1989), 301-309.

24 Polshettiwar, V., Luque, R., Fihri, A., Zhu, H., Bouhrara, M., and Basset, J. M. Magnetically recoverable nanocatalysts. *Chem. Rev.*, 111 (2011), 3036-3075.

25 Zhou, X., Gan, Y., Du, J., Tian, D., Zhang, R., Yang, C., and Dai, Z. A review of hollow Pt-based nanocatalysts applied in proton exchange membrane fuel cells. *J. Power Sources*, J. Power Sources (2013), 310-322.

26 Gual, A., Godard, C., Castillón, S., Curulla-Ferré, D., and Claver, C. Colloidal Ru, Co and Fe-nanoparticles. Synthesis and application as nanocatalysts in the Fischer-Tropsch process. *Catal. today*, 183 (2012), 154-171.

27 Akia, M., Yazdani, F., Motaee, E., Han, D., and Arandiyan, H. A Review on Conversion of Biomass to Biofuel by Nanocatalysts. *Biofuel Res. J.*, 1 (2014), 16-25.

28 Tong, H., Ouyang, S., Bi, Y., Umezawa, N., Oshikiri, M., and Ye, J. Nano-photocatalytic materials: Possibilities and challenges. *Adv. Mater.*, 24 (2012), 229-251.

29 Gao, P. X., Guo, Y., Zhang, Z., and Ren, Z. *U.S. Patent Application No. 14/347,850.* 2012.

30 Asefa, T., Biradar, A. V., and Wang, Y. *U.S. Patent No. 9,283,545*. Washington, DC: U.S. Patent and Trademark Office., 2016.

31 Larsson, M. I. *U.S. Patent No. 7,813,523.* Washington, DC: U.S. Patent and Trademark Office., 2010.

32 Freund, H.-J. and Pacchioni, G. Oxide ultra-thin films on metals: New materials for the design of supported metal catalysts. *Chem. Soc. Rev.*, 37 (2008), 2224.

33 Brodersen, S. H., Grønbjerg, U., Hvolbæk, B., and Schiøtz, J. Understanding the catalytic activity of gold nanoparticles through multi-scale simulations. *J. Catal.*, 284 (2011), 34-41.

34 Gavnholt, J. and Schiøtz, J. Structure and reactivity of ruthenium nanoparticles. *Phys. Rev.* , 77 (2008), 035404.

35 Kubo, R. Electronic properties of metallic fine particles. I. *J. Phys. Soc. Jpn.*, 17 (1962), 975-986.

36 Lui, C. H., Li, Z., Mak, K. F., Cappelluti, E., and Heinz, T. F. Observation of an electrically tunable band gap in trilayer graphene. *Nature Phys.*, 7 (2011), 944-947.

37 Mak, K. F., Lee, C., J., Hone, Shan, J., and Heinz, T. F. Atomically thin MoS_2: a new direct-gap semiconductor. *Phys. Rev. Lett.*, 105 (2010), 136805.

38 Lee, J., Sorescu, D. C., and Deng, X. Tunable lattice constant and band gap of single- and few-layer ZnO. *J. Phys. Chem. Lett.*, 7 (2016), 1335-1340.

39 Zhang, L. Z., Sun, W., and Cheng, P. Spectroscopic and theoretical studies of quantum and electronic confinement effects in nanostructured materials. *Molecules*, 8 (2003), 207-222.

40 Xiao, S., Hu, W., Luo, W., Wu, Y., Li, X., and Deng, H. Size effect on alloying ability and phase stability of immiscible bimetallic nanoparticles. *Eur. Phys. J. B*, 54 (2006), 479-484.

41 Ruiz Puigdollers, A., Illas, F., and Pacchioni, G. Structure and properties of zirconia nanoparticles from density functional theory calculation. *J. Phys. Chem. C*, 120 (2016), 4392-4402.

42 Yang, B. Kaden, W. E., Yu, X., Boscoboinik, J. A. et al. Thin silica films on Ru (0001): monolayer, bilayer and three-dimensional networks of [SiO_4] tetrahedra. *Phys. Chem. Chem. Phys.*, 14 (2012), 11344-11351.

43 Veith, G., Lumpini, A., Rashkeev, S. et al. Thermal stability and catalytic activity of gold nanoparticles supported on silica. *J. Catal.*, 262 (2009), 92-101.

44 Kolmakov, A. and Goodman, D. W. Scanning tunneling microscopy of gold clusters on TiO_2 (110): CO oxidation at elevated pressures. *Surf. Sci. Lett*, 490 (2001), 597.

45 Malashevich, A., Ismail-Beigi, S., Altman, E. I. Directing the structure of two-dimensional silica and silicates. *J. Phys. Chem. C*, 120 (2016), 26770-26781.

46 Schubert, M. M., Hackenberg, S., Van Veen, A. C., Muhler, M., Plzak, V., and Behm, R. J. CO oxidation over supported gold catalysts - "Inert" and "active" support materials and their role for the oxygen supply during reaction. *J. Catal.*, 197 (2001), 113-122.

47 Ftouni, J., Muñoz-Murillo, A., Goryachev, A. et al. ZrO_2 is preferred over TiO_2 as support for the Ru-catalyzed hydrogenation of levulinic acid to valerolactone. *ACS Catal.*, 6 (2016), 5462.

48 Chretien, S. and Metiu, H. Density functional study of the interaction between small Au clusters, Au_n (n = 1-7) and the rutile TiO_2 surface. I. Adsorption on the stoichiometric surface. *J. Chem. Phys.*, 127 (2007), 084704.

49 Yu, X., Yang, B., Boscoboinik, J. A., Shaikhutdinov, S., and Freund, H.-J. Support effects on the atomic structure of ultrathin silica films on metals. *Appl. Phys. Lett.*, 100 (2012), 151608.

50 Pacchioni, G. Two-dimensional oxides: Multifunctional materials for advanced technologies. *Chem. Eur. J.*, 18 (2012), 10144-10158.

51 Niu, W. and Xu, G. Crystallographic control of noble metal nanocrystals. *Nano Today*, 6 (2011), 265-285.

52 Gross, E., Liu, J. H., Alayoglu, S., Marcus, M. A., Fakra, S. C., Toste, F. D., and Somorjai, G. A. Asymmetric catalysis at the mesoscale: gold nanoclusters embedded in chiral self-assembled monolayer as heterogeneous catalyst for asymmetric reactions. *J. Am. Chem. Soc.*, 135 (2013), 3881-3886.

53 Lai, X., Clair, T. P. S., and Goodman, D. W. Oxygen-induced morphological changes of Ag nanoclusters supported on TiO_2 (110). *Farad. Discuss.*, 114 (1999), 279-284.

54 Tao, F., Grass, M. E., Zhang, Y. W. et al. Reaction-driven restructuring of Rh-Pd and Pt-Pd core-shell nanoparticles. *Science* , 322 (2008), 932-934.

55 Sauer, J. and Freund, H.-J. Models in Catalysis. *Catal. Lett.*, 145 (2015), 109-125.

56 Salmeron, M. and Schlögl, R. Ambient pressure photoelectron spectroscopy: A new tool for surface science and nanotechnology. *Surf. Sci. Rep.*, 63 (2008), 169-199.

57 Heinz, T.F. Second-order nonlinear optical effects at surfaces and interfaces. In *Non-linear surface electromagnetic phenomena*. Elsevier, Amsterdam, 1991.

58 Rasmussen, P.B., Hendriksen, B.L.M., Zeijlemaker, H., Ficke, H.G., and Frenken, J.W.M. The ‘‘Reactor STM’’: a scanning tunneling microscope for investigation of catalytic surfaces at semi-industrial reaction conditions. *Rev. Sci. Instrum.*, 69 (1998), 3879-3884.

59 Creemer, J.F., Helveg, S., Hoveling, G.H., Ullmann, S., Molenbroek, A.M., Sarro, P.M., and Zandbergen, H.W. Atomic-scale electron microscopy at ambient pressure. *J. Ultramicr.*, 108 (2008), 993-998.

60 Martínez-Suárez, L., Frenzel, J., Marx, D., and Meyer, B. Tuning the reactivity of a Cu/ZnO nanocatalyst via gas phase pressure. *Phys. Rev. Lett.*, 110 (2013), 1-5.

61 Lyon, J. T., Gruene, P., Fielicke, A., Meijer, G., Janssens, E., Claes, P., and Lievens, P. Structures of silicon cluster cations in the gas phase. *J. Am. Chem. Soc.*, 131 (2009), 1115-1121.

62 Heiz, U. and Landman, U., eds. *Nanocatalysis*. Springer-Verlag, Berlin Heidelberg, 2007.

63 Dawson, P. H. *Quadrupole mass spectrometry and its applications*. Elsevier, Woodbury, 2013.

64 Farrar, J.M. and Saunders, W.H. *Techniques for the study of ion-molecule reactions*. Wiley, New York, 1988.

65 Chen, M. S. and Goodman, D.W. The structure of catalytically active gold on titania. *Science* , 306 (2004), 252-255.

66 Iddir, H., Komanicky, V., Oeguet, S., You, H., and Zapol, P. Shape of platinum nanoparticles supported on $SrTiO_3$: Experiment and theory. *J. Phys. Chem. C*, 111 (2007), 14782-14789.

67 Boies, A. M., Roberts, J. T., Girshick, S. L., Zhang, B., Nakamura, T., and Mochizuki, A. SiO_2 coating of silver nanoparticles by photoinduced chemical vapor deposition. *Nanotech.*, 20 (2009), 295604.

68 Baeck, S. H., Jaramillo, T., Stucky, G. D., and McFarland, E. W. Controlled electrodeposition of nanoparticulate tungsten oxide. *Nano lett.*, 2 (2002), 831-834.

69 Narayanan, R. and El-Sayed, M. A. Effect of nanocatalysis in colloidal solution on the tetrahedral and cubic nanoparticle shape: electron-transfer reaction catalyzed by platinum nanoparticles. *J. Phys. Chem. B*, 108 (2004), 5726-5733.

70 Zhang, Z.C., Xu, B., and Wang, X. Engineering nanointerfaces for nanocatalysis. *Chem. Soc. Rev.*, 43 (2014), 7870-7886.

71 Haruta, M. Size-and support-dependency in the catalysis of gold. *Catal. Today*, 36 (1997), 153-166.

72 Perez-Alonso, F. J., McCarthy, D. N., Nierhoff, A. et al. The effect of size on the oxygen electroreduction activity of mass-selected platinum nanoparticles. *Angew. Chem. Int. Ed.*, 51 (2012), 4641-4643.

73 Tao, A., Sinsermsuksakul, P., and Yang, P. Polyhedral silver nanocrystals with distinct scattering signatures. *Angew. Chem. Int. Ed.*, 45 (2006), 4597-4601.

74 Song, H., Kim, F., Connor, S., Somorjai, G.A., and Yang, P. Pt nanocrystals: Shape control and Langmuir-Blodgett monolayer formation. *J. Phys. Chem. B*, 109 (2005), 188-193.

75 Niu, W., Zhang, L., and Xu, G. Shape-controlled synthesis of single-crystalline palladium nanocrystals. *ACS Nano*, 4 (2010), 1987-1996.

76 Nilius, N., Wallis, T. M., and Ho, W. Localized molecular constraint on electron delocalization in a

metallic chain. *Phys. Rev. Lett.*, 90 (2003), 186102.

77 Piednoir, A., Perrot, E., Granjeaud, S., Humbert, A., Chapon, C., and Henry, C. R. Atomic resolution on small three-dimensional metal clusters by STM. *Surf. Sci.*, 391 (1997), 19-26.

78 Jeangros, Q., Hansen, T. W., Wagner, J. B., Damsgaard, C. D., Dunin-Borkowski, R. E., Hébert, C., and Hessler-Wyser, A. Reduction of nickel oxide particles by hydrogen studied in an environmental TEM. *J. Mater. Sci.*, 48 (2013), 2893-2907.

79 Frenkel, A. Solving the 3D structure of metal nanoparticles. *Z. Kristallogr.*, 222 (2007), 605-611.

80 Small, M. W., Sanchez, S. I., Marinkovic, N. S., Frenkel, A. I., and Nuzzo, R. G. Influence of adsorbates on the electronic structure, bond strain, and thermal properties of an alumina-supported Pt catalyst. *ACS Nano*, 6 (2012), 5583-5595.

81 Frenkel, A. I., Wang, Q., Sanchez, S. I., Small, M. W., and Nuzzo, R. G. Short range order in bimetallic nanoalloys: An extended X-ray absorption fine structure study. *J. Chem. Phys.*, 138 (2013), 064202.

82 Wolf, A. and Schüth, F. A systematic study of the synthesis conditions for the preparation of highly active gold catalysts. *Appl. Catal. A*, 226 (2002), 1-13.

83 Pacchioni, G. Electronic interactions and charge transfers of metal atoms and clusters on oxide surfaces. *Phys. Chem. Chem. Phys.*, 15 (2013), 1737-1757.

84 Bowker, M. and Fourre, E. Direct interactions between metal nanoparticles and support: STM studies of Pd on TiO_2 (110). *Appl. Surf. Sci.*, 254 (2008), 4225.

85 Shekhar, M., Wang, J., Lee, W. et al. Size and support effects for the water-gas shift catalysis over gold nanoparticles supported on model Al_2O_3 and TiO_2. *J. Am. Chem. Soc.*, 134 (2012), 4700.

86 Mistry, H., Reske, R., Zeng, Z., Zhao, Z., Greeley, J., P., Strasser, and Cuenya, B. R. Exceptional size-dependent activity enhancement in the electroreduction of CO_2 over Au nanoparticles. *J. Am. Chem. Soc.*, 136 (2014), 16473-16476.

87 Cuenya, B. R. and Behafarid, F. Nanocatalysis: Size-, and shape-dependent chemisorptions and catalytic reactivity. *Surf. Sci. Rep.*, 70 (2015), 135-187.

88 Mullen, G. M. and Mullins, C. B. Water's place in Au catalysis. *Science*, 345 (2014), 1564-1565.

89 Saavedra, J, Doan, H.A., Pursell, C. J., Grabo, L.C., and Chandler, B. D. The critical role of water at the gold-titania interface in catalytic CO oxidation (2014), 1599-1602.

90 Libuda, J. and Freund, H. J. Molecular beam experiments on model catalysts. *Surf. Sci. Rep.*, 57 (2005), 157-298.

91 Somorjai, G. A. and Y., Park. J. Molecular surface chemistry by metal single crystals and nanoparticles from vacuum to high pressure. *Chem. Soc. Rev.*, 37 (2008), 2155-2162.

92 Pacchioni, G. First principles calculations on oxide-based heterogeneous catalysts and photocatalysts: Problems and advances. *Catal. Lett.*, 145 (2015), 80-94.

93 Vilhelmsen, L. B. and Hammer, B. A genetic algorithm for first principles global structure optimization of supported nanostructures. *J. Chem. Phys.*, 141 (2014), 044711.

94 Musolino, V., Selloni, A., and Car, R. Structure and dynamics of small metallic clusters on an insulating meta-oxide surface: Copper on MgO(100). *Phys. Rev. Lett.*, 83 (1999), 3242-3245.

95 Cox, D. M., Reichmann, K. C., Trevor, D. J., and Kaldor, A. CO chemisorption on free gas phase metal clusters. *J. Chem. Phys.*, 88 (1988), 111-119.

96 Shaikhutdinov, S. and Freund, H.-J. Ultrathin oxide films on metal supports: Structure-reactivity relations. *Annu. Rev. Phys. Chem.*, 63 (2012), 619-633.

97 Lunkenbein, T., Schumann, J., Behrens, M., Schlögl, R., and Willinger, M. G. Formation of a ZnO overlayer in industrial $Cu/ZnO/Al_2O_3$ catalysts induced by strong metal-support interactions. *Angew. Chem. Int. Ed.*, 127 (2015), 4627-4631.

98 Christensen, S. T., Feng, H., Libera, J. L., Guo, N., Miller, J. T., Stair, P. C., and Elam, J. W. Supported Ru-Pt bimetallic nanoparticle catalysts prepared by atomic layer deposition. *Nano lett.*, 10 (2010), 3047-3051.

99 Wu, M. C., Corneille, J. S., Estrada, C. A., He, J. W., and Goodman, D. W. Synthesis and characterization of ultra-thin MgO films on Mo (100). *Chem. Phys. Lett.*, 182 (1991), 472-478.

100 Löffler, D., Uhlrich, J.J., Baron, M. et al. Growth and structure of crystalline silica sheet on Ru (0001). *Phys. Rev. Lett.* , 105 , (2010), 146104.

101 Büchner, C., Lichtenstein, L., Yu, X., Boscoboinik, J. A. et al. Ultrathin silica films: The atomic structure of two-dimensional crystals and glasses. *Chem.-Eur. J.*, 20 (2014), 9176-9183.

102 Destro, F.B., Cilense, M., Nascimento, M.P., Garcia, F.G., Hein, L.R.O., and Simões, A.Z. Corrosion behaviour of polycrystalline Nb_2O_5 thin films and its size effects. *Prot. Met. Phys. Chem. Surf.*, 52 (2016), 104-110.

103 Fortunato, E., Barquinha, P., and Martins, R. Oxide semiconductor thin-film transistors: A review. *Adv. Mater.*, 24 (2012), 2945-2986.

104 Freeman, C. L., Claeyssens, F., Allan, N. L., and Harding, J. H. Graphitic nanofilms as precursors to wurtzite films: Theory. *Phys. Rev. Lett.*, 96 (2006), 066102.

105 De Souza, R. A., Gunkel, F., Hoffmann-Eifert, S., and Dittmann, R. Finite-size versus interface-proximity effects in thin-film epitaxial. *Phys. Rev. B*, 89 (2014), 241401.

106 Ravichandran, J., Yadav, A. K., Siemons, W. et al. Size effects on thermoelectricity in a strongly correlated oxide. *Phys. Rev. B*, 85 (2012), 085112.

107 Trotochaud, L., Ranney, J. K., Williams, K. N., Boettcher, S. W. Solution-cast metal oxide thin film electrocatalysts for oxygen evolution. *J. Am. Chem. Soc.*, 134 (2012), 17253-17261.

108 Benck, J. D., Hellstern, T. R., Kibsgaard, J., Chakthranont, P., Jaramillo, T. F. Catalyzing the hydrogen evolution reaction (HER) with molybdenum sulfide nanomaterials. *ACS Catal.*, 4 (2014), 3957-3971.

109 Mu, R., Fu, Q., Jin, L., Yu, L., Fang, G., Tan, D., and Bao, X. Visualizing chemical reactions confined under graphene. *Angew. Chem. Int. Ed.*, 51 (2012), 4856-4859.

110 Emmez, E., Yang, B., Shaikhutdinov, S., and Freund, H.-J. Permeation of a single-layer SiO_2 membrane and chemistry in confined space. *J. Phys. Chem. C*, 118 (2014), 29034-29042.

111 Baron, M., Stacchiola, D., Ulrich, S. et al. Adsorption of Au and Pd atoms on thin SiO_2 films: The role of atomic structures. *J. Phys. Chem. C*, 112 (2008), 3405.

112 Ulrich, S., Nilius, N., Freund, H.J., Martinez, U., Giordano, L., and Pacchioni, G. Evidence for a size-selective adsorption mechanism on oxide surfaces: Pd and Au atoms on SiO_2/Mo(112). *ChemPhysChem*,

9 (2008), 1367-1370.

113 Nilius, N., Ganduglia-Pirovano, M. V., Brázdová, V., Kulawik, M., Sauer, J. and Freund, H. J. Electronic properties and charge state of gold monomers and chains adsorbed on alumina thin films on NiAl (110). *Phys. Rev. B*, 81 (2010), 045422.

114 Reuter, K., Stampfl, C., and Scheffler, M. Ab initio atomistic thermodynamics and statistical mechanics of surface properties and functions. In *Handbook of materials modeling*. Springer, Netherlands, 2005.

115 Ertl, G. Oscillatory kinetics and spatiotemporal self-organization in reactions at solid surfaces. *Science* , 254 (1991), 1750-1755.

116 Salciccioli, M., Stamatakis, M., Caratzoulas, S., and Vlachos, D. G. A review of multiscale modeling of metal-catalyzed reactions: Mechanism development for complexity and emergent behavior. *Chem. Eng. Sci.*, 66 (2011), 4319-4355.

117 Liu, X. and Salahub, D. R. Molybdenum carbide nanocatalysts at work in the in situ environment: A density functional tight-binding and quantum mechanical/molecular mechanical study. *J. Am. Chem. Soc.*, 137 (2015), 4249-4259.

118 Thiel, W. Computational catalysis - Past, present, and future. *Angew. Chem. Int. Ed.*, 53 (2014), 8605-8613.

119 Maestri, M. and Reuter, K. Molecular-level understanding of WGS and reverse WGS reactions on Rh through hierarchical multiscale approach. *Chem. Eng. Sci.*, 74 (2012), 296-299.

120 Koch, W. and Holthausen, M.C. *A Chemist's Guide to Density Functional Theory*. Wiley-VCH Verlag GmbH, Weinheim, 2001.

121 Henkelman, G. and Jónsson, H. A dimer method for finding saddle points on high dimensional potential surfaces using only first derivatives. *J. Chem. Phys.*, 111 (1999), 7010-7022.

122 Henkelman, G., Uberuaga, B.P., and Jónsson, H. A climbing image nudged elastic band method for finding saddle points and minimum energy paths. *J. Chem. Phys.*, 113 (2000), 9901.

123 Nørskov, J. K., Abild-Pedersen, F., Studt, F., and Bligaard, T. Density functional theory in surface chemistry and catalysis. *Proc. Natl. Acad. Sci. USA*, 108 (2011), 937-943.

124 P. Sabatier, La catalyse en chimie organique, Librairie Polytechnique, Paris et Liège, 1920.

125 Harriman, A., Pickering, I.J., Thomas, J.M., and Christensen, P. A. Metal oxides as heterogeneous catalysts for oxygen evolution under photochemical conditions. *J. Chem. Soc., Faraday Trans.*, 84 (1988), 2795-2806.

126 Eichler, A., Hafner, J., and Kresse, G. Reaction path for the dissociative adsorption of hydrogen on the (100) surfaces of face-centered-cubic transition metals. *Surf. Rev. Lett.*, 4 (1997), 1347-1351.

127 Medford, A.J., Lausche, A.C., Abild-Pedersen, F., Temel, B., Schjødt, N.C., Nørskov, J.K., and Studt, F. Activity and selectivity trends in synthesis gas conversion to higher alcohols. *Top. Catal.*, 57 (2014), 135-142.

128 Logadottir, A., Rod, T.H., Nørskov, J. K., Hammer, B., Dahl, S., and Jacobsen, C.J.H. The Brønsted–Evans–Polanyi relation and the volcano plot for ammonia synthesis over transition metal catalysts. *J. Catal.*, 197 (2001), 229-231.

129 Brønsted, J. N. and Pedersen, K.J. Die katalytische Zersetzung des Nitramids und ihre physikalisch-

chemische Bedeutung. *Z. Phys. Chem.*, 108 (1924), 185-235.

130 Evans, M. G. and Polanyi, M. Further considerations on the thermodynamics of chemical equilibria and reaction rates. *J. Chem. Soc., Faraday Trans.*, 32 (1936), 1340.

131 Nørskov, J.K., Bligaard, T., Hvolbæk, B., Abild-Pedersen, F., Chorkendorffc, I., and Christensen, C.H. The nature of the active site in heterogeneous metal catalysis. *Chem. Soc. Rev.*, 37 (2008), 2163.

132 Nørskov, J. K., Bligaard, T., Logadottir, A. et al. Universality in Heterogeneous Catalysis. *J. Catal.*, 209 (2002), 275-278.

133 Viñes, F., Vojvodic, A., Abild-Pedersen, F., and Illas, F. Brønsted–Evans–Polanyi relationship for transition metal carbide and transition metal oxide surfaces. *J. Phys. Chem. C*, 117 (2013), 4168-4171.

134 Hammer, B. and Nørskov, J.K. Why gold is the noblest of all metals. *Nature*, 376 (1995), 2238-2240.

135 Jiang, T., Mowbray, D.J., Drobin, S., Falsig, H., Hvolbaek, B., Bligaard, T., and Nørskov, J.K. Trends in CO oxidation rates for metal nanoparticles and closed-packed, stepped, and kinked surfaces. *J. Phys. Chem. C*, 113 (2009), 10548.

136 Pacchioni, G. Oxygen vacancy: The invisible agent on oxide surfaces. *ChemPhysChem*, 4 (2003), 1041-1047.

137 Dahl, S., Logadottir, A., Egeberg, R.C., Larsen, J.H., Chorkendorff, I., Törnqvist, E., and Nørskov, J.K. Role of steps in N_2 activation on Ru (0001). *Phys. Rev. Lett.*, 83 (1999), 1814.

138 Imbihl, R. and Ertl, G. Oscillatory kinetics in heterogeneous catalysis. *Chem. Rev.*, 3 (1995), 697.

139 Ertl, G. and Freund, H.J. Catalysis and surface science. *Phys. Today*, 52 (1999), 32.

140 Haaland, D.M. and Williams, F.L. Simultaneous measurement of CO oxidation rate and surface coverage on $PtAl_2O_3$ using infrared spectroscopy: Rate hysteresis and CO island formation. *J. Catal.*, 76 (1982), 450-465.

141 Monaco, G., Toto, M., Guerra, G., Corradini, P., and Cavallo, L. Geometry and stability of titanium chloride species adsorbed on the (100) and (110) cuts of the $MgCl_2$ support of the heterogeneous Ziegler-Natta catalysts. *Macromolecules*, 33 (2000), 8953-8962.

142 Thomas, J.M. and Thomas, W.J. *Principles and Practice of Heterogeneous Catalysis*. Wiley-VCH Verlag GmbH & Co., Weinheim, 2015.

143 Thomas, J.M. Raja, R. and Lewis, D.W. Single-site heterogeneous catalysts. *Angew. Chem. Int. Ed.*, 44 (2005), 6456-6482.

144 Vermeiren, W. and Gilson, J.P. Impact of zeolites on the petroleum and petrochemical industry. *Top. Catal.*, 52 (2009), 1131-1161.

145 Kondo, J., Nishitani, R., Yoda, E., Yokoi, T., Tatsumi, T., and Domen, K. A comparative IR characterization of acidic sites on HY zeolite by pyridine and CO probes with silica–alumina and γ-alumina references. *Phys. Chem. Chem. Phys.*, 12 (2010), 11576-11586.

146 Derouane, E.G. and Chang, C.D. Confinement effects in the adsorption of simple bases by zeolites. *Micro. Mes. Mat.*, 35 (2000), 425-433.

147 Panov, G. I., Uriarte, A. K., Rodkin, M. A., and Sobolev, V. I. Generation of active oxygen species on solid surfaces. Opportunity for novel oxidation technologies over zeolites. *Catal. Today*, 41 (1998), 365-

385.

148 Elliott, D.J. and Lunsford, J.H. Kinetics of the methanation reaction over Ru, RuNi, RuCu, and Ni clusters in zeolite Y. *J. Catal.*, 57 (1979), 11-26.

149 Yang, M., Allard, L., and Flytzani-Stephanopoulos, M. Atomically dispersed Au–$(OH)_x$ species bound on titania catalyze the low-temperature water-gas shift reaction. *J. Am. Chem. Soc.*, 135 (2013), 3768.

150 Lee, S., Molina, L. M., López, M. J. et al. Selective propene epoxidation on immobilized Au_{6-10} clusters: The effect of hydrogen and water on activity and selectivity. *Angew. Chem. Int. Ed.*, 121 (2009), 1495-1499.

151 Behrens, M., Studt, F., Kasatkin, I., Kühl, S., Hävecker, M., Abild-Pedersen, F., and Schlögl, R. The active site of methanol synthesis over $Cu/ZnO/Al_2O_3$ industrial catalysts. *Science*, 336 (2012), 893-897.

152 Lei, Y., Mehmood, F., Lee, S. et al. Increased silver activity for direct propylene epoxidation via subnanometer size effects. *Science*, 328 (2010), 224-228.

153 Schrödinger, E. An undulatory theory of the mechanics of atoms and molecules. *Phys. Rev.*, 28 (1926), 1049-1070.

154 Born, M. and Oppenheimer, J. Zur Quantentheorie der Molekeln. *Ann. Phys.*, 84 (1927), 457-484.

155 Born, M. and Fock, V. A. Beweis des Adiabatensatzes. *Z. Phys.*, 51 (1928), 165-180.

156 Hohenberg, P. and Kohn, W. Inhomogeneous electron gas. *Phys. Rev. Lett.*, 136 (1964), 864-871.

157 Parr, R. G and Yang, W. *Density Functional Theory of Atoms and Molecules*. Oxford University Press, Oxford, 1976.

158 Kohn, W and Sham, L. Self-consistent equations including exchange and correlation effects. *Phys. Rev.*, 14 (1965), 1133-1138.

159 Jones, R. O. and Gunnarson, O. The density functional formalism, its applications and prospects. *Rev. Mod. Phys.*, 61 (1989), 689-746.

160 Perdew, J. P., Burke, K., and Ernzerhof, M. Generalized gradient approximation made simple. *Phys. Rev. Lett.*, 77 (1996), 3865.

161 Perdew, J. P., Burke, K., and Ernzerhof, M. Erratum: Generalized gradient approximation made simple. *Phys. Rev. Lett.*, 78 (1997), 1396.

162 Perdew, P., Kurth, S., Zupan, A., and Blaha, P. Accurate density functional with correct formal properties: A step beyond the generalized gradient approximation. *Phys. Rev Lett.*, 82 (1993), 5179.

163 Becke, A. D. A new mixing of Hartree-Fock and local Density-functional theories. *J. Chem. Phys.*, 98 (1993), 1372-1377.

164 Heyd, J., Scuseria, G. E., and Ernzerhof, M. Hybrid functionals based on a screened Coulomb potential. *J. Chem. Phys.*, 118 (2003), 8207.

165 Heyd, J. and Scuseria, G. E. Efficient hybrid density functional calculations in solids: assessment of the Heyd–Scuseria–Ernzerhof screened Coulomb hybrid functional. *J. Chem. Phys.*, 121 (2004), 1187.

166 Heyd, J., Scuseria, G. E., and Ernzerhof, M. Erratum:"Hybrid functionals based on a screened Coulomb potential"[J. Chem. Phys. 118, 8207 (2003)]. *J. Chem. Phys.*, 124 (2006), 219906.

167 Himmetoglu, B., Floris, A., De Gironcoli, S., and Cococcioni, M. Hubbard-corrected DFT energy functionals: The LDA+U description of correlated systems. *Int. J. Quantum Chem.*, 114 (2014), 14-49.

168 Georges, A. and Kotliar, G. Hubbard model in infinite dimensions. *Phys. Rev. B* , 45 (1992), 6479.

169 Requist, R. and Pankratov, O. Generalized Kohn-Sham system in one-matrix functional theory. *Phys. Rev. B* , 77 (2008), 235121.

170 Hubbard, J. Electron correlations in narrow energy bands. *Proc. R. Soc. London A* , 276 (1963), 238.

171 Liechtenstein, A. I., Anisimov, V. I., and Zaanen, J. Density-functional theory and strong interactions: Orbital ordering in Mott-Hubbard insulators. *Phys. Rev. B*, 52 (1995), R5467.

172 Dudarev, S. L., Botton, G. A., Savrasov, S. Y., Humphreys, C. J., and Sutton, A. P. Electron-energy-loss spectra and the structural stability of nickel oxide: An LSDA+U study. *Phys. Rev. B*, 57 (1998), 1505.

173 Cococcioni, M. and De Gironcoli, S. Linear response approach to the calculation of the effective interaction parameters in the LDA+ U method. *Phys. Rev. B*, 71 (2005), 035105.

174 Carrasco, J., Liu, W., Michaelides, A., and Tkatchenko, A. Insight into the description of van der Waals forces for benzene adsorption on transition metal (111) surfaces. *J. Chem. Phys.*, 140 (2014), 084704.

175 Carrasco, J., Klimeš, J., and Michaelides, A. The role of van der Waals forces in water adsorption on metals. *J. Chem. Phys.*, 138 (2013), 024708.

176 Boese, A. D. and Sauer, J. Accurate adsorption energies for small molecules on oxide surfaces: CH_4/MgO(001) and C_2H_6/MgO(001). *J. Comp. Chem.*, 37 (2016), 2374-2385.

177 Grimme, S. Density functional theory with London dispersion corrections. *Wiley Interdiscip. Rev. Comput. Mol. Sci.*, 1 (2011), 211.

178 Wu, X., Vargas, M. C., Nayak, S., Lotrich, V., and Scoles, G. Towards extending the applicability of density functional theory to weakly bound systems. *J. Chem. Phys.*, 115 (2001), 8748.

179 Patton, D. C. and Pederson, M. R. Application of the generalized-gradient approximation to rare-gas dimers. *Phys. Rev. A*, 56 (1997), R2495.

180 Tsuzuki, S. and Lüthi, H. P. Interaction energies of van der Waals and hydrogen bonded systems calculated using density functional theory: Assessing the PW91 model. *J. Chem. Phys.*, 114 (2001), 3949.

181 Dion, M., Rydberg, H., Schröder, E., Langreth, D. C., and Lundqvist, B. I. Van der Waals density functional for general geometries. *Phys. Rev. Lett.*, 24 (2004), 246401.

182 Klimeš, J., Bowler, D. R., and Michaelides, A. Chemical accuracy for the van der Waals density functional. *J. Phys.: Cond.Matt.*, 22 (2010), 022201.

183 Lee, K., Murray, E. D., Kong, L., Lundqvist, B. I., and Langreth, D. C. Higher-accuracy van der Waals density functional. *Phys. Rev. B 82*, 82 (2010), 081101.

184 Grimme, S. Semiempirical GGA-type density functional constructed with a long-range dispersion correction. *J. Comp. Chem.*, 27 (2006), 1787.

185 Tosoni, S. and Sauer, J. Accurate quantum chemical energies for the interaction of hydrocarbons with oxide surfaces: CH_4/MgO(001). *Phys. Chem. Chem. Phys.*, 12 (2010), 14330-14340.

186 Grimme, S., Antony, J., Ehrlich, S., and Krieg, H. A consistent and accurate ab initio parametrization of

density functional dispersion correction (DFT-D) for the 94 elements H-Pu. *J. Chem. Phys.*, 132 (2010), 154104.

187 Tkatchenko, A. and Scheffler, M. Accurate molecular van der Waals interactions from ground-state electron density and free-atom reference data. *Phys. Rev. Lett.*, 102 (2009), 73005.

188 Ashcroft, N. W. and Mermin, N. D. *Solid State Physics*. Holt Saunders, Philadelphia, 1976.

189 Kohanoff, J. *Electronic Structure Calculations for Solids and Molecules*. Cambridge University Press, Cambridge, 2006.

190 Hamann, D. R., Schlüter, M., and Chiang, C. "Norm-conserving pseudopotentials. *Phys. Rev. Lett.*, 43 (1979), 1494.

191 Vanderbilt, D. Soft self-consistent pseudopotentials in a generalized eigenvalue formalism. *Phys. Rev. B*, 41 (1990), 7892.

192 Kresse, G. and Joubert, J. From ultrasoft pseudopotentials to the projector augmented-wave method. *Phys. Rev. B*, 59 (1999), 1758.

193 Blöchl, P.E. Projector augmented-wave method. *Phys. Rev. B*, 50 (1994), 17953.

194 Kresse, G. and Hafner, J. Ab initio molecular dynamics for liquid metals. *Phys. Rev. B*, 47 (1993), 558.

195 Kresse, G. and Hafner, J. Ab initio molecular-dynamics simulation of the liquid-metal-amorphous-semiconductor transition in germanium. *Phys. Rev. B*, 49 (1994), 1425.

196 Kresse, G. and Furthmüller, J. Efficiency of ab-initio total energy calculations for metals and semiconductors using a plane-wave basis set (1996), 15.

197 Kresse, G. and Furthmüller, J. Efficient iterative schemes for ab initio total-energy calculations using a plane-wave basis set. *Phys. Rev. B.*, 54 (1996), 11169.

198 Schneider, T. and Stoll, E. Molecular-dynamics study of a three-dimensional one-component model for distortive phase transitions. *Phys. Rev. B*, 17 (1978), 1302.

199 Jacobsen, K. W., Nørskov, J. K., and Puska, M. Interatomic interaction in the effective medium theory. *Phys. Rev. B*, 34 (1987), 7423.

200 Jacobsen, K. W. Bonding in metallic systems: An effective medium approach. *Comments Condens. Matter Phys.* , 14 (1988), 129.

201 Jacobsen, K. W., Stoltze, P., and Nørskov, J. K. A semi-empirical effective medium theory for metals and alloys. *Surf. Sci.*, 366 (1996), 394.

202 Foiles, S., Baskes, M., and Daw, M. Embedded-atom-method functions for the fcc metals Cu, Ag, Au, Ni, Pd, Pt, and their alloys. *Phys. Rev. B*, 33 (1986), 7983.

203 Callen, H. B. and Welton, T. A. Molecular-dynamics study of a three-dimensional one-component model for distortive phase transitions. *Phys. Rev. B*, 83 (1951), 34-40.

204 Bahn, S. R. and Jacobsen, K. W. An object-oriented scripting interface to a legacy electronic structure code. *Comput. Sci. Eng.*, 4 (2002), 56-66.

205 Tadmor, E. B., Elliott, R. S., Sethna, J. P., Miller, R. E., and Becker, C. A. The potential of atomistic simulations and the knowledgebase of interatomic models. *JOM*, 63 (2011), 17.

206 Tadmor, E. B., Elliott, R. S., Phillpot, S. R., and Sinnott, S. B. NSF cyberinfrastructures: A new paradigm for advancing materials simulation. *Curr. Opin. Solid St. M.*, 17 (2013), 298-304.

207 Sanches, A., Abbet, S., Heiz, U., Schneider, W. D., Hakkinen, H., R., Barnett, and Landmann, U. When gold is not noble: nanoscale gold catalysts. *J. Phys. Chem. A*, 103 (1999), 9573.

208 Molina, L., Rassmusse, M., and Hammer, B. Adsorption of O_2 and oxidation of CO at Au nanoparticles supported by TiO_2 (110). *J. Chem. Phys.*, 120 (2004), 7673.

209 Molina, L. M., Lee, S., Sell, K. et al. Size-dependent selectivity and activity of silver nanoclusters in the partial oxidation of propylene to propylene oxide and acrolein: A joint experimental and theoretical study. *Catal. Today*, 160 (2011), 116-130.

210 Royer, S. and Duprez, D. Catalytic oxidation of carbon monoxide over transition metal oxides. *ChemCatChem*, 3 (2011), 24-65.

211 Manz, T. A. and Yang, B. Selective oxidation passing through η^3-ozone intermediates: applications to direct propene epoxidation using molecular oxygen oxidant. *RSC Adv.*, 4 (2014), 27755-27774.

212 Mao, B., Chang, R., Shi, L. et al. A near ambient pressure XPS study of subnanometer silver clusters on Al_2O_3 and TiO_2 ultrathin film supports. *Phys. Chem. Chem. Phys.*, 16 (2014), 26645-26652.

213 Valden, M., Lai, X., and Goodman, D. W. Onset of catalytic activity of gold clusters on titania with the appearance of non-metallic properties. *Science*, 281 (1998), 1647-1650.

214 Gosh, T. B., Dhabal, S., and Datta, A. K. On crystallite size dependence of phase stability of nanocrystalline TiO_2. *J. Appl. Phys.*, 94 (2003), 4577-4582.

215 Smith, S. J., Stevens, R., Liu, S. F., Li, G. S., Navrotsky, A., Boerio-Goates, J., and Woodfield, B. F. Heat capacities and thermodynamic functions of TiO_2 anatase and rutile: Analysis of phase stability. *Am. Mineral.*, 94 (2009), 236-243.

216 Hanaor, D. A. H. and Sorrell, C. C. Review of the anatase to rutile phase transformation. *J. Mater. Sci.*, 46 (2011), 855-874.

217 Augustynski, J. The role of the surface intermediates in the photoelectrochemical behavior of anatase and rutile TiO_2. *Electro-chim. Acta*, 38 (1993), 43-46.

218 Linsebigler, A. L., Lu, G. Q., and Yates, J. T. Photocatalysis on TiO_2 surfaces: Principles, mechanisms, and selected Results. *Chem. Rev.*, 95 (1995), 735-758.

219 Hadjiivanov, K. I. and Klissurski, D. G. Surface chemistry of titania (anatase) and titania-supported catalysts. *Chem. Soc. Rev.*, 25 (1996), 61-69.

220 Satterfield, C. N. *Heterogeneous Catalysis in Industrial Practice*. McGraw-Hill, New York, 1991.

221 Lazzeri, M., Vittadini, A., and Selloni, A. Structure and energetics of stoichiometric TiO_2 anatase surfaces. *Phys. Rev. B*, 63 (2001), 155409.

222 Chretien, S. and Metiu, H. Density functional study of the interaction between small Au clusters, Au_n (n = 1-7) and the rutile TiO_2 surface. II. Adsorption on a partially reduced surface. *J. Chem. Phys.*, 127 (2007), 244708.

223 Hu, Z. and Metiu, H. Choice of U for DFT+U calculations for titanium oxides. *J. Phys. Chem. C*, 115 (2011), 5841.

224 Finazzi, E., Di Valentin, C., Pacchioni, G., and Selloni, A. Excess electron states in reduced bulk anatase TiO_2: comparison of standard GGA, GGA+U, and hybrid DFT calculations. *J. Chem. Phys.*, 129 (2008), 154113.

225 Davidson, E. *Methods in Computational Molecular Physics*. Plenum, New York, 1983.

226 Monkhorst, H. J. and Pack, J. D. Special points for Brillouin-zone integrations. *Phys. Rev. B*, 13 (1976), 5188.

227 Djerdj, I. and Tonejc, A. M. Structural investigations of nanocrystalline TiO_2 samples. *J. Alloys Compd.*, 413 (2006), 159-174.

228 Bredow, T., Giordano, L., and Cinquini, F. Pacchioni, G. Electronic properties of rutile TiO_2 ultrathin films: Odd-even oscillations with the number of layers. *Phys. Rev. B*, 70 (2004), 035419.

229 Rocker, G.: Schaefer, J. A. and Göpel, W. Localized and delocalized vibrations on TiO_2 (110) studied by high-resolution electron-energy-loss spectroscopy. *Phys. Rev. B*, 30 (1984), 3704.

230 Kittel, C. *Introduction to Solid State Physics*. John Wiley & Sons, New York, 2005.

231 Haynes, W. M., ed. *CRC Handbook of Chemistry and Physics*. CRC Press, Boca Raton, 2010.

232 Ruiz Puigdollers, A., Schlexer, P., and Pacchioni, G. Gold and silver clusters on TiO_2 and ZrO_2 (101) surfaces: Role of dispersion forces. *J. Phys. Chem. C*, 119 (2015), 15381.

233 Hakkinen, H. and Landman, U. Gold clusters (Au_N, $2 \leq N \leq 10$) and their anions. *Phys. Rev. B*, 62 (2000), R2287-R2290.

234 Wu, X., Senapati, L., Nayak, S. K., Selloni, A., and Hajaligol, M. Growth and structure of small gold particles on rutile TiO_2(110). *J. Chem. Phys. B*, 72 (2005), 205422.

235 Gong, X. Q., Selloni, A., Dulub, O., Jacobson, P., and Diebold, U. Small Au and Pt clusters at the anatase TiO_2(101) surface: Behavior at terraces, steps, and surface oxygen vacancies. *J. Am. Chem. Soc.*, 130 (2008), 370-381.

236 Tong, X., Benz, L., Kemper, P., Metiu, H., Bowers, M. T., and Buratto, S. K. Intact size-selected Aun clusters on a TiO_2 (110)-(1x1) surface at room temperature. *J. Am. Chem. Soc.*, 127 (2005), 13516-13518.

237 Minato, T., Susaki, T., Shiraki, S., Kato, H. S., Kawai, M., and Aika, K. I. Investigation of the electronic interaction between TiO_2 (110) surfaces and Au clusters by PES and STM. *Surf. Sci.*, 566 (2004), 1012-1017.

238 Schwartz, V., Mullins, D. R., Yan, W. F., Chen, B., Dai, S., and Overbury, S. H. XAS Study of Au supported on TiO_2: Influence of oxidation state and particle size on catalytic activity. *J. Phys. Chem. B*, 108 (2008), 15782.

239 Parker, S. C. and Campbell, C. T. Reactivity and sintering kinetics of Au/TiO_2 (110) model catalysts: particle size effects. *Top. Catal.*, 44 (2007), 3.

240 Scanlon, D. O., Dunnill, C. W., Buckeridge, J. et al. Band alignment of rutile and anatase TiO_2. *Nat. Mater.*, 12 (2013), 798.

241 Diebold, U., Anderson, J. F., Ng, K.-O., and Vanderbilt, D. Evidence for the tunneling site on transition-metal oxides: TiO_2(110). *Phys. Rev. Lett.*, 77 (1996), 1322.

242 Perron, H., Domain, C., Roques, J., Drot, R., Simoni, E., and Catalette, H. Optimisation of accurate rutile TiO_2 (110), (100), (101) and (001) surface models from periodic DFT calculations. *Theor. Chem. Acc.*, 117 (2007), 565-574.

243 Howard, C. J., Sabine, T.M., and Dickson, F. Structural and thermal parameters for rutile and anatase. *Act. Cryst. B*, 47 (1991), 462-468.

244 Tersoff, J. and Hamann, D.R. Theory of the scanning tunneling microscope. *Phys. Rev. B*, 31 (1985), 805.

245 Nanda, K. K. Size-dependent melting of nanoparticles: Hundred years of thermodynamic model. *J. Phys.* (2009), 617.

246 Zhu, J., Fu, Q., Xue, Y., and Cui, Z. Comparison of different models of melting transformation of nanoparticles. *Mater. Sci.*, 51 (2016), 4462-4469.

247 Haberland, H., Karrais, M., Mall, M., and Thurner, Y. Thin films from energetic cluster impact: a feasibility study. *J. Vac. Sci. Technol.*, 10 (1992), 3266-3271.

248 Von Issendorff, B. and Palmer, R. E. A new high transmission infinite range mass selector for cluster and nanoparticle beams. *Rev. Sci. Instrum.*, 70 (1999), 4497-4501.

249 Pratontep, S., Carroll, S. J., Xirouchaki, C., Streun, M., and Palmer, R. E. Size-selected cluster beam source based on radio frequency magnetron plasma sputtering and gas condensation. *Rev. Sci. Instrum.*, 76 (2005), 045103.

250 http://denssolutions.com/products/heating/nano-chip/, Accessed on 01/12/2016.

251 https://imagej.nih.gov/ij, Accessed on 02/08/2016.

252 Singh-Miller, N. E. and Marzari, N. Surface energies, work functions, and surface relaxations of low-index metallic surfaces from first principles. *Phys. Rev. B* (2009), 235407.

253 Allen, M. P. and Tildesley, D. J. *Computer Simulation of Liquids*. Oxford University Press, New York, 1991.

254 Jacobsen, K. W., Stoltze, P., and Nørskov, J. K. A semi-empirical effective medium theory for metals and alloys. *Surf. Sci.* (1996), 394-402.

255 Zhou, X. W., Johnson, R. A., and Wadley, H. N. G. *Phys. Rev. B*, 69 (2004), 144113.

256 Zhou, X. W., Wadley, H. N. G., Johnson, R. A. et al. Atomic scale structure of sputtered metal multilayers. *Acta Mater.*, 49 (2001), 4005.

257 Larsen, P. M., Schmidt, S., and Schiøtz, J. Robust structural identification via polyhedral template matching. *Model. Simul. Mater. Sci. Eng.*, 24 (2016), 055007.

258 Nielsen, O. H., Sethna, J. P., Stoltze, P., Jacobsen, K. W., and Nørskov, J. K. Melting a copper cluster: Critical-droplet theory. *Europhys. Lett.*, 26 (1994), 51-56.

259 Alarifi, H. A., Atiş, M., Özdoğan, C., Hu, A., Yavuz, M., and Zhou, Y. Determination of complete melting and surface premelting points of silver nanoparticles by molecular dynamics simulation. *J. Phys. Chem. C*, 117 (2013), 12289-12298.

260 https://sites.google.com/site/eampotentials/Pt, Accessed on 10/09/2016.

261 Yoo, S., Zeng, X.C., and Morris, J.R. The melting lines of model silicon calculated from. *J. Chem.*

Phys., 120 (2004), 1655.

262 Ferrante, J., Rose, J. H., and Smith, J. R. Scaling relations in the equation of state, thermal expansion, and melting of metals. *Appl. Phys. Lett.*, 53 (1984).

263 McFarland, E. W. and Metiu, H. Catalysis by doped oxides. *Chem. Rev.*, 113 (2013), 4391.

264 Shao, X., Prada, S., Giordano, L., Pacchioni, G., Nilius, N., and Freund, H.-J. Tailoring the shape of metal Ad-particles by doping the oxide support. *Angew. Chem. Int. Ed.*, 50 (2011), 11525-11527.

265 Stavale, F., Shao, X., Nilius, N., Freund, H.-J., Prada, S., Giordano, L., and Pacchioni, G. Donor characteristics of transition-metal-doped oxides: Cr-doped MgO versus Mo-doped CaO. *J. Am. Chem. Soc.*, 134 (2012), 11380-11383.

266 Prada, S., Giordano, L., and Pacchioni, G. Charging of gold atoms on doped MgO and CaO: identifying the key parameters by DFT calculations. *J. Phys. Chem. C*, 117 (2013), 9943-9951.

267 Blöchl, P., Först, C., and Schimpl, J. Projector augmented wave method: Ab initio molecular dynamics with full wave functions. *Bull. Mater. Sci.* , 26 (2003), 33-41.

268 Schlexer, P., Ruiz Puigdollers, A., and Pacchioni, G. Tuning the charge state of Ag and Au atoms and clusters deposited on oxide surfaces by doping: A DFT study of the adsorption properties of nitrogen- and niobium-doped TiO_2 and ZrO_2. *Phys. Chem. Chem. Phys.*, 17 (2015), 22.

269 Bauschlicher, C. W., Langhoff, S., and Partridge, H. Theoretical study of the positive ions of the dimers and trimers of the group IB metals (Cu, Ag, and Au). *J. Chem. Phys.*, 93 (1990), 8133.

270 Moazami, N., Mahmoudi, H., Rahbar, K., Panahifar, P., Tsolakis, A., and Wyszynski, M.L. Catalytic performance of cobalt–silica catalyst for Fischer–Tropsch synthesis: Effects of reaction rates on efficiency of liquid synthesis. *Chem. Eng. Sci.*, 134 (2015), 374-384.

271 Baudouin, D., Rodemerck, U., Krumeich, F. et al. Particle size effect in the low temperature reforming of methane by carbon dioxide on silica-supported Ni nanoparticle. *J Catal.*, 297 (2013), 27-34.

272 Falconer, J.L. and Zağli, A.E. Adsorption and methanation of carbon dioxide on a nickel/silica catalyst. *J. Catal.*, 62 (1980), 280.

273 Corvaisier, F., Schuurman, Y., Fecant, A., Thomazeau, C., Raybaud, P., Toulhoat, H., and Farrusseng, D. Periodic trends in the selective hydrogenation of styrene over silica supported metal catalysts. *J. Catal.*, 307 (2013), 352-361.

274 Gabrovska, M., Krsti, J., Tzvetkov, P., Tenchev, K., Shopska, M., Vukeli, N., and Jovanov, D. Effect of the support and the reduction temperature on the formation of metallic nickel phase in Ni/silica gel precursors of vegetable oil hydrogenation catalysts. *Russ. J. Phys. Chem. A*, 85 (2011), 2392.

275 Chen, X., Wang, S., Zhuang, J., Qiao, M., Fan, K., and He, H. Mesoporous silica-supported Ni B amorphous alloy catalysts for selective hydrogenation of 2-ethylanthraquinone. *J Catal*, 227 (2004), 419-427.

276 Tauster, S.J., Fung, S.C., Baker, R.T.K., and Horsley, J.A. Strong interactions in supported-metal catalysts. *Science* , 211 (1981), 1121.

277 Wallace, W.T., Min, B.K., and Goodman, D.W. The nucleation, growth, and stability of oxide-supported metal clusters. *Top. Catal.* , 34 (2005), 17.

278 Lopez, N., Pacchioni, G., Maseras, F., and Illas, F. Hybrid quantum-mechanical and molecular

mechanics study of Cu atoms deposition on SiO_2 surface defects. *Chem. Phys. Lett.*, 294 (1998), 611-618.

279 Giordano, L., Del Vitto, A., and Pacchioni, G. Au and Pd atoms adsorbed on pure and Ti-doped SiO_2/Mo (112) films. *J Chem Phys*, 124 (2006), 034701.

280 Levien, L., Prewitt, C.T., and Weidner, D.J. Structure and elastic properties of quartz at pressure. *Am. Mineral.*, 65 (1980), 920.

281 Goumans, T. P. M., Wander, A., Brown, W.A., Richard, C., and Catlow, A. Structure and stability of the (001) α-quartz surface. *Phys. Chem. Chem. Phys.*, 9 (2007), 2146-2152.

282 Tang, C., Zhu, J., Lid, Z. et al. Surface chemistry and reactivity of SiO_2 polymorphs: A comparative study on α-quartz and α-cristobalite. *Appl. Surf. Sci.*, 335 (2015), 1161-1167.

283 Zhuravlev, L. T. and Potapov, V. V. Density of silanol groups on the surface of silica precipitated from a hydrothermal solution. *Russ. J. Phys. Chem*, 80 (2006), 1119.

284 Schlexer, P. and Pacchioni, G. Adsorption and dimerization of late transition metal atoms on the regular and defective quartz (001) surface. *Top. Catal.* (2016), in press.

285 Radzig, V. A. Defects on Activated Silica Surface. In Pacchioni, G. et al., eds., *Defects in SiO_2 and related dielectrics: science and technology*. Kluwer, Dordrecht, 2000.

286 Giordano, L., Sushko, P. V., Pacchioni, G., and Shluger, A. L. Electron trapping at point defects on hydroxylated silica surfaces. *Phys. Rev. Lett.* , 99 (2007), 136801.

287 Lim, K. H., Zakharieva, O., Shor, A. M., and Rösch, N. Modeling metal adsorption at amorphous silica: Gold atoms and dimers as example. *Chem. Phys. Lett.*, 444 (2007), 280-286.

288 Rink, W. R. and Odom, A. L. Natural alpha recoil particle radiation and ionizing radiation sensitivities in quartz detected with EPR: implications for geochronometry. *Nucl. Tracks Radiat. Meas.*, 18 (1991), 163.

289 Vayssilov, G. N., C., Gates B., and Rösch, N. Oxidation of supported rhodium clusters by support hydroxy groups. *Angew. Chem., Int. Ed.*, 42 (2003), 1391-1394.

290 Hu, C. H., Chizallet, C., Mager-Maury, C., Corral-Valero, M., Sautet, P., Toulhoat, H., and Raybaud, P. J. Modulation of catalyst particle structure upon support hydroxylation: ab initio insights into Pd_{13} and Pt_{13}/γ-Al_2O_3. *J. Catal.*, 274 (2010), 99-110.

291 Mager-Maury, C., Chizallet, C., Sautet, P., and Raybaud, P. Platinum nanoclusters stabilized on γ-alumina by chlorine used as a capping surface ligand: A density functional theory study. *ACS Catal.*, 2 (2012), 1346-1357.

292 Schroeder, T., Adelt, M., Richter, B., Naschitzki, M., Bäumer, M., and Freund, H.-J. Epitaxial growth of SiO_2 on Mo(112). *Surf. Rev. Lett*, 7 (2000), 7.

293 Kundu, M. and Murata, Y. Growth of single-crystal SiO_2 film on Ni(111) surface. *Appl. Phys. Lett.*, 80 (2002), 1921.

294 Z. Zhang, Z. Jiang, Y. Yao, D. Tan, Q. Fu, X. Bao. Preparation and characterization of atomically flat and ordered silica films on a Pd(100) surface. *Thin Solid Films*, 516 (2008), 3741.

295 Lichtenstein, L.,.Heyde, M., and Freund, H.-J. Atomic arrangement in two-dimensional silica: From crystalline to vitreous structures. *J. Phys. Chem. C*, 116 (2012), 20426.

296 Morozkin, A. V. and Seropegin, Yu. D. Sm–Ru–Ge System at 1070 K. *J. Alloys Compd.*, 365 (2004), 168-172.

297 Klimeš, J., Bowler, D.R, and Michaelides, A. Van der Waals density functionals applied to solids. *Phys. Rev. B*, 83 (2011), 195131.

298 Paier, P., Marsman, M., Hummer, K., Kresse, G., Gerber, I.C, and Ángyán, J.G. Screened hybrid density functionals applied to solids. *J. Chem. Phys.*, 124 (2006), 154709.

299 Tosoni, S., Pascale, F., Ugliengo, P., Orlando, R., Saunders, V. R., and Dovesi, R. Quantum mechanical calculation of the OH vibrational frequency in crystalline solids. *Mol. Phys.*, 103 (2005), 2549.

300 Ewing, G. E. and Pimentel, G. C. Infrared spectrum of solid carbon monoxide. *J. Chem. Phys.*, 35 (1961), 925.

301 Włodarczyk, R., Sierka, M., Sauer, J. et al. Tuning the electronic structure of ultrathin crystalline silica films on Ru (0001). *Phys. Rev. B*, 85 (2012), 085403.

302 Schlexer, P., Pacchioni, G., Włodarczyk, R., and Sauer, J. CO adsorption on a silica bilayer supported on Ru(0001). *Surf. Sci.*, 648 (2016), 2-9.

303 Kneitz, S., Gemeinhardt, J., Steinrück, and H.P. A molecular beam study of the adsorption dynamics of CO on Ru(0001), Cu(111) and a pseudomorphic Cu monolayer on Ru(0001). *Surf. Sci.*, 440 (1999), 307-320.

304 Hammer, B., Morikawa, Y., and Nørskov, J.K. CO chemisorption at metal surfaces and overlayers. *Phys. Rev. Lett.*, 76 (1996), 2141-2144.

305 McEwen, J. S. and Eichler, A. Phase diagram and adsorption-desorption kinetics of CO on Ru (0001) from first principles. *J. Chem. Phys.*, 126 (2007), 094701.

306 Boscoboinik, J.A., Yu, X., Emmez, E. et al. Interaction of probe molecules with bridging hydroxyls of two-dimensional zeolites: A surface science approach. *J. Phys. Chem. C*, 117 (2013), 13547-13556.

307 Mantz, A.W., Maillard, J.P., Roh, W.B., and Narahari Rao, K. Ground state molecular constants of $^{12}C^{16}O$. *J. Mol. Spectrosc.*, 57 (1975), 155-159.

308 Badger, R.M. The relation between the internuclear distances and force constants of molecules and its application to polyatomic molecules. *J. Chem. Phys.*, 3 (1935), 710-714.

309 Sicolo, S. and Sauer, J. Interaction of CO with electron-rich defects on MgO (100). *J. Phys. Chem. C*, 117 (2013), 8365-8373.

310 Goniakowski, G. and Noguera, C. Electronic states and Schottky barrier height at metal/MgO (100) interfaces. *Interface Sci.*, 12 (2004), 93-103.

311 Giordano, L., Cinquini, F., and Pacchioni, G. Tuning the surface metal work function by deposition of ultrathin oxide films: Density functional calculations. *Phys. Rev. B*, 73 (2006), 045414.

312 Stampfl, C. and Scheffler, M. Energy barriers and chemical properties in the coadsorption of carbon monoxide and oxygen on Ru (0001). *Phys. Rev. B*, 65 (2002), 155417.

313 Pfnür, H., Menzel, D., Hoffmann, F.M., Ortega, A., and Bradshaw, A.M. High resolution vibrational spectroscopy of CO on Ru (001): The importance of lateral interactions. *Surf. Sci.*, 93 (1980), 431-452.

314 Schlexer, P., Giordano, L., and Pacchioni, G. Adsorption of Li, Na, K, and Mg atoms on amorphous and

crystalline silica bilayers on Ru (0001): A DFT study. *J. Phys. Chem. C*, 118 (2014), 15884-15891.

315 Lichtenstein, L., Büchner, C., Yang, B. et al. The atomic structure of a metal-supported vitreous thin silica film. *Angew. Chem. Int. Ed.*, 51 (2012), 404.

316 Yang, B., Shaikhutdinov, S., and Freund, H.-J. Ultrathin silicatene/silicon-carbide hybrid film on a metal substrate. *Surf. Sci.* , 632, (2015), 9–13.

317 Schlexer, P. and Pacchioni, G. Modelling of an ultra-thin silicatene/silicon-carbide hybrid film. *J. Phys. Cond. Matter.*, 28 (2016), 364005.

318 Chou, M. Y. and Chelikowsky, J. R. First-principles study of hydrogen adsorption on Ru(0001): Possible occupation of subsurface sites. *Phys. Rev. Lett.*, 59 (1987), 1737.

319 Chou, M. Y. Theoretical study of hydrogen adsorption on Ru(0001): Possible surface and subsurface occupation sites. *Phys. Rev. B*, 39 (1989), 5623.

320 Kostov, K. L., Widdra, W., and Menzel, D. Hydrogen on Ru(001) revisited: vibrational structure, adsorption states, and lateral coupling. *Surf. Sci.*, 560 (2004), 130-44.

321 Boscoboinik, J. A., Yu, X., Yang, B. et al. Modeling zeolites with metal-supported two-dimensional aluminosilicate films. *Angew. Chem. Int. Ed.*, 51 (2012), 6005.

322 Farrauto, R. J. and Heck, R. M. Catalytic converters: state of the art and perspectives. *Catal. Today*, 51 (1999), 351-360.

323 Du, M., Sun, D., Yang, H. et al. Influence of Au Particle Size on Au/TiO_2 Catalysts for CO Oxidation. *Phys. Chem. C*, 118 (2014), 19150-19157.

324 Valden, M., Pak, S., Lai, X., and Goodman, D.W. Structure sensitivity of CO oxidation over model Au/TiO_2 catalysts. *Catal. Lett.*, 56 (1998), 7-10.

325 Knell, A., Barnickel, P., Baiker, A., and Wokaun, A. CO oxidation over Au/ZrO_2 catalysts: Activity, deactivation behavior, and reaction mechanism. *J. Catal.*, 137 (1992), 306-321.

326 Schumacher, B., Denkwitz, Y., Plzak, V., Kinne, M., and Behm, R.J. Kinetics, mechanism, and the influence of H_2 on the CO oxidation reaction on a Au/TiO_2 catalyst. *J. Catal*, 224 (2004), 449-462.

327 Kim, H. Y., Lee, H. M., and Henkelman, G. CO oxidation mechanism on CeO_2-supported Au nanoparticles. *J. Am. Chem. Soc.*, 134 (2012), 1560-1570.

328 Widmann, D. and Behm, R.J. Active oxygen on a Au/TiO_2 catalyst: formation, stability, and CO oxidation activity. *Angew. Chem. Int. Ed.*, 50 (2011), 10241.

329 Widmann, D., Krautsieder, A., Walter, P., Brückner, A., and Behm, R. J. How temperature affects the mechanism of CO oxidation on Au/TiO_2: A combined EPR and TAP reactor study of the reactive removal of TiO_2 surface lattice oxygen in Au/TiO_2 by CO. *ACS Catal.*, 6 (2016), 5005-5011.

330 Kotobuki, M., Leppelt, R., Hansgen, D.A., Widmann, D., and Behm, R.J. Reactive oxygen on a Au/TiO_2 supported catalyst. *J. Catal.*, 264 (2009), 67.

331 Widmann, D. and Behm, R. J. Activation of molecular oxygen and the nature of the active oxygen species for CO oxidation on oxide supported au catalysts. *Acc. Chem. Res.*, 47 (2014), 740.

332 Bader, R. F. W. A quantum theory of molecular structure and its applications. *Chem. Rev.*, 91 (1991), 893-928.

333 Setvín, M., Aschauer, U., Scheiber, P. et al. Reaction of O_2 with subsurface oxygen vacancies on TiO_2 anatase (101). *Science*, 341 (2013), 988.

334 Su, X., Xu, J., Liang, B., Duan, H., Hou, B., and Huang, Y. Catalytic carbon dioxide hydrogenation to methane: A review of recent studies. *J. Energy Chem.*, 25 (2016), 1-13.

335 Zittel, W., Wurster, R., and Bolkow, L. *Advantages and Disadvantages of Hydrogen. Hydrogen in the Energy Sector.* Systemtechnik Gmbitt., 1996.

336 Nilsson, A., Pettersson, L.G.M, and Nørskov, J.K. *Chemical bonding at surfaces and interfaces.* Elsevier, 2011.

337 Agnelli, M., Kolb, M., and Mirodatos, C. CO hydrogenation on a Nickel catalyst: 1. Kinetics and modeling of a low-temperature sintering process. *J. Catal.*, 148 (1994), 9-21.

338 Xu, J., Su, X., Duan, H. et al. Influence of pretreatment temperature on catalytic performance of rutile TiO_2-supported ruthenium catalyst in CO_2 methanation. *J. Catal.*, 333 (2016), 227–237.

339 Gupta, N.M., Kamble, V.S., Kartha, V.B., Iyer, R.M., Ravindranathan Thampi, K., and Gratzel, M. FTIR spectroscopic study of the interaction of CO_2 and CO_2 + H_2 over partially oxidized Ru/TiO_2 catalyst. *J. Catal.*, 146 (1994), 173-184.

340 Garbarino, G., Bellotti, Riani, D.P., Magistri, L., and Busca, G. Methanation of carbon dioxide on Ru/Al_2O_3 and Ni/Al_2O_3 catalysts at atmospheric pressure: Catalysts activation, behaviour and stability. *Int. J. Hydrogen Energ.*, 40 (2015), 9171-9182.

341 Abe, T., Tanizawa, M., Watanabe, K., and Taguchi, A. CO_2 methanation property of Ru nanoparticle-loaded TiO_2 prepared by a polygonal barrel-sputtering method. *Energy Environ. Sci.*, 2 (2009), 315-321.

342 Eckle, S., Anfang, H.-G., and Behm, R. J. Reaction intermediates and side products in the methanation of CO and CO_2 over supported Ru catalysts in H_2-rich reformate gases. *J. Phys. Chem. C*, 115 (2011), 1361-1367.

343 Gao, J., Liu, Q., Gu, F., Liu, B., Zhong, Z., and Su, F. Recent advances in methanation catalysts for the production of synthetic natural gas. *RSC Adv.*, 5 (2015), 22759-22776.

344 Studt, F., Behrens, M., Kunkes, E.L. et al. The mechanism of CO and CO_2 hydrogenation to methanol over cu-based catalysts. *ChemCatChem*, 7 (2015), 1105-1111.

345 Kunkes, E. L., Studt, F., Abild-Pedersen, F., Schlögl, R., and Behrens, M. Hydrogenation of CO_2 and CO to methanol on $Cu/ZnO/Al_2O_3$: Is there a common intermediate or not? *J. Catal.*, 328 (2015), 43-48.

346 Bando, K. K., Sayama, K., Kusama, H., Okabe, K., and Arakawa, H. In-situ FT-IR study on CO_2 hydrogenation over Cu catalysts supported on SiO_2, Al_2O_3, and TiO_2. *Appl. Catal. A*, 165 (1997), 391-409.

347 Chen, H. Y. T., Tosoni, S., and Pacchioni, G. Adsorption of ruthenium atoms and clusters on anatase TiO_2 and tetragonal ZrO_2 (101) surfaces: A comparative DFT study. *J. Phys. Chem. C*, 119 (2015), 10856-10868.

348 Chen, H. Y. T., Tosoni, S., and Pacchioni, G. Hydrogen adsorption, dissociation, and spillover on Ru_{10} clusters supported on anatase TiO_2 and tetragonal ZrO_2 (101) surfaces. *ACS Catal.*, 5 (2015), 5486.

349 Akamarua, S., Shimazakib, T., Kuboc, M., and Abe, T. Density functional theory analysis of methanation reaction of CO_2 on Ru nanoparticle supported on TiO_2(101). *Appl. Catal. A*, 470 (2014),

405-411.

350 Islam, M. M., Calatayud, M., and Pacchioni, G. Hydrogen adsorption and diffusion on the anatase TiO_2 (101) surface: A first-principles investigation. *J. Phys. Chem. C*, 115 (2011), 6809-6814.

351 Liu, C., Yang, B., Tyo, E. et al. Carbon dioxide conversion to methanol over size-selected Cu_4 clusters at low pressures. *J. Am. Chem. Soc.*, 137 (2015), 8676-8679.

352 Nørskov, J. K., Bligaard, T., Rossmeisl, J., and Christensen, C. H. Towards the computational design of solid catalysts. *Nat. Chem.*, 1 (2009), 37-46.

List of publications

Status: December 2016

H-index: 4 (Source: scopus.com), 5 × first author, ORCID: 0000-0002-3135-9089

Published papers reported in this thesis

2016 "Modeling of an ultra-thin silicatene/silicon-carbide hybrid film", P. Schlexer, G. Pacchioni, *J. Phys. Condens. Matter*, 28 (2016) 364005

"Adsorption and dimerization of late transition metal atoms on the regular and defective quartz (001) surface", P. Schlexer, G. Pacchioni, *Top. Catal.*, (2016) *in press*.

"CO adsorption on a silica bilayer supported on Ru(0001)", P. Schlexer, G. Pacchioni, R. Włodarczyk, J. Sauer, *Surf. Sci.*, 648 (2016), 2-9

2015 "Tuning the charge state of Ag and Au atoms and clusters deposited on oxide surfaces by doping: A DFT study of the adsorption properties of nitrogen- and niobium-doped TiO_2 and ZrO_2", P. Schlexer, A. Ruiz Puigdollers, G. Pacchioni, *Phys. Chem. Chem. Phys.*, 17 (2015) 22342-22360

"Gold and silver clusters on TiO_2 and ZrO_2 (101) surfaces: Role of dispersion forces", A. Ruiz Puigdollers, P. Schlexer, G. Pacchioni, *J. Phys. Chem. C*, 119 (2015) 15381-15389

Other published papers

"Dense or porous packing? Two-dimensional self-assembly of star-shaped mono-, bi-, and terpyridine derivatives", D. Trawny, P. Schlexer, K. Steenbergen, J. P. Rabe, B. Paulus, H.-U. Reissig, *ChemPhysChem*, 16 (2015) 949-953

"Characterizing crystalline-vitreous structures: from atomically resolved silica to macroscopic bubble rafts", K. M. Burson, P. Schlexer, C. Büchner, L. Lichtenstein, M. Heyde, and H.-J. Freund, *J. Chem. Educ.*, 92 (2015) 1896-1902 **[Open access]**

2014 "Adsorption of Li, Na, K, and Mg atoms on amorphous and crystalline silica bilayers on Ru(0001): A DFT study", P. Schlexer, L. Giordano, G. Pacchioni, *J. Phys. Chem. C*, 118 (2014) 15884-15891

"Topological investigation of two-dimensional amorphous materials", C. Büchner, P. Schlexer, L. Lichtenstein, S. Stuckenholz, M. Heyde, H.-J. Freund, *Z. Phys. Chem.*, 228 (2014) 587-607